Multiscale and Multiphysics of Blood Flow and Arterial Mechanics Growth and Remodeling

A DISSERTATION SUBMITTED TO THE FACULTY OF THE

UNIVERSITY OF MINNESOTA

BY

Marisa S. Bazzi

IN PARTIAL FULFILLMENT OF THE REQUIREMENTS

FOR THE DEGREE OF

DOCTOR OF PHILOSOPHY

Advisor: Victor H. Barocas

January 2024

Acknowledgments

First, I wanted to express my deepest gratitude to my PhD advisor, Prof. Victor Barocas, who has been an incredible mentor throughout my academic journey. Victor’s support and guidance have been instrumental in shaping my growth as a professional. He went above and beyond the role of an advisor. He did not just help me navigate the PhD program; he provided a nurturing environment where I could thrive and be my best version, even during challenging times. His wisdom and encouragement pushed me to achieve more than I thought possible. I am genuinely thankful for his dedication and investment in my success.

I also wanted to thank my M.Sc. advisor, prof. Marcio Carvalho, who I am lucky enough to have as one of my committee members. Marcio, your mentorship during my master's set the base for my transition into the Ph.D. program. Your belief in my potential opened doors and set the stage for my continued academic pursuit. Beyond the limits of academia, your friendship and support during the tough times of my initial year remain engraved in my memory.

To Carly, Shannon, Hadi, Ruturaj, Adam, Jason, Ruskin, Kara, Kayla, and Ryan, thanks for making our lab the best place to be. The camaraderie and positive atmosphere you all create have made every day an absolute joy. How you bounce ideas around and provide insights has been instrumental in shaping my work and pushing boundaries.

Thank you for being an amazing group, fostering such a fantastic climate in our office, and simply being incredible labmates!

To my Brazilian chosen family: Sonia, Siane, Mateus, Beatriz, Ricardo, Raphael and Larissa. I can't express enough gratitude for having such an incredible family away from home. Your presence has made the distance so much easier to bear. You've turned what could've been homesickness into moments of warmth and belonging. Without a doubt, you are the family I feel incredibly fortunate to have chosen. You'll forever hold a special place in my heart. Love you all dearly.

To my best friend, Nicolle. Even though miles separate us, your presence in my life has been my constant anchor. Your support, comforting shoulder, and friendship have been the light on my darkest days. Thank you for being there, no matter the distance. I love you!

To my boyfriend, and life partner Adam. Meeting you was undoubtedly one of the best outcomes of my PhD journey. Your comforting hugs and constant cheerful presence have been my anchor through the ups and downs of navigating the Ph.D. program. I feel incredibly fortunate to share my life with someone as supportive and caring as you. Thank you for not just encouraging my dreams but also joining me on this incredible journey together.

And finally, to my beloved family: Pai e mãe, não há palavras para expressar o quanto sou grata por tudo. Eu sei o quão desafiadora a vida tem sido para nós,

mas ver a força de vocês diante dos obstáculos é o meu lembrete diário de que posso conquistar qualquer coisa. Amo vocês incondicionalmente.

À minha irmã gêmea, obrigada por compartilhar cada momento de vida comigo desde o ventre da nossa mãe. Obrigada por me ensinar a ser forte, mesmo quando o caminho fica dificil. Obrigada por cuidar dos nossos pais com tanto amor e dedicação. Voce é minha fonte de inspiração diaria. Eu tenho tanto orgulho de ser sua irmã. Te amo absurdamente.

À minha irma mais velha, Mari. Nada do que alcancei teria sido possível sem tudo o que você fez por nós. Desde os nossos primeiros momentos de infância até a minha vinda para os EUA, você tem sido uma presença constante, sendo mais do que uma irmã, uma segunda mãe. Agradeço por assegurar que tivéssemos tudo o que precisávamos para ir à escola e por ser nossa maior incentivadora nos estudos. E, acima de tudo, agradeço imensamente por nos acolher em sua casa e fornecer o apoio necessário para eu perseguir os meus sonhos. Te amo demais!

Abstract

The circulatory system, resembling a complex network of pipes (blood vessels) and a ceaseless pumping system (heart), orchestrates the delivery of oxygen and nutrients to every cell and tissue in the human body. Unlike conventional engineering pipes, vascular tissue exhibits the remarkable ability to adapt its physical and mechanical properties in response to its environment, a phenomenon known as growth and remodeling (G&R). This process aims to maintain a balanced stress level, termed homeostatic stress.

In healthy arteries, maintaining mechanical equilibrium involves a clever negative feedback loop that restores the system to its preferred state after any disturbances. However, when this delicate balance is disrupted, it can lead to a phenomenon called pathological G&R, characterized by a positive feedback loop.

Aortic and intracranial aneurysms are prominent examples of this disrupted G&R. Characterized by the enlargement of vessels, aneurysms pose significant health risks, contributing to numerous annual fatalities. Moreover, blood disorders such as sickle cell disease can disrupt mechanical equilibrium by altering blood flow dynamics and creating localized hypoxia, especially in small arteries, such as the one found in our brain. Therefore, recognizing the connection between blood disorders and tissue-related diseases underscores the importance of exploring the interplay between fluid dynamics and tissue mechanics.

This thesis investigates the interplay between computational fluid dynamics, mathematical modeling, and finite element analysis in the context of cardiovascular diseases. It primarily focuses on ascending thoracic aneurysms and intracranial aneurysms related to sickle cell disease. Our objective is to enhance our understanding of the intricate mechanisms underlying vascular diseases. This heightened insight will be central in developing more holistic diagnostic and therapeutic approaches to effectively lessen their significant impact on individuals' health.

Table of Contents

List of Tables

List of Figures

Chapter 1: Introduction

This thesis delves into the intersection of computational fluid dynamics, mathematical modeling, and finite element analysis, applied to better understand cardiovascular diseases, mainly focusing on sickle cell disease (SCD) and ascending thoracic aneurysm (ATAA).

SCD, a genetic disorder, involves polymerizing a mutant hemoglobin molecule (sickle hemoglobin, HbS) in low blood oxygen conditions[1]. This polymerization causes red blood cells to assume a sickle shape and adopt a stiffer structure. These changes affect the blood flow dynamics significantly and can lead to complications like vaso-occlusive crisis, aneurysm, and stroke [2, 3]. This links a blood disorder – SCD - with tissue-related diseases like aneurysms, emphasizing the significance of exploring the intersection of fluid dynamics and tissue mechanics. Therefore, chapters 3 and 4 focus on the ramifications of SCD on blood rheology and how it alters the blood flow dynamics and oxygen transport, especially in ICAs. I employed mathematical modeling and simulations combined with experimental data for those studies.

ATAA refers to the enlargement of the ascending region of the aorta, the main blood vessel leaving the heart. Aortic aneurysms are a particularly dangerous pathology, contributing to over 17,000 deaths per year in the U.S. and ranking as the 15th most prevalent cause of death [4]. The critical concern with ATAA lies not solely in its occurrence; individuals with a stable ATAA can maintain a healthy lifestyle. However, unstable growth can result in aortic failure through rupture or

delamination of the layers (dissection). Existing techniques for assessing the presence of unstable aneurysm, and consequently the risk of failure, primarily focus on monitoring aortic diameter and growth rate [5]. Unfortunately, these approaches fail to provide a comprehensive diagnosis, often resulting in inadequate prediction of the actual risk [6]. Chapter 5 delves into potential new FSI-based biomarkers for aneurysm outcomes using mouse models and blood flow dynamics. Chapters 6 and 7 propose two G&R approaches to investigate the time-dependent nature of the disease.

Beyond its scientific significance, this research addresses diseases with substantial social impact: SCD, a hereditary disorder, exhibits significantly higher prevalence in minority communities [7], while ATAA disproportionally affects Black, Hispanic, and Indigenous people who are more prone to aortic rupture and more severe complications compared to white patients [8].

1.1 Summary of Accomplishments.

Chapter 3: Patient-specific blood rheology in sickle cell disease.

This chapter investigates the impact of SCD on blood viscosity and its implications for brain vasculature stress. We quantified sickle blood velocity fields across varying oxygen tensions and shear rates through a combined experimental-computational approach. Employing a continuum model fitted to our experimental data yielded patient-specific rheological parameters, highlighting systemic alterations in sickle blood flow from arteries to veins.

Integrating patient-specific rheological parameters into a 3D model of patient-derived brain vasculature allowed the estimation of fluid flow parameters. This study showcases the potential of experimentally derived continuum models as predictive tools for patient-specific care. Furthermore, these fully coupled models hold promise in identifying patients at higher risk of cerebrovascular complications like aneurysms and stroke.

I presented a portion of this research at the Summer Biomechanics, Bioengineering, and Biotransport Conference (SB3C) in Seven Springs, PA, USA, in 2019 and as a virtual lightning talk at SB3C in 2020. This work culminated in a co-first-author publication in the Biophysical Journal [9].

Contribution disclaimer: This work was performed in collaboration with the Living Devices Lab at the University of Minnesota. The experimental data were collected by the co-first author, Jose Valdez, and I conducted the computational design and analysis.

Chapter 4: Effects Of Sickle Cell Diseases in The Blood Flow and Oxygen Transport within Intracranial Aneurysms.

This chapter explores the correlation between SCD and intracranial aneurysms (ICA), known for their association with neurological complications like subarachnoid hemorrhage (SAH) in SCD patients. Our hypothesis revolves around the interplay among oxygen levels, blood viscosity, and oxygen transport,

potentially reducing available oxygen in arterial tissue and increasing susceptibility to ICA and SAH in SCD patients.

To test this hypothesis, we conducted a comprehensive study investigating the geometric and rheological effects on oxygen transport within blood. Our findings indicate that reduced oxygen availability within intracranial aneurysms, particularly in SCD patients, impacts the apparent viscosity and oxygen distribution. The diminished oxygen supply potentially contributes to ICA development and compromised tissue stability, leading to SAH.

I presented segments of this research at SB3C in 2023 and the 28th Congress of the European Society of Biomechanics in the Netherlands. The work is currently a co-first-author submission under review at the Journal of Biomechanical Engineering.

Contribution disclaimer: This work was performed in collaboration with Dr. Hadi Wiputra, a postdoctoral associate at Barocas Lab. Both of us were involved in performing computational design and data analysis.

Chapter 5: Mouse-Specific Biofluidic and Geometric Biomarkers of Ascending Thoracic Aortic Aneurysm Outcomes

This chapter explored potential noninvasive predictive indicators for ascending thoracic aortic aneurysm outcomes by studying the correlation between geometrical and biofluid biomarkers. Mouse-specific fluid-structure-interaction

models were constructed for genetically modified mice (Fbln4SMKO) at ages two- and six-months using MRI images and mechanical tests on aortas post-sacrifice.

Comparing various geometrical and biofluidic metrics to the mouse lifespan revealed that measurements linked to wall shear stress, pressure, and flow direction displayed stronger correlations with lifespan than traditional geometric metrics like aortic diameter and growth rate. These findings emphasize the viability of alternative noninvasive biomarkers to supplement current clinical decision-making tools.

I presented a segment of this research as a virtual lightning talk at SB3C in 2021. The culmination of this work resulted in a first-author publication in the Journal of Cardiovascular Engineering and Technology [10].

Contributions disclaimer: This work was performed in collaboration with the Wagenseil Vascular Mechanics Laboratory from the Department of Mechanical Engineering & Materials Science at Washington University in St. Louis. The experimental data were collected at Professor Wagenseil's lab, and I performed the computational design and analysis.

Chapter 6: Hemodynamics-Driven Aortic Growth and Remodeling for Genetically Modified Mice Model.

This chapter explores the maladaptive growth and remodeling of aortic tissue, particularly in ascending thoracic aortic aneurysms (ATAA), focusing on the *Fbln4*^{SMKO} mouse model. For the study, I incorporated a comprehensive Fluid-Solid

Interaction (FSI) approach and growth/remodeling models to analyze and predict the progression of ATAA in a controlled subject-specific setting. The G&R approach was used in mouse models lacking fibulin-4 expression in smooth muscle cells. Those mouse models enabled detailed and controlled longitudinal studies on aortic G&R, allowing for individualized and precise assessments of arterial changes.

The results captured overall aortic growth and provided insights into local growth patterns, particularly in response to biomechanical stress. Correlation analyses were conducted between measured quantities (lifespan, maximum diameter, aortic tortuosity index, and aortic material properties) and growth time constants. This analysis revealed significant correlations, especially between longitudinal growth time constant and ascending aortic stiffness, and well and axial growth time constant and tortuosity index. Additionally, the performance of single-domain and multiple-domain models was evaluated, showcasing differences in precision and accuracy in predicting aortic growth in the Fbln4SMKO mouse models.

Overall, this study advances our understanding of ATAA progression by integrating advanced modeling techniques with subject-specific data, paving the way for personalized risk assessment and potential treatment planning in patients with aortic aneurysms. The work is being prepared for a first-author manuscript to be submitted soon.

Chapter 7: Fluid-Structure-Based Multiscale Model of Hemodynamics-Driven Arterial Growth and Remodeling.

This chapter investigates the hemodynamics-driven multiscale growth and remodeling (G&R) process of aortic aneurysms. For that, we combine experimental and computational approaches to study how macroscale biofluidic, geometrical, and biomechanical factors affect the microscale G&R process of the aortic tissue, potentially leading to the formation of unhealthy growth. To predict and assess the tissue changes during G&R, I created a tool that integrates fluid-solid interaction with microscale growth and remodeling. I can use the stresses from simulations using subject-based models to solve the growth and remodeling on the cellular scale.

The methodology encompasses three illustrative cases: simulated aortic arch inflation, an idealized thoracic aorta analysis, and a subject-specific mouse model mimicking aneurysm development. The results showcase stress-driven growth patterns, microscale remodeling, and local stress concentrations critical in understanding aneurysm progression. This integrated approach offers a significant advancement in comprehending tissue responses to stress, presenting a promising avenue to explore how stress distribution influences tissue remodeling, thereby advancing beyond the constraints of traditional continuum-scale models. I presented a portion of this work at SB3C in 2022 and the 27th Congress of the European Society of Biomechanics in Portugal.

Chapter 2: Background

Copyright Notice: Figures 1 and 2 were created using bioRender.com under the academic license.

The circulatory system functions as intricate machinery, resembling a complex network of pipes (blood vessels) and a ceaseless pumping system (heart), responsible for delivering oxygen and nutrients to every cell and tissue in our body. Unlike conventional engineering pipes, vascular tissue has the ability to adapt its physical and mechanical properties in response to its environment. This process is known as growth and remodeling (G&R), and it is thought to occur to maintain a balanced stress level, known as homeostatic stress[11].

In healthy arteries, mechanical homeostasis is characterized by a negative feedback loop, where a preferred state is restored after a perturbation. However, conditions such as hypertension and vascular aging or diseases like aneurysm and atherosclerosis can disrupt homeostasis. In such cases, a positive feedback loop often emerges, leading to pathological G&R of the arterial tissue[12].

To better understand this process, it is essential to examine the components that constitute each aspect of cardiovascular mechanics and G&R; here, we divide those components into vessel structure and blood flow dynamics, which are generally studied by separated areas (tissue mechanics versus fluid dynamics).

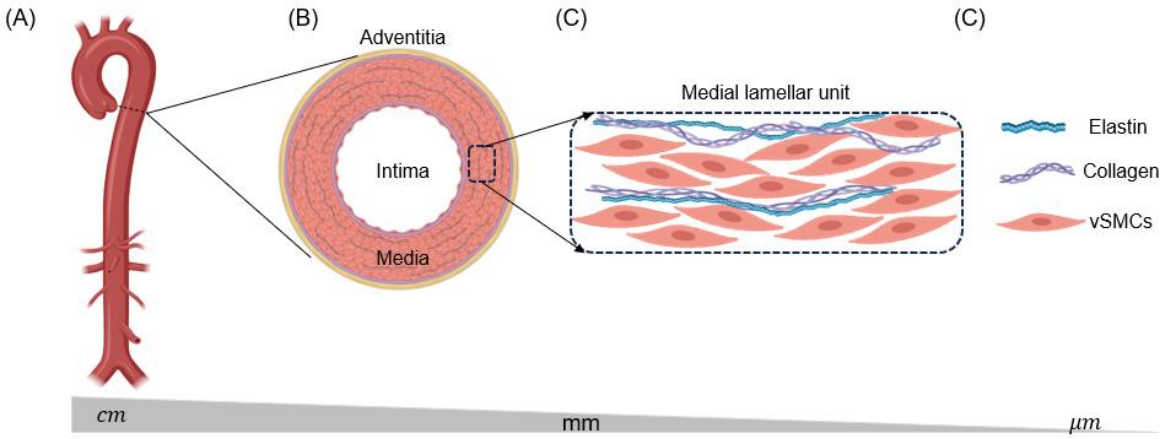

Figure 1: *Schematics of the multiscale nature of the vascular tissue. (A) Full aorta, featuring the ascending and descending region. (B) A section of wall, featuring the three layers: intima, media, and adventitia. (C) Illustration of the medial lamellar unit, featuring the repeated structure of elastin/collagen sheets and vascular smooth muscle cells (vSMCs). (D) Two main components of the extracellular matrix, collagen and elastin and contractile phenotype of the vSMCs*

2.1 Vessel structure

A healthy blood vessel wall is composed of three distinctive layers, as illustrated in **Error! Reference source not found.**, each characterized by functionally distinct t ypes of vascular matrices:

1. Adventitia – the outermost layer: Mostly composed of interconnected collagen fibers, adventitia is essential in providing structural support to the vessel. These collagen fibers are connected with fibroblasts and nerve cells, extending their influence from the adventitia into the media, potentially signaling smooth muscle cells. Additionally, the adventitia is a host to the vasa vasorum, a network of tiny vessels supplying blood to the outer layers of the artery, reaching beyond the diffusion limit within the arterial wall [13].

2. Tunica media or media – the middle layer: Often the thickest layer in most arterial vessels [14], the media comprises elastin and collagen fibers, smooth muscle cells, and fibroblasts. This layer tends to organize into repeated structures of elastin/collagen sheets with some interlamellar collagen fiber and smooth muscle cells between known –medial lamellar unit (MLU) configurations.

3. Tunica intima or intima – the innermost layer: Constituting the interface within blood circulation, the intima presents a unique composition. It comprises a basement membrane and a loose array of collagen and elastic fibers covered by an endothelial sheet. This layer has a central importance in the biochemical and mechano-regulatory processes. The endothelial sheet is a selective barrier to the blood flow and prevents the adhesion of most molecules, circulating cells, and platelets to prevent thrombosis and clotting. The endothelial layer also mediates the contraction of smooth muscle cells in the artery by releasing nitric oxide and other vasoactive chemicals [13].

Suppose we step down a scale from the arterial wall. In that case, we look at the components of the arterial tissue, which, from a mechanical perspective, can be divided into cells (most notably, smooth muscle cells) and extracellular matrix.

Vascular smooth muscle cells (vSMCs) are highly specialized and differentiated cells in adults whose principal function is the contraction of blood vessels, regulating blood vessel tone and diameter, and thus controlling blood pressure and tissue oxygenation in the blood vessels [15]. vSMCs are formed by thin (actin)

and thick (myosin) contractile filaments and cytoskeletal filaments. Actin is the most noticeable feature of the vSMCs, filling most of the cell's cytoplasm.

vSMCs possess remarkable phenotypic plasticity that allows rapid adaptation to fluctuations in the environment cues. They can be found in two distinct phenotypes: contractile and synthetic [16]. Contractile SCMs display a spindle-shaped morphology [17] and are generally found in healthy arteries, while synthetic vSMCs are rhomboidal and have cobblestone morphology [18]. Synthetic vSMCs express lower levels of proteins involved in contraction and are characterized by increased proliferation and migration [19]. Cardiovascular diseases such as atherosclerosis and aneurysms are associated with vSMCs phenotypic switching.

vSMCs produce most of the main components of the ECM, such as proteoglycans, collagen, and elastin, as well as many proteins responsible for the equilibrium between synthesis (lysyl oxidase) and degradation (metalloproteinases, plasminogen activators) of the ECM.

The structural integrity of the vascular wall hinges upon the extracellular matrix (ECM), a complex network of proteins and fibers serving as its foundational scaffold. In arteries and veins, the ECM, often called the stroma or matrix, constitutes more than half of the wall mass and mainly contains elastin and collagen fibers.

The ECM is not an inert supporting network but an active and dynamic structure with a fundamental role in regulating vascular function in normal and pathological conditions. Let us take a closer look at each component:

1- Elastin is an insoluble and hydrophobic protein resulting from the crosslinking of tropoelastin. Tropoelastin is typically produced by vSMCs within the media and by fibroblasts in the adventitia. Once produced, tropoelastin is released to the ECM, which undergoes crosslinking facilitated by lysyl oxidase, along with helper proteins like fibulin-4, -5. Elastin is the dominant ECM component in arterial walls, constituting about 50% of its dry weight, significantly contributing to the mechanical integrity and elasticity of the arteries [20]. Under normal circumstances, the formation of elastic fibers occurs primarily during fetal development and infancy. Once formed, mature elastic fibers last throughout an individual's lifespan, establishing them as the most resilient element of the ECM [21]. Elastin can degrade and fragment with aging and disease, and because elastin expression is turned off in adults, more collagen fibers are deposited in the arterial wall, contributing to increased stiffness [22]. Moreover, beyond its structural role, elastin performs essential regulatory functions. It influences vSMCs by governing their migration, inducing contractile phenotypes [23], and inhibiting proliferation [24].

2- Collagen is a notably stiff protein that limits vessel distension. Within at least 24 distinct subtypes [25], collagen's form and presence varies based on the structure and function of different vessels. Unlike elastin, collagen production persists throughout an individual's life. Cells like fibroblasts and vSMCs actively secrete

collagen, which, in turn, can undergo degradation via many mechanisms. The collagen secretion or breakdown rate varies, depending on the local microenvironment, ranging from few minutes to a few hundred days [26]. Beyond its structural function, collagen interacts with vascular cells, contributing to vSMCs differentiation, adhesion, migration, proliferation, and apoptosis.

Finally, fibulins are a recently recognized family of ECM proteins, encompassing five isoforms known as fibulin-1, -2, -3, -4, -5 [27]. While fibulin-3 is an exception, all other fibulin isoforms have been identified during cardiovascular development and are primarily induced following injury. Notably, the interaction between fibulins like fibulin-4 and -5 and tropoelastin plays a pivotal role in assisting elastin assembly, contributing significantly to the structural integrity of the vessel wall. The absence of fibulin-4 has been observed to disrupt elastogenesis completely. Vascular defects manifest in mice lacking fibulin-4 (Fbln4−/−), leading to artery tortuosity, irregularities, aneurysms, and even rupture. Consequently, genetically engineered mice with a knockout of fibulin-4 have been instrumental in studying cardiovascular diseases, particularly aneurysms [10, 28].

2.2 Blood composition and flow dynamics

Human blood can be visualized as a suspension of solid particles (tiny blood cells) in an aqueous medium

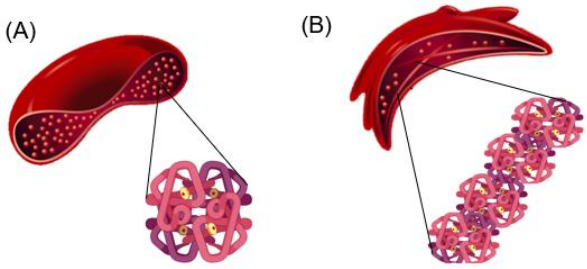

***Figure 2**: (A) Schematics of the structure of a healthy red blood cell, featuring a hemoglobin molecule displaying the 4-heme sites. (B) A sickle red blood cells featuring a polymerized hemoglobin chain.*

(plasma). Roughly 55% of the blood is plasma, composed of dissolved electrolytes, proteins, and metabolites. Plasma is the medium for gas and nutrient transport, waste removal, and immune function. Plasma is a Newtonian fluid [29]. On the other hand, the blood cells, predominantly red blood cells (RBCs), along with white blood cells, including leukocytes, contribute to increased blood viscosity, resulting in their non-Newtonian character [30].

RBCs are packed with hemoglobin, an iron-rich protein responsible for binding oxygen. The hemoglobin structure incorporates four heme groups, facilitating the cooperative binding and release of oxygen and optimizing gas exchange throughout the body, as depicted in Figure 2A. Healthy RBCs are biconcave in shape due to their flexible structure. This shape and mechanics allow the RBCs to navigate the microvascular network, minimize the shear stress, and enhance their movement within the bloodstream [31].

Sickle cell disease (SCD) is a genetic mutation affecting the RBCs' hemoglobin. Sickle hemoglobin, also known as HbS, undergoes a polymerization process when exposed to deoxygenated conditions. This process triggers the formation of fibrous precipitates, as shown in Figure 2B [32], altering the physical and mechanical properties of the RBCs.

Sickle RBCs exhibit increased rigidity and stickiness, adopting a sickle-like shape that makes them more prone to forming clusters in the bloodstream. This clustering elevates the risk of vaso-occlusion. Apart from reduced deformability, sickle RBCs become more prone to hemolysis. Healthy RBCs have about 120 days lifespan,

while sickle RBCs have a much shorter lifespan of around 20 days, which causes hemolytic anemia in sickle cell patients [33].

2.3 Mathematical models of tissue mechanics and blood flow dynamics

The most predominant approach to mathematically describe the mechanical behavior of tissue mechanics and blood flow dynamics is via the discipline of continuum mechanics. Emphasizing the macroscopic behavior, continuum mechanics represents material properties as averages derived from the microscopic activities of individual particles. While continuum mechanics is a complex field, this section briefly overviews some crucial concepts essential for comprehending this work.

The mechanical behavior of both tissue and blood can be described by conservation equations. The main difference between the conservation equation for tissue mechanics and blood flow dynamics is the choice of framework. As a subdivision of solid mechanics, Tissue mechanics is generally represented by the Lagrangian formulation. At the same time, blood flow dynamics is a subdivision of fluid dynamics, generally represented by the Eulerian approach.

2.3.1 Mathematical description of tissue mechanics: basic notation

The Lagrangian framework utilizes a control volume formed by infinitesimally small line segments, where the framework follows the motion of these segments. Thus, the infinitesimally small line segments, $d\boldsymbol{x}$ can deform and transition to new configurations, $d\boldsymbol{X}$. This deformation is characterized by the deformation gradient

tensor $\boldsymbol{F}$, which mathematically describes the transformation between the undeformed and deformed configurations.

$$d\boldsymbol{x} = \boldsymbol{F}d\boldsymbol{X}$$

[1]

The determinant of the deformation gradient $J = \det(\boldsymbol{F})$ is always positive and measures local changes in the volume during the transformation. Using the polar theorem, $\boldsymbol{F} = \boldsymbol{R} \cdot \boldsymbol{U}$ can be decomposed into a rigid body rotation tensor $\boldsymbol{R}$, symmetric and positive definite stretch tensor $\boldsymbol{U}$.

The right Cauchy-Green deformation tensor, defined in the undeformed configuration and invariant concerning rigid body motion, is often preferred in the tissue mechanics formulation, and it is given by:

$$\boldsymbol{C} = \boldsymbol{F}^T \cdot \boldsymbol{F} = \boldsymbol{U}^T \cdot \boldsymbol{R}^T \cdot \boldsymbol{R} \cdot \boldsymbol{U} = \boldsymbol{U}^T \cdot \boldsymbol{U}$$

[2]

Additionally, a standard strain measure defined in the undeformed configuration is the Green-Lagrange strain tensor:

$$\boldsymbol{E} = \frac{1}{2}(\boldsymbol{C} - \boldsymbol{I})$$

[3]

In terms of stress definition, we have the Cauchy stress tensor $\boldsymbol{\sigma}$, which is defined concerning the deformed configuration, and the first Piola-Kirchhoff stress tensor $\boldsymbol{P}$, defined in the undeformed configuration, and they are related as follows:

$$\boldsymbol{P} = J\boldsymbol{\sigma} \cdot \boldsymbol{F}^{-T}$$

[4]

Additionally, the second first Piola-Kirchhoff stress tensor $\boldsymbol{S}$ can be obtained from $\boldsymbol{P}$ or $\boldsymbol{\sigma}$ as:

$$\boldsymbol{S} = \boldsymbol{F}^{-1} \cdot \boldsymbol{P} = J\boldsymbol{F}^{-1} \cdot \boldsymbol{\sigma} \cdot \boldsymbol{F}^{-T}$$

[5]

A strain energy density function, Ψ, is generally employed to model hyper-elastic behavior, such as cardiovascular tissue. Strain energy functions are used to describe the energy stored or transmitted in the process of mechanical deformation. It approximates the phenomenological behavior of the tissue, and it's given by:

$$\mathbf{S} = 2\frac{\partial \Psi}{\partial \boldsymbol{C}} = \frac{\partial \Psi}{\partial \boldsymbol{E}}$$

[6]

2.3.2 Mathematical description of tissue mechanics: balance equations

We can define the conservation equations now that all the important notations are established. The two main ones we will highlight here are the conservation of mass and linear momentum.

The conservation of mass, also known as the continuity equation, assumes that, without growth and remodeling, the body's mass is conserved. Using the undeformed configuration, it yields to [34]:

$$\frac{dm}{dt} = \frac{d}{dt}\int \rho_0 dV = 0$$

[7]

Where ρ_0 is the mass density per unit of volume in the undeformed configuration.

The linear momentum conservation states that change in the linear momentum must equal all external forces acting on the body, and it can be written as [34]:

$$\overline{\nabla} \cdot \boldsymbol{\sigma} + \boldsymbol{b} = \rho \boldsymbol{a} \quad [8]$$

Where $\boldsymbol{\sigma}$ is the Cauchy stress tensor, $\boldsymbol{b}$ is the body force per unit of deformed volume, ρ is the mass density per unit of volume in the deformed configuration, $\boldsymbol{a}$ is the material acceleration.

2.3.3 Mathematical description of tissue mechanics: a strain energy density for arteries.

Holzapfel, Gasser, and Ogden [35, 36] proposed a strain energy function to describe the behavior of arterial tissue, also known as the HGO model. The HGO strain energy density model $\Psi_{\mathrm{HGO}}(\boldsymbol{C}, \boldsymbol{H})$ accounts for the superposition of the isotropic, non-collagenous ground matrix $\Psi_{\mathrm{g}}(\boldsymbol{C})$ and the two transversely isotropic embedded collagen fiber families $\sum_{i=1}^{2} \Psi_{\mathrm{fi}}(\boldsymbol{C}, \boldsymbol{H_i})$.

$$\Psi_{\mathrm{HGO}}(\boldsymbol{C}, \boldsymbol{H}) = \Psi_{\mathrm{g}}(\boldsymbol{C}) + \sum_{i=1}^{2} \Psi_{\mathrm{fi}}(\boldsymbol{C}, \boldsymbol{H_i}) \quad [9]$$

The non-collagenous matrix is modeled as a neo-Hookean [37]:

$$\Psi_{\mathrm{g}}(\boldsymbol{C}) = \frac{c}{2}(I_1 - 3) \quad [10]$$

Where $I_1 = \mathrm{tr}\boldsymbol{C}$ is the first invariant of $\boldsymbol{C} = \boldsymbol{F}\boldsymbol{F}^{\boldsymbol{T}}$, and c is the neo-Hookean parameter. The collagenous matrix is given by:

$$\Psi_{\mathrm{fi}}(\boldsymbol{C}, \boldsymbol{H_i}) = \frac{k_1}{2k_2}[\exp(k_2(\boldsymbol{H}_i : \boldsymbol{C} - 1)^2) - 1] \quad [11]$$

$$\boldsymbol{H}_i = \kappa \boldsymbol{I} + (1 - 3\kappa)(\boldsymbol{a_{oi}} \otimes \boldsymbol{a_{oi}}) \quad [12]$$

Where $k_1 > 0$, and $k_2 > 0$ is the stress-like and dimensionless parameter, respectively. $\boldsymbol{H}_i : \boldsymbol{C}$ denotes an invariant of the symmetric generalized structure tensor $\boldsymbol{H}_i$, κ characterize the fiber dispersion of fiber *i* with mean orientation $\boldsymbol{a_{oi}}$.

2.3.4 Mathematical description of blood flow dynamics: balance equations

For blood dynamics, a Eulerian frame of reference is preferred. The Eulerian frame assumes that the control volume is fixed, but the direction of the flow field inside can change. Thus, mass, momentum, and energy depend on the fluxes caused by fluid flow through the boundaries of the control volume. In this case, the conservation of mass is written as:

$$\frac{d\rho}{dt} + \nabla \cdot (\rho \mathbf{v}) = 0 \quad [13]$$

Where ρ is the mass density of the blood, ∇ the gradient operator, and $\mathbf{v}$ is the velocity.

The linear conservation of momentum is written as:

$$\frac{\partial(\rho \mathbf{v})}{\partial t} + \nabla \cdot (\rho \mathbf{v}\mathbf{v}) = -\nabla p + \nabla \cdot \boldsymbol{\tau} + \boldsymbol{B} \quad [14]$$

Where p is pressure, $\boldsymbol{\tau}$ is the stress tensor, and $\boldsymbol{B}$ is the body forces. The stress tensor is generally a function of the velocity gradient of the fluid velocity $\nabla \mathbf{v}$ or the local strain rate tensor. It depends on the rheological model used to define the fluid.

In this work, two main rheological models are Newtonian and non-Newtonian Carreau Yasuda models. The Newtonian model assumes the Cauchy stress is linearly correlated to the local strain rate tensor, $\nabla \mathrm{v}$, and the blood viscosity, η, is constant [38]:

$$\boldsymbol{\tau} = \eta(\nabla \mathbf{v}^T + \nabla \mathbf{v}) \quad [15]$$

The Carreau-Yasuda model accounts for the shear-thinking behavior of the blood by making the viscosity dependent on the shear rate, $\dot{\gamma}$:

$$\eta = \eta_\infty + (\eta_0 - \eta_\infty)[1 + (\lambda\dot{\gamma})^a]^{\frac{n-1}{a}}, \quad [16]$$

where η_0 is the zero-shear-rate viscosity, η_∞ is the infinite-shear-rate viscosity, n is an exponent that determines the steepness of the viscosity curve, a is a dimensionless parameter that describes the transition from the zero-shear-rate region to the power-law region, and λ is a time constant associated with the critical shear-rate $\dot{\gamma}_{cr} \propto 1/\lambda$ where the power-law region starts.

2.4 Growth and remodeling approaches

As previously discussed, vascular tissue, like other living tissue, has the ability to adjust its physical (growth) and mechanical (remodeling) properties to maintain a hemostatic stress level. Mathematically, descriptions of the G&R processes come in various approaches, and they can be broadly divided into two main groups: phenomenological and mechanistic models.

Phenomenological models are typically based on the nonlinear continuum mechanics approach. These models attempt to simulate cause-and-effect relationships within the tissue, such as changes in vessel diameter due to an increase in arterial pressure. In contrast, mechanistic models aim to incorporate aspects of biological processes, such as cell activity and microenvironment [39].

2.4.1 The finite growth theory

The finite growth theory, known as kinematic growth, is a widely used phenomenological approach due to its simplicity and low computational cost [40], [41]. This model describes the growth process via a growth gradient tensor. $\boldsymbol{F}_g$, which captures the stress-free changes due to change in mass. In this case, the total deformation experienced by the tissue is described by combining elastic and growth deformation. $\boldsymbol{F} = \boldsymbol{F}_e \boldsymbol{F}_g$.

This approach has been used to look at aortic remodeling [42, 43], even incorporating some features of development and maturity of the tissue [44]. The

challenge of the model comes from the fact that the growth deformation needs to be prescribed constitutively.

2.4.2 The constrained-mixture theory

The constrained mixture theory is a robust mechanistic framework that can capture individual tissue constituents' different behaviors and properties, such as the variation in half-lives between elastin and collagen [45 – 48]. In its most basic form, the theory assigns a volume fraction to each constituent, represented by ϕ^i, where *i* denotes the specific constituent (e.g., collagen, elastin, or vascular smooth muscle cells). The total solid volume fraction ϕ^s of the tissue is then calculated as the sum of the individual constituent volume fractions:

$$\phi^s = \sum_i \phi^i \qquad [17]$$

The theory assumes that the constituents are independent and possess unique strain energy density functions. The overall stress and strain of the tissue are obtained by summing the contributions from each constituent:

$$\boldsymbol{\sigma} = \sum_i \phi^i \, \boldsymbol{\sigma}^i \qquad [18]$$

While the constrained mixture theory offers a robust and deterministic approach to modeling cardiovascular tissue's growth and remodeling (G&R), its implementation can be computationally expensive and complex. Consequently, hybrid models

have emerged in recent years [49 – 52] to investigate the development of aneurysms. These models combine elements of the constrained mixture theory, including mass turnover and prestress, with simpler equations for mass production and deposition rates, offering a more computationally efficient approach.

2.4.3 Micromechanical models

Micromechanical models are concerned about fiber level response to changes in the level of stress. Jia and Nguyen [48] proposed a G&R model for soft tissue based on the concurrent action of collagen deposition and degradation, and they used the model to investigate the development of stress and strain homeostasis of a spherical collagenous tissue membrane in response to a perturbation in the internal pressure. The model recovered the equilibrium membrane stress before the pressure perturbation, similar to the experimental observations [54, 55].

Extending Jia and Nguyen's work, Mahutga *et al.* [56, 57] have proposed a computational microstructural model for the G&R process using a fiber network approach. The fiber network represents the medial lamellar unit, containing the three main fiber families relevant to wall mechanics: collagen, elastin, and actin, or stress fibers. In Mahutga's model, the G&R laws are applied directly to discrete, individual fibers, with the models tailored to different fiber families.

2.5 Current simulation techniques to model blood flow dynamics and tissue mechanics

Numerous numerical techniques tackle the partial differential equations resulting from conservation laws. In this thesis, finite element analysis (FEA) is the primary approach [58]. FEA is versatile, handling complex geometries, a wide range of boundary conditions, and material properties.

Detailed mathematical aspects are omitted, given the utilization of open-source software—SimVascular [59] for fluid mechanics and fluid-solid interaction and FEBio [60] for tissue mechanics.

2.5.1 Subject-specific modeling

Advances in three-dimensional imaging alongside robust computational capacities have revolutionized medical modeling and simulations. These innovations enable the creation of personalized subject-specific models tailored to individual anatomical and physiological nuances using high-resolution medical images, such as MRI, CT, ultrasound, and PET scans.

These models can often integrate clinical measurements such as pressure, blood flow, and tissue biomechanics to simulate how organs respond to various conditions. They significantly contribute to personalized treatments, disease prognosis, and enhanced precision in healthcare.

This thesis employs SimVascular[59], open-source subject-specific cardiovascular flow modeling software, with supplemental editing performed in Meshmixer (Autodesk, Inc.). In SimVascular, image processing entails four steps:

1) DICOM Import: Import a Digital Imaging and Communications in Medicine (DICOM) image format obtained from MRI or CT scans of a patient or a mouse into SimVascular. With three 2D and one 3D view, the multi-window tool helps accurately identify the artery of interest (Fig. 3A).

2) Centerline Identification: Using the multi-window tool, we can locate the centerlines of the vessel to create a path. The path is a one-dimensional curve to identify the main branches of the arterial system (Fig. 3B).

3) Segmentation: From the path, we can segment the scan using a 2D cross-segmentation technique to identify the boundaries of the medical image. This process generates ring-like shapes along the aorta (Fig. 3C).

4) 3D Model generation: The interpolation of 2D curves from the segmented shapes forms the groundwork for creating a 3D model (Fig. 3D).

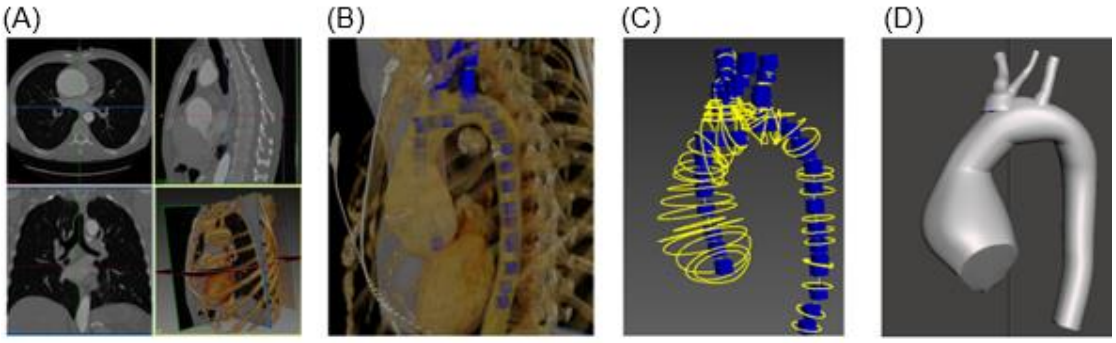

***Figure 3**:SimVascular image processing steps, a) import and visualize a DICOM image, b) generate a path (shown in blue) to represent the branches, c) create a segmentation (shown in yellow), and d) generate the solid model.*

Following the rough artery lumen model from SimVascular, Meshmixer is employed to refine and remesh the lumen, forming the vessel wall. Figure 4A depicts the smoothed and remeshed lumen obtained from this process.

The vessel wall is created by extruding the lumen wall in its normal direction. In this process, the thickness is given by a constant (or not constant) value chosen

according to the artery to be modeled (Fig. 4B). The integration of the lumen and wall is facilitated using SimVascular (Fig. 4C).

2.5.2 Subject-specific boundary conditions

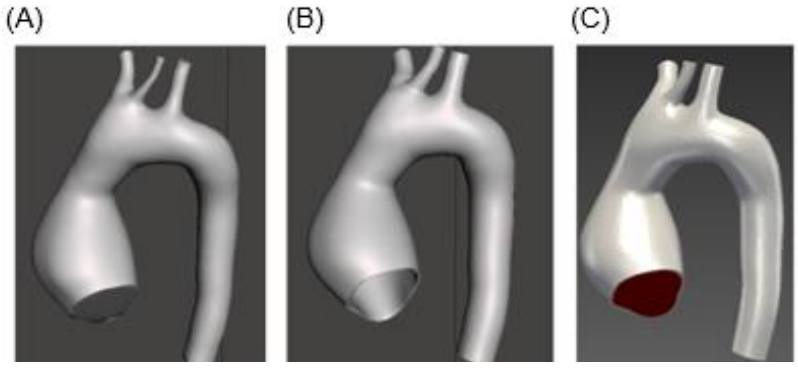

Figure 4*:Meshmixer image tool applied to (A) smooth and remesh the lumen model created in SimVascular, and (B) create a constant thickness vessel wall by extruding the lumen wall, (C) shows both lumen and wall combined in SimVascular.*

Subject-specific modeling requires physiologically relevant boundary conditions (BCs). A summary of the boundary conditions for an FSI subject-specific simulation of the aorta is shown in **Figure 5**. The general approach, and the one used in this thesis, is to use a waveform as the inlet boundary conditions. The waveform contains information about how the blood flow changes over one cardiac cycle, as shown in **Figure 5**B.

A three-element Windkessel model [59],[60] is often applied as outlet boundary conditions to model the peripherical circulation. The model is composed of a proximal resistance. R_p, a capacitance C, and a distal resistance R_d as shown in **Figure 5**B. The proximal resistance models the viscous resistance of the vasculature immediately downstream of the vessel. The distal resistance accounts for the resistance of the capillaries and venous circulation. The capacitance

represents the compliance of the downstream vessels. The boundary condition is described by:

$$\frac{\partial p}{\partial t} + \frac{p}{CR_d} = \frac{Q}{C}\left(1 + \frac{R_p}{R_d}\right) + R_p \frac{\partial Q}{\partial t}$$

Where *p* represents the average pressure at the outlet, and Q represents the flow rate through the vessel. Typically, resistance and capacitance parameters for the Windkessel model are tuned to match the pressure and flow rate from an in vivo measurement.

Finally, to account for the viscoelastic nature of tissue support, a Robin-type boundary condition is commonly applied at the outer wall of the solid domain. This condition is expressed as:

$$\boldsymbol{\sigma} \cdot \boldsymbol{n} = -k_s \boldsymbol{u} - c_s \frac{\partial \boldsymbol{u}}{\partial t} - p_0 \boldsymbol{n}$$

Where $\boldsymbol{u}$ is the displacement, $\boldsymbol{\sigma}$ is the Cauchy stress, $\boldsymbol{n}$ is the normal unit vector. k_s and c_s are parameters that model the viscoelastic response, p_0 the external pressure in the thoracic and abdominal cavity.

2.5.3 Prestress of the solid domain

The arterial wall is never stress-free; rather, it is constantly subjected to mechanical load for the blood pressure and viscous forces. Thus, the anatomical models derived from medical scans are in equilibrium with hemodynamic conditions at diastole. The models must be prestressed to account for the initial loading state.

Two main approaches exist to solve the prestress condition of a medical-based geometry. The first is an iterative approach. The initial zero-stress solution is determined by deflating the model and concurrently inflating it until the prestress geometry matches the original segmentation [63, 64]. The second approach is proposed by Hsu and Bazilevs [65], in which a prestress tensor is calculated in the following steps:

1- An approximation of the traction vector $\boldsymbol{h}$ due to hemodynamic equilibrium condition during diastole is calculated by running a steady-state rigid-wall simulation for the fluid domain. The outlet boundary condition is tuned for the average pressure to match the subject-specific diastolic pressure.

2- The prestress tensor $\boldsymbol{S}_0$ is determined by solving the momentum balance between the structure's internal stresses and the fluid traction. More details on how this step is performed can be found in Baumler *et al*. [66].

3- Once the prestress tensor $\boldsymbol{S}_0$ is determined, FSI

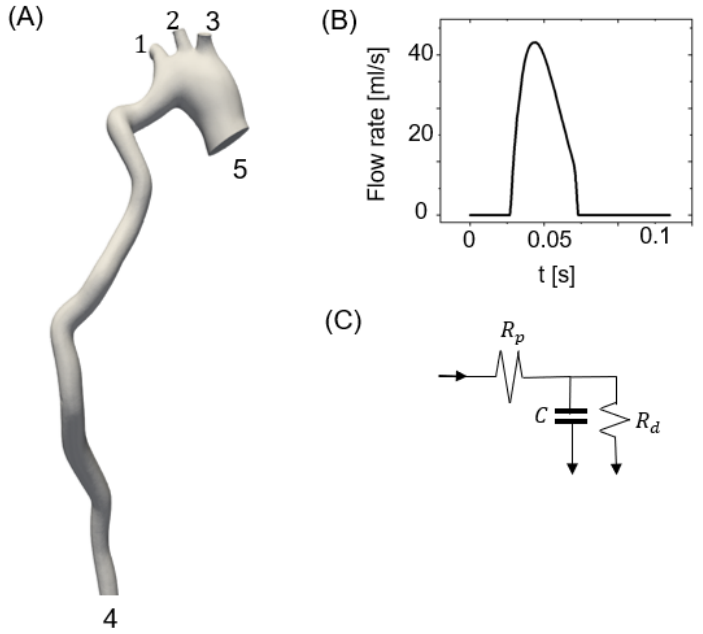

***Figure 5**:(A) Summary of the boundary conditions for an FSI subject-specific simulations of the aorta including: (B) Inflow flow rate waveform for inlet at location 5. (C) Three-element Windkessel model for outlets at locations 1-4,*

simulations are performed by adding $\boldsymbol{S}_0$ to the stress tensor. This way, under diastolic flow conditions, the prestressed wall maintains the shape extracted from the medical scan.

Chapter 3: Patient-Specific Blood Rheology in Sickle Cell Disease.

***Bazzi MS**, Valdez JM, Barocas VH, and Wood DK. An Experimental-Computational Approach to Quantify Blood Rheology in Sickle Cell Disease, Biophys. J. 119, 1-9 (2020); https://doi.org/10.1016/j.bpj.2020.10.011*

Contribution disclaimer: This work was performed in collaboration with the Living Devices Lab at the University of Minnesota. The experimental data were collected by the co-first author, Jose Valdez, and I conducted the computational design and analysis.

Summary

In sickle cell disease, aberrant blood flow due to oxygen-dependent changes in red cell biomechanics is a crucial driver of pathology. Most studies have focused on the potential role of altered red cell deformability and blood rheology in precipitating vaso-occlusive crises. Numerous studies, however, have shown that sickle blood flow is affected even at high oxygen tensions, suggesting a potentially systemic role for altered blood flow in driving pathologies, including endothelial dysfunction, ischemia, and stroke. In this study, we applied a combined experimental-computation approach that leveraged an experimental platform that quantifies sickle blood velocity fields under a range of oxygen tensions and shear rates. We computationally fit a continuum model to our experimental data to generate physics-based parameters that capture patient-specific rheological alterations. Our results suggest that sickle blood flow is altered systemically, from the arterial to the venous circulation. We also demonstrated the application of this approach as a tool to design patient-specific transfusion regimens. Finally, we

demonstrated that patient-specific rheological parameters can be combined with patient-derived vascular models to identify patients who are at higher risk for cerebrovascular complications such as aneurysm and stroke. Overall, this study highlights that sickle blood flow is altered systemically, which can drive numerous pathologies, and this study demonstrates the potential utility of an experimentally parameterized continuum model as a predictive tool for patient-specific care.

3.1 Introduction

Sickle cell disease (SCD) is a hereditary disorder in which a mutant hemoglobin molecule (sickle hemoglobin, HbS) polymerizes under hypoxic conditions [67], [68]. Complications associated with the disease include vaso-occlusive crisis, chronic organ damage, acute chest syndrome, aneurysm, and stroke [69]. To date, our understanding of SCD pathophysiology has been centered around the proximal causes of vaso-occlusion, including altered red cell deformability [70], [71], endothelial adhesion [72], and immune response [73]. With the exception of free heme-induced oxidative stress [74], much less attention has been paid to chronic mechanisms that promote endothelial inflammation and enhanced immune response and that precipitate acute complications including vaso-occlusion and stroke. One potentially significant but overlooked mechanism is systemically altered blood flow due to oxygen-dependent changes in red cell biomechanics and blood rheology [75, 76]. There is evidence that changes in red cell deformability and sickle blood rheology occur even at arterial oxygen tensions [77, 78], suggesting that altered flow could arise throughout the circulation, and could

contribute to endothelial injury, tissue ischemia, inflammation, and other acute pathologies including vaso-occlusive crisis, aneurysm, and stroke [79]. Understanding the potential impact of altered flow will require us to predict important physiologic metrics – e.g. velocity, pressure, shear stress, etc. – in realistic vascular geometries. Making such predictions is complicated by the non-Newtonian nature of blood and the complex nonlinear changes that may occur in sickle blood as it transits the vasculature.

A number of experimental and computational approaches have been applied to understand the biophysical mechanisms of SCD at every scale from molecules to whole blood [80 – 83]. These methods have all provided new insights into factors that impact the erratic rheology that occurs in SCD and that drive the complex clinical behavior patients also exhibit. To describe how sickle blood rheology changes throughout the wide range of vessel sizes, oxygen tensions, and shear rates in the vasculature, however, requires a continuum model that predicts the blood's non-Newtonian flow under a range of conditions using well-defined functions. Moreover, a sickle blood constitutive model should be parameterized using experiments that replicate the physiologic conditions under which altered flow is observed. A constitutive model so specified and validated could, in principle, be used to design patient-specific treatment regimens by understanding how, for example, a well-defined transfusion regimen will alter the patient’s rheological parameters. Moreover, such a model could be combined with patient-specific

vascular models to predict patients at risk for complications such as cerebral aneurysm, which are common in SCD patients [84].

In this study, we applied a combined experimental/computational approach to examine sickle blood rheology under a range of physiologically relevant conditions. We took advantage of recent advances in blood flow imaging and analysis to measure submicron-resolution velocity fields, and we constructed a computational model of the channel flow and regressed model parameters to the measured velocity fields. This approach leverages the richer information content contained in the experimental velocity fields, and it provides simple parameters for a constitutive equation that can be used to translate the data to other geometries and flow conditions. By creating constitutive models, we obviate the need to iterate experimentally the limitless variability in vascular geometries needed to characterize the rheological behavior. In this work, we (1) developed a protocol for the experimental/computational approach proposed in the previous paragraph, (2) used that approach to analyze the rheological behavior of blood from healthy and SCD donors under varying oxygen tension and perfusion level, and (3)

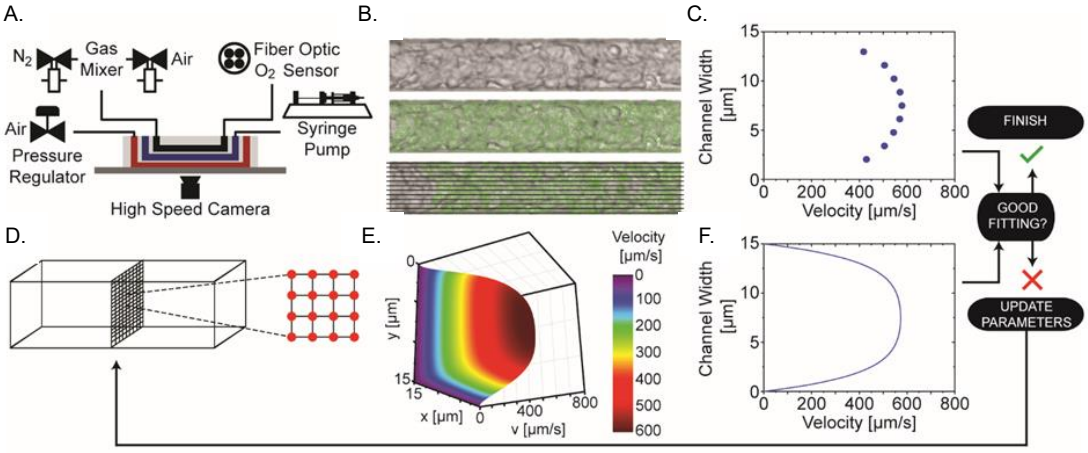

***Figure 6**: Schematic of the combined experimental-computational method, (A) Blood is pumped through a microfluidic system with controlled pressure drop and oxygen tension. (B) Blood flow is recorded by a high-speed camera (top), analyzed to identify trackable features (middle), and tracked to generate a velocity profile (bottom). (C) An experimental profile of velocity vs. position across the channel is generated. (D) Concurrently, a rectangular finite-difference model is generated of the flow in the channel using an initial guess for the Carreau-Yasuda model parameters. (E) Solution of the model equations gives a full velocity profile (i.e., v_z vs. x and y). (F) The velocity profile is averaged through the channel height to give a velocity profile comparable to the experimental profile in (C). The model parameters are adjusted iteratively to minimize the sum of squared error between the model profile and the experimental profile.*

incorporated the derived parameters into an illustrative finite-element simulation of blood flow in a realistic vessel geometry.

3.2 Materials and Methods

3.2.1 Blood Sample Collection

Blood samples from SCD patients and from normal, healthy donors were collected at the University of Minnesota Medical Center and Massachusetts General Hospital under Institutional-Review-Board-approved protocols. All blood samples were stored for a few hours and up to three days prior to testing in the microfluidic

device setup (**Figure 6**A). *Additional blood sample testing and data collection details are given in the Supplemental Information.*

3.2.2 Combined Experimental - Computational Approach

The essence of our approach is shown in **Figure 6**. Briefly, the experimental component consists of a microfluidic system (**Figure 6**A), described previously [85], that allows control of flow rate and oxygen tension, with simultaneous pressure-drop monitoring (allowing pressure drop control) and high-speed, high-resolution video recording of the blood flow (**Figure 6**B). Taking the flow direction to be z, the channel width to be x, and the channel height to be y, the video recording allows generation of a height-averaged velocity profile $v_z(x)$, as in **Figure 6**C. The same profile is generated computationally via a finite-difference model of Carreau-Yasuda flow (**Figure 6**D, E) in the channel and appropriate averaging of the finite-difference solution. The model equation is:

$$\eta = \eta_\infty + (\eta_0 - \eta_\infty)[1 + (\lambda\dot{\gamma})^a]^{\frac{n-1}{a}}, \quad [19]$$

where η is the apparent viscosity as a function of shear rate $\dot{\gamma}$, η_0 is the zero-shear-rate viscosity, η_∞ is the infinite-shear-rate viscosity, n is an exponent that determines the steepness of the viscosity curve, a is a dimensionless parameter that describes the transition from the zero-shear-rate region to the power-law region, and λ is a time constant associated with the critical shear-rate $\dot{\gamma}_{cr} \propto 1/\lambda$ where the power-law region starts. The parameters $\eta_\infty,\ \eta_0,\ n,\ a,$ and λ are iterated to minimize the error between the experimental and model profiles (**Figure 6**F). A

slip velocity is introduced along the wall to match the apparent slip observed experimentally (cf. [85, 86]). *Further methodological details are given in Supplemental Information.*

3.3 Results

3.3.1 Model Validation: Pressure Drop Sweep on Healthy Blood

Initial validation was performed by conducting a study of healthy blood over a range of pressure drops (**Figure 12**A-B). For the approach to be valid, the model parameters should be the same or nearly so for the same blood under different flow conditions. All parameters showed a variation of less than 5% over three different oxygen levels (0, 6, 12%, oxygen level defined as the percentage of oxygen in atmospheric air), and five different pressure drops (0.2, 1, 2, 3, 4 psi). In addition to providing a good validation test, the calculated parameter values established a healthy-blood baseline used in the other studies described in this paper. *Detailed results from the validation study are provided in the Supplemental*

Information.

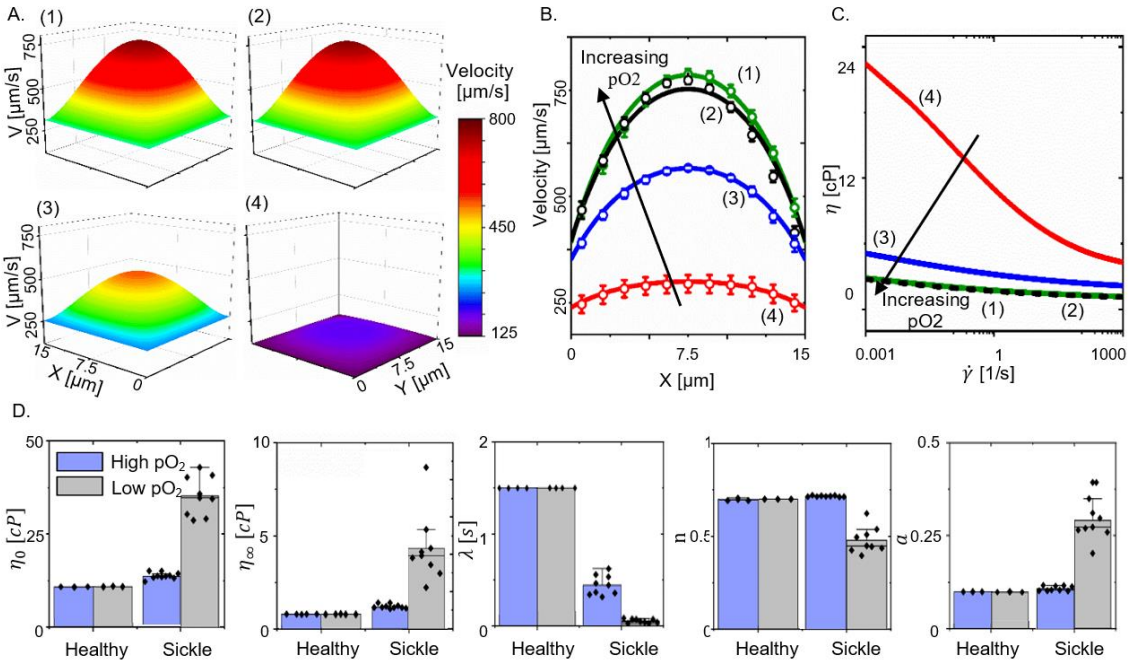

Figure 7: *Healthy vs. SCD Blood at high and low oxygen tensions at 1 psi pressure drop. (A) 4 dimensional velocities for healthy at 12% oxygen tension for four cases: (1), healthy at 0% oxygen tension (2), sickle at 12% oxygen tension (3), and sickle at 0% oxygen tension (4). Even at 0% oxygen tension, the healthy blood (2) shows a much higher flow rate than the SCD blood at 12% oxygen tension (3), and the thickening of the SCD blood at 0% oxygen tension is even more pronounced. (B) Experimental (circles) and model (lines) velocity profiles for the four cases shown in (A). (C) Viscosity-shear-rate plot constructed using the fitted model parameters. The SCD blood shows a high degree of shear thinning and a very large low-shear modulus. (D) Comparison of the specific model parameter values shows no significant change for any parameter with oxygen tension for the healthy blood. For the SCD blood, in contrast, both viscosities increase sharply at low oxygen tension, and the other parameters also change.*

3.3.2 Healthy vs. Sickle-Cell Disease, High vs. Low Oxygen Tension

In light of the well-established sensitivity of SCD blood to changes in oxygen tension, we compared parameter values determined at high (12%) and low (0%) oxygen tension for both SCD blood (>70% HbS) and healthy blood (0% HbS); all

experiments were performed at 1.0 psi pressure drop. The gross observations were as expected and consistent with previous studies [83, 85]: at high oxygen tension, the flow rate of SCD blood was lower than that of healthy blood at the same pressure drop, indicating a higher viscosity, and at low oxygen tension, the difference was amplified considerably as the healthy blood remained unchanged but the SCD blood thickened. The blunting of the velocity profile near the center of the channel (**Figure 7**A, B) is indicative of high low-shear viscosity. The model was able to fit the data quite well for all cases.

Because the entire profile was fit, not just the total flow rate, a single experiment was sufficient to generate a viscosity-vs.-shear-rate curve (**Figure 7**C), in which the extreme thickening of the SCD blood at low oxygen tension is seen. It is also clear from **Figure 7**C that the amount of shear-thinning exhibited by the SCD blood at low oxygen tension was higher than that for high oxygen tension or healthy blood.

Turning to the model details, the most striking feature of the curves in **Figure 7**C is supported by the first two plots in **Figure 7**D. Both the low-shear (η_0) and high-shear (η_∞) viscosity rose sharply for the low-oxygen, SCD case. Other, more subtle changes also occurred. A decrease in λ corresponds to an increase in the transition shear rate, indicating that the SCD blood not only has a higher viscosity at high and low shear, but it tends more strongly towards the (higher) zero-shear viscosity, further increasing its resistance to flow. The increase in a for the low-oxygen SCD blood suggests a sharper transition to the power-law regime, and the decrease in

n suggests a stronger dependence on the shear rate at high viscosity. Taken together, these results indicate that the SCD blood becomes more resistant to flow via multiple different effects.

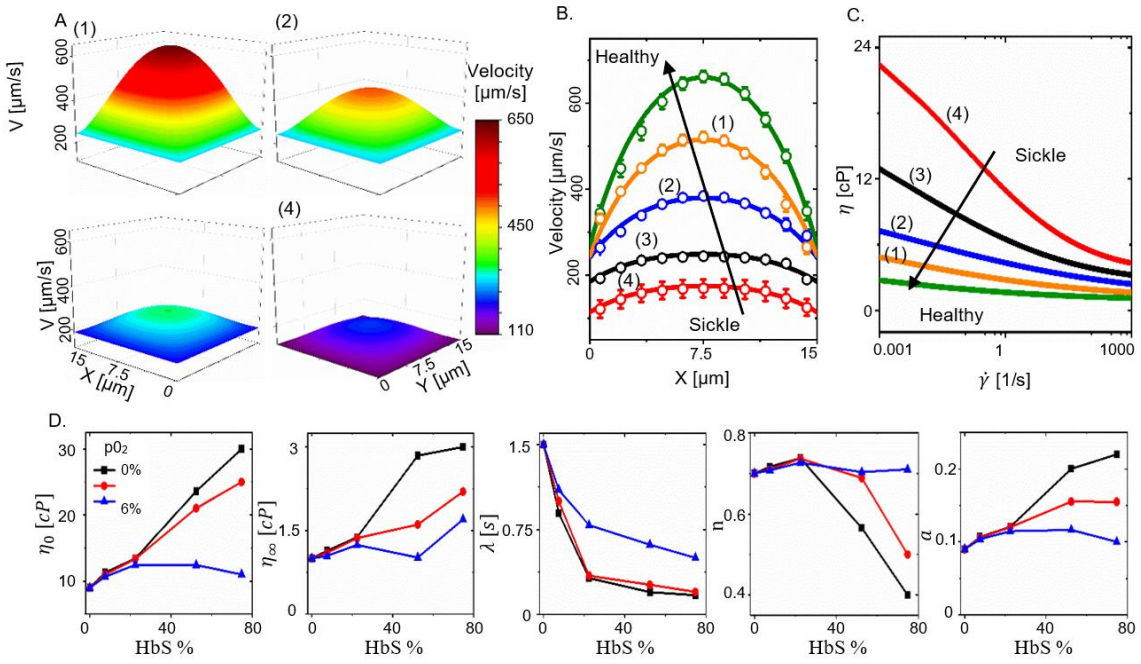

***Figure 8**: Dose-dependent effect of transfusion on low-oxygen-tension SCD blood flow. (A) The velocity profile for the highest-transfused case (1) is slightly lower than that observed for healthy blood, as seen in Figure 2a above. As the sickle cell fraction is increased, the blood becomes increasingly more viscous, leading to reduced velocity and a blunter velocity profile. HbS levels: (1) 7.4% (2) 22.4% (3) 52.8% (4) 74.8% (B) The velocity profile becomes lower and flatter with increased sickle cell fraction (numbers correspond to panels in (A). (C) The calculated viscosity increases with sickle cell fraction at all shear rates; the curve for 52.4% sickle cells (black) is very close to that for 74.8% sickle cells (red). (D) The individual model parameters show little oxygen-dependence at low HbS% but diverge at higher HbS%.*

3.3.3 Transfusion Effects on the Blood Rheology

Blood transfusion is a primary treatment method for severe SCD [87], with two main goals:1) to provide healthy red blood cells to the patient to increase oxygen capacity, and (2) to lower the blood viscosity, allowing the blood to flow more freely

[88]. Although chronic transfusion is beneficial in the treatment of the disease, there are many risks associated with the procedure, such as alloimmunization and excess iron, which leads to damage in the liver, heart, and other organs. At present, the target levels of chronic transfusion therapy aim for a hemoglobin level of 10 g/dl and <30% HbS cells [89]. These target levels, however. are not patient-dependent, and less aggressive targets could still prove beneficial while easing the burden on blood supply and limiting transfusion-associated risks. To study the effect of transfusion, we applied our analytical procedure to blood from an SCD patient mixed with healthy blood to create HbS fractions from 0% (pure healthy blood) to 74.8% (pure SCD blood). Again, oxygen tensions of 0, 6%, and 12% were used, with a focus on the 0% oxygen case since the effect of SCD is most pronounced at low oxygen tension.

As can be seen in **Figure 8**, there was a dose-dependent response, with the velocity profile becoming faster and steeper (i.e., less blunted) as the fraction of healthy blood was increased (**Figure 8**A, B). The wall slip velocity increases as the HbS fraction increases from 22.4% HbS to 74.8% HbS (**Figure 8**B, line (2) to (4)), but is nearly identical for lower HbS fraction (**Figure 8**B, line (1) vs (2)). Viscosity-shear-rate curves showed an increase in viscosity and more pronounced shear thinning behavior with an increase in the HbS fraction at all shear rates (**Figure 8**C).

The dose-dependency was explored in further detail by plotting the different model parameters vs. HbS at different oxygen tensions (**Figure 8**D). There are two

striking results. First, even very low HbS fractions (7.4%) lead to changes in the blood rheology, which are quantifiable in terms of the model parameters. Second, the lack of dependence of the model parameters on oxygen tension, seen in the healthy blood case in **Figure 8**D, is maintained for 7.4% HbS and for 22.4% HbS for all parameters except for some change in λ; that is, the different curves in the plots of **Figure 8**D nearly overlap for 0%, 7.4%, and 22.4% HbS, and then start to spread for larger HbS levels. At low levels of HbS (up to 22.4%), the presence of the sickle cells alters blood rheology, but in an oxygen-independent manner. As the HbS fraction increases, however, the oxygen dependence emerges and intensifies.

Further analysis (**Figure 13**A-B, details in *Supplemental Information*) showed a strong correlation among the model parameters, especially at low oxygen tensions. In particular, the low-shear and high-shear viscosities, η_0 and η_∞, were highly correlated ($r^2 = 0.96$) whereas the correlation between η_0 and λ was less strong ($r^2 = 0.69$). Thus, we focused on the parameters η_0 and λ as descriptors of blood rheology. As can be seen in **Figure 9**A, the viscosity changes with pO2 and HbS% were quite smooth, with the highest viscosity in the low pO2 – high HbS% region in the upper left corner of the contour plot. **Figure 9**A also shows the relatively small effect of oxygen tension on viscosity at low HbS fraction, transitioning to a

large effect at high HbS fraction. **Figure 9**B shows similar behavior, with the lowest λ value (i.e., the highest transition shear rate) in the low-oxygen, high-HbS region.

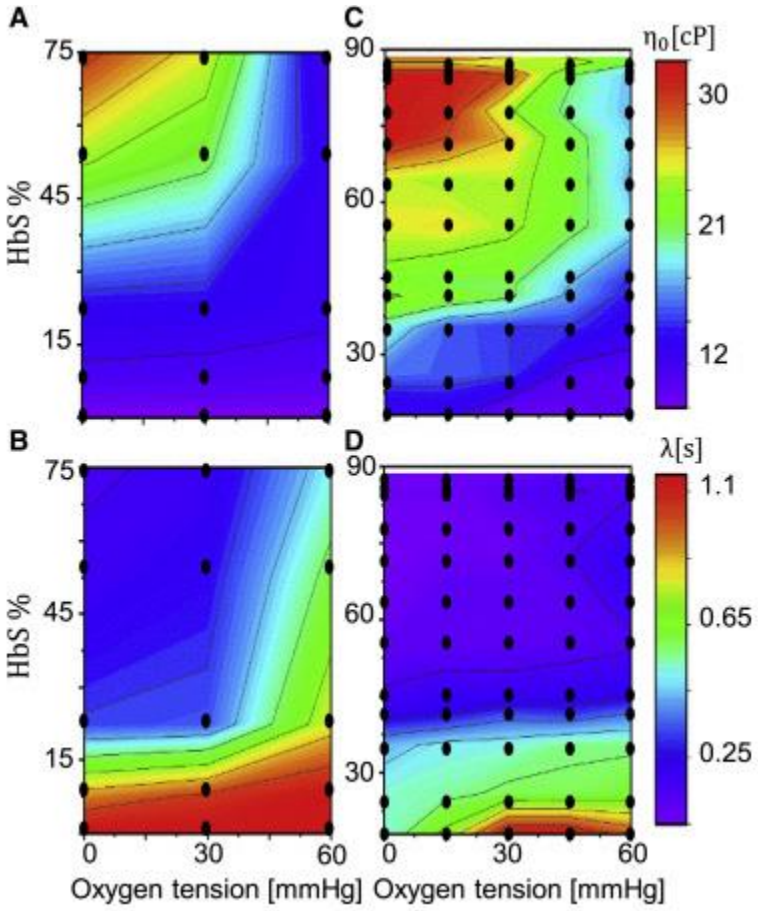

Figure 9*: Contours plots for non-Newtonian model parameters. Each black dot represents one blood sample at one oxygen tension. Contours for (A) η_0, and (B) λ for the transfusion study of a single patient shows that non-Newtonian parameters change smoothly with sickle cell fraction and oxygen tension. Contours plots for (C) η_0, and (D) λ based on blood from 12 different patients suggest that other individual factors can affect blood viscosity in different patients. Each black dot represents one blood sample at one given oxygen tension.*

3.3.4 PO2 Effects on the Blood Rheology for Multiple Patients

The data of **Figure 9**A and **Figure 9**B were combined with additional data on blood from 12 different SCD patients, leading to the contour plots of **Figure 9**C

and **Figure 9**D. In spite of the fact that numerous other individual factors may affect blood viscosity in different patients [70], the contour plots show consistent trends, with the most severe features (high η_0 and low λ) arising at high HbS% and low pO2, as expected. Fitting the data with a simple biquadratic model yields the expressions.

$$\eta_0 = 2.44 + 60.8x + 24.4y - 116xy - 32.2x^2 - 853y^2 \quad [20]$$

$$\lambda = 1.27 - 3.59x - 4.40y - 3.04xy + 2.54x^2 - 11.2 \quad [21]$$

where x is HbS fraction from 0.18 to 0.886 and y is the oxygen tension from 0.02 to 0.08. The goodness of fit was found to be $r^2 = 0.92$ for λ and $r^2 = 0.91$ for η_0.

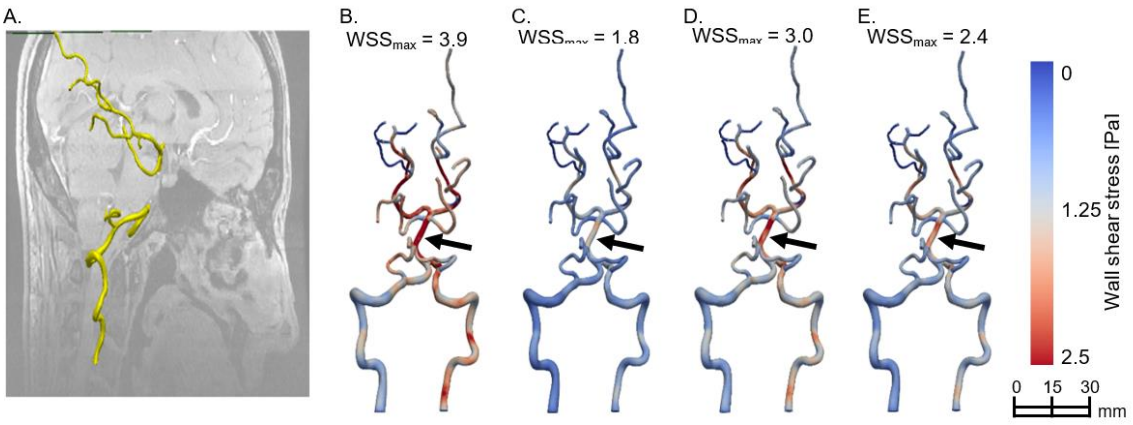

***Figure 10**: (A) 3D model of the vertebrobasilar system constructed based on MR scan from a 23-year-old female subject. Wall shear stress (WSS) distribution along the wall is calculated for (B) Newtonian model for healthy blood, non-Newtonian model for (C) healthy blood, (D) sickle blood (>70%), and (E) transfused blood (22.4% HbS). The arrows mark the high WSS region, which values are provided on top of the figure. The Newtonian model showed the largest local WSS, since the model fails to account for the shear-thinning of the blood. For the non-Newtonian model, changes in the non-Newtonian parameters with increased sickle cell fraction leads to an increases WSS in the vessel wall. The transfused blood with lower sickle cell fraction is less viscous leading to a lower WSS when compared to the sickle blood.*

3.3.5 Non-Newtonian effects on simulated blood flow in a realistic geometry

Studies have associated SCD with cerebrovascular health problems such as intracranial aneurysm, and aneurysm subarachnoid hemorrhage [3, 90]. Patients with SCD have presented multiple intracranial aneurysms, generally located in the posterior cerebrovascular circulation and not associated with traditional risk factors such as systemic hypertension, hypercholesterolemia, renal insufficiency, or arteriosclerosis [91]. Changes in blood rheology can lead to altered wall shear stress (WSS), which can ultimately lead to endothelial injury, a possible triggering event in the development of aneurysm [92]. Finite-element modeling of cerebrovascular blood flow provides a useful platform to explore the potential consequences of the observed changes in blood rheology.

To explore how rheological changes in the blood due to SCD could alter the WSS profile in a realistic geometry, we used a 3D model of the vertebrobasilar system, constructed from an MR scan of a 23-year-old female subject (**Figure 10**A) and provided by the Open Source Medical Software Corporation [93]. The hemodynamics problem was solved using the open-source SimVascular [59] biofluid mechanics software for Newtonian and non-Newtonian blood rheology, assuming rigid vessel walls. For the non-Newtonian model, parameters were found previously for healthy blood and 74.5% HbS blood were used as inputs. In the SCD cases, 12% and 6% oxygen tensions were selected to represent a range of possible oxygen levels in the brain arteries. For the Newtonian model, a constant viscosity of 3 cP was used. Resistance boundary conditions were used on the

smaller vessels and mean flow input for the larger ones. Values for the boundary conditions were obtained from [94]. Although there is an observable pressure pulse in the cerebral arteries, steady flow was used for this illustrative study. It is emphasized that this computation was made to demonstrate the potential impact of rheological changes on a relevant vascular mechanics problem, not to make any specific clinical conclusion – the MR subject was healthy, and the blood rheology was from different individuals.

Figure 10 B shows the calculated wall shear stress (WSS) along the vessels for the different parameter values studied, with the maximum value marked with an arrow and provided at the top of each panel. All of the results shown are at 12% oxygen tension. The Newtonian model (Figure 10B) overpredicts the WSS badly compared to the other models because it fails to account for the shear-thinning of the blood, which is most pronounced near the wall and thus has a large effect on WSS in a controlled-flow-rate model. The healthy blood model (Figure 10C) had the lowest WSS over most of the domain and also had the lowest peak WSS. The SCD model for a sickle blood fraction higher than 70% showed elevated WSS even at high oxygen tension (Figure 10D), the result of the SCD blood being more viscous than the healthy blood. The transfused blood model (22.4% HbS) showed a reduced WSS compared to the sickle model. The transfusion reduced sickle cell fraction in the blood, decreasing the blood viscosity and thus lowering WSS when compared to sickle blood. These effects were exaggerated when oxygen tension was reduced to 6% (Figure 14A-D).

3.4 Discussion

The most important contribution of this work is the development and demonstration of a combined microfluidic and computational approach that allows us (1) to make rheological measurements that are relevant to the patients' likely in vivo experience and (2) to extract physically meaningful parameters from the rheology to improve our understanding of the complexities of sickle cell blood flow. The resulting parameterization of a full constitutive model for blood under given conditions (HbS fraction and oxygen tension) allows us to begin exploring and pinpointing alterations in SCD blood flow under the full range of physiologic conditions and to compare blood rheology across patients quantitatively. The resulting constitutive equation can also be applied to other complex geometries without the need for lengthy experimentation and variable changes, enabling realistic simulations of blood flow in the vascular system and forming the basis for potential future patient-specific treatment design. Although behavior in capillaries is too complex to be described by a continuous model such as the Carreau-Yasuda model, the higher risk of SCD patients for vascular anomalies [95] points to the need for and potential benefit of the approach described here.

The experimental and computational components of our approach are both essential. Unlike traditional rheometric tools, our microfluidic device can characterize the unique non-Newtonian aspects of SCD blood flow and explore them systematically at a series of shear rates and oxygen tensions. This capability is a strength in our system, as the ability to generate high-quality data sets has

been limited, which, in turn, has restricted the availability and utility of data for computational models. Experimentally, we found that SCD blood rheology responds to oxygen tension, which we observed as a decreasing average velocity and increasingly blunted flow profile as oxygen tension was decreased. The more blunted profile is consistent with a rise in low-shear-viscosity, as seen by an increase in η_0 and a decrease in λ in the analysis. The response was notably different among patients with different levels of HbS, and there was even variation in the response among patients with similar HbS levels, consistent with the patient phenotypic heterogeneity observed in the clinic [96], [97]. Nevertheless, the plots of **Figure 9** indicate that general trends emerge - the blood properties become farther from healthy values as the HbS level increases and as the oxygen tension decreases - and that for an individual patient, a relatively simple curve fit of the overall data could be used to describe the patients HbS-level-dependent blood rheology.

For our computational analysis, we used the Carreau-Yasuda model, describing sickle blood as a shear-thinning fluid. The Carreau-Yasuda model has been used to characterize the known shear-dependent viscosity of normal, healthy blood in past studies; the approach described herein could be applied with any of the models normally used for blood rheology (see reviews [98], [99]). Also, the detailed velocity profile could be used as a test of mesoscale models that account for individual cell-cell interactions [86]. We found that, as expected, normal blood shear thins, and the associated model parameters are independent of oxygen

tension. For sickle blood, however, the results show a high dependence on oxygen tension with all fitting parameters - η_∞, η_0, n, a, and λ - exhibiting a significant change between 0% and 12% oxygen tension (**Figure 7**). The change in λ is of particular note in that it suggests not only an overall increase in blood viscosity (via increases in η_0 and η_∞) but also a shift towards the (higher) low-shear viscosity. That is, not only is the sickle blood more viscous at all shear rates, but it also requires a larger shear rate to shift into the presumably less dangerous high-shear viscosity regime. One major implication of our findings is that SCD blood flow is likely to be altered throughout the vasculature, from the low shear, low oxygen venous circulation to the high shear, high oxygen arterial circulation, including the pulmonary and cerebral vasculatures, where the most severe complications occur. Thus, the vascular endothelium is chronically exposed to aberrant shear stress, potentially causing vascular inflammation, increasing red cell adhesion, and promoting leukocyte accumulation. The overall result is an increased likelihood of vaso-occlusion throughout the vasculature and severe complications such as acute chest syndrome, cerebral aneurysm, and stroke.

To explore the potential utility of our approach in a clinical setting, we examined how the model parameters would change via a simulated transfusion experiment. Transfusions are common clinically and work by diluting the unhealthy red blood cells with healthy transfused ones, but transfusions do not come without their issues. Iron overload, circulatory overload, and alloimmunization symptoms can be expressed by patients [87, 89], and limiting the need and amount of transfusions

by detailing a patient-specific treatment method could be beneficial. Moreover, decreasing the blood needed for transfusions would free up this precious resource for other health care needs. We found that all model parameters changed as expected when SCD blood was diluted with healthy blood, but not all to the same degree. At a 22.4% HbS concentration or lower, η_∞, η_0, n, and a stopped showing any oxygen-dependent differences, while λ continued to show differences even at a small HbS concentration of 7.5%. We demonstrated that a simple curve-fit can be performed to estimate the model parameters for a patient as a function of HbS level and oxygen tension.

The availability of an HbS- and pO2-dependent model points to a potential opportunity for patient-specific transfusion strategy decisions. Clinically, a common target for chronic transfusion therapy is a hemoglobin level of 10 g/dl and <30% HbS cells recurring every 3-4 weeks [89]. This amount of blood transfused, however, may be unnecessary, and smaller or less frequent transfusions could be sufficient, limiting complication risk and saving blood and personnel resources. It may be possible to identify target rheological parameters rather than target HbS levels; an initial test of the patients' blood could be used to specific model parameters as in Equations [2] and [3], which in turn could be used to tune an individual patient's target HbS level. Such an approach, if successful, would improve both patient care and resource management. Importantly, sickle cell disease complications depend heavily on blood rheology, so a successful model

could provide enough information to aid the patient even with minimal inclusion of biological factors that also contribute to disease pathology.

The role of blood rheology in cerebral aneurysm formation is an active research area, and there is a recognized association between SCD and some cerebrovascular anomalies [84, 95]. These observations suggest that an effective approach to treatment design for SCD patients could include both patient-specific blood rheology and patient-specific cerebrovascular geometry (via, e.g., magnetic resonance angiography). We demonstrated in this work (**Figure 10**) that the changes in blood properties we observed were sufficient to produce substantial changes in the hemodynamic outcomes (e.g., wall shear stress) in a realistic biofluid dynamic model. The altered hemodynamics of sickle blood provide a likely biophysical mechanism behind the observation that patients with high transcranial Doppler velocities are at greater risk for stroke. Given the multiple challenges involved in identifying at risk patients, especially before an aneurysm forms, the ideas put forward herein for a patient-specific approach must be seen as exploratory rather than prescriptive - the concept is worth further investigation but requires considerable work before it might be of clinical use.

3.5 Conclusions

In summary, the combined experimental and computational approach in our study affords the opportunity to develop a physics-based understanding of sickle cell disease complexities. The model can be used as both an explorational tool to understand the impact certain physical parameters have on sickle cell disease as

well as a potential clinical tool to aid in the diagnosis and prognosis of patients. Our study was limited in tracking clinical course so there is still a need for future studies to determine the utility of our model predictive capabilities among patient populations as well as exploring additional fluid models that may better describe the disease. Regardless, this work highlights the important need for integrated experimental and computational approaches and the potential utility of model-based indicators to better understand and treat disease. This approach, combined with growing biological characterization modalities, could provide an improved clinical framework to better understand and treat patient's disease.

S.3 Supplemental Information

S.3.1 Materials and Methods

S.3.1.1 Microfluidic System

A polydimethylsiloxane microfluidic device previously described [85] was used for all experimental data collection. Briefly, the device's major function is controlling oxygen tension delivered to a blood microchannel. To accomplish this, the device consists of three layers: 1) an arteriole/venule sized 15 μm x 15 μm blood channel split into a bypass and experimental zone, 2) a 100 μm tall hydration channel to prevent blood dehydration at 37°C experiment temperature, and 3) a 150 μm tall gas reservoir allowing gas tension control diffusively delivered to the blood channel. The bypass and experimental zone splits prevent blood packing during blood occlusive events by maintaining the bypass section at a supraphysiological 21% oxygen tension which is known to lead to no further hemoglobin polymerization preventing occlusions [100]. The hydration and gas layers also have independent zones over each area to ensure no crosstalk occurs. Blood is perfused using a pressure regulator (PCD-15PSIG, Alicat Scientific) while the hydration layer is perfused with a syringe pump (NE-500, New Era Pump Systems). For control of the oxygen tension, a custom solenoid valve mixing assembly was used which periodically duty cycles 21% oxygen gas (21% O2, 5% CO2, balance N2) and 0% oxygen gas (5% CO2, balance N2). Oxygen gas tension monitoring was accomplished using a fiber optic oxygen sensor (NeoFox-GT,

Ocean Optics) and video data of blood flow collected using a high-speed camera (GS3-U3-23S6M-C, FLIR).

***Table 1**: Blood sample complete blood count and hemoglobin values*

Sample	Genotype	HCT	MCV	MCHC	WBC	HbS	HbF	HbA	HbA2
1	HbAA	40.5	89.2	33.3	5.64	0.00%	0.00%	97.60%	2.40%
2	HbSS	27.1	110.6	34.7	9.69	74.80%	7.30%	13.50%	4.40%
3	HbSS	23.9	91.2	33.9	9.85	55.2%	14.6%	26.7%	3.5%
4	HbSS	23.3	94	33.9	9.23	26.0%	9.1%	62.1%	2.8%
5	HbSS	23.3	112.6	36.5	9.95	64.5%	31.6%	0.0%	3.9%
6	HbSS	26.5	86.9	32.8	14.18	77.9%	5.9%	9.3%	6.9%
7	HbSS	22.7	98.7	34.4	7.83	35.4%	8.8%	52.1%	3.7%
8	HbSS	23.6	100.9	33.9	6.6	44.7%	9.2%	41.9%	4.2%
9	HbSS	19.8	109	34.8	8.22	72.6%	10.5%	11.5%	5.3%
10	HbSS	24.3	109.9	35.1	9.26	87.5%	6.1%	0.0%	6.4%
11	HbSS	23.8	67.2	33.2	16.87	85.1%	0.0%	9.3%	5.7%
12	HbSS	26.3	82.4	32.3	15.97	88.6%	4.3%	0.0%	7.1%
13	HbSS	27.7	105.7	33.9	10.8	41.4%	2.1%	52.6%	3.9%
14	HbSS	20.3	95.3	34.5	8.73	18.0%	0.0%	78.9%	3.1%

S.3.1.2 Blood Sample Storage and Testing

Collected blood samples from sickle cell disease patients and normal, healthy donors were stored at 4°C and up to three days; appropriate storage conditions which have shown no major changes to blood rheology [101], [102]. Blood analytical tests to measure hematocrit and hemoglobin fractions for each sample were conducted using a Sysmex XE-5000 automated analyzer and a Tosoh G7 column (**Table 1**). For all measurements, sample plasma was removed, and hematocrit fixed at 25% by centrifuging blood, removing the supernatant plasma, and adding replacement phosphate-buffered saline solution based on individual patient native hematocrit.

To characterize the blood sample, we varied both the pressure drop applied from the inlet to the outlet of the device and the oxygen tension to identify the blood response of these two parameters. For the pressure drop experiment, the oxygen tension was stabilized at 12%, 6%, and 0% targeting high, middle, and low oxygen levels and then the pressure drops increased stepwise. An oxygen stabilization step at 21% was included between each pressure sweep. For the oxygen tension experiment, the pressure drop was stabilized targeting a 750 μm/s blood average velocity and then the oxygen tension varied. Between each tested oxygen step (namely 0%, 2%, 4%, 6%, and 8%), the blood was re-stabilized by setting the oxygen to 21% for 3 minutes giving ample time for the velocity to stabilize and the hemoglobin polymer dissipate. Both healthy hemoglobin A (HbA) as a control and hemoglobin S (HbS) samples were tested with each protocol. For our transfusion pressure experiments, type-matched samples of HbA and HbS were mixed at different ratios targeting 75%, 50%, 25%, 7.5%, and 0% HbS content to determine the effects of HbS concentration for our model parameters.

S.3.1.3 Image Feature Tracking

For the analysis of collected video data, a custom MATLAB script based on the Kanade-Lucas-Tomasi feature tracker algorithm was implemented. The feature tracker uses spatial intensity information to identify contrast differences among objects and lays points on the identified features (**Figure 6**b). The points are then tracked among a set of four frames and using known device dimensions and camera frames per second capture information, the flow velocity can be calculated.

To analyze velocity data across the channel width, the channel is compartmentalized into 30 horizontal bins. The point tracker algorithm position data is sorted into each bin based on position and an average velocity acquired for each bin. The velocity can then be plotted across the channel width to acquire a flow profile and the data used to feed our model fitting equations (**Figure 6**c).

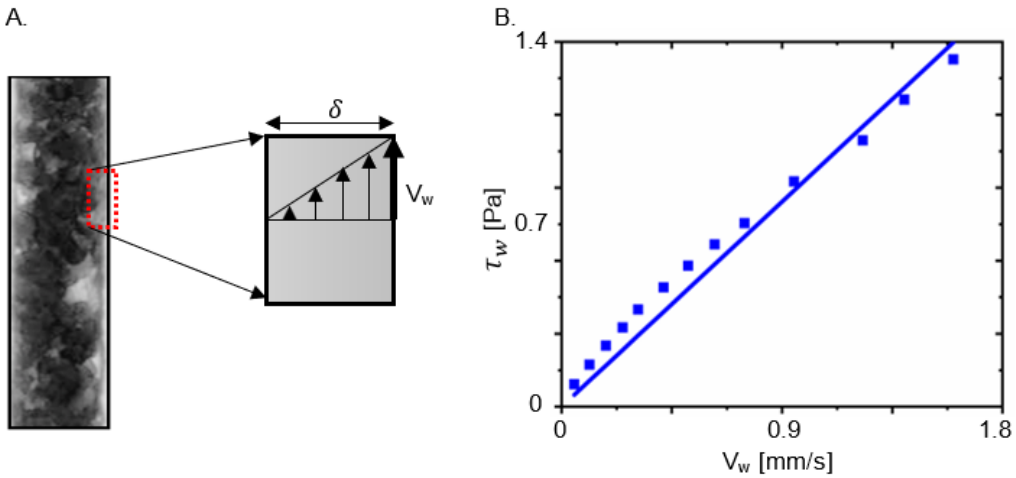

Figure 11*: (A) A non-constant CFL layer can be observed close to the wall. (B) Plotting the wall shear stress and wall velocity we can observe a linear relationship. Using the analytical expression for the wall shear stress, we can calculate the thickness of the CFL.*

S.3.1.4 Simulated Non-Newtonian Flow in a Rectangular Channel

Flow in the microchannel was assumed to be fully developed, steady-state, and laminar, for which case the momentum balance reduces to

$$-\nabla \mathrm{p} + \nabla \cdot (\eta \dot{\boldsymbol{\gamma}}) = 0$$

[22]

where p is pressure, $\dot{\boldsymbol{\gamma}}$ is the rate-of-strain tensor, and η is the apparent viscosity which was expressed by Carreau-Yasuda model.

It was observed experimentally that the fluid velocity does not go smoothly to zero when it gets closer to the wall [85]. The same observation was made by Lei et al. when studying healthy human blood flow in small tubes [103]. They observed that shear stress distribution is nonlinear along the cross-sectional region due to a non-uniform RBC distribution. This non-uniform RBC distribution leads to the formation of a cell-free layer (CFL) near to the wall, which is dominated by plasma properties. The presence of CFL leads to an abrupt transition in the shear rate profile and, therefore, in the local viscosity profile at the CFL edge. Comparing dissipative particle dynamics (DPD) model to slip and no-slip boundary condition models, Lei et al. observed that the slip model better approximated the results obtained in DPD simulations. Slip condition is a reasonably good approach to accurately solve the blood flow profile in small geometries correcting for the non-continuum character of it. Thus, a slip boundary condition given by a wall velocity was used to solve Eq. 22. The wall velocity is calculated from the experimental data by using a quadratic interpolation of the measured values close to the wall. The domain was split in two; the CFL which is assumed to be composed only by plasma, and the bulk where we have red cells, plasma, and others blood components. The size of the CFL was calculated using the linear relationship between the wall velocity (V_w) and the wall shear stress (τ_w) (**Figure 11**a),

$$\tau_w = \eta_w \frac{V_w}{\delta}$$

[23]

Where η_w is the viscosity at the wall, which was assumed to plasma viscosity (1cP), and δ is the size of the CFL. From the slope of curve given by wall shear stress and wall velocity (**Figure 11**b) we calculated δ, which was found to be about 1.5 μm. Although bigger than the value observed experimentally, this value agrees with Lei et al. solution, where the CFL thickness was found to be between 0.25 to 0.6 the radius of the geometry for geometries of R=10. This large value for the CFL thickness can be associated to the assumption of a continuum solution in a limit of the non-continuum regime; Lei et al. showed that continuum approximation fails for tubes smaller than 100 μm.

Since the velocity is only in the z direction and variation is only the x and y directions, the problem was solved by a two-dimensional, centered finite difference model in the x-y plane (**Figure 7**d). The Newton-Raphson iteration solved the resulting nonlinear algebraic problem with an analytical Jacobian. The model was verified and tested for mesh convergence by running the code for $\mu_0 = \mu_\infty$ which reduces Eq.19 to that of a Newtonian fluid in a square channel, for which an analytical series solution is available. It was found that for a 40x40 grid, the root-mean-square error between the model solution and the analytical solution was 2.5%, which we considered acceptable. A validation study was performed by fitting a series of experiments at different pressure drops for the same blood sample. The

assumption underlying our approach is that the model of Eq. 19 captures all shear-dependent viscosity, so the parameters fit the same sample at different pressures should be similar. In contrast, because blood shear-thins, one would expect a change in, e.g., the apparent viscosity based on flow resistance and a Newtonian model.

S.3.1.5 Iterative Model Fit to Experimental Velocity Profiles

Since the model produces a full two-dimensional velocity profile (**Figure 6**d) and the experiment produces only a one-dimensional projected velocity profile (**Figure 6**c), it was necessary to perform a computational projection on the simulation results by averaging the velocity over all points in the y direction.

$$V(x) = \frac{1}{N_y} \sum v(x, y) \qquad [24]$$

where $V(x)$ is the y-averaged velocity that is expected to match the experimental profile, N_y is the number of grid points in the y direction, which was chosen to 40, and $v(x, y)$ is the full two-dimensional velocity profile.

The simulated profile (**Figure 6**f) was then compared to the experimentally observed profile (**Figure 6**c). The parameters in Eq. 19 were adjusted to minimize the error between the experimental and numerical velocity. The error was minimized using a damped least-square method known as the Levenberg-Marquardt algorithm [104]

$$[\boldsymbol{J^T W J} + \lambda\, diag(\boldsymbol{J^T W J})]\boldsymbol{h} = \boldsymbol{J^T W}(\boldsymbol{V} - \widehat{\boldsymbol{V}})$$

[25]

where $\boldsymbol{J}$ is the Jacobian matrix and represents the local sensitivity of the velocity $\boldsymbol{V}$ to the change in the parameters k, $\boldsymbol{W}$ is the weighting matrix given here by the inverse of covariance matrix σ, $\boldsymbol{h}$ is the update in the parameters k, and λ is the damping parameter. The damping parameter λ is initialized as a large value for a small step in the first iteration. The solution is evaluated by the chi-square criterion, if the new solution is a better approximation, $\chi^2(\boldsymbol{k} + \boldsymbol{h}) < \chi^2(\boldsymbol{k})$, λ is decreased to accelerate to the local minimum. Otherwise, λ is increased.

The goodness of fit was defined by the chi-square error criterion.

$$(\boldsymbol{k}) = \sum_{i=1}^{N_L} \left[\frac{V_i - V(x_i, \boldsymbol{k})}{\sigma}\right]^2$$

[26]

where N_L is the number of lanes in the experiment (i.e., the number of points in the experimental flow profile), V_i is the experimentally measured velocity in lane i, x_i is the position in the center of the lane I, $\boldsymbol{k}$ is the vector of the fitting parameters, and σ is the measurement error covariance.

S.3.2 Results

S.3.2.1 Model Validation: Pressure Drop Sweep

Figure 12a shows a series of velocity profiles for healthy blood at low oxygen tension in a 15 μm channel over a range of pressure drops from 0.2 to 4 psi. As expected, the flow rate is higher at higher pressure drops. It is also notable that

the velocity profile becomes less blunt with increasing pressure drop. The model assumption that the parameters are independent of pressure drop and depend only on blood condition is valid as shown in **Figure 12**b. Thus, Carreau-Yasuda is a suitable model to describe the change in the blood rheology observed in the study. As expected, the fitting results for the parameters for a healthy blood sample were approximately independent of the oxygen tension, as shown in **Table 2**.

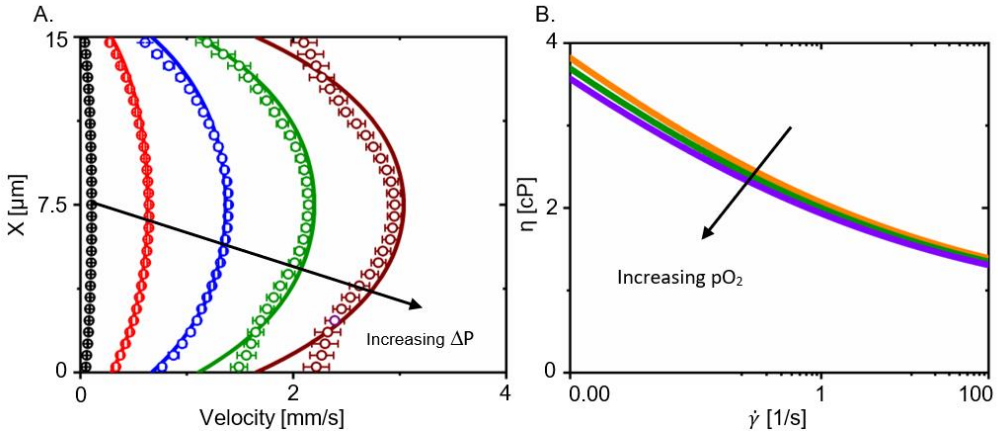

***Figure 12**: Pressure sweep for healthy blood. (A) Experimental (open circles) and numerical (solid lines) velocity profiles for pressure drop of 0.2, 1, 2, 3, and 4.0 psi at low oxygen tension. The same model parameters (Table S2) were used for each pressure drop. (B) Viscosity profile is approximately independent for three levels of oxygen tension (0, 6%, 12%).*

S.3.2.2. Correlation Analysis for Model Parameters

A correlation matrix was built to evaluate the relation between fitting parameters and the sickle blood percentage for the transfusion sample at 0% oxygen (**Figure 13**A). As expected, there was a high correlation between η_0 and HbS. η_0 was also found to be heavily correlated to parameters η_∞, a, and n so η_0 was selected as one of the main parameters to characterize. λ did not show as high of correlation to η_0 compared to other parameters so it was also pursued when determining the

clinical prediction potential of our model in **Figure 9**. A similar correlation analysis was conducted for the 12 SCD samples with HbS > 70% (**Figure 13**B). Again, HbS is correlated with η_0 and λ though less strongly than in the transfusion study.

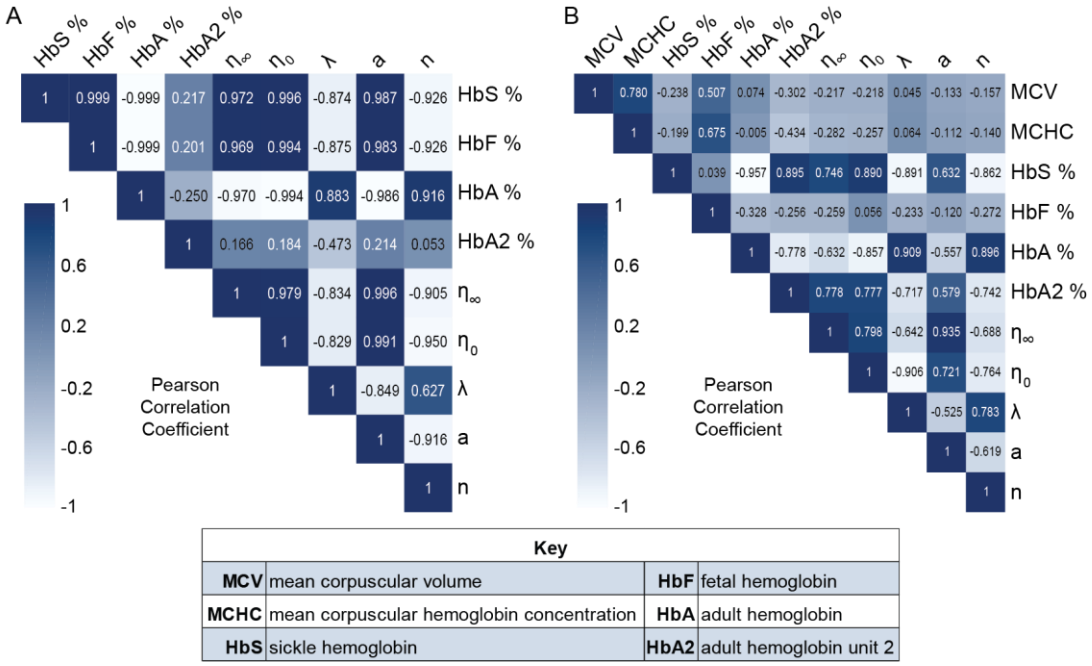

Key			
MCV	mean corpuscular volume	**HbF**	fetal hemoglobin
MCHC	mean corpuscular hemoglobin concentration	**HbA**	adult hemoglobin
HbS	sickle hemoglobin	**HbA2**	adult hemoglobin unit 2

***Figure 13**: Correlation matrix for parameters at 0% oxygen tension for (A) transfusion study, and (B) 12 SCD samples with HbS>70%. In the transfusion study, η_0 was significantly correlated to HbS concentration (0.996). In addition, η_∞, a, and n were significantly positively or negatively correlated to η_0, so we focused attention on η_0. λ showed lesser correlation to η_0 and it was explored independently, focusing our studies attention on these two parameters. For the 12 SCD samples λ and η_0 showed the highest correlation to HbS at 0.890 and -0.891, respectively.*

S.3.2.3 Non-Newtonian Effects on Simulated Blood Flow in a Realistic Geometry for Low Oxygen Tension

Figure 14b-4e show the calculated wall shear stress (WSS) along the vessels for the different parameter values studied at 6% oxygen tension. The healthy model has not changed when compared to **Figure 10**, due to viscosity to be independent

of oxygen tension for healthy blood. The SCD model showed an increase in 17% of the WSS for lower oxygen tension condition (**Figure 14**d) when compared to SCD model in **Figure 10**. The transfused blood model (22.4% HbS) also showed an increase in the WSS compared to **Figure 10**. The change in the WSS is a result of the altered blood rheology induced by polymerization of the RBCs under hypoxic conditions.

***Table 2**: List of parameter findings for pressure sweep.*

PO_2	η_0 [cP]	η_∞ [cP]	λ[s]	a	n
0	11.2	0.82	1.5	0.103	0.7
6	11	0.8	1.5	0.1	0.7
12	10.8	0.78	1.5	0.099	0.7

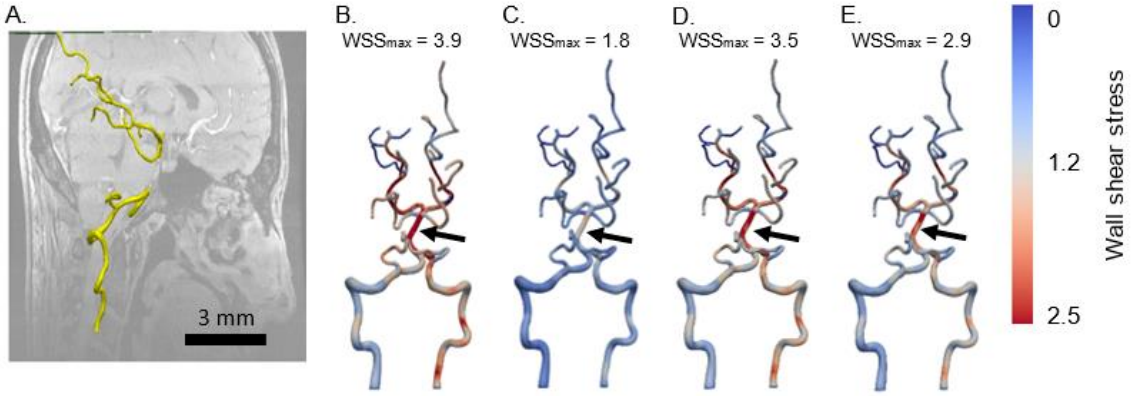

***Figure 14**: A) 3D model of the vertebrobasilar system constructed based on MR scan from a 23-year-old female subject. Wall shear stress (WSS) distribution along the wall is calculated for (B) Newtonian model for healthy blood, non-Newtonian model for (C) healthy blood, (D) sickle blood (>70%), and (E) transfused blood (22.4% HbS). The arrows mark the high WSS region, which values are provided on top of the figure.*

Chapter 4: Effects of Sickle Cell Diseases in the Blood Flow and Oxygen Transport Within Intracranial Aneurysms.

***Bazzi MS**, Wiputra H, Wood DK and Barocas VH. Computational analysis of flow and transport suggests reduced oxygen levels within intracranial aneurysms, especially in individuals with sickle-cell disease, submitted in November 2023.*

Contribution disclaimer: This work was performed in collaboration with Dr. Hadi Wiputra, a postdoctoral associate at Barocas Lab. Both of us were involved in performing computational design and data analysis.

Abstract

Sickle cell disease (SCD) is a genetic condition characterized by an abundance of sickle hemoglobin in red blood cells. SCD patients are more prone to neurological complications like subarachnoid hemorrhage or intracranial aneurysms compared to the general population, with distinctive features such as multiple intracranial aneurysms and posterior circulation location. The exact mechanism behind these associations is not fully understood, but there is a hypothesized link between hypoxic conditions in blood vessels and impaired synthesis of extracellular matrix, which may weaken the vessel walls, favoring aneurysm formation and rupture. SCD patients experience reduced oxygen levels in their blood, potentially exacerbating hypoxia in intracranial aneurysms, creating a feedback loop that could contribute to aneurysm development and early onset in these patients. In this study, we used a series of idealized geometries to investigate the key differences in the oxygen transport and blood flow dynamics inside an aneurysm formation for sickle and non-sickle cases. We found that sickle cell disease results in reduced blood flow and oxygen availability within the aneurysm due to factors

including oxygen-dependent viscosity and alteration in oxygen transport. The results indicate that some degree of hypoxia exists in certain aneurysms, particularly in patients with sickle-cell disease. Although the scope of this study does not determine whether hypoxia affects aneurysm growth, it suggests that if it does, the impact is likely more significant in sickle-cell disease patients.

4.1 Introduction

Sickle cell disease (SCD) is a genetic condition characterized by an abundance of sickle hemoglobin (HbS) in red blood cells. Exposure to moderate to low oxygen levels prompts HbS to polymerize, causing the cells to become stiffer with an altered morphology, leading to increased blood viscosity [105, 106]. Alterations in red blood cells due to SCD can result in various complications, such as acute pain, anemia, organ damage, and increased risk of infection (for general reviews on SCD, see [1, 7, 107]).

Patients with SCD often present neurological complications, such as subarachnoid hemorrhage or intracranial aneurysm (ICA), at higher rates than the general population [108, 109]. There are also known effects of SCD on the formation and failure of ICAs. In particular, 66% of SCD patients with ICAs have multiples ICAs, whereas only 20% of non-sickle patients do [110]. Also, ICAs are primarily located in the posterior circulation for 50% of the SCD patients with aneurysms against 5-14% in the general population [111]. Finally, among those who experience

aneurysmal subarachnoid hemorrhage (due to ICA rupture), the age of onset is 40 to 65 for the general population but 25 to 30 for SCD patients [111].

Although these associations are compelling, the exact mechanism underlying them is not well understood. There is a prevailing hypothesis in the literature that links hypoxic conditions of the blood vessel to impaired synthesis of extracellular matrix, which leads to wall weakening and favors aneurysm formation and rupture [112–118]. The presence of oxygen is essential for synthesis of elastin and collagen by endothelial cells, vascular smooth muscle cells (vSMCs) and fibroblasts. Under low oxygen concentration, aortic endothelial cells exhibit reduced collagen synthesis [118], while hypoxic arterial vSMCs exhibit decreases both in collagen synthesis [114, 115] and in tropoelastin mRNA expression and synthesis [112]. Fibroblasts exposed to hypoxic conditions also produce lower amounts of collagen [116, 117]. Additionally, collagen synthesized by hypoxic cells is found to be abnormal due to the requirement of oxygen for proline hydroxylation [116].

If hypoxia does play a role in aneurysm growth and rupture, then special attention should be paid to the link between SCD and hypoxia. The amount of oxygen carried systemically in the blood of sickle patients is reduced, due to the lower oxygen affinity of HbS [119] and the shorter lifespan of sickle red blood cells themselves [120]. Furthermore, the advective transport of oxygen may be affected by sickle blood rheology due to sickling when exposed to a low-oxygen environment. The increase in the viscosity of the blood due to sickling [121]

happens in a low oxygen environment. As a result, one can envision a scenario in which a positive feedback loop arises: reduced oxygen levels lead to higher viscosity, which impedes advection and thus leads to even lower oxygen levels, driving severe hypoxia in the ICA.

To evaluate the hypoxia-viscosity feedback hypothesis, this study characterized the flow and oxygen distribution in idealized ICAs of both non-sickle and SCD blood, varying geometrical features, blood rheology, and the oxygen diffusion coefficient within the range of non-sickle and SCD patients.

4.2 Methods

The model problem consisted of an idealized saccular ICA with finite-thickness walls. Within the vessel/ICA lumen (i.e., the blood domain), the relevant laws were conservation of mass and momentum for the blood and conservation of mass for oxygen. The two problems were fully coupled because the blood flow advects oxygen, and the oxygen transport affects the blood momentum equation via oxygen-dependent blood viscosity. Within the vessel wall, there was assumed to be no blood flow but diffusion and consumption of oxygen. At the wall-lumen interface, no slip and no penetration were enforced for blood flow, and continuity of concentration and flux were enforced for oxygen transport. Details on the geometry and model equations are provided below, followed by a description of the solution technique and the case studies performed.

4.2.1 Model Geometry

The geometry of the aneurysm was described by geometrical primitives: a spherical aneurysmal bulge with a radius (R_a) of 9 mm, attached to an arched cylindrical blood vessel with a diameter of 4 mm (**Figure 15**). The curvature of the cylindrical tube (κ) is considered positive when it bends away from the aneurysm, and negative when it bends towards the aneurysm. A straight 10 mm extension was attached to the ends of the curved section at a 60-degree angle to the horizontal to allow for flow development. Six different curvatures were studied, as shown in **Figure 15**. The spherical shape was attached to the vessel with an offset *d*, defined as the distance between the center of the sphere and the lumen wall. The throat length (L_t) is the size of opening that connects the spherical bulge to the arched pipe. It is calculated in relation to *d* and R_a by the Pythagorean theorem: $L_t = 2\sqrt{R_a^2 - d^2}$. Therefore, the ratio of L_t/R_a varied between 0.1 to 1. A uniform wall thickness (t) of 0.2 mm was used to represent the arterial tissue around the vessel and the aneurysm [122].

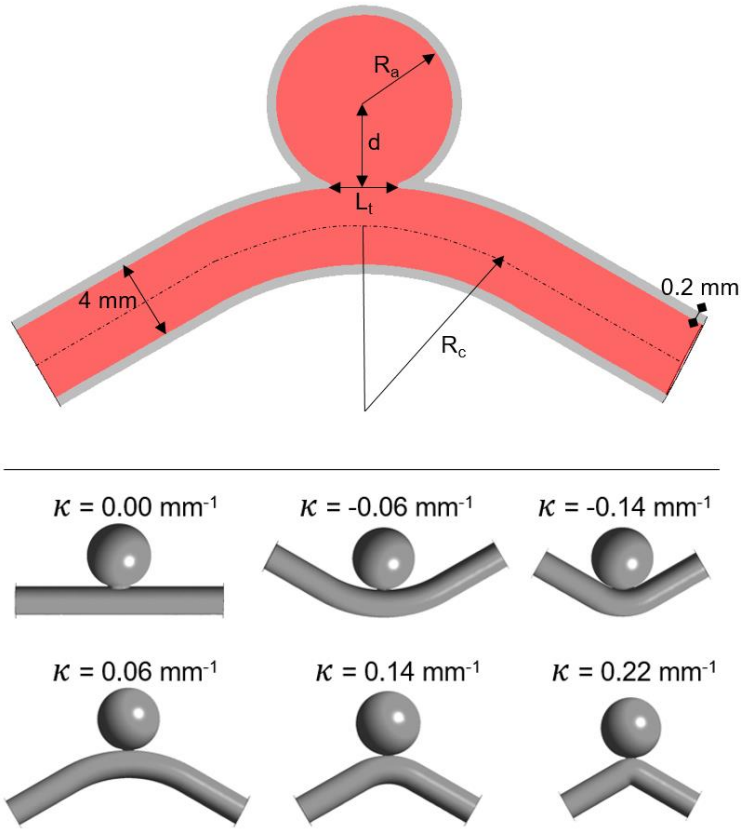

***Figure 15**: Sketch of primitive geometries composed by an arched 4-mm diameter cylindrical tube representing the vessel and an attached 9-mm spherical bulge. The geometrical parameters used for the study were: aneurysm radius (R_a), throat length (L_t).*

For this study, the geometric parameters considered were throat length to the aneurysm radius ratio (L_t/R_a) and the vessel curvature (κ). The parameter L_t/R_a accounts for the geometrical aspects of the aneurysm. Increasing (L_t/R_a) alters the level of blood supply to the aneurysm and indirectly represents the accessibility of the aneurysm bulge. The parameter κ accounts for the geometrical aspects of the parent blood vessel which might be highly curved, e.g., within the circle of Willis[123]. These parameters generate simplified geometries that describe a reasonable range of shapes of clinically observed ICAs, as shown in **Table 3**.

***Table 3**: Ranges of parameters used in the simulations[124]*

Swept Parameter	Range	Increment
L_T/R_a	0.1-1.0	0.2
κ (mm^{-1})	-0.44-0.44	0.07

4.2.2 Blood flow model

Intracranial arterial diameters are quite large with respect to the size of red blood cells, which allows the blood to be modeled as a continuum. Assuming the blood flow to be laminar and incompressible, the conservation equations are given by:

$$\nabla \cdot \boldsymbol{u} = 0 \quad [27]$$

$$\rho \frac{\partial \boldsymbol{u}}{\partial t} + \rho \boldsymbol{u} \cdot \nabla \boldsymbol{u} = -\nabla p + \nabla \cdot (\eta[\nabla \boldsymbol{u} + \nabla \boldsymbol{u}^T]) \quad [28]$$

Where u is the flow velocity vector, p is fluid pressure, ρ is the blood density (assumed to be constant 1050 kg/m^3 [125]), and η is the fluid viscosity described by the Carreau-Yasuda model:

$$\eta = \eta_0 + (\eta_0 - \eta_\infty)[1 + (\lambda \dot{\gamma})^a)^{\frac{n_{CY}-1}{a}} \quad [29]$$

where η is the effective viscosity as a function of the shear rate $\dot{\gamma}$, where η_0 is the zero-shear-rate viscosity, η_∞ is the infinite-shear-rate viscosity, n_{CY} is the exponent that determines the steepness of the viscosity curve, ***a*** is a dimensionless parameter that describes the transition from the zero-shear-rate to the power-law region, and λ is a time constant. In our previous work [121], we found the

parameters η_∞, n, and *a* to be determined by the fraction of sickle hemoglobin (HbS%), as given in **Table 4**.

Table 4: *Carreau-Yasuda parameters for non-sickle versus sickle*

	η_∞ [cP]	*n*	*a*
Non-Sickle	1	0.75	0.1
Sickle (>75% HbS)	3.5	0.5	0.23

In contrast, the parameters η_0 and λ are dependent on both HbS% and partial pressure of oxygen (pO_2) [121] and are expressed by the polynomial Eqs:

$$\eta_0 = 2.44 + 60.8[\mathrm{HbS}] + 24.4[\mathrm{pO_2}] - 116[\mathrm{HbS}][\mathrm{pO_2}] - 32.2[\mathrm{HbS}]^2 - 853[\mathrm{pO_2}]^2$$

[30]

$$\lambda = 1.27 - 3.5559[\mathrm{HbS}] + 4.4[\mathrm{pO_2}] - 3.04[\mathrm{HbS}][\mathrm{pO_2}] - 2.54[\mathrm{HbS}]^2 - 11.2[\mathrm{pO_2}]^2$$

[31]

where η_0 has a unit of centipoise and λ is in seconds.

4.2.3 Oxygen Transport in the Blood

It was assumed that the time scale of the oxygen-hemoglobin association-dissociation reaction is much faster than the time scale of transport, so the oxygen concentration in plasma is always in equilibrium with that in the red blood cells. This simplification allows direct use of the oxygen association-dissociation curve to calculate total oxygen carried per unit volume of blood $[O_T]$ as given by [126]:

$$[O_T] = [O_p] + [O_{Hb}] = \alpha[pO_2] + S(\beta[Hb])$$

[32]

Where $[O_p]$ and $[O_{Hb}]$ are oxygen concentration found in plasma and red blood cells respectively. The parameter $\alpha = 0.003\ \frac{\text{mL of O2}}{\text{dL·mmHg}}$ is the solubility coefficient of oxygen in plasma, $[Hb]$ is hemoglobin concentration in blood, and $\beta = 1.39\ \frac{\text{mL of O2}}{\text{g of hemoglobin· dL}}$ is the volume of oxygen carried by fully saturated hemoglobin [126]. The hemoglobin concentration is assumed to be $15\ \frac{g}{dL}$ for non-sickle blood [127] and 8 $\frac{g}{dL}$ for the sickle blood[128]. S is the oxygen saturation obtained from the oxygen association-dissociation [129].

$$S = \frac{\left(\frac{P}{P_{50}}\right)^{n_{Hill}}}{\left[1 + \left(\frac{P}{P_{50}}\right)^{n_{Hill}}\right]}$$

[33]

Where $P_{50} = 28$ mmHg is the partial pressure of oxygen at half saturation for non-sickle hemoglobin, and n_{Hill}=2.7 is the Hill coefficient[130]. Due to changes in the biding affinity in sickle hemoglobin, the association-dissociation curve has a shift to the right, leading to an increased value of $P_{50} = 40$ mmHg [119] for sickle hemoglobin.

The transport of oxygen inside a large blood vessel can be modeled by the unsteady convection-diffusion equation.

$$\frac{\partial [O_T]}{\partial t} + u \cdot \nabla [O_T] = D_{eff} \nabla^2 [O_T]$$

[34]

Where O_T is the total (bound + unbound), u is the blood velocity, and D_{eff} is the effective diffusivity of oxygen in blood given by:

$$D_{eff} = K_1 D_p + K_2 D_{RBC}$$

[35]

Where D_p is the diffusivity of oxygen in the plasma, and D_{RBC} is the dispersity of the red blood cells due to the shear flow. The term $K_1 D_p$ represents the plasma oxygen's diffusion flux enhanced by increased oxygen supply from hemoglobin, whose effect can be approximated by the constant K_1. The term $K_2 D_{RBC}$ represents the transport of oxygen by red blood cells as they disperse in the presence of shear flow. The effect can be described, for a rapid-equilibrium solute, in the continuum as a diffusion term [131], where D_{RBC} and K_2 are given by.

$$D_{RBC} = \hat{r}_{RBC}{}^2 \dot{\gamma} f \phi (1-\phi)^c$$

[36]

$$K_2 = 1 + g\phi m$$

[37]

where $\hat{r}_{RBC}$ is the average RBCs radius, ϕ is the RBCs volume fraction, $f = 0.15$ and $c = 0.8$ are fitting parameters determined empirically[131], γ is the fluid shear rate, $0 \leq g \leq 1$ is a measure of departure of Hb-O_2 reaction from equilibrium, for $g = 1$, the reaction is in equilibrium, and m is proportional to the slope of the oxyhemoglobin dissociation curve given by:

$$m = \frac{C_{Hb}}{\alpha} \frac{dS}{dP}$$

[38]

Where C_{Hb} is the oxygen-binding capacity, and α is the solubility of oxygen in plasma. Similar to K_1 and D_p, the slope *m* was treated using average values for oxygen- and shear-dependent parameters, so D_{RBC} did not vary spatially in the model.

4.2.4 Oxygen Transport in the Vessel Wall

The transport of oxygen in vessel wall is modeled by the diffusion-reaction equation given by

$$\frac{\partial [O_W]}{\partial t} = D_w \nabla^2 [O_W] - C$$

[39]

where O_W is the concentration of oxygen in the vessel wall, $D_w = 1.08x10^{-9}$ m^2/s is the diffusivity of oxygen in the tissue[132]. The oxygen consumption rate *C* is described by Michaelis-Menten kinetics.

$$C = -\frac{V_{Max}[O_W]}{([O_W] + K_M)}$$

[40]

where $V_{Max} = 9.37\text{x}10^{-4}\,\frac{mol}{m^3 s}$-1 (or $2.1\text{x}10^{-5}\,\frac{mol\ O_2\ (at\ STP)}{ml\ tissue \cdot s}$) is the maximum reaction rate, based on range of values found in literature [132]. $K_M = 10^{-4}\,\frac{mol}{m^3}$ is the Michaelis-Menten constant. K_M was chosen mimic the constant consumption rate used in Moore and Ethier [132] but prevent over consumption at low oxygen concentration.

4.2.5 Boundary conditions

For the blood flow model, a prescribed flowrate waveform [133] was given as the inlet boundary condition. The outlet was set to zero pressure for all cases. At the wall-lumen interface, no slip and no penetration were enforced for blood flow, and continuity of concentration and flux were enforced for oxygen transport. The wall was assumed to be rigid.

4.2.6 Simulation settings

The constitutive equations were solved with ANSYS Fluent 2023, with about 300,000 tetrahedral and prismatic inflation cells. For the unsteady state simulation, an initial condition for the unsteady flow problem was obtained by solving the steady-state flow problem with a time-averaged inlet flow rate. The unsteady problem was run for 5 cardiac cycles to achieve periodic solution. The time step was 0.00189s, resulting in 400-time steps per cardiac cycle. Convergence in the unsteady simulation was set with residual $<10^{-4}$ for the flow equations (momentum and continuity), but $<10^{-7}$ for the oxygen transport.

4.2.7 Calculated parameters for results analysis

The throat Reynolds number (Re_T) measures the flow through the throat, and it is given by the following equation:

$$Re_T = \frac{\rho V_T L_T}{\eta_T}$$

[41]

Where V_T is the surface averaged velocity at the throat, L_T is the throat length scale, and η_T is the surface averaged viscosity at the throat.

The Sherwood number (Sh), which calculates the aneurysmal surface average mass transfer of oxygen from the blood to the surrounding tissue, is given by the following expression

$$Sh = \frac{1}{A_S} \frac{\int \nabla([O_T] - [O_T]^{Wall}) dS}{[O_T]^{Bulk} - [O_T]^{Wall}}$$

[42]

where $[O_T]$ is the concentration of oxygen inside the aneurysm, $[O_T]^{Wall}$ is the concentration of oxygen at the aneurysm wall, $[O_T]^{Bulk}$ is bulk concentration of oxygen, or the concentration found in the vessel, and A_S is surface area of the aneurysm wall.

4.3 Results

4.3.1 Blood flow and oxygen concentration: sickle versus non-sickle models

Figure 16 shows the velocity distribution at the peak systole in a mid-plane longitudinal cut through the aneurysm (**Figure 16**A) and a cut transverse to the flow (**Figure 16**B) for a zero-curvature vessel with a throat radius equal to 30% of aneurysm diameter. Although the flow patterns were broadly similar, there was a decreased flow entering the aneurysm cavity in the sickle case (**Figure 16**C-**Figure 16**F), which leads to reduced transfer of momentum to the aneurysmal region. The center of the vortex (represented by the star) shifted proximally with respect to the vessel and closer to the aneurysm throat in the sickle case.

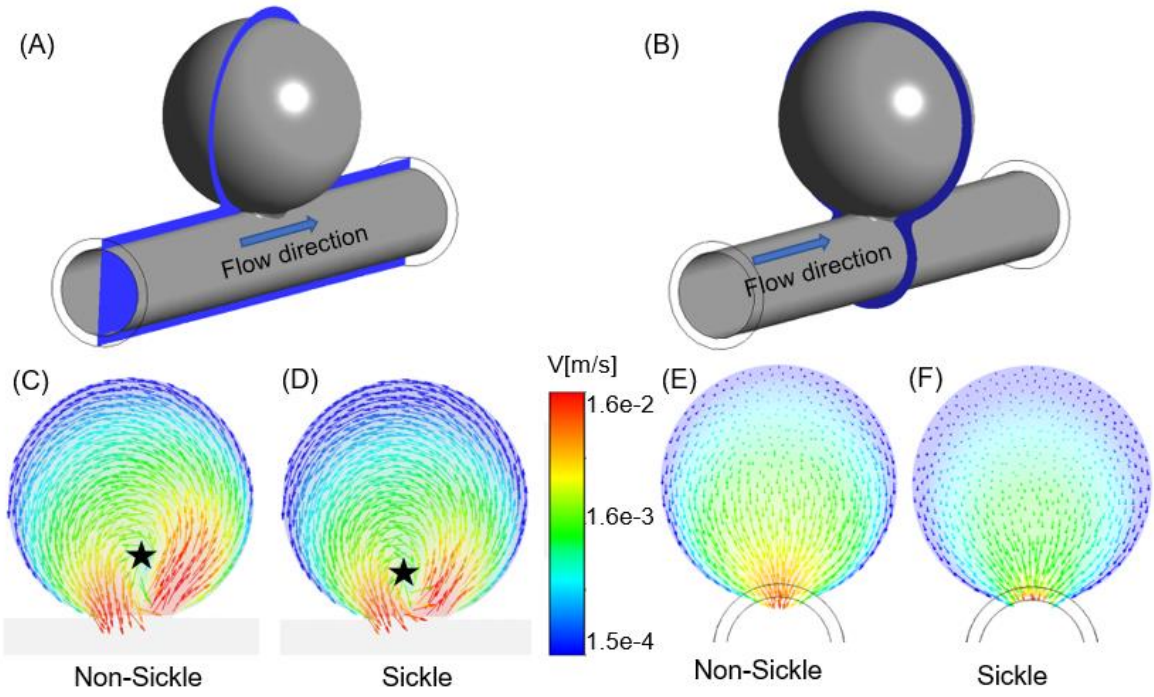

***Figure 16**: Effect of sickle blood on blood velocity in base case model. (A) Longitudinal mid-plane slice of aneurysm. (B) Orthogonal mid-plane slice of aneurysm. Velocity vector shows the blood flow distribution inside the aneurysm for non-sickle (C and E) and sickle (D and F). Results are calculated at the peak systole.*

Figure 17 shows the oxygen concentration distribution along a longitudinal mid-plane cut for non-sickle (**Figure 17**C) and sickle (**Figure 17**D) blood. The oxygen-dependent viscosity impedes transport of oxygen inside the aneurysm. As shown in **Figure 17**, the flow into the aneurysm is reduced in the sickle case, which leads to a reduced oxygen distribution, even relative to the systemic levels (**Figure 17** vs **Figure 17**). The volume-averaged oxygen concentration inside the aneurysm was $7.31\frac{g}{dl}$ for the non-sickle case (11% below the systemic value) and 3.95 $\frac{g}{dl}$ for the sickle case (20% below the sickle systemic value). A lower concentration of oxygen leads to impaired oxygen transport to the vessel wall, as assessed by the Sherwood number. **Figure 17**G shows a lower mass transfer rate for the sickle case even in the artery, and a substantial drop inside the aneurysm for both cases.

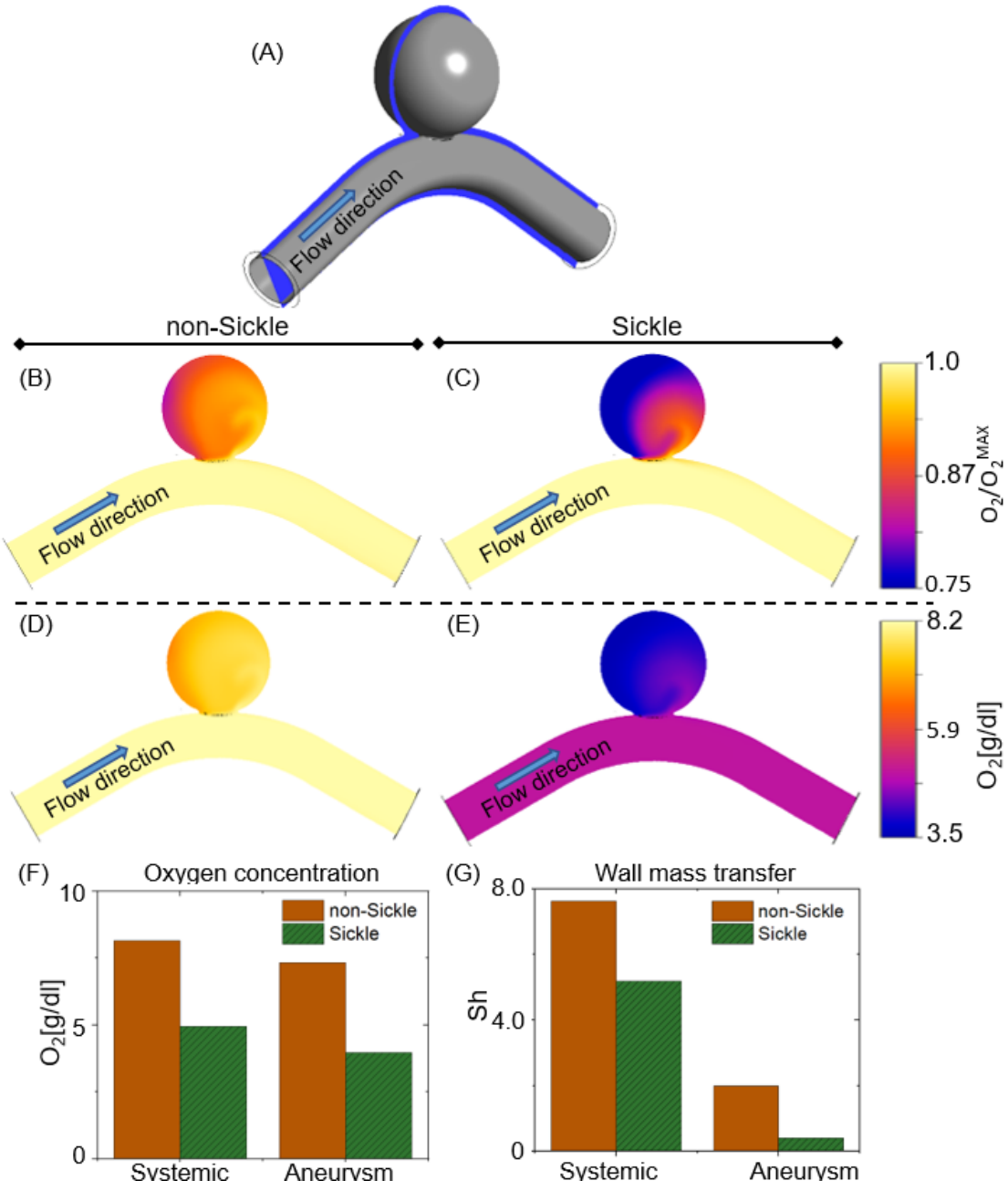

***Figure 17**: Plane cut longitudinal (A) compares normalized and total oxygen concentration in the vessel and inside the aneurysm for non-sickle (B and D) and sickle (C and E) respectively. Figure (F) and (G) show a volume average value for oxygen concentration and mass transport of oxygen through the wall (given by Sherwood number) respectively. Not only there is less oxygen available in the system, but also lower oxygen concentration transported inside the aneurysm; a 20% drop occurs in the SCD case when compared to only a 11% in the non-sickle case.*

4.3.2 Geometrical effects: blood flow dynamics

Figure 18 shows the velocity streamlines at peak systole for the different geometries for (**Figure 18** A) non-sickle and (**Figure 18** B) sickle cases. We can observe clockwise Dean vortices for positive curvatures and counterclockwise Dean vortices for negative curvatures. As expected, a larger throat size resulted in more blood flow into the aneurysm. The non-sickle results are consistent with the experimental study of Chassagne *et al.* [133]

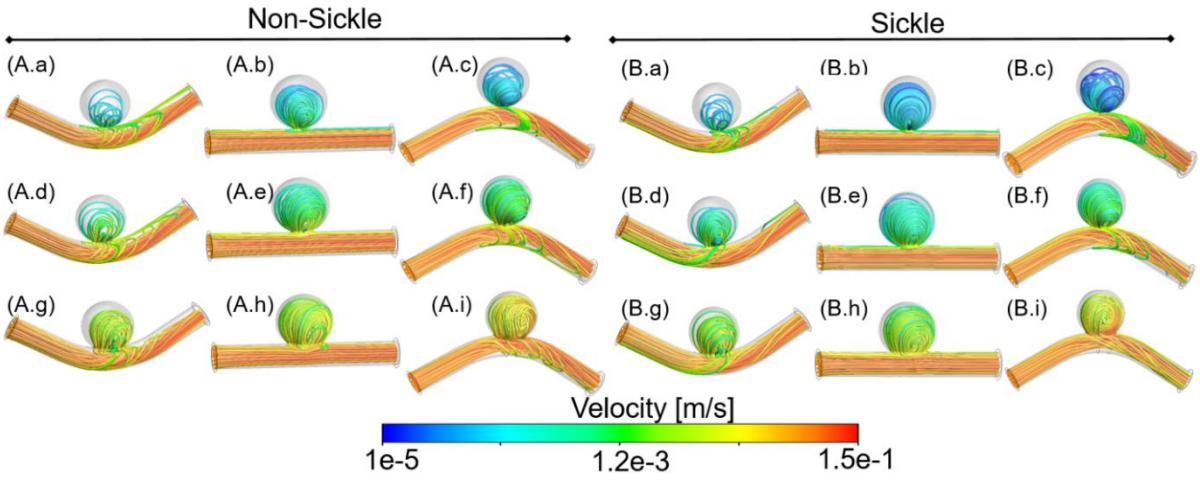

***Figure 18**: Velocity streamlines in the vessel and inside the aneurysm for non-sickle (A) and sickle (B) models due to changes in curvature and throat length. Curvature increases from left to right going from -0.06, 0, and 0.06 respectively. The throat-to-aneurysm diameter ratio increases from top to bottom, going from 0.1. 0.3, and 0.6. All the measurements are at peak systolic pressure, for the 5th cardiac cycle.*

Figure 19 shows the color maps of time-averaged measurements of relevant blood flow dynamics quantities at the aneurysm site. The first row displays non-sickle results, and second row displays sickle results. All the figures illustrate how measurements change with curvature, κ (x axis) and throat-to-aneurysm-radio

ratio, L_T/R_A (y axis). The first column is the throat Reynolds number (Re_T), which provides a measure of the inflow of blood inside the aneurysm. The sickle model (**Figure 19** B) had an overall reduced Re_T, presumably due to increased effective viscosity (**Figure 19**C-D) and consequently decreased blood inflow for comparable geometrical conditions. The time average wall shear stress (TAWSS) showed a slight increase, more pronounced for smaller value of L_T/R_A. The oscillatory shear index (OSI), which measures changes in the blood flow direction during the cardiac cycle had more elevated values for non-sickle cases, and unlike the other parameters, showed little dependence on κ, particularly in the sickle case, suggesting that the geometrical changes in the aneurysm dominate the flow direction in the aneurysm site.

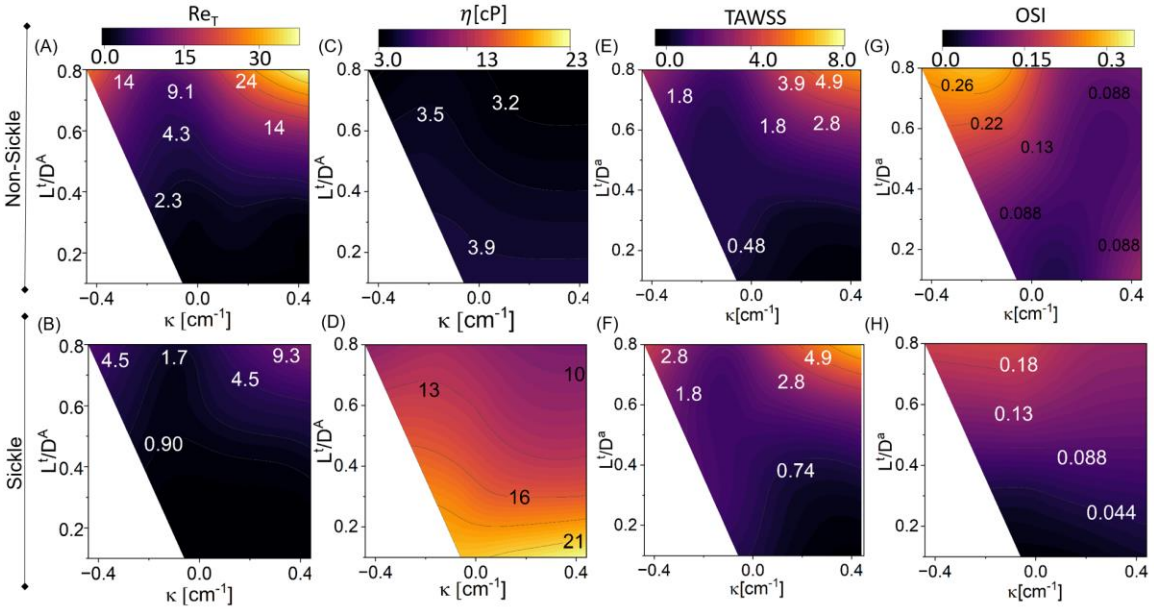

***Figure 19**: Color maps show throat Reynolds number (Re_T) for non-sickle (A) and sickle (B), oscillatory shear index (OSI) for non-sickle (C) and sickle (D), time average wall shear stress (TAWSS) for non-sickle (E) and sickle (F), and effective*

viscosity (η) for non-sickle (G) and sickle (H). All the measurements are time averaged of the 4th cardiac cycle and calculated at aneurysm site.

4.3.3 Geometrical effects: oxygen transport

In **Figure 20**, we investigate the influence of geometrical changes on oxygen transport for (**Figure 20** A) non-sickle and (**Figure 20** B) sickle cases. Overall, the sickle cell model shows more oxygen depletion inside the aneurysm cavity for similar geometrical conditions to the non-sickle model. For medium to large throat sizes, positive curvature drives the blood flow to the aneurysm, facilitating oxygen transport when compared to negative curvatures. Positive curvature led to an improved distribution of oxygen inside the aneurysm for cases with medium to large throat sizes (**Figure 20**A.d-A.i for non-sickle and **Figure 20**B.d-B.i for sickle).

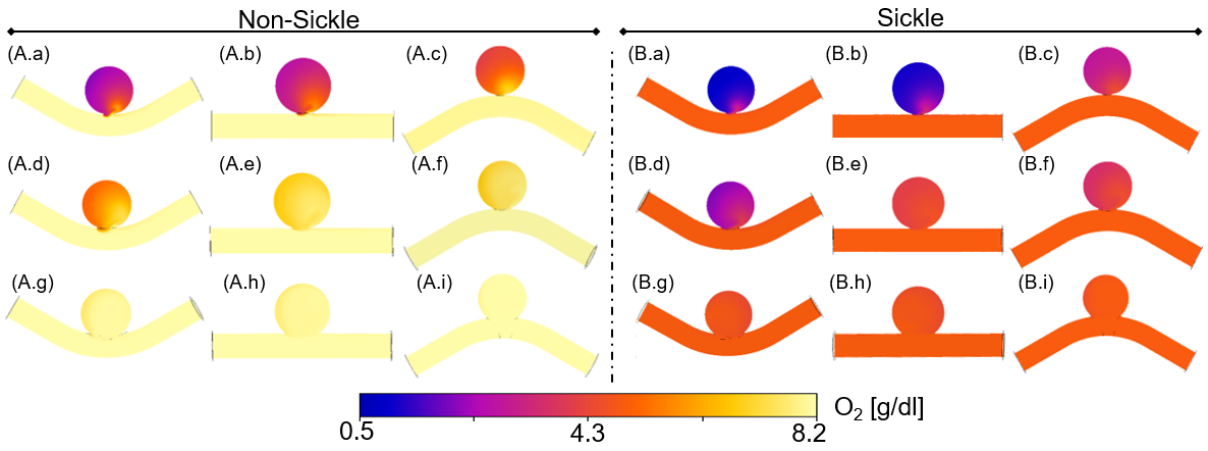

***Figure 20**: Plane cut longitudinal shows the oxygen distribution in the vessel and inside the aneurysm for non-sickle (A) and sickle (B) models due to changes in curvature and throat length. Curvature increases from left to right going from -0.06, 0, and 0.06 respectively. The throat-to-aneurysm diameter ratio increases from top to bottom, going from 0.1. 0.3, and 0.6. All the measurements are at systolic pressure, for the 4th cardiac cycle.*

For large enough throat sizes, the jet created by the incoming flow in the positive curvature is directed into the aneurysm, facilitating the advection-driven oxygen transport inside the aneurysm site.

A lower oxygen concentration inside the aneurysm leads to reduced availability of oxygen for the surrounding tissue. To quantify oxygen distributed to the tissue surrounding the aneurysm, the time-averaged Sherwood (Sh_A) number is shown in **Figure 21**A-B for different geometrical shapes. As with Re_T, the sickle model had a reduced Sh_A, suggesting possible hypoxia in the aneurysm wall, even for moderate throat sizes. **Figure 21**C-D depict the normalized volume- and time-averaged oxygen concentration inside the aneurysm lumen. A higher overall oxygen concentration was found for non-sickle cases. In terms of geometrical parameters, a dependence on both L_T/R_A and κ is observed, with an increased concentration for positive curvature. Figures 7E-F depict the normalized volume- and time-averaged oxygen concentration in the surrounding tissue of the aneurysm. Similar to the lumen, a reduction of oxygen was observed for sickle cases.

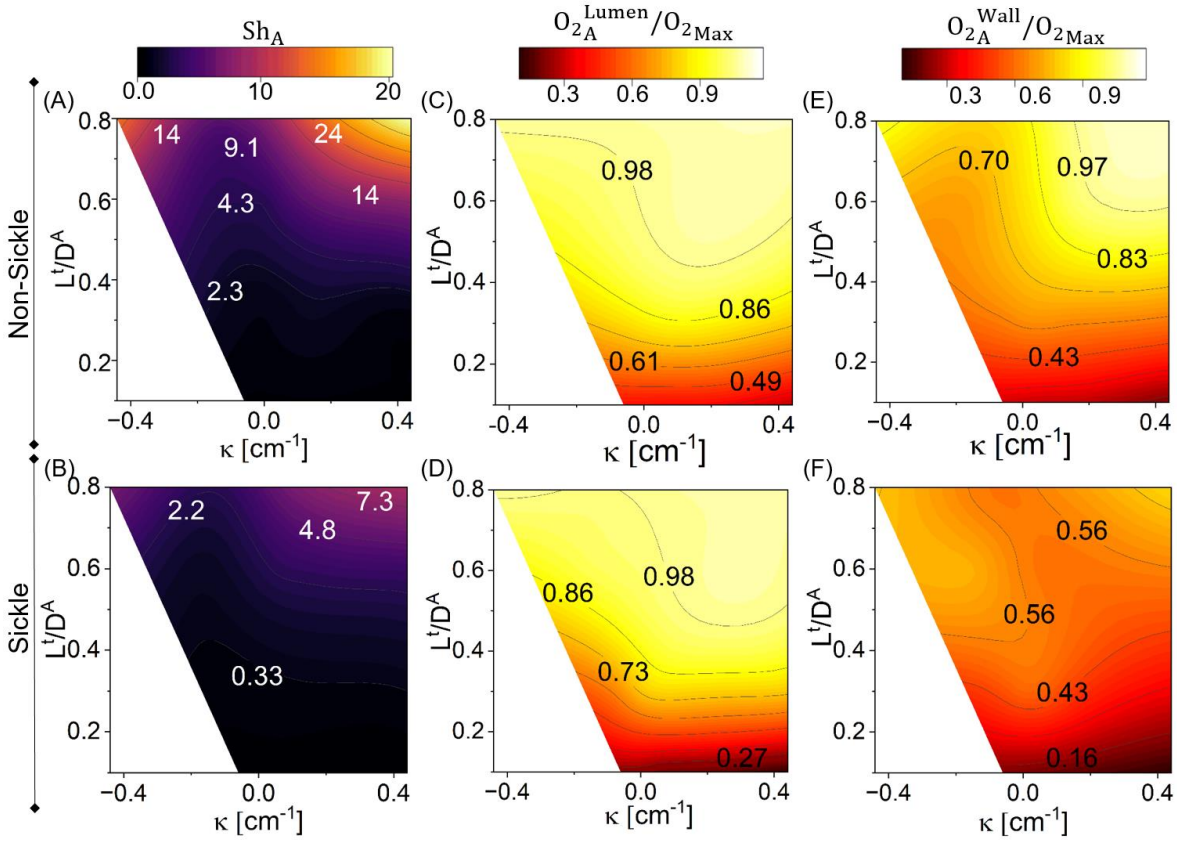

***Figure 21**: Color maps of Sherwood number for (A) non-sickle vs (B) sickle, normalized volume-averaged oxygen concentration inside the lumen of aneurysm (C) non-sickle vs (D) sickle, and normalized volume-averaged oxygen concentration inside the tissue surrounding the aneurysm (E) non-sickle vs (F) sickle. The normalization is based on the maximum concentration of oxygen found in the vessel, which is 8.19 g/dl for non-sickle, and 4.95 g/dl for sickle. All the values are time averaged.*

4.4 Discussion

The most important contribution of this work is the comparison of blood flow and oxygen transport in intracranial aneurysm for sickle and non-sickle cases. Results suggest there is in fact a hypoxia-viscosity positive feedback loop for sickle cell disease models. In SCD, we observed reduced blood flow inside the aneurysm,

associated with an increased viscosity, and decrease availability of oxygen concentration in the aneurysmal site.

Additionally, sickle cell patients have a systemically lower concentration of oxygen, due to the shorter survival time of sickle red blood cells [120]. Thus, for similar aneurysmal and arterial geometries, there was observed a decrease in mass transfer of oxygen to the surrounding tissue, measured by Sh_A.

The analysis in this paper relates only to biotransport of blood and oxygen and does not address the tissue biological response to alteration in the oxygen level. Thus, this study makes no conclusion regarding the potential role of hypoxia in intracranial aneurysm, a role suggested by others [112 – 118]. Rather, the results suggest that there must be some degree of hypoxia within some aneurysms, and that any such hypoxia would be more severe for a geometrically identical aneurysm in a patient with sickle-cell disease. Similarly, the study makes no conclusion regarding whether hypoxia affects intracranial aneurysm growth, but we do conclude that if hypoxia affects the aneurysm growth process, then any such effect will be more pronounced in sickle-cell disease patients. The oxygen-driven flow changes would also alter transport dynamics for any bloodborne species.

When compared to the non-sickle case, the greater viscosity in the sickle case led to lower flow rates, higher time-averaged wall shear stress but lower time-averaged wall shear rate, and a lower oscillatory index. One can speculate that the lower flow might be expected to increase the risk of thrombosis[134], but, as in the

previous paragraph, our results address only the effect on the flow, not any potential consequences.

Only two geometric parameters were varied in this study, aneurysm throat size and parent vessel curvature. While these parameters are by no means exhaustive, they did allow study of an informative range of aneurysm geometries, and the small number of parameters allowed for a full factorial study design. We found a very strong effect of aneurysm throat size on flow and oxygen transport into the aneurysm bulb, as one might expect. The effect of parent vessel curvature was subtler, perhaps because different factors (Dean vortices, inertial jet vs. viscous drag driving flow in the aneurysm) may be at play for different geometries. The role of curvature thus merits a larger-scale future study, as does the interaction of throat size and vessel curvature to determine the flow field. Similarly, this study considered only a spherical aneurysm of a single diameter, whereas actual intracranial aneurysms can be highly non-spherical, can have different sizes, and obviously change size (i.e., grow) over time; all these factors could be important.

Our work cannot evaluate potential reasons for the difference in number and locations of intracranial aneurysms between sickle-cell disease patients and non-sickle patients. Sickle-cell-disease-driven alterations of blood viscosity could affect intracranial hemodynamics, and such alterations could be more pronounced or more impactful in different regions of the brain. Further, altered oxygen transport could lead to preferential growth of newly formed aneurysms in certain regions more than others.

In summary, we found that the reduced oxygen level and oxygen-dependent viscosity in sickle cell disease acted synergistically to produce less blood flow and lower oxygen levels in an idealized model of a saccular intracranial aneurysm.

Chapter 5: Mouse-Specific Biofluidic and Geometric Biomarkers of Ascending Thoracic Aortic Aneurysm Outcomes.

Bazzi, M.S., *Balouchzadeh, R., Pavey, S.N. et al. Experimental and Mouse-Specific Computational Models of the Fbln4SMKO Mouse to Identify Potential Biomarkers for Ascending Thoracic Aortic Aneurysm. Cardiovasc Eng Tech 13, 558–572 (2022).* *https://doi.org/10.1007/s13239-021-00600-4*

Contributions disclaimer: This work was performed in collaboration with the Wagenseil Vascular Mechanics Laboratory from the Department of Mechanical Engineering & Materials Science at Washington University in St. Louis. The experimental data were collected at Professor Wagenseil's lab, and I performed the computational design and analysis.

Abstract

The prediction of risk to the patient in ascending thoracic aortic aneurysm (ATAA) is a significant challenge and the subject of much active research. In the present work, a combination of mouse model experiments and computer simulations was used to explore potential biomarkers that correlate with mouse lifespan, used as a surrogate for risk of a catastrophic event. Image-based, mouse-specific fluid-structure-interaction models were developed for *Fbln4*^{SMKO} mice (n = 10) at ages two and six months. The results of the simulations were used to quantify potential

biofluidic biomarkers, complementing the geometrical biomarkers obtained directly from the images. Comparing the different geometrical and biofluidic biomarkers to the mouse lifespan, it was found that mean oscillatory shear index (OSI_{mean}) and minimum time-averaged wall shear stress ($TAWSS_{min}$) at six months showed the largest correlation with lifespan (r^2 = 0.70, 0.56), with both correlations being positive (i.e., mice with high OSI_{mean} and high $TAWSS_{min}$ tended to live longer). When change between two and six months was considered, the change in $TAWSS_{min}$ showed a much stronger correlation than OSI_{mean} (r^2 = 0.75 vs. 0.24), and the correlation was negative (i.e., mice with increasing $TAWSS_{min}$ over this period tended to live less long). The results highlight potential biomarkers of ATAA outcomes that can be obtained through noninvasive imaging and computational simulations.

5.1 Background

Ascending thoracic aortic aneurysms (ATAAs) are bulging enlargements of the aorta at the ascending segment near the brachiocephalic trunk. They affect approximately 15,000 people in the US per year and, in critical cases, they will grow in size and eventually rupture. When an ATAA ruptures, it can be fatal in up to 80% of the cases [135]. Surgical intervention to replace the diseased region with a synthetic graft is the most common clinical treatment, but the surgical intervention itself presents risks, having a significant mortality rate (3-5%) [136]. The criteria to determine whether to perform surgery are defined primarily in terms of the maximum diameter and growth rate. About 60% of the patients, however,

present complications before the intervention criteria are reached [137], indicating a need to improve the predictability efficiency for ATAA outcomes.

Numerous biomarkers [138–142] have been explored as a potential basis for predicting ATAA outcome. The biomarkers fall into different broad categories: genetic, microstructural, geometrical, and biofluidic. The primary genetic biomarkers are mutations known to lead to the formation of ATAA, such as Marfan syndrome [143] and Ehlers-Danlos syndrome [144]. Microstructural biomarkers are associated with alteration in the extracellular matrix proteins that lead to global or localized weakness of the arterial wall and have been associated with the formation and growth of ATAAs [145]. Geometrical biomarkers are the most well-known and are easily obtained from noninvasive imaging. They characterize changes in the overall geometry of the aorta, such as diameter and tortuosity [146]. Finally, biofluidic biomarkers are alterations in luminal pressure, wall shear stress, and intramural stress, that are associated with ATAA [147]. Biofluidic and geometrical biomarkers are particularly appealing because they are potentially noninvasive and patient specific.

Although the ideal would be to use human subjects to identify the appropriate biomarkers and develop guidelines to interpret them, such experiments are impossible because of the ethical considerations regarding patient care and the long-life cycle of the human. Recent advances *in vivo* measurement of aortic wall mechanical properties [148] and availability of surgical waste tissue [149, 150] have provided some human data, but mouse models are more practical and offer

the added benefit of tight control over genetic and environmental factors, hence they are an attractive tool to study ATAA [151].

The *Fbln4*^{SMKO} mouse model [152] was used in the current study. *Fbln4*^{SMKO} mice are genetically modified to eliminate expression of the gene encoding fibulin-4 in smooth muscle cells. FBLN4 mutations are associated with autosomal recessive cutis laxa type 1B (OMIM 614437) [153], so the mice have a known genetic biomarker for a disease associated with ATAA. Fibulin-4 is an extracellular matrix protein associated with microfibrils surrounding elastic fibers, and its deletion in smooth muscle cells in mice results in disorganized and fragmented elastic fibers, providing a known structural biomarker of ATAA [152]. *Fbln4*^{SMKO} mice develop ATAA postnatally, demonstrate aortic tortuosity [152], have altered biomechanics[151, 154, 155] and have an abbreviated lifespan [151, 152], providing an appropriate model to investigate geometrical and biofluidic biomarkers associated with adverse disease outcomes. Longitudinal images of the entire *Fbln4*^{SMKO} mouse aorta were captured at two different time points throughout disease progression. Those images were used, along with in vitro mechanical data, to build a mouse-specific fluid-structure interaction (FSI) model and to obtain aortic tortuosity and diameter measurements. The FSI models, mechanical

properties, and aortic shape measurements were used to identify geometrical and biofluidic biomarkers that correlated with the mouse lifespan.

5.2 Methods

5.2.1 Study design

We used a combination of experimental and numerical techniques to capture changes in the geometry, mechanical properties, and fluid-solid dynamics during the development and formation of ATAA in mice. **Figure 22** provides an overview

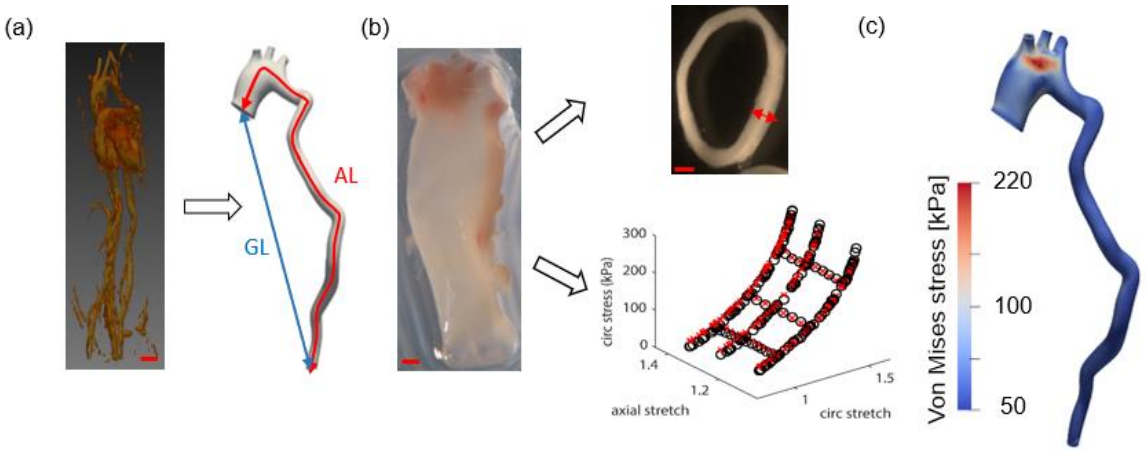

***Figure 22**: Summary of Models and Methods. FBLN^{SMKO} mice [16] were used, which are known to exhibit elastic fiber fragmentation and ascending thoracic aortic aneurysm. **(a)** MRI scans were taken at ages two and six months (representative six-month scan of the heart and visible vasculature is shown), and the scans were used to generate geometric models of the aorta, from which the actual length (AL) and the geometric length (GL) were calculated. **(b)** After the animals died naturally or were euthanized, the aorta was isolated and used for mechanical testing, and rings were cut from the sample to allow measurement of wall thickness. **(c)** The geometric and mechanical data were combined to form the basis of age-specific, mouse-specific fluid-structure interaction models of aortic blood flow. Bars indicate 200 μm.*

of the study design. More details about each step are given in the following sections.

5.2.2 Genetically modified mice

Five male and five female mice lacking expression of fibulin-4 in smooth muscle cells (*Fbln4*^{SMKO}) were used in this study [152]. Fibulin-4 is critical for elastic fiber assembly, and *Fbln4*^{SMKO} mice have ATAAs with about 50% penetrance. Mice were monitored regularly; deceased mice were immediately collected, and the thoracic aorta was removed for mechanical testing. Any mice still alive at 25 months of age were euthanized by CO_2 inhalation, and the thoracic aorta was removed for mechanical testing. All animal procedures were approved by the Institutional Animal Care and Use Committee at Washington University.

5.2.3 Magnetic resonance imaging (MRI)

Mice were imaged at two and six months of age. For the imaging procedure, mice were anesthetized with 1-2% isoflurane and imaged in the supine position on an Agilent DirectDrive 4.7T MRI (Agilent Technologies, Santa Clara, CA) with a 3.5 cm birdcage radiofrequency coil. Axial 2D gradient echo cine images at 21 cardiac phases were acquired using prospective cardiac and respiratory gating. The imaging parameters were as follows: field of view = 2.4 x 2.4 cm, imaging matrix 128 x 128, echo time 1.3 ms, the repetition time was determined by the cardiac rate, flip angle = 90 degrees, 70-80 slices at 0.5 mm thickness covering the aortic arch through the renal arteries (acquired sequentially in groups of 10 to account for variation in cardiac rate). The acquired images had a resolution of 187.5 x 187.5 x 500 μm^3. The images corresponding to diastole were averaged and interpolated

to 250 μm slice thickness for further analyses. Representative images of axial slices (Figure S1) and a coronal maximum intensity projection (Figure S2) are included in the supplementary data.

Geometrical parameters were determined from the MR images using MATLAB (Mathworks, Natick, MA). The aorta was segmented from the axial image stacks from the aortic root to the bifurcation. The outer surface of the aortic lumen was identified, and circles were fit perpendicular to the outer surface. The centroid and diameter (D) of each circle were identified, as well as the actual length (AL = length following the aortic contour of the fitted centroids) and geometric length (GL = straight-line length between centroids), as seen in **Figure 22**a. The maximum diameter was calculated from the fitted circles and the aortic tortuosity index (ATI) was calculated as (AL/GL-1) x 100[156].

5.2.4 Mechanical testing

The ascending and descending aorta were removed for mechanical testing (Fig 1b), as previously described [157, 158]; for the present analysis, only the ascending aorta data were used. Briefly, the aorta was mounted in a pressure myograph (DMT USA, 110P) in physiologic saline at 37°C and preconditioned for at least three cycles in each direction (circumferential and axial). The aorta then underwent six mechanical testing protocols: three cyclic inflation cycles at a constant axial stretch (0 – 175 mmHg pressure at approximately 1.3, 1.4, and 1.5 axial stretches) and three cyclic axial stretch cycles (from approximately 1.3 – 1.5

axial stretches at 50, 100, and 150 mmHg pressures). Thin rings were cut from the aorta after testing, and images were taken to measure the unloaded diameter and thickness (**Figure 22**b).

5.2.5 Aortic wall constitutive equation

To account for the anisotropic and nonlinear mechanical behavior of the arterial wall, we described the tissue using the Holzapfel, Gasser, and Ogden (HGO) model [35] for the strain energy density function**.**

$$\Psi = \frac{c}{2}(I_1 - 3) + \sum_{i=1}^{2} \frac{k_1}{k_2}[\exp\{k_2[\kappa I_1 + (1 - 3\kappa)I_{4i} - 1]^2\} - 1]$$

[43]

Where the first term represents an isotropic neo-Hookean matrix, the quantity $I_1 = \mathrm{tr}(\boldsymbol{F}^T\boldsymbol{F})$ is the first invariant of $\boldsymbol{F}^T\boldsymbol{F}$, where $\boldsymbol{F}$ is the deformation gradient tensor, and *c* denotes the neo-Hookean parameter. The second term accounts for the anisotropic behavior of a fibrillar component comprising two fiber families. The invariant $I_{4i} = \lambda_\theta^2 \cos^2\gamma_i + \lambda_z^2 \sin^2\gamma_i$ describes the stretch along the fiber direction γ_i, where λ_θ is the tissue stretch ratio along the circumferential direction, and λ_z is the stretch ratio along the axial direction. The parameter κ characterizes the fiber dispersion, $k_1 > 0$ is a modulus-like parameter, and $k_2 > 0$ is a dimensionless nonlinearity parameter.

It was assumed that $\gamma_1 = -\gamma_2 = \gamma$, and that k_1, k_2, and κ were the same for both fiber populations, leaving five parameters (c, k_1, k_2, κ, and γ) that were fit for each

mouse using MATLAB. Experimental data for the ascending aorta region were used since most of the aneurysms were formed in that region. The fitting was obtained by minimizing the mean squared error between the theoretical and the experimental circumferential and axial stresses. Assuming incompressibility and negligible shear, the wall stresses were calculated as follows:

$$\sigma_z = \lambda_z \frac{\partial \Psi}{\partial \lambda_z} \quad [44]$$

$$\sigma_\theta = \lambda_\theta \frac{\partial \Psi}{\partial \lambda_\theta} \quad [45]$$

Two out of the ten *Fbln4*^{SMKO} mice did not have the mechanical or unloaded geometry data available, so for those two mice, we estimate the parameters by using the average data for the other eight mice. An elastic modulus (E) was calculated from the isotropic contribution of HGO model, by using the relation E=c(1+v), where v is the Poisson's ratio of the tissue. This modulus, although not used in the computations, provided a rough measure of the overall tissue stiffness, and was considered as a potential biomarker.

5.2.6 Mouse-specific FSI simulations

5.2.6.1 Model construction and mesh generation

FSI models were constructed for each mouse using two- and six-month MRI scans. Two domains are required for the FSI simulations: the fluid domain, given by the vessel lumen, and the solid domain, representing the aortic wall. A 3D model of the

fluid domain was generated from MRI scans. Scans were segmented using image segmentation and model generation in SimVascular [159], with supplemental editing in Meshmixer (Autodesk, Inc.). The 3D model included the brachiocephalic trunk, the left common carotid, and the left subclavian artery.

Because the aortic wall is too thin to measure directly from the MR images, the aortic wall was generated by extruding the lumen wall outward. The mouse-specific unloaded wall thickness was based on experimental measurement for the ascending aortic region shown in **Table 5** and was treated as constant over the length of the aorta.

A tetrahedral mesh was created using the TetGen mesh generator that is embedded in SimVascular [160]. The mesh included both the solid and the fluid domains, with matching nodes at the interface between the domains to satisfy the kinematic and dynamic boundary conditions at the interfaces.

***Table 5**: Mouse-specific parameters*				
Mouse ID	Elastic modulus [MPa]	Wall thickness [mm]	Lifespan [months]	ATI
15469_3 F	1.14**	0.142**	12.4	35.4
15398_3 M	0.47	0.142	13.3	52.0
15392_1 M	2.23	0.129	17.8	45.3
15392_2 M	1.16	0.122	18.2	59.5
15466_1 F	0.88	0.125	21.9	53.6
15398_1 M	1.22	0.140	22.4	37.9
15466_3 F	1.59	0.122	25*	39.9
15474_2 F	0.93	0.180	25*	38.8
15474_3 F	0.64	0.162	25*	22.8
15389_1 M	1.14**	0.142**	25*	28.7
M = male and F = female in mouse ID. Elastic modulus and unloaded wall thickness are for the ascending aorta * Euthanized after reaching approximately 25 months of age **Average from the other 8 mice data since mechanical and geometrical data were not available ATI – Aortic Thoracic Index				

5.2.6.2 Boundary conditions

For the solid domain, a fixed boundary at the inlet and outlets was assumed. For the outer boundary of the arterial wall, to account for the fact that the aorta is surrounded by various tissues and organs that restrict the aorta movement and dilation, a Robin-type boundary condition was imposed [161]:

$$\boldsymbol{\sigma}_s \cdot \boldsymbol{n} = -k_s \boldsymbol{u} - c_s \frac{\partial \boldsymbol{u}}{\partial t} - p_0 \boldsymbol{n}$$

[46]

Where $\boldsymbol{\sigma}_s \cdot \boldsymbol{n}$ is the traction arising when the Cauchy stress tensor $\boldsymbol{\sigma}_s$ at the wall is projected along the normal direction $\boldsymbol{n}$. The variable $\boldsymbol{u}$ is boundary displacement**,** and $\frac{\partial \boldsymbol{u}}{\partial t}$ is the local tissue velocity. Parameters $k_s$and c_s account for the viscoelastic

response of the external tissue, and p_0 is the external pressure of the abdominal and thoracic cavity. Parameters values were set as follow: $k_s = 10^7$ N.s/m^3, $c_s = 10^4$ N.s^2/m^3, and $p_0 = 0$ Pa. Those values are in the range of the values reported in the literature [162, 163].

The fluid domain boundary conditions are shown in **Figure 23**. A waveform from the mouse study of Cuomo et al. [164] (**Figure 23**b) was used as the inlet boundary condition and was assumed to be the same for all mice. For the outlet arteries, a three-element circuit analog model (**Figure 23**c) was prescribed as boundary conditions.

$$\frac{\partial p}{\partial t} + \frac{p}{R_d C} = \frac{Q}{C}\left(1 + \frac{R_p}{R_d}\right) + R_p \frac{\partial Q}{\partial t}$$

[47]

where p is the spatially averaged pressure at each outlet, Q is the inflow rate at each outlet, R_d is the distal resistance, R_p is the proximal resistance, and C is the compliance of the downstream vasculature. The values for R_d, R_p, and C were based on literature [164] and are given in Table 2.

***Table 6**: Outflow model parameter values.*

	R_p [Pa. s/mm^3]	C [Pa/mm^3]	R_d [Pa. s/mm^3]
1. Left subclavian artery	19.58	5.5×10^{-4}	286.2
2. Left common carotid	44.70	3.23×10^{-4}	488.0
3. Brachiocephalic trunk	21.55	3.54×10^{-4}	443.2
4. Outlet	10.30	5.41×10^{-4}	443.2

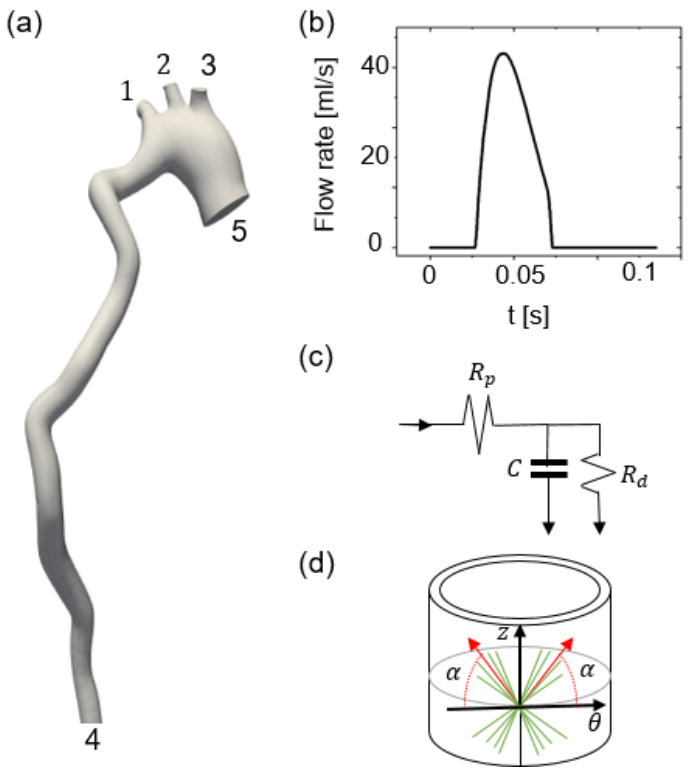

***Figure 23**: **(a)** Summary of the boundary conditions for FSI simulations including: **(b)** Inflow flow rate waveform for inlet at location 5. **(c)** Three-element Windkessel model for outlets at locations 1-4, values are giving inn Table 2. **d)** Anisotropic hyperelastic material model for the wall described in Eq.[43] that accounts for 2 fiber families oriented with an angle α with θ-direction.*

5.2.6.3 Blood rheology

Although non-Newtonian behavior is often neglected in a large artery, blood flow in the mouse aorta presents a Reynolds number of the order of 200 [165], which is much lower than the values observed in humans (~1000) [166]. Consequently, the shear stress may not be large enough for blood to be treated as a Newtonian fluid. To account for the non-Newtonian behavior of the mouse blood, we describe the blood viscosity using the shear-thinning Carreau-Yasuda model:

$$\eta = \eta_\infty + (\eta_0 - \eta_\infty)(1 - (\lambda\dot{\gamma})^a)^{\frac{n-1}{a}} \quad [48]$$

where η is the apparent viscosity as a function of the shear rate $\dot{\gamma}$. η_∞ is the infinite-shear-rate viscosity, which describes the low-viscosity plateau region for high shear rate flow conditions. The zero-shear-rate viscosity η_0 describes the high-

viscosity plateau region for low shear rate flow conditions. The parameters *a*, *n*, and λ describe the power-law region between the two plateaus. Parameter values were based on our previous analysis of healthy human blood [167], which is similar to mouse blood rheology for the shear rate range of the interest [168]: $\eta_\infty = 2\ cP,\ \ \eta_0 = 11\ cP, \lambda = 1.5, a = 0.2, n = 0.71.$

5.2.6.4 Prestress of the structural domain

In vivo, the aortic wall is subjected to mechanical load from the blood pressure, even during diastole. Accounting for this underlying mechanical loading state is crucial to get an accurate material response during FSI, especially when the model is constructed from *in vivo* image acquisition. In particular, Baumler *et al.* [169] showed that the prestress helps to reduce the numerical artifacts such as deviations in the aortic diameter and the drop in diastolic pressure.

We used the approach proposed by Hsu and Bazilevs [65] and embedded it in the FSI solver of SimVascular [170, 171]. A prestress tensor is determined via a three-step process: 1) An approximation for the diastolic load exerted on the aortic wall is derived based on the traction obtained from rigid-wall blood flow simulation for the fluid domain under diastolic inflow rate and using the same boundary conditions as in the FSI simulation, 2) the balance of momentum between the solid domain and the fluid traction is used to obtain the prestress tensor, and 3) the prestress tensor is used for the FSI simulations.

Once the prestress had been determined, dynamic simulations were performed for ten cardiac cycles using the svFSI solver from SimVascular [172] at the Minnesota Supercomputer Institute (MSI) using 120 CPUs for about sixty hours.

5.2.7 Data analysis and statistics:

5.2.7.1 Tobit model

Four out of the ten mice were euthanized at age 25 months, censoring the data at a maximum of 25 months. To account for the censored data, we used the Tobit model [173] given by.

$$Y_t = X_t\beta + u_t \qquad \text{if} \quad X_t\beta + u_t < Y_{max}$$
$$Y_t = Y_{max} \qquad \text{if} \quad X_t\beta + u_t \geq Y_{max}$$

[49]

In this model Y_t is the dependent variable, in our case, the mouse lifespan; X_t are the independent variables, being fluid dynamics and geometrical biomarkers; β is the fitting coefficient; and Y_{max} is the censor cut off, 25 months in our case. The stochastic error, u_t is assumed to have a normal distribution, mean at zero, and a constant variance σ^2. Here $t = 1,2, \dots, N$, with N being the number of observations.

Since the Tobit model limits the dependent variable, the traditional r^2 is not the best measurement to evaluate the goodness-of-fit. We used the modified McKelvey and Zavoina pseudo-r^2 [174] since it has been shown to recover the standard r^2 values for non-censored data.

$$r^2 = \frac{\sum_{i=1}^{N}(Y_t - \overline{Y_t})^2}{\sum_{i=1}^{N}(Y_t - \overline{Y_t})^2 + N\sigma^2}$$

[50]

where $\overline{Y_t}$ is the mean of Y_t.

5.2.7.2 Correlation analysis

A correlation map was built using selected fluid-dynamical, geometrical, and mechanical biomarkers. The list of the biomarkers used in this study is given in ***Table 7***. Here, Δ represents the absolute difference between the parameters' values from two to six months. Maximum, minimum, and mean values are calculated throughout the tenth cardiac cycle and in the whole aorta. Parameters calculated at six months of age were considered possible biomarkers for lifespan, as was the change in the parameter values from two to six months of age for an individual mouse.

***Table 7**: List of geometrical and biofluidic markers*

Abbreviation	Description	Range
P_{max}	Max Pressure	110-172 mmHg
vMs_{max}	Max von Mises Stress	320 – 770 kPa
Re_{max}	Max Reynolds Number	143 - 227
OSI_{min}	Minimum Oscillatory Shear Index	$3.3 \times 10^{-8} - 1.2 \times 10^{-5}$
OSI_{mean}	Mean Oscillatory Shear Index	0.17 – 0.38
$TAWSS_{mean}$	Mean Time Average Wall Shear Stress	0.9 - 3.42 Pa
$TAWSS_{max}$	Max Time Average Wall Shear Stress	6.1 – 11 Pa
$TAWSS_{min}$	Min Time Average Wall Shear Stress	0.005 – 0.33 Pa
Wo	Womersley Number	1.1 – 2.3
ATI	Aortic Tortuosity Index	22.8 – 59.5
D_{max}	Max Aortic Diameter	1.20 – 3.30 mm
ΔP_{max}	Change in Max Pressure	0 – 67.5 mmHg
ΔvMs_{max}	Change in Max von Mises Stress	10 – 210 kPa
ΔRe_{max}	Change in Max Reynolds Number	18 - 75
ΔOSI_{min}	Change in Minimum Oscillatory Shear Index	$1 \times 10^{-9} - 2 \times 10^{-6}$
ΔOSI_{mean}	Change in Mean Oscillatory Shear Index	0.012 – 0.063

$\Delta TAWSS_{mean}$	Change in Max Time Average Wall Shear Stress	0.09 – 4.3 Pa
$\Delta TAWSS_{max}$	Change in Max Time Average Wall Shear Stress	0.064 – 2.3 Pa
ΔWo	Change in Womersley Number	0.07 – 1.2
ΔD_{max}	Change in Max Aortic Diameter	0.01 – 0.73 mm
LS	Lifespan	12.37 – 25* months
* Mice that did not die naturally earlier were euthanized after reaching approximately 25 months of age		

$Re_{max} = \frac{\rho V_{max} D_{max}}{\mu_{avg}}$ was calculated using maximum velocity V_{max} at the peak of the 10th cardiac cycle, and the maximum aortic diameter D_{max}. The blood density was assumed to be $\rho = 1027$ kg/m^3. The average viscosity $\mu_{avg} = 3.35\ cP$ was calculated for the physiological murine shear rate range. The time average wall shear stress (TAWSS) is the average of the wall shear stress (WSS) during a full cardiac cycle:

$$TAWSS = \frac{1}{T}\int_0^T |\boldsymbol{\tau}| dt$$

[51]

where T is one cardiac cycle, and $|\boldsymbol{\tau}|$ is the magnitude of the WSS. The oscillatory shear index (OSI) accounts for the direction change in the WSS vector $\vec{\boldsymbol{\tau}}$ during the cardiac cycle:

$$OSI = \frac{1}{2}\left(1 - \frac{\left|\int_0^T \boldsymbol{\tau} dt\right|}{\int_0^T |\boldsymbol{\tau}| dt}\right)$$

[52]

OSI ranges from 0 to 0.5, with an OSI of 0 meaning that $\boldsymbol{\tau}$ does not change during the cardiac cycle and an OSI of 0.5 meaning that $\boldsymbol{\tau}$ fluctuates in 180°. The pseudo–r^2 given by Eq. [50] and based on the Tobit model fit Eq. [49]

was calculated for each biomarker.

5.3. Results

5.3.1 Experimental measurements and mechanical model

5.3.1.1 Mechanical model fitting and analysis.

We fitted the mechanical data for the ascending the aorta of each *Fbln4^{SMKO}* mouse separately using the HGO model of Eq. [43]. **Figure 24**a shows the experimental and fitted strain energy density function for a representative sample over the range of loading conditions. Results show a good agreement between experimental measurements and the material model.

Table 8 shows the summary data of fitting parameters for all eight mice. High standard deviations are observed for all the parameters, suggesting widely different mechanical behavior among the mice.

***Table 8**: HGO model fitting results for Fbln4^{SMKO} mouse ascending aorta.*

	Mean	Minimum	Maximum	Standard deviation
C [MPa]	1.77	0.23	4.91	1.53
k1[MPa]	0.43	0.30	10.01	3.37
k2[-]	2.01	2.7e-7	4.30	1.38
α[°]	44.95	9.5e-5	89.9	43.0
κ[-]	0.17	7.64e-8	0.41	0.16

Geometrical biomarkers obtained experimentally, such as aortic tortuosity index (ATI) for 6-month *Fbln4*^{SMKO} mice, and post-mortem diameter (D) and thickness (h) for the ascending aorta were also analyzed. Although the descending aorta data were not treated as potential biomarkers, they were obtained and are shown in **Figure 24**b for comparison, along with the other geometric data, all normalized by the means. Mean values and standards deviation are: $ATI = 39.2 \pm 11.4$, $\mathrm{D_{desc}} = 0.87 \pm 0.065\ \mathrm{mm}$, $\mathrm{h_{desc}} = 0.12 \pm 0.0062\ \mathrm{mm}$, $\mathrm{D_{asc}} = 1.59 \pm 0.38\ \mathrm{mm}$, $\mathrm{h_{asc}} = 0.16 \pm 0.043\ \mathrm{mm}$. As can be seen in **Figure 24**b, there was a considerable variation in ATI, and descending aortic geometry (D_{des}, h_{des}) was much more stable across mice than ascending aortic geometry (D_{asc}, h_{asc}). This difference was to be expected since aneurysms were present in the ascending aortic region.

The fitted parameters for the tissue material properties were used as input for FSI simulations. The geometrical data is used directly as biomarkers and potential predictors for aneurysm outcomes.

5.3.2 Mouse-specific FSI simulations

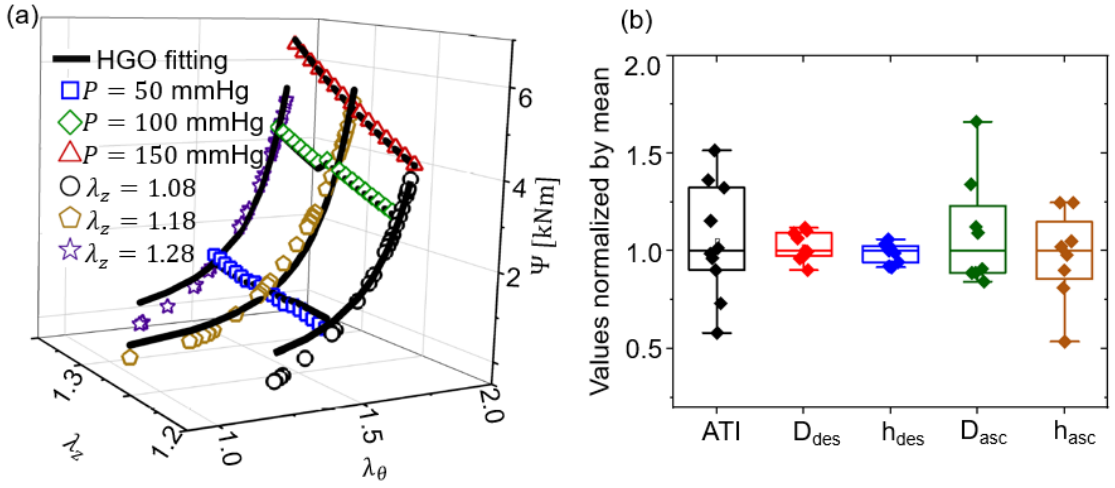

***Figure 24**: (a) Strain energy density for different experimental protocols (individual symbols) and the fitted HGO model (solid line) for a representative aorta. (b) Geometrical measurements normalized by mean, where means are:* $ATI = 39.2$, $D_{desc} = 0.87\ mm$, $h_{desc} = 0.12\ mm$, $D_{asc} = 1.53\ mm$, $h_{asc} = 0.16\ mm$

Figure 25 shows the Oscillatory Shear Index (OSI) distribution along the wall for all ten six-month-old *Fbln4*^{SMKO} mice at the 10th simulated cardiac cycle. The geometrical differences among the mice are easily seen, with a wide range of aneurysm size and shapes at this age, as well as a large spectrum of tortuosity in the descending thoracic aorta. For the OSI, higher values were observed close to tortuous regions in the descending aorta, and in the ascending aorta and arch, especially for large aneurysms. *Fbln4*^{SMKO} Mice exhibiting large aneurysms (e.g. **Figure 25**a) and **Figure 25**d) presented a lower OSI along the descending aorta. Time average wall shear stress (TAWSS) for each individual aorta is shown in the supplemental information (**Figure 32**).

5.3.3 Sensitivity analysis on the material properties and blood rheology

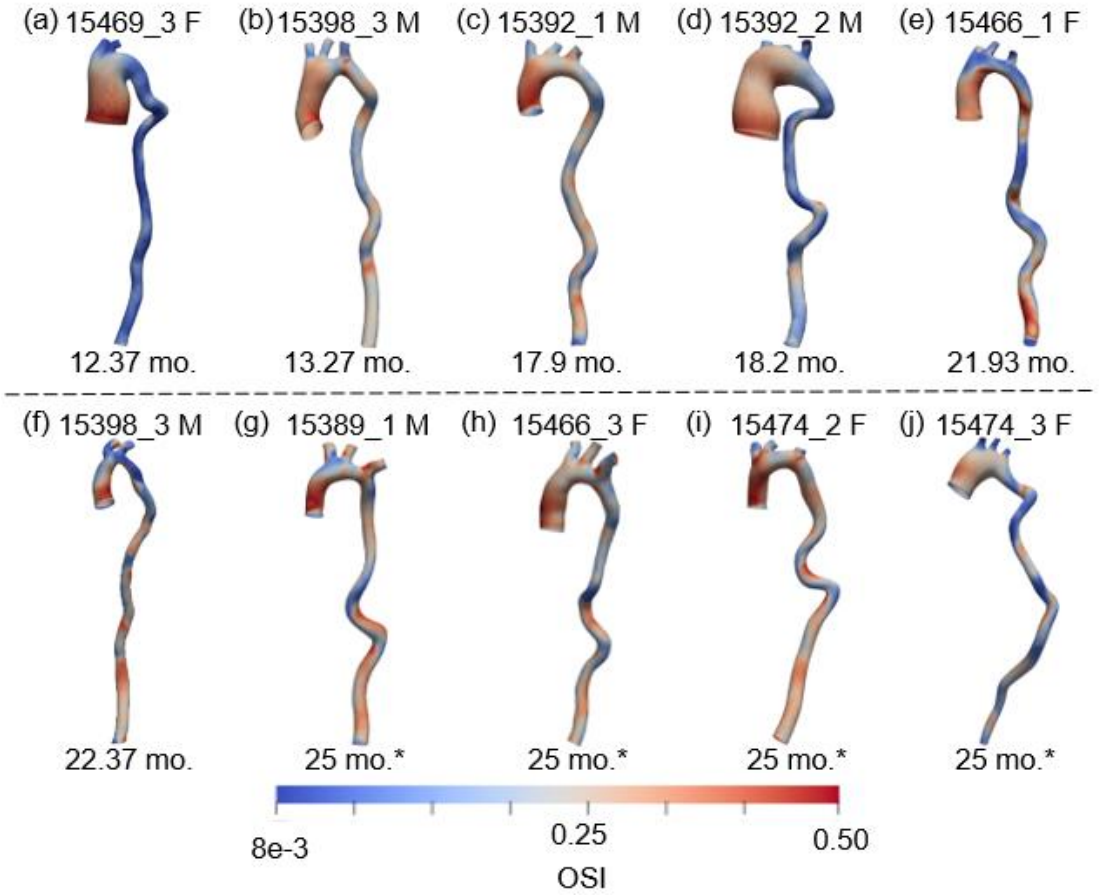

***Figure 25**: OSI distribution along the wall for all ten Fbln4^{SMKO} mice. Models are organized by increasing lifespan. Mouse ID code and sex (M/F) is given at the top of each model, and lifespan is displayed on the bottom. Asterisks refer to mice that were euthanized at 25-month age.*

A sensitivity analysis was performed to evaluate the impact of the material properties and fluid rheology on the results. For the material property analyses, four different variations of the modulus-like parameters (c, k_1 from Eq. [43]) for one *Fbln4^{SMKO}* mouse were explored: 50% and 25% smaller and 25% and 50% larger than the fitted values. **Figure 26** shows the results of the analysis. For the parameter c (**Figure 26**a) and parameter k_1 (**Figure 26**b) of the HGO model

presented in Eq. [43], the results suggest that moderate changes in the parameters (25% increase or decrease) have little or no impact on the results of the blood flow dynamics biomarkers.

For the fluid rheology analyses, a Carreau-Yasuda model was compared against the Newtonian approximation.

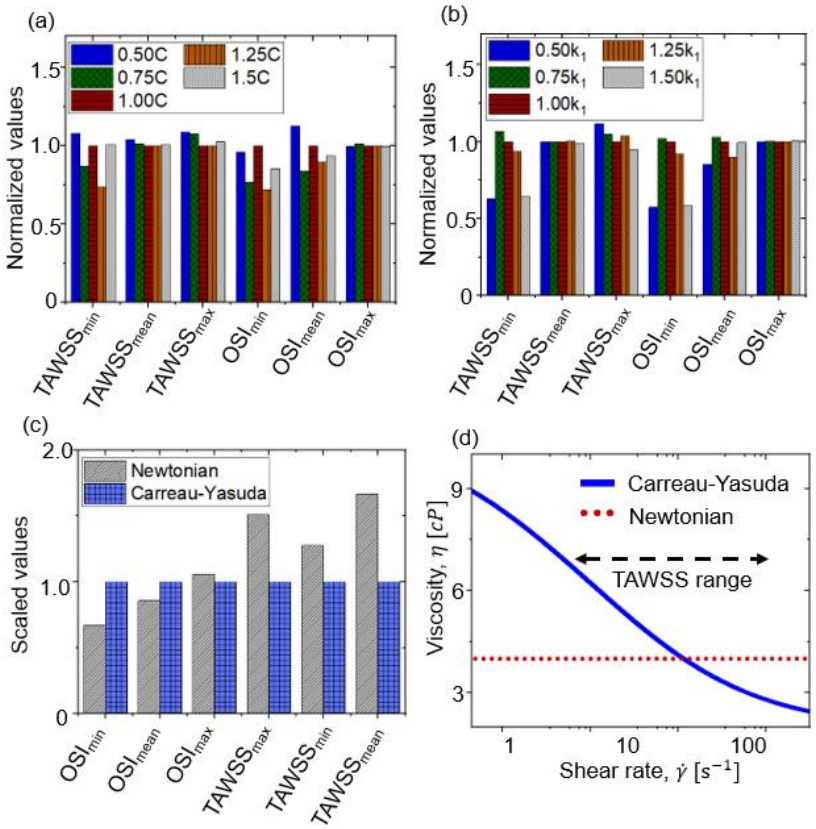

***Figure 26**: Sensitivity analysis for (a) Parameter c of the HGO model (Eq. [43]) normalized by the fitted value 1.00c (b) parameter k_1 of the HGO model (Eq. [43]) normalized by the fitted value 1.00k_1 (c) blood rheology comparing Carreau-Yasuda and Newtonian approximation normalized by the Carreau-Yasuda results. (d) Viscosity versus shear rate for Carreau-Yasuda model (solid line) and Newtonian model (dashed line)*

Figure 26c shows a substantial change in all the parameters for the Carreau-Yasuda model in contrast to the Newtonian approximation. This effect could have occurred because the biomarkers used in the analysis are sensitive to changes in velocity. Close to the wall, the shear rate is moderately high (~350 1/s) leading to a drop in the viscosity as shown in **Figure 26**d.

5.3.4 Statistical analysis

Taking the results obtained from the FSI simulations, we explored the relevance of each biofluidic, geometrical, and mechanical biomarker as a predictive indicator for the outcome of ATAA. We used mouse lifespan as a surrogate indicator for ATAA outcomes, assuming that reduced lifespan was due to complications associated with ATAA.

Figure 27a shows a pseudo-r^2 correlation matrix for the results from the FSI simulation and experimental measurements. The bottom row highlights the correlation or lack thereof between the main biomarkers and the mouse lifespan. Red indicates a positive correlation meaning that mice tend to live longer with an increase in the parameter. Conversely, blue indicates a negative correlation.

Among these, OSI_{mean} showed the highest positive correlation (r^2=0.70) to the mouse lifespan, followed closely by $TAWSS_{min}$ (r^2 = 0.56), as shown in more detail in **Figure 27**b and c. Note that the minimum and mean OSI calculations are dominated by the contribution of the descending aorta (**Figure 25**), meaning that a low OSI_{mean}, which corresponded to a shorter lifespan, indicated less oscillatory flow in the descending aorta, well downstream of the diseased segment and the presumed ultimate site of tissue failure. A low OSI downstream would be consistent with greater flow damping by the ascending aorta, which would result from a larger and more distensible aneurysm. In contrast $TAWSS_{min}$ was generally observed in

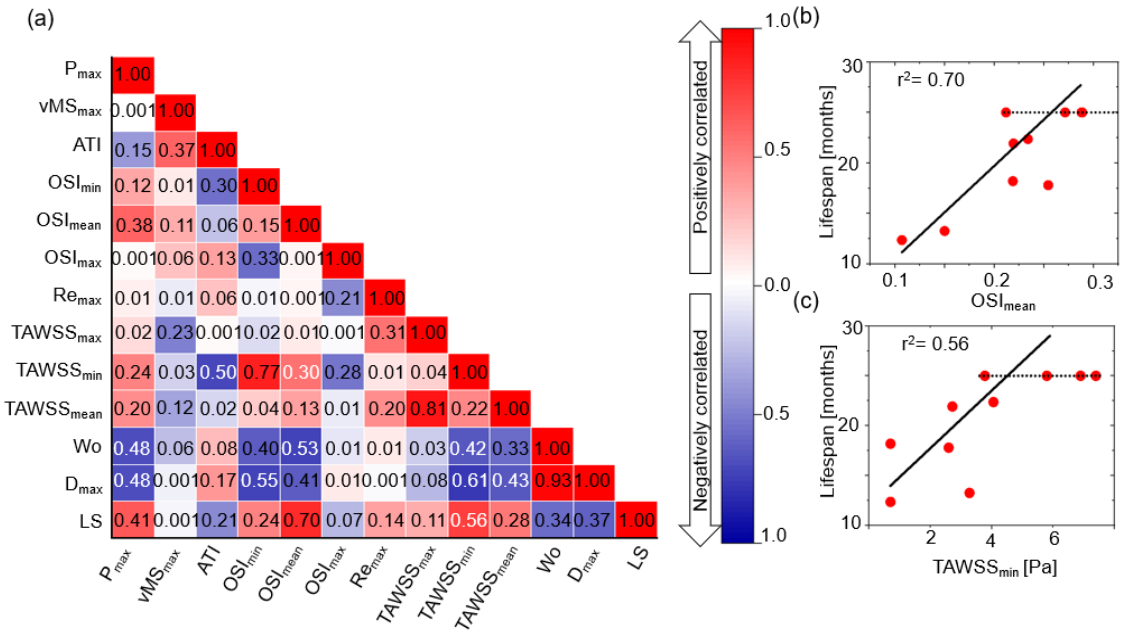

***Figure 27**: (a) Correlation map for biofluidic and geometrical biomarkers for six-month-old Fbln4^{SMKO} mice. The numbers in the map are the pseudo-r2 values based on Eq. [50], and the colors indicate positive (red) vs. negative (blue) correlation, with darker colors signifying a stronger correlation. (b) Mean OSI and lifespan correlation plot. The solid line is the Tobit model fit, and the dashed line is the censoring cut-off. (c) Minimum TAWSS and lifespan correlation plot.*

the ascending aorta (Supplemental **Figure 32**), suggesting that, unlike OSI_{mean}, it is acting as a direct biomarker of biofluidic events in the aneurysmal region.

We also investigated the change from 2 to 6 months of age in the biofluidic, geometrical, and mechanical biomarkers and their correlation to the *Fbln4^{SMKO}* mouse lifespan. ***Figure 28***a shows the correlation matrix for the absolute change in each biomarker between two- and six-month-old mice. Similar to the single-time-point analysis, ΔOSI and ΔTAWSS have some of the highest correlations with mouse lifespan, however the value that correlates with lifespan in each case is different. For the change in values over time, ΔOSI_{min} has a moderate positive correlation with lifespan (r^2=0.24, ***Figure 28***

b), while $\Delta TAWSS_{mean}$ has a high negative correlation with lifespan (r^2=0.75, ***Figure 28***c), followed closely by $\Delta TAWSS_{max}$ (r^2=0.52). These results indicate that longitudinal monitoring of biofluidic biomarkers, such as TAWSS, may provide

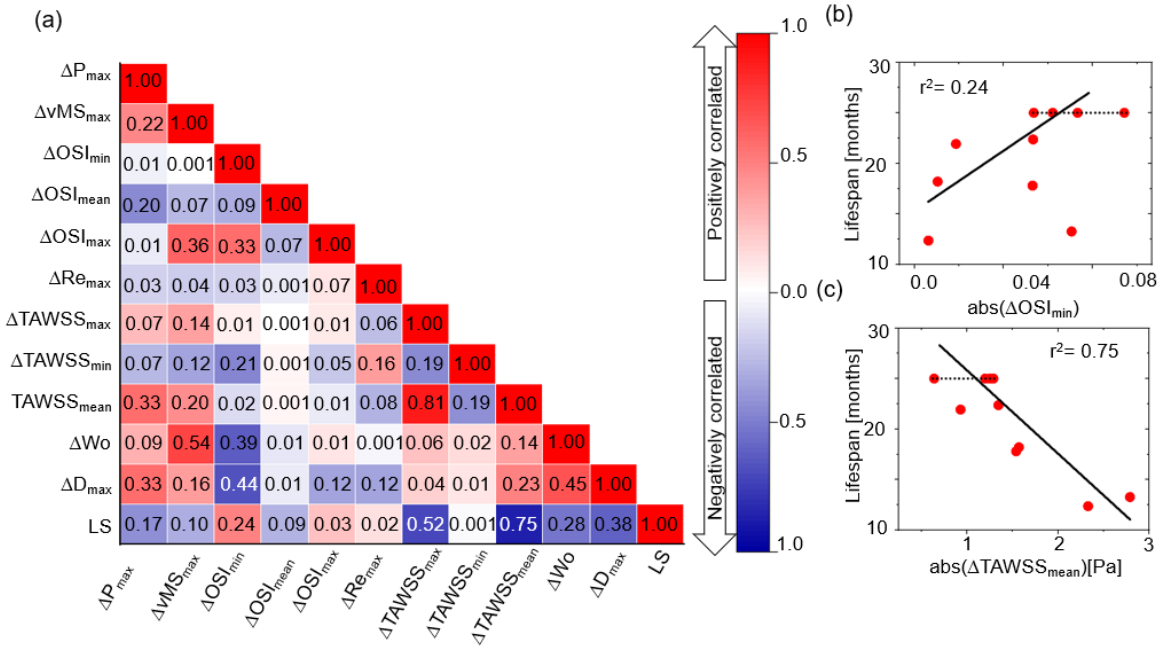

Figure 28*:(a) Correlation map for temporal changes in biofluidic and geometrical biomarkers from 2 to 6 months of age in Fbln4SMKO mice. The numbers in the map are the pseudo-r2 values based on equation (8), and the colors indicate positive (red) vs. negative (blue) correlation, with darker colors signifying a stronger correlation. (b) Minimum OSI and lifespan correlation plot. (c) Mean TAWSS and lifespan correlation plot.*
additional predictive information about ATAA outcomes.

Figure 29 shows the correlation plot for correlation between the maximum diameter (D) and the lifespan (LS) and change in the diameter (ΔD) and the lifespan. Both show a negative correlation with lifespan, which is expected. There was a moderate correlation for both cases: r^2=0.37 for diameter and lifespan, and r^2=0.38 for change in diameter and lifespan. Although the maximum diameter and temporal change are clinical criteria for the surgical treatment of patients, our results support our argument for additional and more accurate biomarkers for

predicting ATAA outcomes. In fact, previous work has shown that diameter and change in diameter criteria fail to predict an aneurysm rupture event, especially

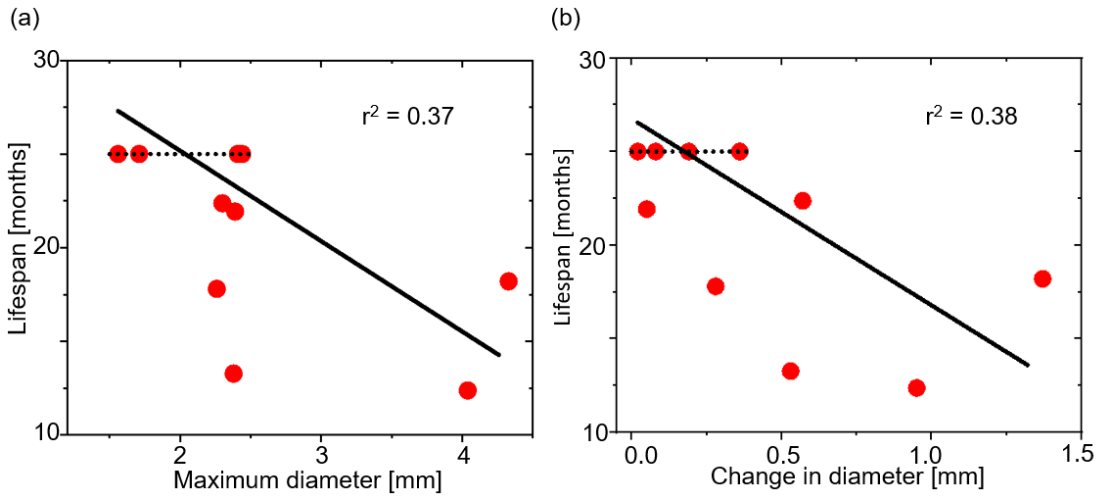

***Figure 29**: (a) Maximum aortic diameter and lifespan correlation plot. (b) Aortic diameters change from two to six month of age and lifespan correlation plot.*

with patients who have presented prior dissection of the aorta [137].

5.4 Discussion

The most important contribution of this work is its use of combined experimental and computational techniques to study the temporal evolution of ATAA in ten *Fbln4*^{SMKO} mice. The combined approach allowed us to extract geometrical and mechanical data for each mouse to build mouse specific FSI simulations and use the results to study the predictive capacity of non-invasive biomarkers of aneurysm disease.

Mouse-specific blood flow models are not novel per se [175–178], and [175] in particular provides a thorough description of the advantages and challenges of applying computational fluid dynamics to small animals. The novelty of the current

work is in (1) its specific application to ATAA, (2) its use of post-mortem biomechanical data to construct an FSI model with each mouse's specific aortic wall thickness and mechanical properties, (3) its use of computational analyses based on two different imaging time points, and (4) its direct comparison of biomarkers to mouse lifespan without intervention, an obviously relevant metric of long term outcomes of ATAA that cannot ethically be used in humans. Although the sample size was small (N = 10), certain key results arose that could help guide future animal and human studies.

The strongest correlation of a single measurement with lifetime was for the calculated OSI_{mean} (r^2 = 0.70, **Figure 27**b), followed by the $TAWSS_{min}$ (r^2=0.56, Fig. **Figure 27**c). These two quantities, which can be readily calculated from simulations based on human patient images [179, 180], showed considerably more correlation with lifetime than aneurysm diameter (r^2 = 0.37, **Figure 29**a), which is routinely used to access risk. TAWSS [181, 182] and OSI [183, 184] have both been associated with arterial remodeling, although the impact of these factors on ATAA has not been defined conclusively. Some studies [179, 185–187] suggest that low WSS values are related to wall weakening and dilation, whereas another study [188] found low WSS to be associated with decreased ATAA rupture risk. In the current study, we found that $TAWSS_{min}$ had a positive correlation with lifespan, meaning that a lower value of $TAWSS_{min}$ was associated with a shorter lifespan. The FSI simulations showed low TAWSS in the aneurysmal region (Supplemental Figure S3), consistent with TAWSS being an important potential biomarker.

We found that OSI_{mean} had a positive correlation with lifespan, indicating that a higher mean oscillatory flow correlated with longer life. Similar to WSS, the effect of OSI on aortic rupture is controversial and not yet fully understood. Some studies suggest that high OSI values are associated with a high risk of aortic rupture [189], [190], while others argue that OSI has no effect on rupture risk [191]–[193]. It may also be important to consider where OSI is being measured. In our simulations, OSI in the descending thoracic aorta may be an indirect indicator of disease state in the ascending aorta because of the effects on downstream flow. More broadly, the current work supports the idea that biofluidic biomarkers can complement and improve upon the information provided by geometrical biomarkers alone.

Despite the fact that previous studies have shown that aortic tortuosity index (ATI) [146] (or related metrics of axial stretch[15],) and maximum diameter (D_{max}) [151, 194] are important geometrical biomarkers for ATAA in humans and mice, our results showed only a moderate correlation between ATI (r^2 =0.21) and Dmax (r^2 =0.37) with mouse lifespan. Additionally, other mouse models with genetic defects in the elastic fibers show aortic tortuosity without evidence of ATAA [195], suggesting that tortuosity is related to elastic fiber integrity and overall mechanical behavior, but is not a sufficient independent metric for ATAA outcomes. This lack of strong correlation is indicative of a highly complex process that cannot be captured by a single measurement, and it also indicates the importance of individual variations among mice (and, even more so, among humans).

The availability of two- and six-month imaging data allowed consideration of temporal changes in parameters as additional possible biomarkers. We found that change in diameter (ΔD, i.e. growth rate) had a moderate correlation with the lifespan (r^2 = 0.38, **Figure 29**b). This point has received considerable attention as regards human patients (see [6]) with no clear conclusion and challenges because of the slow growth rate of most of ATAAs in humans. It is also notable that although both $\Delta TAWSS_{mean}$ and ΔOSI_{min} showed a correlation with lifespan (r^2=0.75, r^2 = 0.24, ***Figure 28***), there was almost no correlation between them (r^2 = 0.02 ***Figure 28***), suggesting that the two metrics are complementary. These possibilities require further study in animals and, when possible, in humans. In considering the longitudinal data, we note that the aneurysm had already begun to form in most mice at the first scans that we took at two months. It would be informative to have earlier timepoint data to observe the initial formation of the aneurysm, rather than the growth of the existing aneurysm, although there will be technical challenges and limited imaging resolution in juvenile mice. The data would be particularly valuable in testing and parameterizing *in vivo* models of aneurysm growth [57, 196].

In the current study, some limitations and areas of potential improvement need to be highlighted. The lack of available data for mouse-specific inlet blood flow and outlet boundary conditions (i.e. RCR parameters) presents a limitation on this study. Previous investigations in mice [197, 198] and humans [199, 200] showed that idealized (i.e. parabolic and Womersley) velocity profile had substantial

implications on the WSS distribution in the aortic region close to the inlet. Similarly, it has been shown that hemodynamic quantities are also affected by the choice of the outlet boundary conditions [197, 200]. Additionally, absent detailed regional wall properties, wall thickness and material properties were considered to be constant along the aortic length, ignoring heterogeneities of the arterial tissue that have been shown previously [201], which can potentially lead to skewed stress distribution along the wall. Limitations with respect to the MRI resolution and the small size of the mouse aorta, as well as positioning of the mouse that may affect aortic length measurements, add uncertainties to the calculated biomarker values [202]. We note that, given the relatively small test population and the large number of potential biomarkers, this study should be viewed as demonstrative of technique and as identifying hypothetical biomarkers for future study but not as a definitive determination of the validity of biomarkers. Finally, we used mouse lifespan as a surrogate measure for ATAA outcomes. We euthanized four of the ten mice at 25 months of age and did not do detailed necropsies on the mice with shorter lifespans, so it is possible that these mice died for other reasons than ATAA complications. Despite these shortcomings, the model outputs showed good correlation with mouse lifespan, suggesting that human patients - for whom flow profiles and regional wall properties may not be available - may still benefit from analysis of this type to predict disease outcomes, especially if the large pool of potential biomarkers can be reduced in size by a statistical technique such as principal component analysis. Although this paper is not intended to compare

mouse to human studies, we provided a brief discussion of the differences in terms of the current study and its results. Perhaps, most significantly, we used post-mortem, isolated mouse aorta mechanical test data as inputs to the model, whereas if one intended to use a patient-specific model for clinical application, *in vivo* estimates of the properties would be needed. Recent advances in this area [203], [204] offer hope for such data to be readily available in the future. Also, the variability from mouse to mouse, both in terms of aneurysm shape (**Figure 25**) and in terms of longevity (**Table 5**) was dramatic, and the wide range of genetic, environmental, and lifestyle factors in humans implies even more variation. We conclude with the observation that there are countless parameters and combinations of parameters that could be considered as potential geometrical and biofluidic biomarkers. Pulse wave velocity [205], for example, is easy to measure and non-invasive, and it could be estimated from FSI calculations, like the ones performed in this study, or could be used to tune the model's estimate of the wall properties. Diameter and tortuosity are simple measures, but many other measures (e.g., vessel curvature in the aneurysm, aneurysm volume, or some measure of aneurysm length) could be created and might be meaningful. Machine learning tools to describe the geometry and mechanics of the aorta [206] may provide a platform for more efficiently identifying potential novel biomarkers. Finally, the study was performed using fully coupled FSI simulations with a nonlinear constitutive equation for the vessel wall, which can be computationally expensive. The Small on Large approach [207], which is significantly cheaper

computationally while still capturing much of the vessel behavior, could be considered if the full simulations prove intractable.

5.5 Supplemental information

5.5.1. Methods

5.5.1.1 Magnetic resonance imaging (MRI)

Heavily T1-weighted axial images were acquired at 187.5 x 187.5 x 500 μm^3 resolution using prospective cardiac and respiratory gating. The images below show an example of the diastolic angiographic images from one mouse (Fbln4het/LOX +- #3). At this resolution, the aorta is typically over five voxels across, making it relatively easy to identify and accurately manually segment.

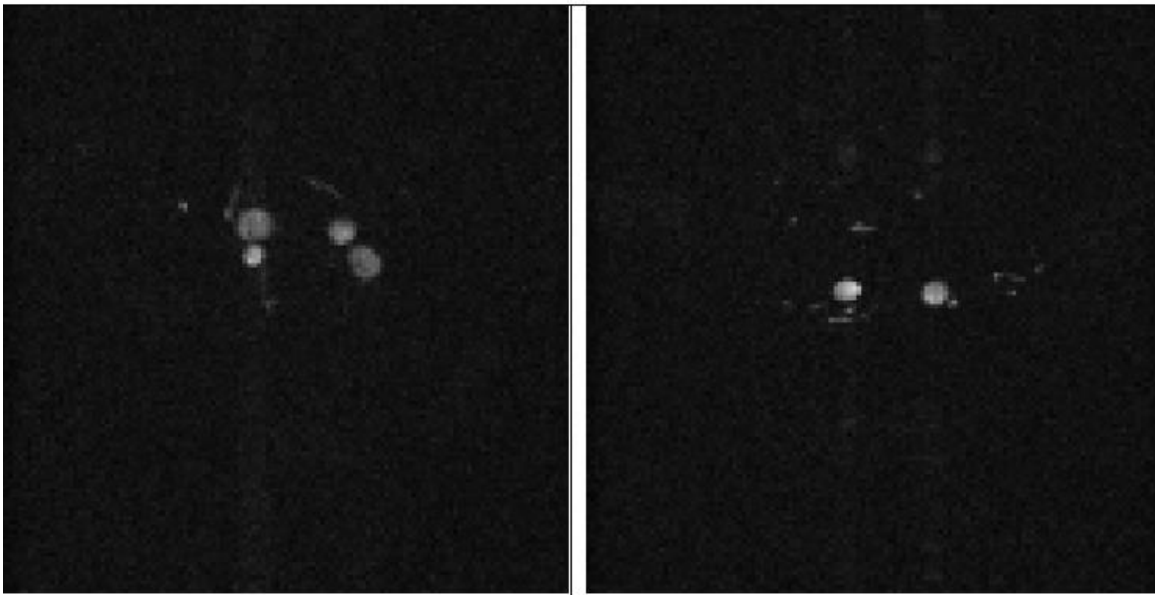

Figure 30*: Axial MRI images at 187.5 x 187.5 x 500 μm3 resolution from above (left) and below (right) the heart. Images are shown after averaging across all diastolic images but without interpolation or smoothing.*

For analysis, the images were interpolated to 187.5 x 187.5 x 250 μm^3 resolution to improve the ability to detect changes in vessel orientation. The Maximum Intensity Projection (MIP) image below illustrates the conspicuity of vessels much smaller than the aorta across the mouse thorax and abdomen.

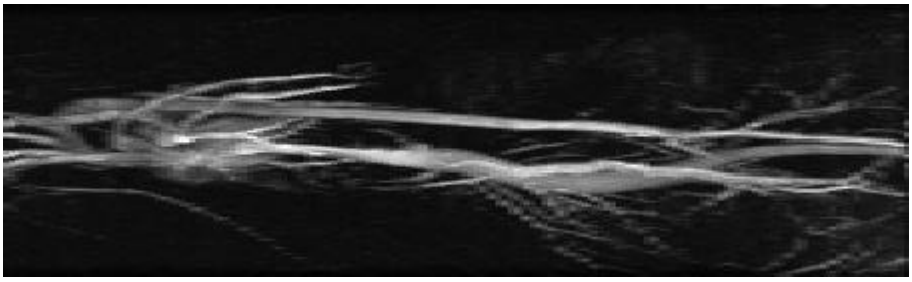

***Figure 31**:Coronal MIP (Maximum Intensity Projection) diastolic image (cranial to left) after interpolation across slices but without any further processing.*

5.5.1.2 Blood rheology

Blood rheology was modeled using the Carreau-Yasuda model. The model parameters were used based on previous measurements obtained in using human healthy blood. Table one shows the comparison between measured viscosity for mice and humans and the Carreau-Yasuda model prediction. We can observe that the Carreau Yasuda model predicts well the mice measured viscosity. And for the moderate to high shear rate range, which is the range of interest for this study, all the three measurements are similar within the confidence interval.

***Table 9:** Viscosity values for mouse, human, and Carreau Yasuda model prediction for four levels of shear rate.*

	WBV (0.7 s^{-1}) [cP]	WBV (2.4 s^{-1}) [cP]	WBV (94s^{-1}) [cP]	PV [cP]
Mice experimental measured	13.367 (10.691/16.568)	10.563 (8.929/12.289)	4.879 (4.506/5.345)	1.31 (1.29/1.34)

Human experimental measured	33.487 (26.264/39.584)	18.529 (15.729/21.493)	5.996 (5.140/6.938)	1.24 (1.2/1.31)
Carreau-Yasuda model	15.12 (10.93/19.18)	12.79 (7.33/16.48)	6.54 (5.08/7.36)	1.2 (1.1/1.31)

5.5.2 Results

5.5.2.1 Mouse-specific FSI simulations

Figure S3 shows the Time Average Wall Shear Stress (TAWSS) distribution along the wall for all ten six-month-old Fbln4SMKO mice at the 10th simulated cardiac cycle. A wide range of TAWSS can be observed, but for almost all geometries, low

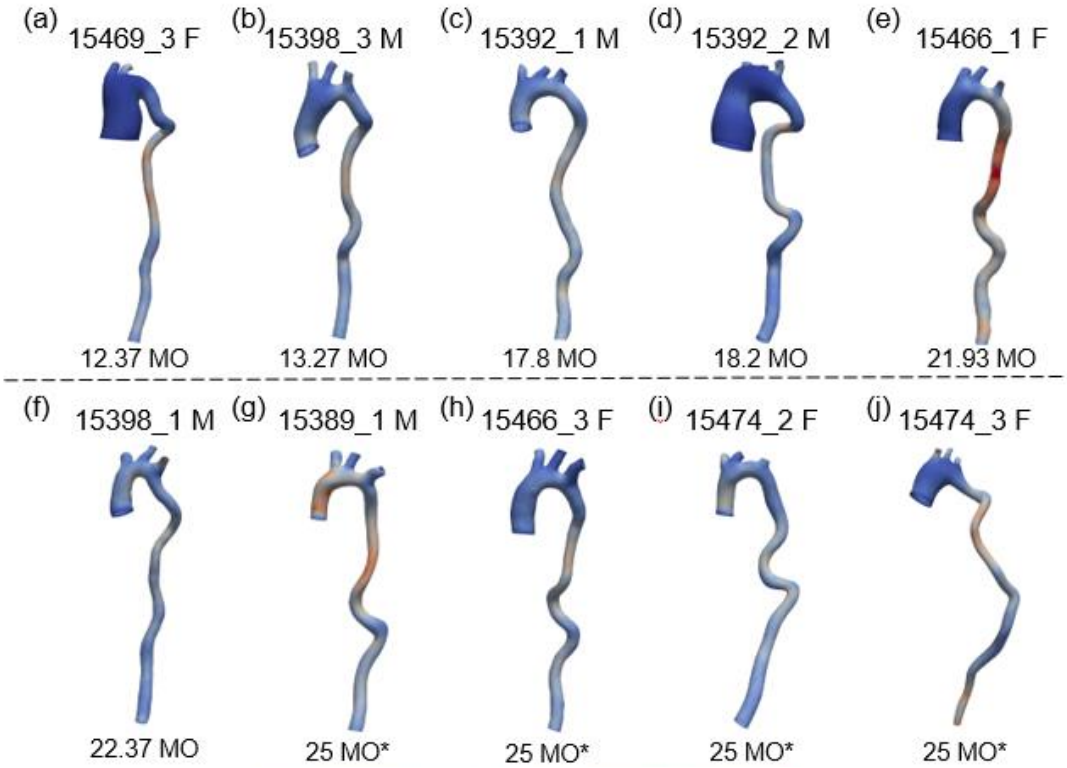

Figure 32: *TAWSS distribution along the wall for all ten Fbln4^{SMKO} mice. Models are organized by increasing lifespan. Mouse ID code and gender is given at the top of each model, and lifespan is displayed on the bottom.*

values were observed in the aortic arch, especially for large aneurysms (**Figure 32**a and **Figure 32**b). Interestingly, the opposite behavior was observed for OSI, especially for large aneurysm formation, large values of OSI were observed along the aortic arch.

Chapter 6: Hemodynamics-Driven Aortic Growth and Remodeling for Genetically Modified Mice Model.

Abstract

Arterial growth and remodeling (G&R) in response to biomechanical stimuli play a pivotal role in vascular health. Disruptions in this process, often seen in conditions like aneurysms and atherosclerosis, can lead to pathological changes, posing significant health risks. Predicting the risk of aneurysm rupture remains a challenge, prompting investigations into additional metrics beyond traditional diameter measurements.

This study delves into a controlled subject-specific assessment of maladaptive aortic tissue growth and remodeling using the *Fbln*^{SMKO} mouse model. The proposed model leverages a continuum G&R approach applied locally and Fluid-Solid-Interaction (FSI) simulations. Ten *Fbln*^{SMKO} mice were studied, showcasing varying degrees of aneurysm formation over time. The investigation primarily focused on the ascending aorta region, the site of aneurysm development in these models. Using a growth and remodeling model rooted in hemodynamics, the study employed a mesh-based approach, analyzing stress-based growth laws and

remodeling formulations. The model was tuned and validated using 4-month and 6-month geometrical information extracted from medical scans.

The single-domain G&R model showed variable accuracy in predicting radial growth across different mice, exhibiting both underestimations and overestimations compared to in-vivo measurements. Correlation analysis revealed a positive association between circumferential growth time constants and ascending aortic young modulus, and axial growth time constant and the tortuosity index. Multiple-domain modeling improved predictions, resulting in a closer approximation to scanned geometries.

While this study presents advancements in understanding ATAA progression in *Fbln*^{SMKO} mice, limitations include simplified material assumptions and a small sample size. Future research should focus on integrating biochemical factors into models, accounting for tissue complexity, and validating across diverse mouse models to enhance applicability. Overall, this study demonstrates the potential for personalized risk assessment and treatment planning in ATAA using hemodynamics-driven G&R models.

6.1 Introduction

Arterial growth and remodeling (G&R) refer to the ability of living tissues to change their physical and mechanical properties in response to their biomechanical environment. A popular principle is that the G&R process maintains a homeostatic stress level in the vessel walls [11]. In healthy arteries, mechanical homeostasis is characterized by a negative feedback loop, where a preferred state is restored

after a perturbation. However, when risk factors, such as hypertension and vascular aging, are present, or in diseased arteries like aneurysm and atherosclerosis, the homeostasis can be disrupted, producing a positive feedback loop that promotes a pathological G&R of the arterial tissue [12].

For ascending thoracic aortic aneurysms (ATAA), the positive feedback loop triggers continuous growth and gradual weakening of the vessel wall, increasing the risk of aortic rupture or dissection. When such rupture occurs, it is estimated that more than 50% of the patients succumb before reaching the hospital, resulting in an overall mortality between 11% and 90% [208]. A major challenge in ATAA management derives from our inability to predict accurately which patients are at risk of having a ruptured aneurysm. While aneurysm diameter and growth rate are the measurements guiding surgical decisions, they fall short in providing a comprehensive diagnosis, frequently providing inadequate prediction of the actual risk [6].

To advance the diagnostic accuracy and improve the prediction of rupture risk, additional metrics beyond growth and maximum diameter must be considered. Several studies have investigated alternative biomarkers, such as blood flow dynamics, mechanical properties, and tortuosity index as potential additional indicators predicting adverse outcome in patients with aneurysms [10, 209–211]. However, those metrics typically evaluate a snapshot rather than accounting for the time-dependence nature of the diseases.

In this study, our goal was to investigate the progressive changes that occur in the maladaptive growth and remodeling of aortic tissue using a controlled subject-specific setting. The *Fbln*^{SMKO} mouse [212] provided an ideal system for this study. The genetic and lifestyle reproducibility of mouse studies, combined with the short lifespan, yield a much better controlled system. In addition, a completed and detailed longitudinal study of aortic G&R in the *Fbln*^{SMKO} mouse, including CT imaging and post-mortem mechanical testing on each mouse have been performed [10]. Herein, we used a simplified growth and remodeling model rooted in a continuum approach, combined with a comprehensive Fluid-Solid-Interaction (FSI) simulations tailored to individual mice. Reconstructed 3D geometric models were used in conjunction with the longitudinal scans to tune and to validate the G&R. Finally, the fitted G&R model parameters were correlated with the lifespan of the mouse, measured postmortem ascending, and descending aortic young modulus, tortuosity index and maximum diameter at 6-month age.

6.2 Methods

In this study we brought together FSI and G&R models, as shown in Figure 33. This framework is split into tuning and validation stages. For the tuning stage, information for two- and four-month is used to fit the growth parameters. Figure 33A shows the workflow for the tuning stages, and steps are as follows:

1- Subject-specific FSI simulation: The unsteady blood flow simulation was solved for a subject-specific geometry using svFSI solver from SimVascular [213]. The time average wall stresses were extracted for each element and

used as input for the growth and remodeling (G&R) model. More details about the FSI simulation step can be found in section 2.3.

2- G&R model: The G&R model is solved for each element in ascending aortic region for an increment of a 10-days-period tissue growth (about couple second for simulation). After a 10-day-period, the local growth tensor is extracted and serves as input for FEBio to solve the equilibrium solution of the ascending aortic region, from where we can extract residual stress (S_{re}) and use to update the total stress in the G&R model. More details about the G&R model can be found in section 2.5 and 2.6.

3- Fitting parameters: After a period of 60-day period, the predicted geometry is calculated from the G&R model and compared the axial and circumferential growth to the *in-vivo* measurements. If the predicted measurements are not similar to in-vivo measurements, a new set of G&R parameters is calculated using Levenberg-Marquard algorithm[214], and restarts at step 2, until it converges. More details on how the fitting is performed are given in section 2.8 and 2.9.

For the validation stage, shown in Figure 33B, information for two- and six-month is used to assess the model performance. In this stage, the G&R step is solved for 120-day period using the fitted G&R parameters obtained from the tuning stage. After this period, predicted metrics are extracted from the grown geometry, and compared to the in-vivo metrics from the 6-month mice.

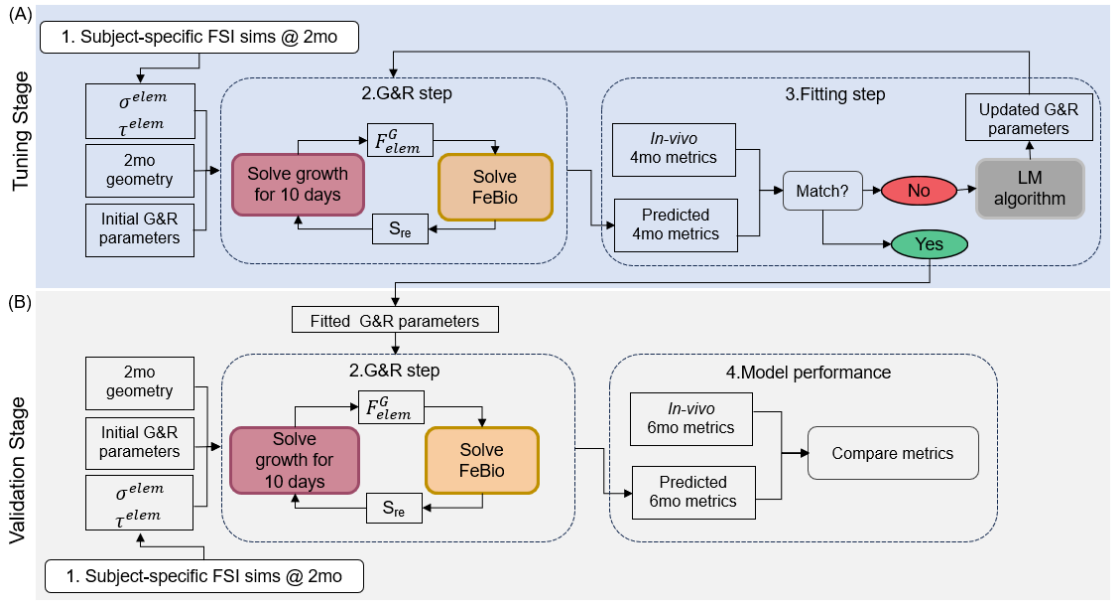

***Figure 33**: Workflow of subject-specific hemodynamics-driven growth and remodeling model. (A) Steps for the tuning stage using data from 2- and 4-month mouse models. (B) Steps for validation stage using the fitted parameters from the tuning stage to evaluate the model performance against the 6-month in-vivo metrics.*

6.2.1 Mice models

The study was performed using data previously published for ten mice lacking expression of fibulin-4 in smooth muscle cells (*Fbln4^{SMKO}*) [10]. Fibulin-4 is critical for elastic fiber assembly, and *Fbln4^{SMKO}* mice have ATAAs with about 50% penetrance. Mice were monitored regularly; deceased mice were immediately collected, and the thoracic aorta was removed for mechanical testing. Any mice still alive at 25 months of age were euthanized by CO2 inhalation, and the thoracic aorta was removed for mechanical testing, details are shown in ***Table 11***. All animal procedures were approved by the Institutional Animal Care and Use

Committee at Washington University. More details about the mouse models, image acquisition, and mechanical testing can be found in our previous study [10].

6.2.2 Region of interest

Although the FSI simulations were performed on the entire thoracic aorta, the analysis focuses on the ascending thoracic aorta, which is the region delimited by the heart and the brachiocephalic trunk (BCT), and it is where aneurysms are formed for *Fbln*^{SMKO} mouse models. Figure 34A shows the 3D geometry of ascending aorta of the four representing mice from the ten mouse models used in this study. The different mice show a considerable variation in radial growth with mouse 1 and 4 exhibiting large aneurysm formation, mouse 2 a moderate aneurysm and mouse 3 a mild aneurysm. In terms of temporal change in the diameter, mouse models 1 and 3 had a 34% and 33% increase in the ascending thoracic artery mean radius from 2 to 6 months, respectively, mouse 2 had 28% increase and mouse model 3 had a 20% increase.

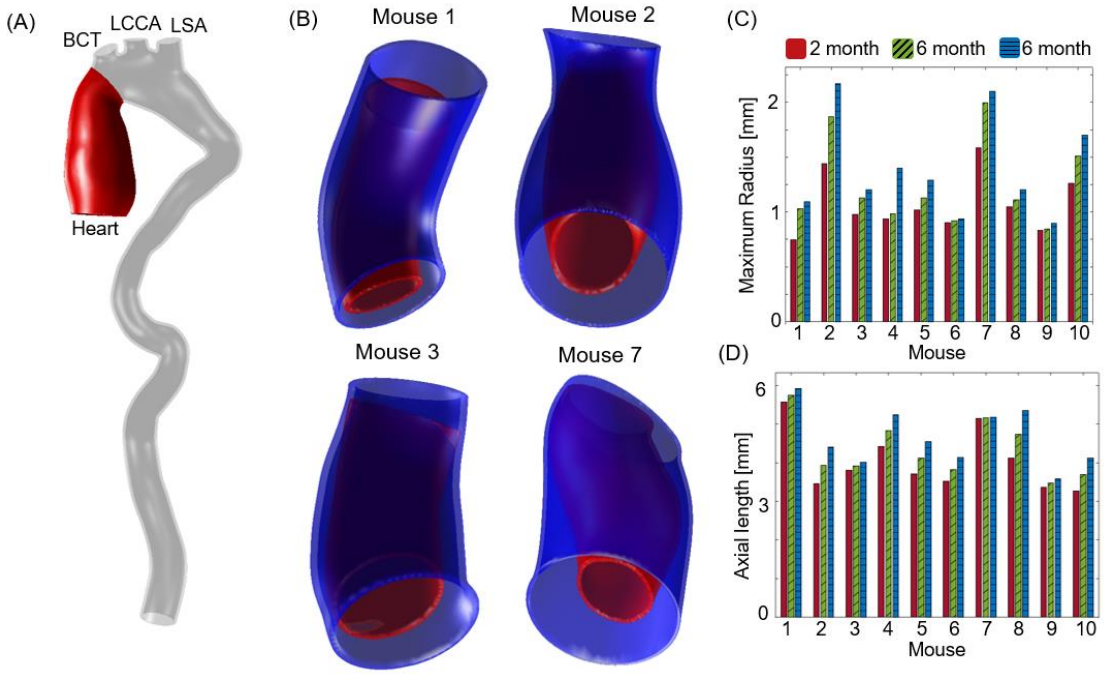

Figure 34: *(A) Region of interested (in red) delimited by the heart and brachiocephalic trunk (BCT). (B) Geometries of ascending aorta for 2-month (red) and 6-month (blue) of four different mice models. (C) Comparison between maximum diameter (D) and axial lengthening found in the ascending region for all the ten mouse models. Red bars are 2-month-old, green bars are 4-month-old and blue bars are 6-month-old measurements.*

6.2.3 Fluid-solid interaction simulations

We segmented both 2-month and 6-month geometries using the CT images at mid-diastole as described in our previous work [10]. Two main landmarks – the heart in the ascending region and the celiac artery in the descending region, were used to ensure the selection of the same portion of the aorta from the medical images. The brachiocephalic trunk (BCT) left common carotid artery (LCCA) and left subclavian artery (LSA) were also partially segmented and used as part of boundary conditions for the blood flow simulations. The image segmentation,

model generation, and 3D meshing were performed in SimVascular [213] with Meshmixer (Autodesk, Inc.) for supplemental editing.

***Table 10**: Outflow model parameter values*

	R_p [Pa. s/mm^3]	C [Pa/mm^3]	R_d [Pa. s/mm^3]
1. Left subclavian artery	19.58	5.5×10^{-4}	286.2
2. Left common carotid	44.70	3.23×10^{-4}	488.0
3. Brachiocephalic trunk	21.55	3.54×10^{-4}	443.2
4. Outlet	10.30	5.41×10^{-4}	443.2

The FSI simulation requires two separate conforming meshes: a mesh for the fluid domain, and a mesh for the structural domain. For the structural domain, a mouse-specific unloaded wall thickness was imposed based on experimental measurement for the ascending aortic region and was treated as constant over the length of the aorta.

For the fluid domain, a waveform from the mouse study of Cuomo *et al.*[215] was used as the inlet boundary condition, as shown in **Figure 35**B and was assumed to be the same for all mice. For each outflow boundary condition,

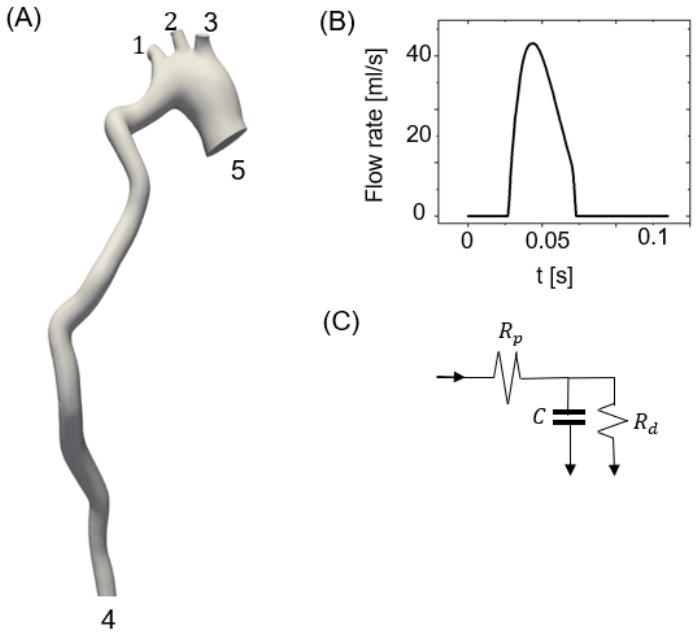

***Figure 35**:(A) Summary of the boundary conditions for an FSI subject-specific simulations of the aorta including: (B) Inflow flow rate waveform for inlet at location 5. (C) Three-element Windkessel model for outlets at locations 1-4.*

a three-element circuit analog model was prescribed, as shown in **Figure 35**C. The value for the distal resistance (R_d), proximal resistance (R_p) and compliance (C) were based on literature value and tuned for an average aortic pressure of about 90 mmHg. Values are shown in ***Table 10***.

The blood viscosity was described using the non-Newtonian Carreau-Yasuda model to account for shear-thinning of the blood in the moderate Reynolds number present in the mouse aorta (order of 200) [165], as described previously [10].

A Robin-type boundary condition was used to account for the viscoelastic support of the outer arterial wall[169] given by:

$$\sigma_s \cdot \boldsymbol{n} = -k_s \boldsymbol{u} - c_s \frac{\partial \boldsymbol{u}}{\partial t} - p_0 \boldsymbol{n}$$

[53]

Where k_s and c_s are viscoelastic parameters that modulate the external tissue response, p_0 is the external pressure in the thoracic and abdominal cavity, $\boldsymbol{u}$ is the displacement field, σ_s is the Cauchy stress tensor in the structural domain, and $\boldsymbol{n}$ is unit the normal vector for the outer wall surface. We prescribed a non-zero value for $k_s = 1 \times 10^7\ \mathrm{N.s.m^{-3}},\ p_0 = c_s = 0,$ which is within the range of parameters reported in the literature [169].

To account for the mechanical load of the structure domain from the blood pressure, we pre-stressed the initial geometry using the approach proposed by Hsu and Bazilevs [65], which is embedded in the svFSI solver in SimVascular [171].

6.2.4 Solid domain constitutive model

The solid domain was modeled as a homogenous, isotropic, nonlinear hyperelastic material, described by the Neo Hookean model, where the strain energy density is written as

$$W_{NH} = \frac{\mu}{2}(I_1 - 3) - \mu \ln(J) + \frac{\lambda}{2}[\ln(J)]^2$$

[54]

Where, I_1 is the first invariant of the right Cauchy-Green deformation tensor ***C***. J is the determinant of elastic deformation tensor F^e, λ is the first Lame parameter, and μ is the shear modulus or the second Lame parameter. The Lame parameters can be written as functions of the elastic modulus, E and bulk modulus, ν

$$\mu = \frac{E}{2(1+\nu)}$$

[55]

$$\lambda = \frac{\nu E}{(1+\nu)(1-2\nu)}$$

[56]

For the simulation, the values of E were subject-specific and based on postmortem measurements of the ascending aorta, as given on ***Table 11***.

Table 11*: Sex, lifespan, aortic tortuosity index (ATI) and postmortem measurements of ascending aortic elastic modulus E_{desc} and descending aortic modulus $E_{desc.}$*

Mouse	Sex	Lifespan [months]	E_{asc} [KPa]	E_{desc} [KPa]	ATI
1	Male	17.87	2234	700	45.34
2	Male	18.2	1164	719	59.53
3	Male	22.37	1222	1094	37.87

4	Male	13.27	464	418	52.03
5	Female	21.93	881	867	53.57
6	Female	25*	1595	781	39.86
7	Female	12.37	113	748	35.44
8	Female	25*	930	961	38.78
9	Female	25*	644	631	22.8
10	Male	25*	1033	684	28.74

**Sacrificed at 25 months.*

6.4.5 Growth law

Tissue growth in the aortic wall is modeled as kinematic growth in response to chronic changes in the hemodynamics. The hemodynamics-based stress was calculated using the svFSI solver from SimVascular[213]. The stresses were then extracted for each mesh element and used to determine the local growth and remodeling. The growth laws are based on Alford *et. al.*[44] and given by

$$\frac{\partial \lambda_{rg}^{elem}}{\partial t} = \frac{1}{T_r}\left(\frac{\sigma_\theta^{elem}}{\hat{\sigma}_\theta} - 1\right)\lambda_{rg}^{elem} \quad [57]$$

$$\frac{\partial \lambda_{g\theta}^{elem}}{\partial t} = \left[\frac{1}{T_\theta}\left(\frac{\sigma_\theta^{elem}}{\hat{\sigma}_\theta} - 1\right) + \frac{1}{T_\tau}\left(\frac{\tau_w^{elem}}{\hat{\tau}_w} - 1\right)\right]\lambda_{g\theta}^{i} \quad [58]$$

$$\frac{\partial \lambda_{gs}^{elem}}{\partial t} = \frac{1}{T_s}\left(\frac{\sigma_s^{elem}}{\hat{\sigma}_s} - 1\right)\lambda_{gs}^{elem} \quad [59]$$

Where T_r, T_θ, T_τ, and T_s are time constants, and hats (^) indicates homeostatic target stress values. λ_{rg}^{elem}, $\lambda_{g\theta}^{elem}$, and λ_{gs}^{elem} are radial, circumferential, and axial growth stretch ratios, respectively, for each element $elem$. σ_θ^{elem}, σ_s^{elem}, τ_w^{elem} are the circumferential, axial, and wall shear stresses for each element $elem$, and they

are calculated using the full FSI simulation. For G&R equilibrium, $\sigma_\theta = \hat{\sigma}_\theta$, $\tau_w = \hat{\tau}_w$, and $\sigma_s = \hat{\sigma}_s$ at all points in the artery.

Based on Eqs. [57]-[59], the growth tensor G^i is defined for each element in the mesh, and it written in the principal coordinate system as:

$$\boldsymbol{F}_g^i = \begin{bmatrix} \lambda_{gr}^i & 0 & 0 \\ 0 & \lambda_{g\theta} & 0 \\ 0 & 0 & \lambda_{gz} \end{bmatrix} \quad [60]$$

The total deformation F experienced by the tissue relative to its initial state at any given time is:

$$\boldsymbol{F} = \boldsymbol{F}_e \boldsymbol{F}_g \quad [61]$$

Where $\boldsymbol{F}_e$ elastic deformation tensor due to external loads

6.2.6 Remodeling law

Given that this growth model is based on a single-component approach [48], rather than a constrained mixture [216], changes in the individual constituents are not tracked over time. However, we can draw on the constrained mixture idea here and assume that our strain energy density W_{Total} is associated with the mass fraction $\phi(t)$:

$$W_{Total} = \phi(t) W_{NH} \quad [62]$$

Thus, changes in the mass fraction due to growth of the tissue can be tracked over time as:

$$\phi(t) = \int \frac{\rho(t)}{\rho_0}\ dt\ \approx \det(\boldsymbol{F}_g) = J_g$$

[63]

So, we can approximate the temporal remodeling as a linear relation to the total growth of the tissue.

$$W^i_{Total} = J^i_g \left(\frac{\mu}{2}(I_1 - 3) - \mu \ln(J) + \frac{\lambda}{2}[\ln(J)]^2\right)$$

[64]

Where W^{elem}_{Total} is defined locally for each element $elem$ and is allowed to change over time based on the local growth Jacobian J^{elem}_g.

6.2.7 Solving the G&R solution.

The G&R problem was solved by the finite-element method, using the prestrain framework [217] in FEBio 2.9.1 [60]. Each element of the FE mesh was prescribed as a prestrained elastic material to solve the compatibility in growth problem. Consistency was maintained by utilizing the same material model and initial properties as the prior fluid-structure interaction (FSI) simulation, ensuring a seamless transition between methodologies.

Boundary conditions were established by imposing displacements at both the inlet and outlet. These displacements were calculated through linear interpolation between the 2-month and 6-month time points.

6.2.8 Mapping meshes from 2-month to 6-month.

Given that the meshing was performed independently for each age, we used a diffusion-based technique [218] to define a coordinate system and map between geometries to ensure a one-to-one mapping between the time points. In this approach, we solve the elliptic problem $\nabla^2 T = 0$ twice, once to determine the axial mapping and once to determine the longitudinal mapping, for each geometric model. For the axial mapping (s), the inlet temperature was set to be $T = 0$, and the outlet $T = 1$. The solution shown in Figure 36A and Figure 36C provides a smooth function that varies from 0 to 1 along the length of the domain. For the circumferential mapping (θ), the mesh is cut throughout the axial direction along the shortest geodesic distance that connects the inlet to the outlet. The boundary conditions of the problem are $T = 0$ on one surface of the cut and $T = 1$ on the other surface; this solution results in a smooth circumferential mapping around the vessel surface, as shown in Figure 36B and D. Since the wall

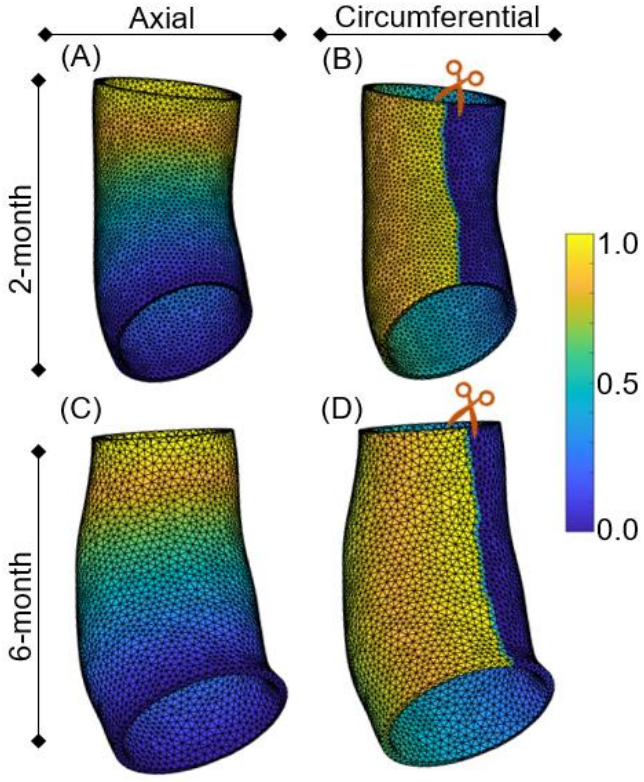

***Figure 36**: Heat-transfer-based mapping solves the steady-state heat transfer equation for 2-month (A and B) and 6-month (C and D) geometry.*

thickness is assumed constant, a more straightforward linear mapping through the thickness is sufficient to define the radial position.

6.2.9 Fitting G&R parameters

The time constants associated with circumferential (T_θ) and axial (T_s) growth were used as fitting parameters. The choice was based on our ability to calculate both changes in radius and axial growth from the images. Since we had no information about changes in the thickness, we kept the time constant for radial growth (T_r) fixed.

For the same reason, circumferential growth and axial lengthening measurements were used to optimize the growth parameters. For the circumferential growth, the axial and circumferential mapping were used to create equally spaced rings from the heart to BCT as shown in **Figure 37**. The radius ($\hat{r}_r$) for each ring *r* were calculated by taking the mean distance between each point in the ring to the centroid, as shown in **Figure 37**B. For the axial lengthening (l_c), the distance between two consecutives centroids was calculated. Optimization was conducted relative to a projected 4-month geometrical growth. However, since only measurements of the maximum radius and axial lengthening were available for the four months and not the entire geometry, the projected 4-month geometry was estimated by assuming uniform growth across the entire geometry based on these

measurements.

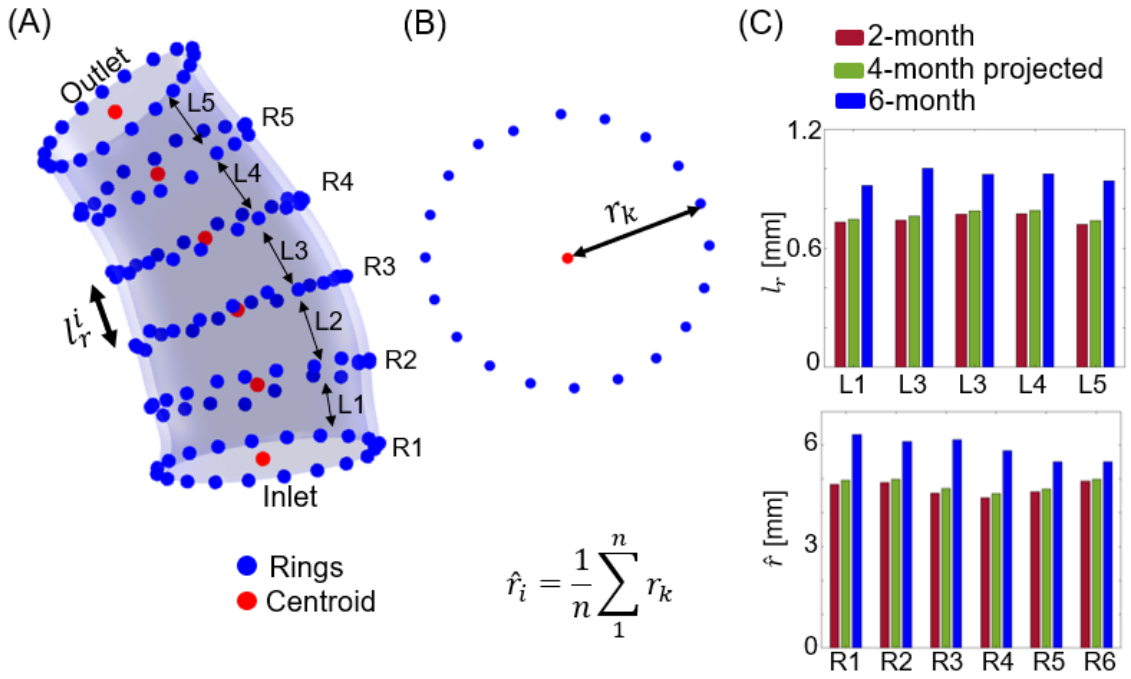

***Figure 37**: Ascending aorta (transparent blue) with selected nodes forming six equally-spaced rings along the geometry (A) from which we can calculate lengthening (l_r^i) giving by the distance between two consecutive rings and the radius ($\hat{r}_i$) calculated by the average distance between each node and the centroid (B) in the rings. And the axial (l_r) and radial ($\hat{r}$) measurements for each ring (C).*

The error was minimized using the Levenberg-Marquardt damped least-square algorithm[214]. The chi-square error criterion defined the goodness of fit.

$$\chi_i^2 = \sum_{i=1}^{2n-1} \left[\frac{X_i^{4mo} - X_i(\boldsymbol{k})}{\sigma}\right]^2 \quad [65]$$

Where X_i^{4mo} is the 4-month projected growth, and σ is the measurement error covariance.

6.2.10 Multiple-domain segmentation

The 3D geometries were segmented into four equally spaced domains along the centerline, as shown in **Figure 38**. For each domain (labeled as k), specific time constants T_θ^k, and T_s^k, were assigned. This segmentation approach served the purpose of evaluating the model's performance systematically by increasing the number of fitting parameters while ensuring their physical relevance.

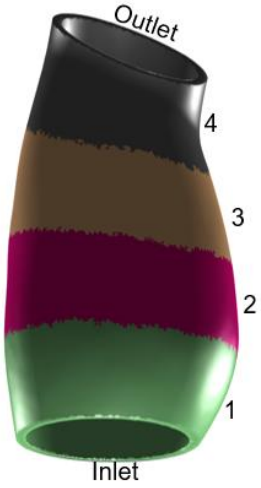

***Figure 38**: Four-domain segmentation along the centerline*

6.2.11 Performance analysis

The convergence performed in the model was based on the chi-square error criterion given in Eq. [*65*]. For the results, the performance analysis for the validation step was calculated using the percentage difference for radius, $\Delta r\%$ and percentage difference for axial lengthening, $\Delta l\%$.

$$\Delta r\% = \frac{r^m - r^p}{r^m} \times 100 \quad [66]$$

$$\Delta l\% = \frac{l^m - l^p}{l^m} \times 100 \quad [67]$$

Where r stands for radius and l for axial length, **Figure 37** shows how those values are calculated. The superscript m stands for measures coming from medical

images, and the superscript p stands for measures obtained from the predicted geometry. The percentage difference measures how close the predicted values are from the *in vivo* measure values and is normalized by the *in vivo* measured values. In this way, when the new geometry approaches the target geometry, the axial length and radial distance tend to zero, i.e., $l^m - l^p \to 0$ and $r^m - r^p \to 0$, resulting in a percentage difference tending towards zero as well.

6.2.12 Correlation analysis

The correlation between the fitted radial and axial growth constant and the measured quantities is calculated. The quantities we focus on here are lifespan (LS), as an indicator of the aneurysm outcome, maximum diameter at six months (D_{6mo}^{Max}), radial growth from 2mo to 6mo $(\Delta \mathrm{D})$, aortic tortuosity index at 6 months (ATI), and postmortem measurements of ascending and descending material properties of the aorta, given the Young modulus, $E_{asc,}$ and E_{desc}, respectively.

Out of the group of ten mice, four were sacrificed at the age of 25 months, leading to data being capped at this maximum limit. To accommodate this censored data, we employed the Tobit model [173], which is expressed as:

$$Y_t = X_t\beta + u_t \qquad \text{if} \quad X_t\beta + u_t < Y_{max}$$

$$Y_t = Y_{max} \qquad \text{if} \quad X_t\beta + u_t \geq Y_{max}$$

[68]

In this model Y_t is the dependent variable, which in our study is the lifespan of the mouse; X_t stands for the independent variables; β is the fitting coefficient; and Y_{max}

is the censor cut off, 25 months in our case. The stochastic error, u_t is assumed to have a normal distribution, mean at zero, and a constant variance σ^2. Here, the subscript t ranges from 1 to N, where N represents our dataset's total number of observations.

Due to the Tobit model's restriction on the dependent variable, the conventional R-squared is not the most suitable metric for assessing goodness-of-fit. Instead, we opted for the modified McKelvey and Zavoina pseudo-R-squared [174], as it has demonstrated an ability to restore standard R-squared values typically applicable to non-censored data.

$$r^2 = \frac{\sum_{i=1}^{N}(Y_t - \overline{Y_t})^2}{\sum_{i=1}^{N}(Y_t - \overline{Y_t})^2 + N\sigma^2}$$

[69]

where $\overline{Y_t}$ is the mean of Y.

6.3 Results

6.3.1 Single domain model: detailed analysis of a representative case

The initial part of the results focuses on the single-domain model and its performance in both the tuning and validation stages. To begin, we examine a specific mouse, mouse #1. This particular mouse was selected due to its development of a severe aneurysm, showcasing significant growth from the 2-month to 6-month mark, with an approximate 90% increase in the maximum diameter.

Figure 39 depicts a 2-month geometry (A) and the contrast between the geometry projected from the model (B) and the geometry extracted from CT scans (C). Figure 39D displays the temporal evolution of the average radius of predicted geometry (green) compared to the in-vivo measurements (blue). We can observe that the model underestimates the average radius at 4mo and overestimates it at 6mo.

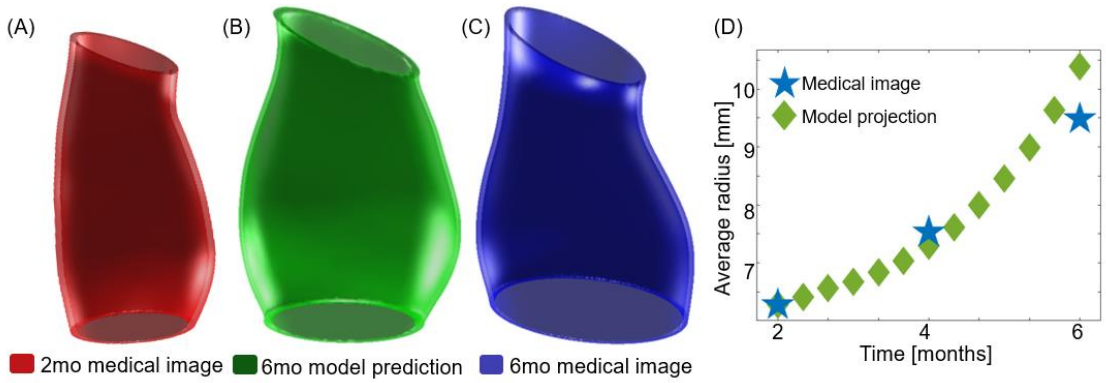

Figure 39: *(A) 2mo medical image obtained in vivo and used as the initial geometry for the growth model, (B) 6mo projected geometry from the growth model and (C) 6mo in-vivo geometry obtained from medical images. (D) Show the time evolution of the average radius of the model (green) compared to in vivo measurements (blue).*

6.3.2 Single domain model: radial performance assessment

To evaluate the radial performance of the single-domain growth model for both tuning and validation, we use the percentage change calculation given by Eq. [*66*]. The proximity of Δr to 0% indicates the effectiveness of the model's performance

- the closer the proximity to 0%, the better the model's performance is deemed to be.

For the radial analysis, we specifically chose four rings along the geometry, named R2 (blue), R3 (red), R4 (yellow), and R5 (in purple), as shown in ***Figure 40***A. R1 and R4 were inlet and outlet rings excluded from the analysis to avoid bias from the boundary conditions. The rings provide some sense of how the model performed through geometry.

Figure 40B shows the radial performance results for the tuning stage. Here, we compare the predicted measurements with the in vivo derived measurements. Negative $\Delta r\%$ means that the measurements from the predicted geometry overestimated the in vivo measurements. Conversely, positive $\Delta r\%$ means that the measurements from the predicted geometry underestimated the in vivo measurements. The average results show that the model was quite effective in capturing the 4-month geometry, with the minimum $\Delta r\%$ being -0.26% for mice 7 and 9 and the maximum $\Delta r\%$ being 9% for mouse 10. Most mouse models show local measurements between -8.5% (ring 4 for mouse 5) and 11.8% (ring four mouse 2). Mouse 7, however, despite displaying one of the smaller $\Delta r\%$ average, expressed the most significant local discrepancy, with Δr=14% for ring 2, near the inlet, and $\Delta r = -7.5\ \%$ for ring 4 close to the outlet.

Figure 40C displays the radial performance analysis conducted on the validation dataset, leveraging the parameters derived from the tuning stage to predict the 6-

month geometry. Notably, the model's radial performance varies across different mice within this stage. Mouse 8 showcases an exceptional radial performance, exhibiting minimal discrepancies across the rings with a Δr=-5%. Conversely, mice 5 and 7 demonstrate poor radial performance. Mice 5 shows a Δr=-45% with a moderate discrepancy across the rings, while mice 7 displays a Δr=-32% with a large discrepancy across the rings.

Despite these variations, the model's overall radial performance against the validation dataset demonstrates a positive outcome. Eight out of ten mice showed an $|\Delta r|$<=20%. Among those, five out of ten showed a $|\Delta r|$<=10%. This indicates the model's generally favorable predictive radial accuracy for most instances in the validation dataset.

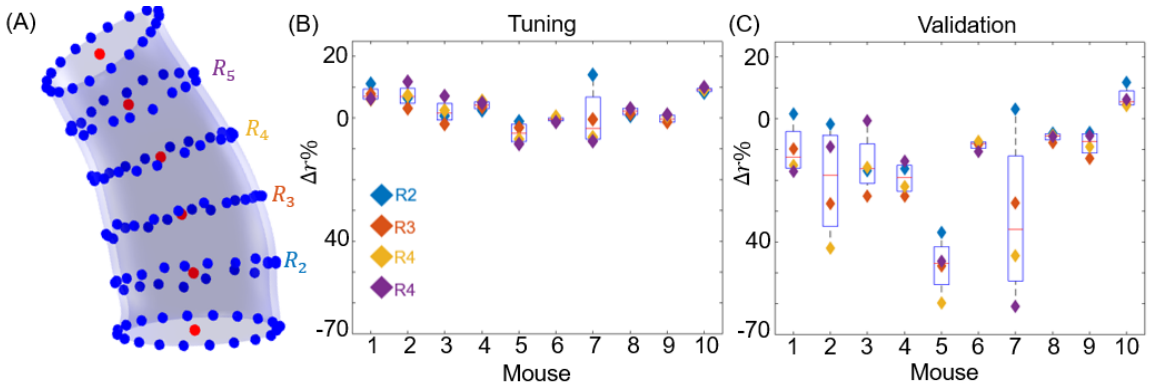

***Figure 40**: (A) The ascending thoracic region with equally spaced centroids (red dots). The approximation of total length estimation is obtained by summing the distances between consecutive centroids. (B) Radial performance analysis of a single-domain model within the tuning dataset. This assessment evaluates the model's ability to fine-tune predicted 4-month radial growth to match observed values using G&R time constants. (C) Radial performance analysis for the validation dataset. Employing parameters derived from the tuning stage, this analysis compares predicted axial growth against observed 6-month geometry. The proximity to 0% indicates superior model performance.*

6.3.3 Single domain model: correlation analysis between measured quantities and growth time constant.

Figure 41A shows the correlation map between these quantities. The correlation is measured through the r^2 values. Blue means the quantities are positively correlated, and red means they are negatively correlated.

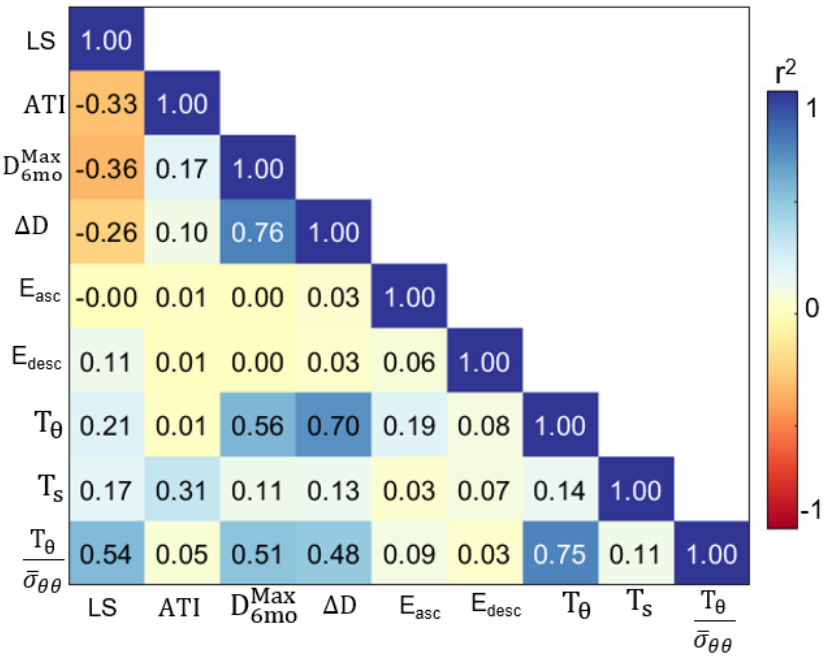

***Figure 41**:* (A) Correlation map between fitted circumferential (T_θ) and axial (T_s) growth constant lifespan (LS), aortic tortuosity index (ATI), maximum diameter at 6 months(D_{6mo}^{Max}), radial growth from 2mo to 6mo (ΔD) and postmortem measurements of ascending and descending young Modulus, E_{asc} and E_{desc}, respectively. The ratio between the fitted circumferential growth constant and the mean value of the time averaged $\bar{\sigma}_{\theta\theta}$ is incorporated in the analysis.

The positive correlation between T_θ and both D_{6mo}^{Max} and ΔD, is expected, considering that the radial measurements were used to tune these parameters. A modest positive correlation between the T_θ and LS (r^2=0.21). However, a significantly stronger correlation appears for T_θ divided by mean value of the time averaged $\bar{\sigma}_{\theta\theta}$ (r^2=0.54). This normalization comes from Eq. [*57*], and is particularly insightful because it takes into account variations in stress levels and distribution

experienced by each mouse model. Recognizing that the stress conditions and distribution may differ among the mouse models, the analysis of this ratio provides a more comprehensive understanding of the growth response and the impact of stress levels.

Moreover, T_θ showed a modest correlation with E_{asc}, showing a potential association between circumferential growth and remodeling and stiffness of ascending thoracic aorta. In a final note, a moderate correlation is observed between T_s and ATI, connecting axial growth with geometrical changes along the ascending, especially the descending thoracic aorta.

6.3.4 Performance of single-domain approach versus multiple-domain approach: mouse 1 analysis

Figure 42A shows the 2-month geometry constructed directly from medical scans (orange) and used the starting point for the G&R model compared to and 6-month geometry constructed directly from medical scans (black outline). s 42B and C compare the 6-month predicted solution based on the G&R model's solution to a 6-month geometry constructed directly from medical scans (black outline) for a single domain (Figure 42B) and multiple domain (Figure 42C). The use of multiple domains seems to yield a more accurate prediction than the single-domain approach in **Figure 42**B.

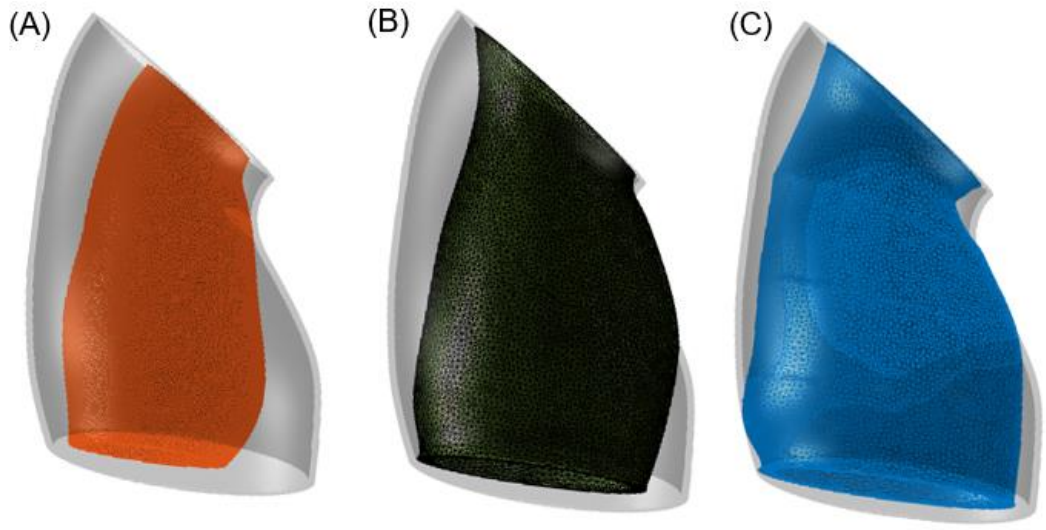

***Figure 42**:Comparison between (A) 2-month geometry constructed directly from medical scans (orange) and 6-month geometry constructed directly from medical scans (black outline). (B) 6-month predicted geometry using the single-domain approach of the G&R model (dark green) and 6-month geometry constructed directly from medical scans (black outline). (C) 6-month predicted geometry using the multiple-domain approach of the G&R model (blue) and 6-month geometry constructed directly from medical scans (black outline).*

Figure 50B illustrates the qualitative differences between these approaches. There is an approximate 17% reduction in the mean radial approximation (shown by the red line), decreasing from about 7.5% in the single-domain method to roughly 3.75% in the multiple-domain approach. This decrease indicates that the multiple-domain approach results in a more precise or closer approximation to the directly scanned 6-month geometry compared to the single-domain method.

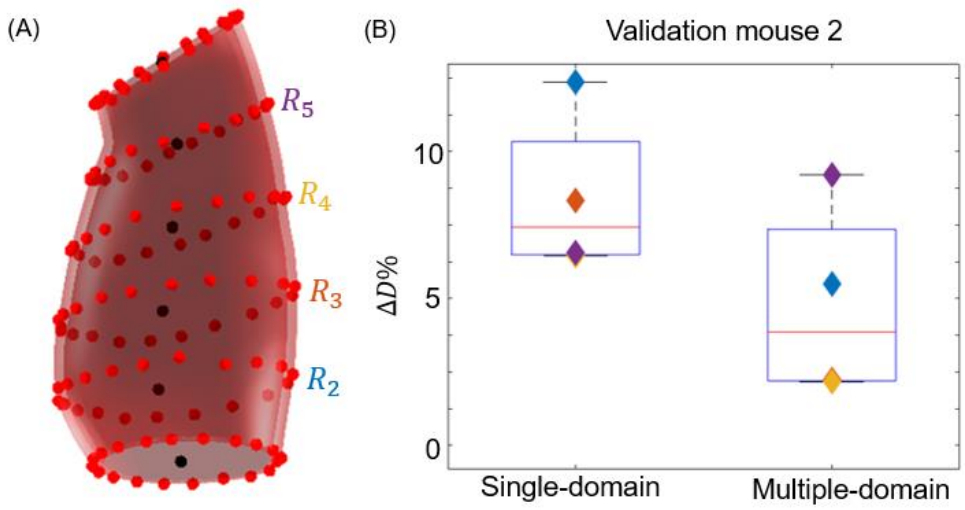

***Figure 43**: (A) Displays the six equally spaced rings along the geometry. (B) Comparison of single-domain and multiple-domain, showcasing the local differences for rings 2 through 5.*

6.4 Discussion

This study marks a significant advance by applying a combination of (1) subject-specific modeling (2) fluid-solid-interaction FSI simulations, and (3) a simple growth and remodeling law to maladaptive growth and remodeling of the ascending thoracic aorta in the *Fbln*^{SMKO} mouse. Each one of the three aspects of the simulations was important. The subject-specific models allowed mouse-specific analysis, including comparison to lifespan, and provided a reference for future patient-specific studies. The FSI simulations provided accurate estimates of pressure-induced wall stress and wall shear stress. The growth and remodeling model predicted the time evolution of the aortic growth in response to calculated animal-specific stresses.

The primary outcome of our study centered on deriving mouse-specific circumferential and longitudinal growth rate constants as described by Equations [*57*]-[*59*]. We found that both growth rates show a modest correlation to the lifespan, r^2 of 0.21 for T_θ and r^2 of 17 for T_s. However, a notable shift occurred when normalizing the circumferential growth rate constant T_θ against the time-averaged circumferential stress $\sigma_{\theta\theta}$ revealing a much stronger correlation. This normalization suggests that the ratio offers a more comprehensive insight into the growth response, emphasizing the influence of stress levels on lifespan.

Moreover, a moderate correlation is observed between T_s and ATI r^2 of 0.31, hinting a potential association between axial growth and unhealthy geometrical changes along descending thoracic aorta. Finally, a positive strong correlation between T_θ and both D_{6mo}^{Max} and $\Delta\mathrm{D}$ was calculated, underscoring their relationship with circumferential growth. The correlation between T_θ and T_s was considerably weak, indicating potential independence or minimal association between these factors.

The validation of the uniform growth laws, also referred to as the single domain approach, showcased highly encouraging results in our study. An impressive 80% of the models demonstrated a radial error of less than 20% when compared to in-vivo measurements, with 40% achieving an even more remarkable accuracy, exhibiting errors of less than 10%. These findings underscore the effectiveness of this approach in modeling and predicting growth dynamics within this experimental context. Furthermore, our investigation delved deeper, comparing the performance of a domain-based growth model against the single-domain approach in this

specific mouse model. Interestingly, the domain-based growth model exhibited slightly superior predictive capabilities, offering marginally more accurate estimations than the single-domain approach. This nuanced difference in accuracy suggests the potential benefits of considering domain-specific growth dynamics, highlighting the complexity of growth processes.

The computational model successfully captured the overall growth of the aorta in the *Fbln*^{SMKO} mouse and provided insights into the local growth patterns. However, some limitations need to be addressed for the model to be more widely applicable. Currently, the model primarily considers hemodynamic factors, yet substantial evidence points to the critical role of biochemical factors such as inflammatory markers and matrix metalloproteinases in growth and remodeling [219]. Incorporating these elements into the model framework could significantly heighten its predictive accuracy. Another limitation is the simplified assumption of homogeneous and isotropic material properties in the aortic tissue, disregarding its inherently anisotropic and heterogeneous nature [37, 154, 220, 221]. Future research should aim for more sophisticated material models to represent these complexities accurately. The study also focused on a relatively small number of mice. While the results are encouraging, validating the model with a larger dataset is essential to confirm its generalizability. Additionally, investigating the model's performance across different mouse models of ATAA would further strengthen its applicability and perhaps provide insights into how different genetic challenges drive aneurysm formation and growth.

Despite its limitations, this study has significantly contributed to understanding ATAA progression. The development of hemodynamics-driven G&R models offers a promising approach for personalized risk assessment and treatment planning for patients with ATAA. Future research should address the limitations mentioned above and explore other potential applications of these models in vascular disease research.

Chapter 7: Fluid-Structure-Based Multiscale Model of Hemodynamics-Driven Arterial Growth and Remodeling.

Abstract

The growth and remodeling (G&R) processes within tissues represent essential adaptations to external stimuli, especially notable in cardiovascular tissues affected by altered stress conditions. Aneurysms, often stemming from maladaptive G&R, significantly impact health, with high mortality rates upon rupture. Understanding the complex physical and biomechanical factors linked to aneurysm development, growth, and rupture is crucial for more effective diagnostics and treatment planning.

This study proposes a novel approach integrating fluid-solid interaction (FSI) with a multiscale, stress-driven growth and remodeling model to describe aneurysm progression. By bridging macroscale hemodynamics with microscale cellular behavior, this method holds promise in elucidating key stress-induced growth and microstructural remodeling patterns influencing aneurysm evolution.

The methodology is applied to three illustrative cases: simulated aortic arch inflation, an idealized thoracic aorta analysis, and a subject-specific mouse model mimicking aneurysm development. The results showcase stress-driven growth patterns, microscale remodeling, and local stress concentrations critical in understanding aneurysm progression. This integrated approach offers a significant advancement in comprehending tissue responses to stress, presenting a promising avenue to explore how stress distribution influences tissue remodeling, thereby advancing beyond the constraints of traditional continuum-scale models.

7.1 Introduction

The process by which tissues in our body respond to external stimuli through changes in biophysical properties is known as growth and remodeling (G&R). The G&R process happens naturally in all living tissues. In cardiovascular tissues, in particular, G&R is driven by changes in stress along the vessel wall. Under altered stress conditions, the vessel appears to modulate its physical and mechanical properties to maintain a homeostatic stress state [11]. In some cases, however, the G&R process goes awry, leading to a bulging or/and enlargement of the aorta, known as an aneurysm. Aneurysms affect approximately 15,000 people in the USA per year [135]. In critical cases, they will keep growing until dissecting or rupturing. Rupture events have a mortality rate of nearly 50% [136, 208].

Surgical intervention is the most common treatment to repair an aneurysm, yet the procedure poses a significant risk to patients [222]. Clinical intervention guidelines rely mainly on diameter and growth rate. However, about 60% of the patients

experience complications without meeting those criteria [6], [138]. Hence, we must better understand the physical and biomechanical factors linked to aneurysm formations, growth, and rupture to improve diagnostic efficacy.

Arterial walls are composed of a complex microstructure, which responds to macroscale pressure- and flow-induced stress by deforming, growing, and remodeling. The scale of differences involved presents a fundamental challenge to our understanding. The driving physical phenomena (blood flow and pressure-induced wall stresses) and observable consequences (aneurysm formation and dissection/rupture) occur on the macroscale, but the remodeling process is driven by individual cells at the microscale. Computational and mathematical tools have proven to be a great ally in pursuing understanding of the G&R process due to their ability to model complex systems and simulate bio-chemo-mechanical behaviors using population-based or patient-specific data without invasive procedures.

The most prevailing theoretical models of growth and remodeling to date function entirely at the macro (continuum) scale for both fluid and solid mechanics, treating the tissue as locally homogenous and the constituent deformation as affine [41, 44]. Although this approach has been effective in incorporating real anatomy and mapping the stress distribution along the vessel wall, it cannot account for the multiscale nature of the tissue G&R. To data, the multiscale mechanical G&R models developed [57, 223, 224] are not able to account for hemodynamics-induced stress distribution in realistic geometries.

Here we developed an approach to solve tissue G&R accounting for multiphysics and multiscale processes. We combine a fluid-solid-interaction (FSI) model and a multiscale local-stress-driven growth model. The methodology was applied in three illustrative cases: simulated aortic arch inflation, an idealized thoracic aorta analysis, and a subject-specific mouse model mimicking aneurysm development. The results showcase stress-driven growth patterns, microscale remodeling, and local stress concentrations critical in understanding aneurysm progression.

7.2 Methods

The hemodynamics-driven multiscale G&R model integrates the FSI solver from SimVascular [159], the G&R model [172] that has been developed by Mahutga *et al.* [57], the Prestrain plugin from FEBio [217], and a discrete-to-continuum fitting tool proposed by Nikpasand *et. al.* [225, 226]. **Figure 44** shows proposed workflow that integrates all the pieces of the model. Each piece of the model is discussed in more detail bellow.

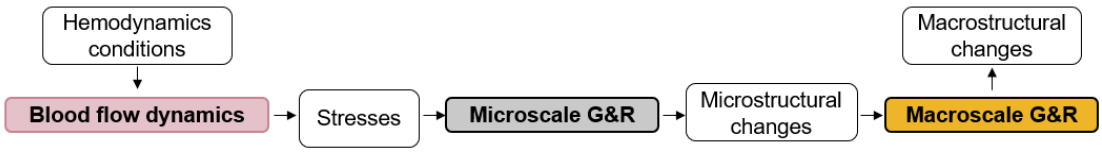

***Figure 44**: Workflow of the hemodynamics-driven multiscale G&R model*

7.2.1 Blood flow dynamics

Subject-specific model construction and mesh generation

The goal of this step is to allow the use of subject-specific geometry derived from medical scans. For subject-specific flow dynamics, a model based on the subject anatomic geometry is built from a medical scan (**Figure 45**A). The image segmentation and model generation were performed using SimVascular [159], with supplemental editing in Meshmixer (Autodesk, Inc.)

The FSI simulation requires two separated meshes: one for the lumen, or fluid domain, and one for the vessel wall, or solid domain (**Figure 45**B). The meshes were built following the procedure detailed in Baumler *et al.* [169] to allow the outer wall of the fluid domain to coincide with the inner wall of the solid domain.

Additionally, for subject-specific simulations, it is important to choose appropriate boundary conditions, that generally include a cardiac waveform in the inlet and a prescribed three-element Windkessel for the outlets, in the fluid domain. A Robin type boundary condition is applied to mimic the external tissue support, for the solid wall (**Figure 45**C). The subject-specific part of this study is based on our previous work, more details available in Bazzi *et. al.* [10].

From the FSI simulation, we obtained both the internal Cauchy and the flow-induced wall shear stress throughout the geometry. The stresses were averaged for each mesh element and extracted using Paraview. The extracted stresses were then used as input for the next step, solving the microscale growth and remodeling mechanics.

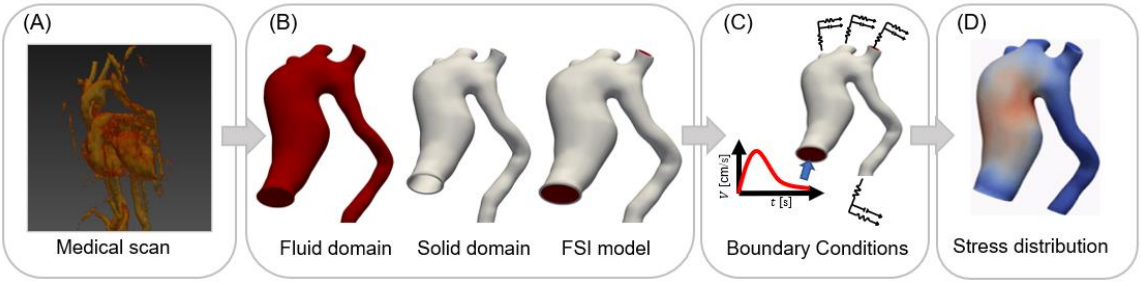

***Figure 45**: Schematics of subject-specifics FSI simulations*

7.2.2 Microscale growth and remodeling model

The microscale G&R model uses a discrete fiber network to represent the structure of vascular smooth muscle cells (vSMCs) and the extracellular matrix (ECM) known as the medial lamellar unit (MLU) based on Mahutga *et al*. [57] as shown in **Figure 46**B. The networks are generated from a periodic Delauney tessellation, where the tetrahedron edges represent the fibers and the nodes are pin joints between fibers. The fiber network is composed of a combination of three different fiber types: a 2D tessellation of interconnected elastin (in red) and collagen (in black) in the circumferential-axial plane, and a 3D periodic network of actin fibers (in yellow). More details about how the network is built can be found in [57], [226].

The model assumes the fibers undergo either deposition or degradation processes as shown in **Figure 46**C. The fiber remodeling is described as a change in radius with time $\frac{dr}{dt}$ in response to the fiber stress magnitude σ_f. The deposition process

occurs when the fiber stress is larger than the target stress, σ_{target}, i.e., $\sigma_f > \sigma_{target}$. Conversely, there is a degradation process which occurs when the fiber stress is below the target stress. The model also assumes that the undeformed fiber length l^0 changes proportionally to radial deposition/degradation. The remodeling process continues with each individual fiber either approaching the target stress, which is a local application of the tensional homeostasis [227], [228] or decaying from the network. In the model, the decay process leaves behind very small fibers which are insignificant to the bulk behavior of the material, but which help to mechanically stabilize the nodes when any new deformations are applied. For example, when a large change in deformation occurs, such as an instantaneous pressure increase or the application of torsion, the network can be unstable because the network has remodeled itself to be below the Maxwell stability limit. The governing equations are:

$$\frac{dr^f}{dt} = \frac{1}{\tau}\left(\frac{\sigma_f}{\sigma_{target}} - 1\right) r^f \quad [70]$$

$$\frac{dl^0}{dt} = k\frac{dr^f}{dt} \quad [71]$$

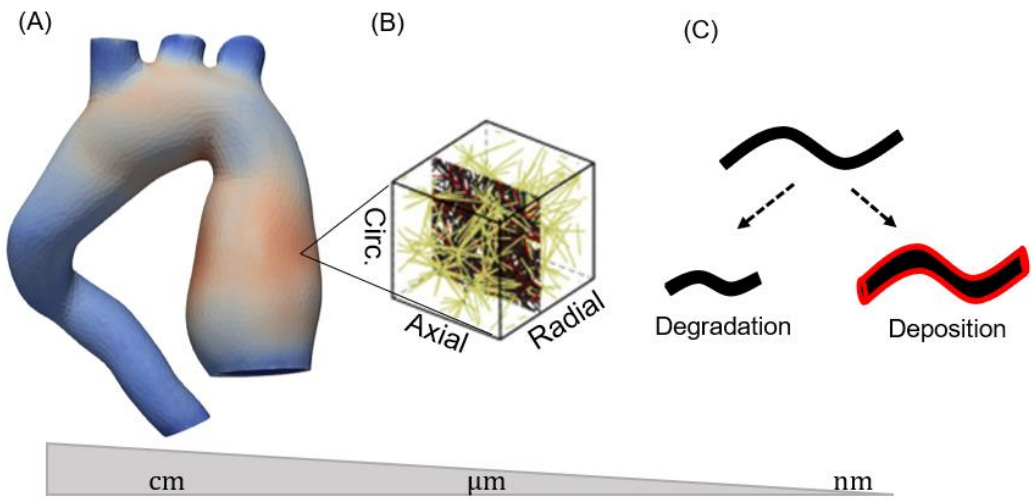

***Figure 46**:* Schematic of the multiscale representation of the G&R model. The stress distribution is solved using FSI simulation in the macroscale, here given by a mouse aorta (A). The stresses lead to a deformation in the fiber network, defined elemental level of mesh, and composed by three fiber families, collagen (black), elastin (red) and actin (yellow). The G&R is solved in each fiber individual, assuming a deposition or degradation processes, depending on the level of stress the fiber is sensing.

where r^f is the radius of fiber f, the if the remodeling time, τ is the remodeling time constant, and k is the parameter relating changes in fiber length to change in fiber radius. Fibers are allowed to degrade and (nearly) disappear from the network, but the current model form does not prescribe the addition of any new fibers or fiber-fiber crosslinks. The fiber remodeling properties for each demonstration case and fiber type are given in **Table 12**.

***Table 12**: Fiber remodeling parameters*

	τ [days]	σ_{target} [MPa]	k	$r^f_{initial}$[nm]
Actin	4	0.750	0.2	80
Elastin	NA	NA	NA	120
Collagen	90	0.2	0.2	260

As the fibers remodel, the network zero-stress state is updated by finding a new deformation such that the volume averaged stress in the network is zero. From this

new deformation, a growth tensor F^g can be calculated for each fiber network, relative to the original network size.

7.2.3 Macroscale growth and remodeling model

The output of the microscale G&R is a remodeled networked, which could directly couple with the macrostructure [229–234] however doing that can become computationally expensive, and for more complex geometry and loading, that approach can be intractable both from a pure computational standpoint and from a theoretical standpoint as one may have to refine a mesh such that it cannot have appropriate scale separation. Therefore, an alternative solution is to convert the microstructural changes into an approximate continuum-scale strain energy density function and growth tensor [225, 226].

For the energy density, the anisotropic hyperelastic HGO model [35] was used

$$\Psi(\boldsymbol{C},\boldsymbol{H}) = \Psi_{\mathrm{g}}(\boldsymbol{C}) + \sum_{i=1}^{3} \Psi_{\mathrm{fi}}(\boldsymbol{C},\boldsymbol{H_i}) \quad [72]$$

Where $\Psi(\boldsymbol{C},\boldsymbol{H})$ is represented by a superposition of the isotropic, non-fibrillar ground matrix $\Psi_{\mathrm{g}}(\boldsymbol{C})$ and three embedded fiber families $\sum_{i=1}^{3} \Psi_{\mathrm{fi}}(\boldsymbol{C},\boldsymbol{H_i})$, representing collagen, actin and elastin in the fiber network. The non-fibrillar matrix is modeled as a neo-Hookean[37]:

$$\Psi_{\mathrm{g}}(\boldsymbol{C}) = \frac{c}{2}(I_1 - 3) \quad [73]$$

Where $I_1 = \mathrm{tr}\boldsymbol{C}$ is the first invariant of $\boldsymbol{C}$, and c is the neo-Hookean parameter. The fibril matrix is given by:

$$\Psi_{\mathrm{fi}}(\boldsymbol{C}, \boldsymbol{H_i}) = \frac{k_1}{2k_2}[\exp(k_2(\boldsymbol{H}_i : \boldsymbol{C} - 1)^2) - 1]$$

$$\boldsymbol{H}_i = \kappa \boldsymbol{I} + (1 - 3\kappa)(\boldsymbol{a_{oi}} \otimes \boldsymbol{a_{oi}}) \quad [74]$$

[75]

Where $k_1 > 0$, and $k_2 > 0$ the stress-like and dimensionless parameter, respectively. $\boldsymbol{H}_i : \boldsymbol{C}$ denotes an invariant $\boldsymbol{C}$ based on a double contraction of the symmetric generalized structure tensor $\boldsymbol{H}_i$, κ characterize the fiber dispersion of fiber *i* with mean orientation $\boldsymbol{a_{oi}}$, for each one of the fiber families. Fiber orientation and dispersion is obtained directly from the network, and parameters k1 and k2 were fitted using the strategy presented at Nikpasand *et al.* [225]. The fiber orientation and fiber dispersion were calculated directly from the eigenvectors and eigenvalues of the structure tensor obtained from the fiber networks.

7.2.4 First principal-stress-based segmentation

Given that we have a complex geometry requiring many mesh elements for accurate representation, the computational time to solve the network for each element is a significant challenge. Therefore, we instead segmented the 3D geometries into multiple domains based on the first principal Piola-Kirchhoff (PK1) stress. This segmentation strategy enables the assignment of a dedicated network to each domain. The domain-specific approach not only helps us retain both scale

separation and the fidelity of our FE solutions, but also alleviates the computational burden associated with addressing G&R within each individual element.

The segmentation was performed using a hidden Markov model [235], inspired by image segmentation methods [236] .The segmentation was done recursively where the object was first split into two partitions and each partition is further split into two and so on. Thus, the segmentation problem at each recursive loop is simplified to a binary segmentation, performed using the following steps.

(1) Use K-means clustering to split the FE mesh nodes into two partitions based on the 1st principal PK-1 stress. The k-means centroids were initially assigned as the PK1 stresses of the two partitions.

(2) Create an equivalent graph of the finite element mesh, with each graph node representing a mesh node and graph connectivity follows that of the mesh edges.

(3) Connect each mesh node to two hidden Markov nodes: one is the source node, and the other is sink node. The hidden nodes represent the binary label (or partitioning) that each mesh node can be assigned to.

(4) Assign weights to the graph edges where:

a. Weights of the edges ($edge$) that connect mesh nodes to the hidden nodes are determined by the difference between nodal mesh's PK1 stresses and the centroid of k-means of the PK1 stresses representing the inverse of likelihood that the node belongs to the source or sink nodes.

$$edge(n_1, n_S) = \left|PK1_{n_1} - PK1_{n_S}\right|$$

[76]

where n_1 is a mesh node, n_s is a hidden node (can be sink or source). $PK1_{n1}$ is the mesh node value of PK1 stress, and $PK1_{ns}$ is the PK1 value of the sink/source nodes, determined by the k-means clustering performed previously.

b. Edges obtained from the mesh are given weights as a function of the Cartesian coordinate distance. This represents the inverse of likelihood that the two mesh nodes share the same partition label.

$$edge(n_1, n_2) = w\left|X_{n_1} - X_{n_2}\right|$$

[77]

Where n_1, n_2 are two connected mesh nodes for an edge, X are their mesh coordinates. w represents the relative importance of Euclidean distance and PK1 difference that is connected to the hidden nodes. We could imagine w to be a combination of two things: first, a normalization factor, so that the units of distance and PK1 match and second, scaling factor to determine the significance of the neighbor's connectivity against its PK1 value. w is chosen by the user and might vary across cases.

We perform a max-flow/min-cut optimization on this graph with the flow from the source node towards the sink node using Boykov-Kolmogorov algorithm [237]. Here, max flow was used since the edges represent the inverse of the likelihood that any two nodes are connected. The edges that represent maximum flow from

the source to sink are equivalent to cut edges that minimize the cost of partitioning (as the likelihood of two connected nodes) when we break two connected nodes (min-cut). At the end of the optimization, whichever hidden node (sink or source) the mesh nodes are connected to after the cut would then be the assigned label.

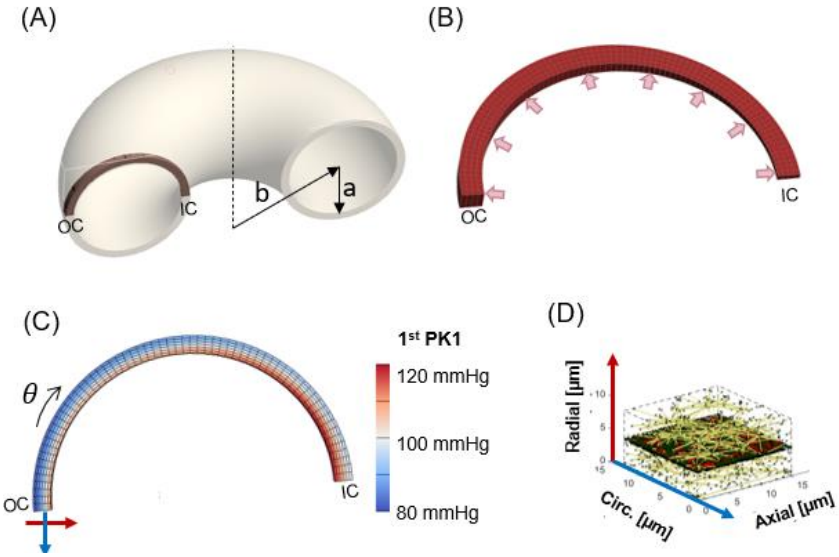

***Figure 47**: G&R based on the simple inflation of an edge of the aortic arch.*

7.3 Results

By employing this methodology, we aim to highlight the potential and scope of this approach rather than offering specific analytical conclusions. Here we will be focusing on three distinct cases, highlighted bellow.

7.3.1 Case1: Inflation of the aortic arch with a finite thickness wall

The first case tests the performance of the model against the work by Alford *et al.* [44]. Here we skipped the FSI simulation and performed a simple inflation as shown **Figure 47**A-B. Because of the asymmetry of the aortic arch, the stress

distribution depends on the circumferential location θ as shown in **Figure 47**C. The fiber network was aligned so that the collagen-elastin ECM sheet was in the circumferential-axial plan, as shown on **Figure 47**D.

Figure 48 shows the results of growth after 10 days for a geometry with b/a = 3.4, with the vessel exposed to the asymmetric stress distribution shown on **Figure 47**C. Results match observation made by Alford *et. al.*[44], with a larger radial and circumferential growth observed in the inner curvature.

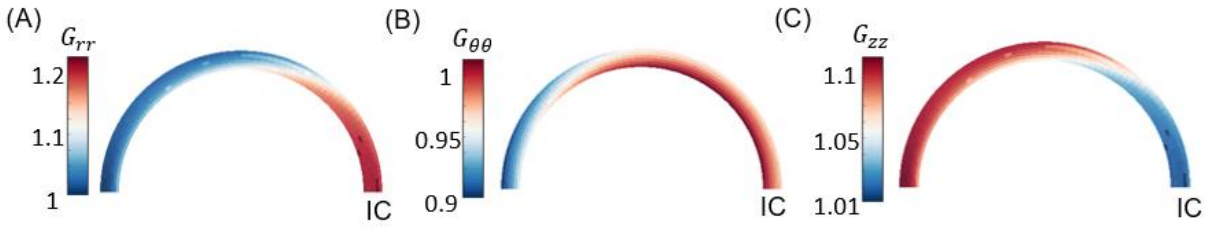

***Figure 48**: Growth in radial (A) circumferential (B) and axial (D) direction of the torus edge after 10 days using the multiscale G&R approach.*

7.3.2 Case 2: Idealized aorta

In Case 2, our focus was on solving an idealized aorta—a structure resembling a torus with an attached straight tube, depicted in **Figure 49**A. We conducted a comprehensive fluid-structure interaction (FSI) analysis, employing a waveform as the inlet boundary condition, and integrating a three-element Windkessel for the outlet boundary condition. The solution led to a concentration of stress in the inner arch of the geometry. Lighter regions in the PK1 stress close to the inlet and outlet are the effects of no displacement boundary condition imposed in the solid domain. To manage computational costs effectively, we adopted a domain-based approach, as shown in **Figure 49**C. Thirty different domains, based on the PK1 stresses were used for this simulation. Additionally, we utilized a Gaussian-based smoothing function to mitigate discontinuities in the growth tensor and material parameters, ensuring smoother and more consistent results.

Figure 50 depicts the overall growth during a 10-day period, driven by the stress distribution highlighted in **Figure 49**B. The concentration of stress observed within

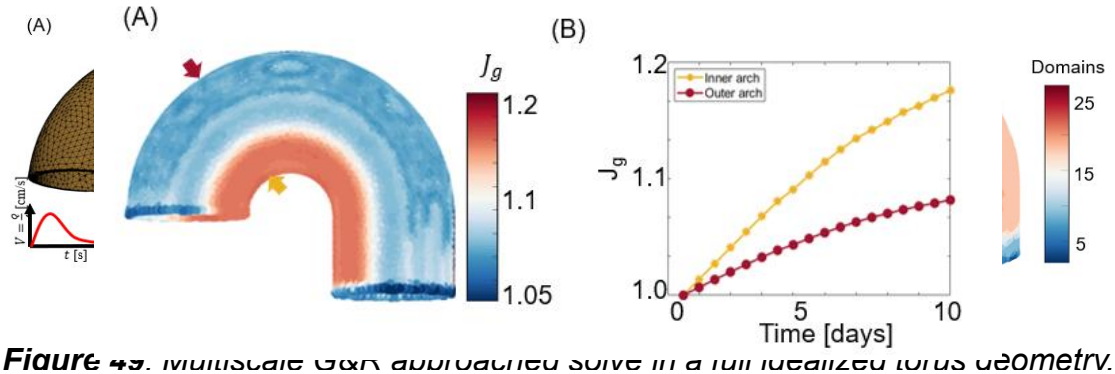

***Figure 49**: Multiscale G&R approached solve in a full idealized torus geometry.*
***Figure 50**: (A) Shows the total growth along the geometry from 10-day remodeling period. (B) Depicts the difference in the total growth for the inner arch (yellow) versus outer arch (red).*

based on the first principal PK1 stress (C), where each domain is represented by a fiber network.

the inner arch of the geometry results in a localized, amplified total growth in this specific region. The total growth is calculated by the determinant of the growth tensor, i.e., $\mathrm{J_G} = \det(\boldsymbol{F}_G) = \lambda_{\theta\theta}\lambda_{\mathrm{rr}}\lambda_{\mathrm{zz}}$. Note that we have a smoother growth distribution as a consequence of the domain-based approach and the Gaussian-based smoothing.

Figure 50B compares the time evolution of the growth in an element in the inner arch (yellow) versus an element in the outer arch (red). A faster growth rate is observed in the inner arch, as a direct consequence of the stress concentration.

The multiscale G&R model enables an assessment of local microstructural changes. **Figure 51** fiber dispersion resulting from a 10-day remodeling period. The fiber dispersion is determined by the eigenvalues of the structure tensor, with κ thing values between 0 and 1/3. κ=1/3 for an isotropic fiber matrix and tend to 0 with larger along the principal direction. We can observe a change in fiber dispersion with larger alignment along the principal direction of the fiber orientation in the inner curvature.

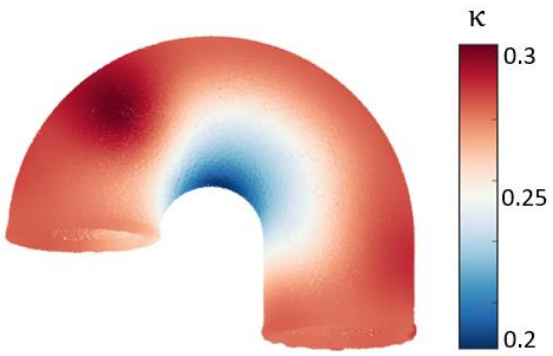

***Figure 51**: Results of fiber remodeling after ten days displaying fiber dispersion, with a larger alignment in the inner arch.*

7.3.3 Case 3: Subject-specific: mouse model

In Case 3, we employed a subject-specific model based on mouse lacking expression of fibulin-4 in smooth muscle cells (*Fbln4*^{SMKO}; the same mice as studied in Chapters 5 and 6). These particular mice exhibit a heightened susceptibility to developing aneurysms in the ascending aorta. For comprehensive insights into the mouse models, image acquisition, and mechanical testing procedures, please refer to our prevoius study [10].

Figure 52 illustrates the sequence of steps undertaken: a medical scan conducted on a 2-month-old mouse (A) enabled the generation of a detailed 3D geometry (B). This geometry served as the foundation for our Fluid-Structure Interaction (FSI)

simulations, outlined in the methods section. For specifics regarding boundary conditions and solution methodologies, our prior work [18]provides details. **Figure 52**C depicts the PK1 stress distribution along the geometry obtained from the FSI simulation. **Figure 52**D shows the 30 domains distribution along the geometry based on the PK1 stress.

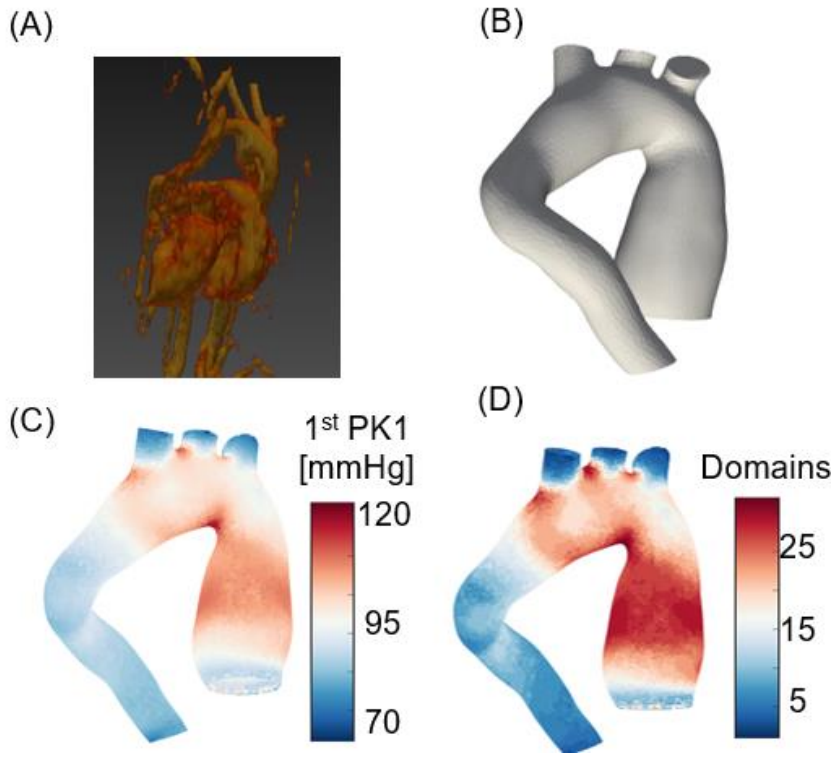

***Figure 52**: (A) Medical scan of a Fbln4SMKO mouse with an ascending aortic aneurysm. (B) 3D geometry constructed based on the medical scan. (C) 1st PK1 stress along the geometry obtained from a fully coupled FSI simulation. (D) Domain segmentation based on the PK1. A total of 30 domains was used for this model.*

7.3.3.1 Tunning time constant parameter

With access to longitudinal data regarding the maximum diameter over the mouse's lifespan, we can use it to fine-tune the G&R time constant from Eq [*70*]. This involved a manual adjustment of τ to replicate the growth pattern observed in vivo. Here we only adjusted the time constant associated to the collagen remodeling.

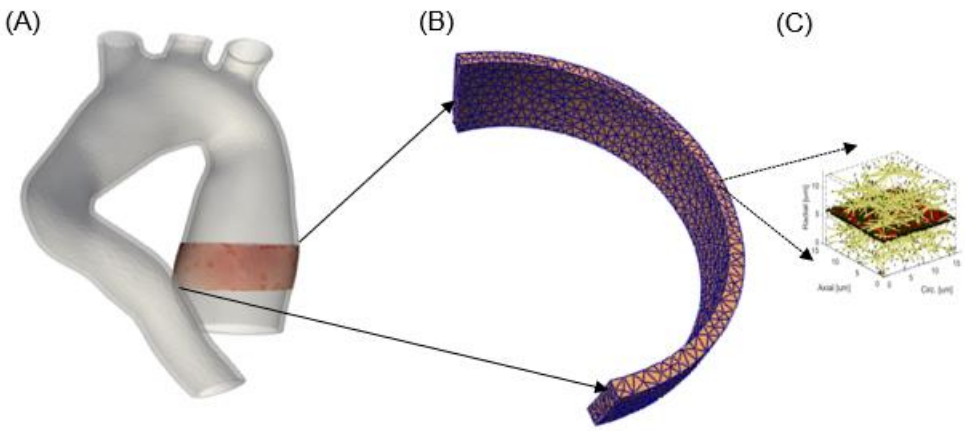

***Figure 53**: (A) The region in the ascending aorta where the ring was extracted to. (B) Show the ring mesh, where each element was represented by a three-family fiber network (C)*

To execute this process, we isolated a ring encompassing the maximum diameter within the ascending aorta, as depicted **Figure 53**A. Due to the straightforward geometry involved, we opted for a simplified approach, bypassing the previously described domain partitioning method. Instead, we allocated a fiber network for each element within the selected aortic ring, illustrated in **Figure 53**B. The procedural steps for this solution align with the methodologies outlined in our Methods.

Figure 54A shows the longitudinal progression of the maximum diameter of the aneurysm (blue markers) and a quadratic interpolation (dashed line) was performed to capture the trend in between these measurements. The diameter is normalized by the 2-month measurement. **Table 13** shows the final time constant

for collagen G&R. **Figure 54**B shows the diameter progression obtained from the multiscale G&R model for the initial 15 days of remodeling.

The G&R values given on **Table 13** where then used to solve the G&R for the full ascending aortic geometry.

***Table 13**: Fitted collagen time constant.*

	τ [days]	σ_{target} [MPa]	k	$r^f_{initial}$[nm]
Collagen	70	0.2	0.2	260

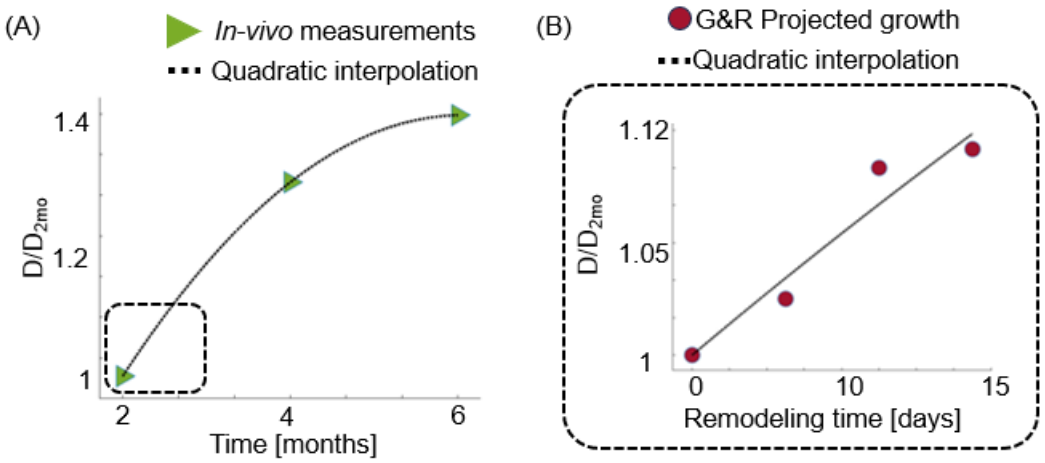

***Figure 54**: (A) Green marker are in vivo measurements of the maximum diameter found in the ascending aorta. Values are normalized by the maximum diameter at 2-month. Dashed line is the quadratic interpolation used to predict the growth trend observed in vivo. (B) Red circles are the projected growth based on the multiscale G&R model for a 15-day growth period compared to the quadradic interpolation for this period*

7.3.3.2 Full ascending aortic geometry

For the comprehensive solution of the full ascending aortic geometry, we adopted the domain-based approach followed by Gauss interpolation, similar to the process used in the idealized ascending thoracic aorta geometry. In **Figure 55**A, the distribution of PK1 stress is depicted alongside growth given by $J_g$in **Figure 55**B

due to this stress. As expected, regions with higher stress showed a lager total growth. We can investigate the components of the total growth. **Figure 55**C shows the circumferential growth for this geometry. We can notice a larger growth in the inner arch, and close to the brunches. The time evolution of the circumferential component of the growth is shown in **Figure 55**D. The yellow markers represent a mesh element from the inner arch, and the red markers represent a mesh element

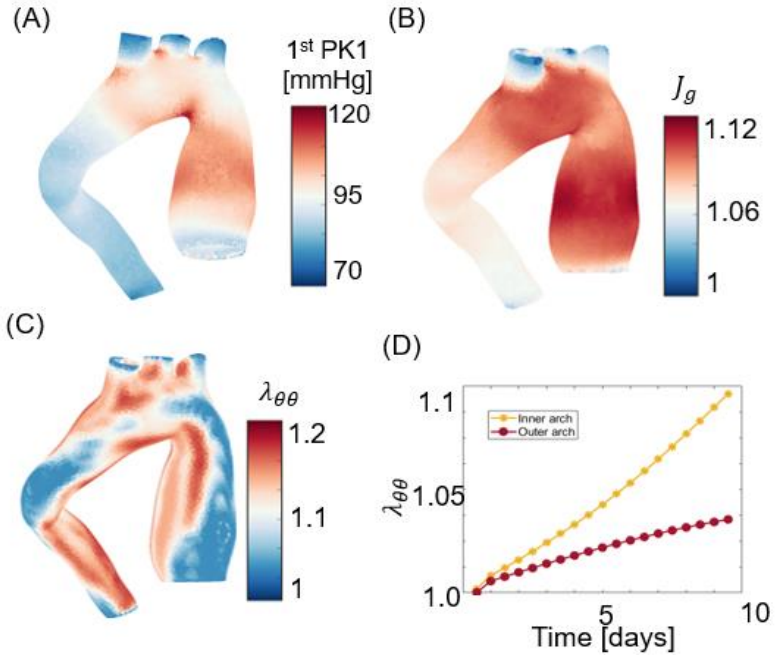

***Figure 55**: Multiscale G&R approached solve in the thoracic aorta of a mouse model. A concentration of PK1 is observed in the inner curvature and close to the branches (A) which leads to a concentration of growth in these regions (B), leading to a faster growth in the inner arch, compared to the outer arch (C).*

from the outer arch. A faster growth rate is observed in the inner arch.

7.4 Discussion

This study presents a novel approach to understanding aneurysm development and growth through a multiscale model integrating fluid-solid interaction (FSI) and

micromechanical stress-driven growth mechanisms. The investigation encompassed three distinct cases: simulated inflation in an aortic arch, analysis of an idealized aorta, and a subject-specific mouse model with an aneurysm.

By combining FSI simulations with a microscale growth and remodeling model, we identified stress-induced growth and microscale remodeling patterns crucial for comprehending aneurysm progression. The proposed model potentially fills this gap by elucidating physical and biomechanical factors associated to the multiscale and multiphysics nature of the cardiovascular tissue.

While computational models offer significant potential in tackling the complexity of cardiovascular tissue, we acknowledge several limitations in our approach:

1- Computational demands: Simulations like the one proposed here, integrating full two-way FSI with a multiscale G&R model, can demand substantial computational resources, taking several days to complete even on a cluster with 128 nodes. This poses challenges in its clinical applicability, especially for patient-specific analysis.
2- Lack of feedback loop for hemodynamics: The model uses hemodynamic-driven stress for the G&R model without updating stresses during the process, neglecting the feedback loop between structural changes, mechanical properties, and alterations in blood flow. Addressing this feedback loop deficiency is a priority in the next model generation.

3- Assumed fiber network initial structure: The initial isotropic assumption for the fiber network throughout the geometry lacks a study into how it influences the G&R process.
4- Focus solely on stress mechanics of the G&R model: The model predominantly considers stress-driven factors, overlooking biochemical aspects, particularly those related to inflammation, which have shown relevance in other studies.

Despite the limitations, our integrated approach of FSI and a microscale growth model demonstrates a promising advancement in modeling tissue response to stress. This technique enables a more comprehensive understanding of how stress distribution influences tissue remodeling, surpassing the limitations of traditional continuum-scale models.

Chapter 8: Conclusions and Future Work.

8.1: Major finding and its impact

8.1.1 Impact of sickle cell disease in blood rheology

This research represents a significant stride forward by integrating microfluidic experimentation and computational modeling to comprehend sickle cell disease (SCD) blood flow complexities. This innovative approach enables the extraction of crucial parameters from rheological data, facilitating the formulation of a comprehensive constitutive model for blood under specified conditions of HbS fraction and oxygen tension. By elucidating alterations in SCD blood flow across

diverse physiological conditions, this model offers a platform to quantitatively compare blood rheology among patients. Moreover, it presents an adaptable tool for realistic simulations of blood flow in various vascular systems, potentially paving the way for tailored patient-specific treatment strategies.

Both experimental and computational parts of this research are essential. The microfluidic device's unique capability to characterize non-Newtonian aspects of SCD blood flow, combined with systematic exploration across different shear rates and oxygen tensions, stands out as a crucial strength. Experimentally, the investigation revealed distinct responses of SCD blood rheology to varying oxygen tension levels, highlighting differences among patients with differing HbS levels. Meanwhile, computational analysis employing the Carreau-Yasuda model delineated stark contrasts in shear-thinning behavior between normal and sickle blood, indicating heightened dependence of SCD blood on oxygen tension. These findings imply altered blood flow throughout the vasculature in SCD patients, which could potentially contribute to increased vaso-occlusion likelihood and severe complications such as stroke and cerebral aneurysms. Additionally, the study's exploration of simulated transfusion experiments hints at the potential for patient-specific treatment strategies, offering insights into optimizing transfusion protocols and resource management in clinical settings.

The research's broader implications lie in its potential to revolutionize treatment strategies by leveraging patient-specific blood rheology data for more precise therapeutic interventions. The study lays the groundwork for potential biophysical

mechanisms underlying observed clinical phenomena in SCD by linking altered hemodynamics with disease complications, particularly in cerebral vasculature. While promising, the translational potential of these findings necessitates further investigation and refinement before clinical application, particularly in designing patient-specific treatment modalities and improving risk assessment for cerebrovascular anomalies in SCD patients.

8.1.2 Influence of sickle cell disease on the blood flow and oxygen transport

This research underscores the complex interplay between blood flow dynamics and oxygen transport within intracranial aneurysms, particularly in sickle cell disease (SCD). The study explores a compelling hypoxia-viscosity feedback loop specific to SCD scenarios, revealing reduced blood flow, heightened viscosity, and decreased oxygen availability within the aneurysmal site. By comparing SCD and non-SCD cases, this study shows that SCD patients exhibit lower systemic oxygen levels due to the shorter lifespan of sickle red blood cells and experience diminished oxygen transfer to surrounding tissues within identical aneurysm geometries. The altered flow dynamics, characterized by lower flow rates and distinct wall shear stress profiles in SCD cases, prompt consideration of potential implications for thrombosis risk. However, the study refrains from directly addressing these consequences, instead focusing on elucidating the biotransport dynamics of blood and oxygen.

These findings bear significance in both theoretical and clinical realms. This research contributes to a foundational understanding of how altered oxygenation and viscosity impact flow dynamics, laying the groundwork for future targeted interventions and opening the door to use this knowledge to expand our comprehension of aneurysm development. As this study explores idealized aneurysm scenarios, it points toward the necessity for broader investigations encompassing diverse aneurysm shapes and sizes, indicating directions for future research to bridge the gap between theoretical models and the complexities of real-world intracranial aneurysms. Finally, this study offers critical insights into the nuanced relationship between oxygen levels, viscosity, and blood flow within aneurysms, which could potentially be used to guide clinical assessments and treatment strategies, especially in managing SCD-related complications.

8.1.3 Engineered mice models as a tool to investigate potential new biomarkers to predict aneurysm formation.

This study unveils promising insights into potential biomarkers for thoracic aortic aneurysm (ATAA) outcomes, particularly in *Fbln4*^{SMKO} mice. Identifying non-invasive biomarkers like OSI and TAWSS, exhibiting stronger correlations with mouse lifespan compared to conventional measures, offers a potential avenue for refining risk assessment strategies. The study's consideration of temporal changes in specific biomarkers underscores their potential complementarity and hints at their significance as additional indicators for future investigations.

However, limitations in model inputs, resolution constraints, and surrogate measures for ATAA outcomes underscore the need for methodological refinements. While promising correlations with mouse lifespan suggest potential applicability in predicting disease outcomes for humans, addressing uncertainties and refining methodologies will be crucial for improving the accuracy and reliability of predictive models. These findings advocate for further exploration into novel biomarkers, leveraging advanced computational approaches and machine learning to enhance diagnostic precision for ATAA and potentially inform tailored treatment decisions in clinical settings. Ultimately, this study serves as a steppingstone, emphasizing the importance of refining methodologies and addressing limitations to enhance diagnostic and predictive capabilities for ATAA outcomes.

8.1.4 Use of hemodynamics-driven aortic growth and remodeling applied to Fbln4^{SMKO} mice.

This research presents an advance in the study of ascending thoracic aortic aneurysm (ATAA) progression through the integration of subject-specific modeling, fluid-solid-interaction (FSI) simulations, and a growth and remodeling law applied to the *Fbln*^{SMKO} mouse model. The study's significant findings center around deriving mouse-specific circumferential and longitudinal growth rate constants and investigating their correlations with lifespan and stress levels.

The study's implications are significant, offering insights into potential connections between growth rates, stress, and aneurysm outcomes. The observed correlations between growth rates and lifespan hint at the predictive value of these parameters for identifying aneurysm risk. Moreover, the moderate correlation between axial growth and geometrical changes in the descending thoracic aorta suggests a link worth exploring further. The validation of growth laws and comparative analysis between domain-based and single-domain approaches demonstrate promising accuracy in modeling growth dynamics. The study's success in capturing aortic growth patterns in the mouse model presents a potential foundation for personalized risk assessment and treatment planning for ATAA patients. However, limitations exist, including the model's focus on hemodynamics and its simplified representation of aortic tissue properties. Addressing these limitations, broadening the model's scope by incorporating biochemical factors, and refining material models would enhance its predictive accuracy and applicability.

8.1.5 Multiscale hemodynamics- driven growth and remodeling model

The significant findings of this study revolve around the successful application of a novel multiscale, multiphysics modeling approach that integrates fluid-solid interaction (FSI) simulations with stress-driven growth and remodeling (G&R) in understanding aneurysm development and progression. By employing FSI simulations and G&R models, the research elucidated the impact of stress distribution on structural, mechanistic, and geometric changes in aneurysms. This approach contributes significantly to understanding the multifaceted influences of

stress on tissue remodeling. However, the computational demands, feedback loop deficiencies, initial fiber network structure assumptions, and a focus primarily on stress mechanics are still limitations of this model. These findings pave the way for future research to address these limitations, potentially incorporating biochemical aspects and refining modeling techniques for improved accuracy and clinical applicability. Despite its limitations, this integrated approach offers a leap forward in understanding how stress distribution influences tissue remodeling, surpassing traditional modeling constraints and opening new avenues for comprehensive cardiovascular tissue modeling and clinical applications.

8.2 Future work

8.2.1 In the connection between hypoxia and intracranial aneurysm formation

Sickle cell disease (SCD), a blood disease, has been correlated with the development and rupture of aneurysms, characterized as tissue diseases. Notably, oxygen transport and availability levels play a crucial role in SCD. A promising avenue for further investigation involves examining hypoxia's medium and long-term effects on arterial tissue.

Numerous studies have established a connection between hypoxia and the subsequent expression of angiogenic factors, particularly vascular endothelial growth factor (VEGF), known for its potent ability to induce angiogenesis[238], [239]. This hypoxia-induced process contributes to the formation of vasa vasorum, which is especially evident in cases of IAs [240].

The formation of vasa vasorum is a foundation for inflammatory cells, predominantly macrophages, and neutrophils, allowing their infiltration into lesions. This infiltration triggers an exacerbation of inflammation within the lesions, ultimately leading to the development and rupture of intracranial aneurysm [3], [4].

Additionally, the stiffened shape of the sickle red blood cells has been reported to lead to endothelial damage. Sustained endothelial injury can lead to vessel wall weakening, which can make the vessel wall more prone to unhealthy growth, and development of aneurysms [242].

Thus, a growth and remodeling model should be developed to better understand how hypoxia, inflammation, and endothelial damage can lead patients with sickle disease to be more prone to the development of intracranial aneurysm and rupture. The model could be hybrid, accounting for the phenomenological growth due to stress changes and the mechanistic biochemical pathway that connects SCD, hypoxia, angiogenic factors, vasa vasorum formation, and inflammatory cell infiltration to tissue remodeling and growth.

8.2.2 In search of better predictive and affordable markers of aortic aneurysm, dissection, and rupture

In pursuing better clinical outcomes, discovering non-invasive predictive markers for cardiovascular complications linked to abnormal growth remains paramount. However, the reliance on biomarkers such as growth rate, maximum diameter, tortuosity index, and blood flow analysis necessitates medical imaging, posing a

challenge due to limited access, especially in low- and middle-income countries [6] [243].

Addressing this imaging gap becomes imperative, prompting the exploration of alternative diagnostic measures independent of medical imaging. One promising avenue involves leveraging pulse wave velocity (PWV) or extracting diagnostic insights from pulse waveforms, given the broader accessibility of pulse wave sensors compared to medical imaging devices.

While studies have explored associations between aortic aneurysms and PWV[244], along with other metrics like intrinsic frequencies [245], conclusive evidence remains elusive. Surprisingly, there is a notable absence of investigation of the information encapsulated within the waveform, particularly regarding how dissections and aneurysms may modify this waveform.

This highlights an intriguing area for further exploration: comprehending how conditions such as dissections and aneurysms alter the pulse wave form. Scrutinizing these waveform alterations could unveil novel diagnostic avenues, offering fresh insights into understanding and diagnosing cardiovascular complications without relying on conventional imaging modalities.

8.2.3 In the connection between women's health and cardiovascular disease

The influence of gonadal hormones on the body's equilibrium, notably within the cardiovascular system, has long been recognized. This understanding prompts an exploration into instances where chronic fluctuations in these hormones occur,

such as during pregnancy [246], [247], or menopause [248], which often disrupt the balance of cardiovascular homeostasis.

Pregnancy presents a remarkable period characterized not only by a sudden surge in hormonal levels but also by an intensified demand on the cardiovascular system to ensure adequate blood supply to the developing fetus. Consequently, this prompts significant adaptations in the heart, resulting in overall cardiac enlargement and an augmented cardiovascular output[249].

The repercussions of these hormonal and cardiovascular alterations during pregnancy are substantial. Shockingly, cardiovascular diseases emerge as the primary cause of maternal mortality and birth complications, underscoring the critical role of these physiological changes in maternal health [250].

Despite these observations, a conspicuous gap exists in our understanding of the intricate correlation between gonadal hormones, heightened cardiovascular load, and their effects on the growth and remodeling of the cardiovascular system. This gap presents an opportunity for extensive research to unravel the nuanced interplay between hormonal dynamics and cardiovascular adaptations during pivotal life stages.:

Chapters 5 and 6 have laid the groundwork for models exploring cardiovascular dynamics. Expanding these models to incorporate the impact of hormonal alterations presents an exciting opportunity. These refined models could serve as

valuable tools to delve deeper into the repercussions of hormonal changes on arterial tissue, specifically during pregnancy.

By extending existing models to accommodate hormonal influences and applying them to explore pregnancy's effects on arterial tissue, researchers can make significant strides in comprehending the complex relationship between hormonal dynamics and cardiovascular adaptations. This endeavor addresses an existing knowledge gap and holds promise for advancing our understanding of cardiovascular health in the context of hormonal fluctuations during pivotal life stages.

References

[1] F. B. Piel, M. H. Steinberg, and D. C. Rees, “Sickle Cell Disease,” *New England Journal of Medicine*, vol. 376, no. 16, pp. 1561–1573, Apr. 2017, doi: 10.1056/NEJMra1510865.

[2] M. H. Steinberg, “Management of Sickle Cell Disease,” *New England Journal of Medicine*, vol. 340, no. 13, pp. 1021–1030, Apr. 1999, doi: 10.1056/NEJM199904013401307.

[3] J. A. Anson, M. Koshy, L. Ferguson, and R. M. Crowell, “Subarachnoid hemorrhage in sickle-cell disease,” *Journal of Neurosurgery*, vol. 75, no. 4, pp. 552–558, 1991, doi: 10.3171/jns.1991.75.4.0552.

[4] “National Vital Statistics Reports, Volume 64, Number 2, 02/16/2016”.

[5] J. C. S. Dean, “Marfan syndrome: clinical diagnosis and management,” *Eur J Hum Genet*, vol. 15, no. 7, pp. 724–733, Jul. 2007, doi: 10.1038/sj.ejhg.5201851.

[6] M. A. Coady, J. A. Rizzo, G. L. Hammond, G. S. Kopf, and J. A. Elefteriades, “Surgical intervention criteria for thoracic aortic aneurysms: a study of growth rates and complications.,” *The Annals of thoracic surgery*, vol. 67, no. 6, pp. 1922–1928, Jun. 1999, doi: 10.1016/s0003-4975(99)00431-2.

[7] S. L. Reeves, H. K. Jary, J. P. Gondhi, M. Kleyn, K. Spector-Bagdady, and K. J. Dombkowski, “Incidence, demographic characteristics, and geographic distribution of sickle cell trait and sickle cell anemia births in Michigan, 1997–2014,” *Molecular Genetics and Genomic Medicine*, vol. 7, no. 8, Aug. 2019, doi: 10.1002/mgg3.795.

[8] M. H.-Y. Lee *et al.*, “Racial and ethnic differences in presentation severity and post-operative outcomes in vascular surgery,” *Journal of Vascular Surgery*, Oct. 2022, doi: 10.1016/j.jvs.2022.08.043.
[9] M. S. Bazzi, J. M. Valdez, V. H. Barocas, and D. K. Wood, “A combined experimental-computational approach to quantify patient-specific blood rheology predicts altered systemic blood flow in sickle cell disease,” *Biophysical journal*, doi: 10.1016/j.bpj.2020.10.011.
[10] V. H. ; Bazzi, M.S.; Balouchzadeh, R.; Pavey, S.N.; Quirk, J.D.; Yanagisawa, H.; Vedula, V.; Wagenseil, J.E.; Barocas, “Experimental and mouse-specific computational models of the Fbln4SMKO mouse to identify potential biomarkers for ascending thoracic aortic aneurysm,” *Cardiovascular Engineering and Technology*.
[11]E. K. Rodriguez, A. Hoger, and A. D. McCulloch, “Stress-dependent finite growth in soft elastic tissues,” *Journal of Biomechanics*, vol. 27, no. 4, pp. 455–467, 1994, doi: 10.1016/0021-9290(94)90021-3.
[12] J. D. Humphrey and M. A. Schwartz, “Vascular Mechanobiology: Homeostasis, Adaptation, and Disease,” *Annu. Rev. Biomed. Eng.*, vol. 23, no. 1, pp. 1–27, Jul. 2021, doi: 10.1146/annurev-bioeng-092419-060810.
[13] K. Saladin S., *Human Anatomy*. Rex Bookstore, Inc., 2005.
[14] C. Fornieri, D. Quaglino, and G. Mori, “Role of the extracellular matrix in age-related modifications of the rat aorta. Ultrastructural, morphometric, and enzymatic evaluations.,” *Arterioscler Thromb*, vol. 12, no. 9, pp. 1008–1016, Sep. 1992, doi: 10.1161/01.ATV.12.9.1008.
[15] B. R. Berridge, J. F. Van Vleet, and E. Herman, “Cardiac, Vascular, and Skeletal Muscle Systems,” in *Haschek and Rousseaux’s Handbook of Toxicologic Pathology*, Elsevier, 2013, pp. 1567–1665. doi: 10.1016/B978-0-12-415759-0.00046-7.
[16] S. Sugita, E. Mizutani, M. Hozaki, M. Nakamura, and T. Matsumoto, “Photoelasticity-based evaluation of cellular contractile force for phenotypic discrimination of vascular smooth muscle cells,” *Sci Rep*, vol. 9, no. 1, p. 3960, Mar. 2019, doi: 10.1038/s41598-019-40578-7.
[17] J. Chamley-Campbell, G. R. Campbell, and R. Ross, “The smooth muscle cell in culture,” *Physiological Reviews*, vol. 59, no. 1, pp. 1–61, Jan. 1979, doi: 10.1152/physrev.1979.59.1.1.
[18] P. Petsophonsakul *et al.*, “Role of Vascular Smooth Muscle Cell Phenotypic Switching and Calcification in Aortic Aneurysm Formation: Involvement of Vitamin K-Dependent Processes,” *ATVB*, vol. 39, no. 7, pp. 1351–1368, Jul. 2019, doi: 10.1161/ATVBAHA.119.312787.
[19] S. S. M. Rensen, P. A. F. M. Doevendans, and G. J. J. M. van Eys, “Regulation and characteristics of vascular smooth muscle cell phenotypic diversity,” *Netherlands heart journal : monthly journal of the Netherlands Society of Cardiology and the Netherlands Heart Foundation.*, vol. 15, no. 3, Mar. 2007.

[20] J. Rosenbloom, W. R. Abrams, and R. Mecham, “Extracellular matrix 4: the elastic fiber,” no. 13, pp. 1208–1218, Oct. 1993, doi: 10.1096/fasebj.7.13.8405806.
[21] S. M. Arribas, A. Hinek, and M. C. González, “Elastic fibres and vascular structure in hypertension,” *Pharmacology & Therapeutics*, vol. 111, no. 3, pp. 771–791, Sep. 2006, doi: 10.1016/j.pharmthera.2005.12.003.
[22] S. Greenwald, “Ageing of the conduit arteries,” *The Journal of Pathology*, vol. 211, no. 2, pp. 157–172, Jan. 2007, doi: 10.1002/path.2101.
[23] S. Q. Liu, C. Tieche, and P. K. Alkema, “Neointima formation on vascular elastic laminae and collagen matrices scaffolds implanted in the rat aortae,” *Biomaterials*, vol. 25, no. 10, pp. 1869–1882, May 2004, doi: 10.1016/j.biomaterials.2003.08.044.
[24] D. Y. Li *et al.*, “Elastin is an essential determinant of arterial morphogenesis,” *Nature*, vol. 393, no. 6682, pp. 276–280, May 1998, doi: 10.1038/30522.
[25] J. Myllyharju and K. I. Kivirikko, “Collagens and collagen-related diseases,” *Annals of Medicine*, vol. 33, no. 1, pp. 7–21, 2001, doi: 10.3109/07853890109002055.
[26] J. D. Humphrey, *Cardiovascular Solid Mechanics: Cells, Tissues, and Organs*. SpringerVerlag, 2002.
[27] J. T. Cirulis *et al.*, “Fibrillins, fibulins, and matrix-associated glycoprotein modulate the kinetics and morphology of in vitro self-assembly of a recombinant elastin-like polypeptide,” *Biochemistry*, vol. 47, no. 47, pp. 12601–12613, Nov. 2008, doi: 10.1021/BI8005384.
[28] J. E. Wagenseil and R. P. Mecham, “New insights into elastic fiber assembly,” *Birth Defects Research Part C - Embryo Today: Reviews*, vol. 81, no. 4, pp. 229–240, Dec. 2007, doi: 10.1002/BDRC.20111.
[29] H. Schlichting and K. Gersten, *Boundary-Layer Theory*. Berlin, Heidelberg: Springer Berlin Heidelberg, 2017. doi: 10.1007/978-3-662-52919-5.
[30] D. Biswas, *Biswas D. Blood Flow Models: A Comparative Study*. Mittal Publications, 2002.
[31] L. Dean, “Blood Groups and Red Cell Antigens”.
[32] E. Nader *et al.*, “Blood Rheology: Key Parameters, Impact on Blood Flow, Role in Sickle Cell Disease and Effects of Exercise,” *Front. Physiol.*, vol. 10, p. 1329, Oct. 2019, doi: 10.3389/fphys.2019.01329.
[33] P. Connes *et al.*, “Haemolysis and abnormal haemorheology in sickle cell anaemia,” *Br J Haematol*, vol. 165, no. 4, pp. 564–572, May 2014, doi: 10.1111/bjh.12786.
[34] L. A. Taber, *Continuum Modeling in Mechanobiology*. Cham: Springer International Publishing, 2020. doi: 10.1007/978-3-030-43209-6.
[35] T. C. Gasser, R. W. Ogden, and G. A. Holzapfel, “Hyperelastic modelling of arterial layers with distributed collagen fibre orientations,” *Journal of the Royal Society Interface*, vol. 3, no. 6, pp. 15–35, 2006, doi: 10.1098/rsif.2005.0073.
[36] G. A. Holzapfel, T. C. Gasser, and R. W. Ogden, “A new constitutive framework for arterial wall mechanics and a comparative study of material

models," *Journal of Elasticity*, vol. 61, no. 1–3, pp. 1–48, 2000, doi: 10.1023/A:1010835316564.
[37] G. A. Holzapfel and H. W. Weizsäcker, "Biomechanical behavior of the arterial wall and its numerical characterization," *Computers in Biology and Medicine*, vol. 28, no. 4, pp. 377–392, Jul. 1998, doi: 10.1016/S0010-4825(98)00022-5.
[38] R. L. Panton, *Incompressible Flow*, 1st ed. Wiley, 2013. doi: 10.1002/9781118713075.
[39] S. C. Cowin, "Tissue Growth and Remodeling," *Annual Review of Biomedical Engineering*, vol. 6, no. 1, pp. 77–107, 2004, doi: 10.1146/annurev.bioeng.6.040803.140250.
[40] G. Himpel, E. Kuhl, A. Menzel, and P. Steinmann, "Computational modelling of isotropic multiplicative growth," *CMES - Computer Modeling in Engineering and Sciences*, vol. 8, no. 2, pp. 119–134, 2005, doi: 10.3970/cmes.2005.008.119.
[41] D. Ambrosi *et al.*, "Perspectives on biological growth and remodeling," *Journal of the Mechanics and Physics of Solids*, vol. 59, no. 4, pp. 863–883, 2011, doi: 10.1016/j.jmps.2010.12.011.
[42] L. A. Taber and D. W. Eggers, "Theoretical Study of Stress-Modulated Growth in the Aorta," *Journal of Theoretical Biology*, vol. 180, no. 4, pp. 343–357, Jun. 1996, doi: 10.1006/jtbi.1996.0107.
[43] L. A. Taber, "A model for aortic growth based on fluid shear and fiber stresses," *Journal of biomechanical engineering*, vol. 120, no. 3, p. 348, doi: 10.1115/1.2798001.
[44] P. W. Alford and L. A. Taber, "Computational study of growth and remodelling in the aortic arch," *Computer Methods in Biomechanics and Biomedical Engineering*, vol. 11, no. 5, pp. 525–538, 2008, doi: 10.1080/10255840801930710.
[45] J. D. Humphrey and K. R. Rajagopal, "A constrained mixture model for arterial adaptations to a sustained step change in blood flow.," *Biomechanics and modeling in mechanobiology*, vol. 2, no. 2, pp. 109–126, 2003, doi: 10.1007/s10237-003-0033-4.
[46] J. D. Humphrey, E. R. Dufresne, and M. A. Schwartz, "Mechanotransduction and extracellular matrix homeostasis," *Nature Reviews Molecular Cell Biology*, vol. 15, no. 12, pp. 802–812, 2014, doi: 10.1038/nrm3896.
[47] J. D. HUMPHREY and K. R. RAJAGOPAL, "A CONSTRAINED MIXTURE MODEL FOR GROWTH AND REMODELING OF SOFT TISSUES," *Mathematical Models and Methods in Applied Sciences*, vol. 12, no. 3, pp. 407–430, doi: 10.1142/S0218202502001714.
[48] J. D. Humphrey, "Constrained Mixture Models of Soft Tissue Growth and Remodeling – Twenty Years After," *Journal of Elasticity*, vol. 145, no. 1–2, pp. 49–75, Aug. 2021, doi: 10.1007/s10659-020-09809-1.
[49] T. S. E. Eriksson, P. N. Watton, X. Y. Luo, and Y. Ventikos, "Modelling volumetric growth in a thick-walled fibre reinforced artery," *Journal of the*

Mechanics and Physics of Solids, vol. 73, no. C, pp. 134–150, doi: 10.1016/j.jmps.2014.09.003.

[50] P. Watton and N. Hill, “Evolving mechanical properties of a model of abdominal aortic aneurysm,” *Biomechanics and Modeling in Mechanobiology*, vol. 8, no. 1, pp. 25–42, doi: 10.1007/s10237-007-0115-9.

[51] P. Watton, N. Hill, and M. Heil, “A mathematical model for the growth of the abdominal aortic aneurysm,” *Biomechanics and Modeling in Mechanobiology*, vol. 3, no. 2, pp. 98–113, doi: 10.1007/s10237-004-0052-9.

[52] P. Watton, A. Selimovic, N. Raberger, P. Huang, G. Holzapfel, and Y. Ventikos, “Modelling evolution and the evolving mechanical environment of saccular cerebral aneurysms,” *Biomechanics and Modeling in Mechanobiology*, vol. 10, no. 1, pp. 109–132, doi: 10.1007/s10237-010-0221-y.

[53] Z. Jia and T. D. Nguyen, “A micromechanical model for the growth of collagenous tissues under mechanics-mediated collagen deposition and degradation,” *Journal of the Mechanical Behavior of Biomedical Materials*, vol. 98, pp. 96–107, doi: 10.1016/j.jmbbm.2019.06.004.

[54] R. A. Brown, R. Prajapati, D. A. Mcgrouther, I. V. Yannas, and M. Eastwood, “Tensional homeostasis in dermal fibroblasts: mechanical responses to mechanical loading in three-dimensional substrates,” *Journal of cellular physiology*, vol. 175, no. 3, p. 323, doi: 10.1002/(SICI)1097-4652(199806)175:33.0.CO;2-6.

[55] J. Foolen, C. C. van Donkelaar, S. Soekhradj-Soechit, and K. Ito, “European Society of Biomechanics S.M. Perren Award 2010: An adaptation mechanism for fibrous tissue to sustained shortening,” *Journal of Biomechanics*, vol. 43, no. 16, pp. 3168–3176, 2010, doi: 10.1016/j.jbiomech.2010.07.040.

[56] R. R. Mahutga, “A DISSERTATION SUBMITTED TO THE FACULTY OF THE UNIVERSITY OF MINNESOTA”.

[57] R. R. Mahutga and V. H. Barocas, “Investigation of Pathophysiological Aspects of Aortic Growth, Remodeling, and Failure Using a Discrete-Fiber Microstructural Model,” *Journal of Biomechanical Engineering*, vol. 142, no. 11, 2020, doi: 10.1115/1.4048031.

[58] M. R. Eslami, *Finite Elements Methods in Mechanics*, vol. 216. in Solid Mechanics and Its Applications, vol. 216. Cham: Springer International Publishing, 2014. doi: 10.1007/978-3-319-08037-6.

[59] H. Lan, A. Updegrove, N. M. Wilson, G. D. Maher, S. C. Shadden, and A. L. Marsden, “A Re-Engineered Software Interface and Workflow for the Open-Source SimVascular Cardiovascular Modeling Package,” *Journal of Biomechanical Engineering*, 2018, doi: 10.1115/1.4038751.

[60] S. A. Maas, B. J. Ellis, G. A. Ateshian, and J. A. Weiss, “FEBio: Finite Elements for Biomechanics,” *Journal of Biomechanical Engineering*, vol. 134, no. 1, Feb. 2012, doi: 10.1115/1.4005694.

[61] T. Kind, T. J. C. Faes, J.-W. Lankhaar, A. Vonk-Noordegraaf, and M. Verhaegen, “Estimation of three- and four-element windkessel parameters

using subspace model identification.," *IEEE transactions on bio-medical engineering*, vol. 57, no. 7, pp. 1531–1538, Jul. 2010, doi: 10.1109/TBME.2010.2041351.

[62] R. M. Romarowski, A. Lefieux, S. Morganti, A. Veneziani, and F. Auricchio, "Patient-specific CFD modelling in the thoracic aorta with PC-MRI–based boundary conditions: A least-square three-element Windkessel approach," *International Journal for Numerical Methods in Biomedical Engineering*, vol. 34, no. 11, 2018, doi: 10.1002/cnm.3134.

[63] K. Takizawa, T. E. Tezduyar, and T. Sasaki, "Estimation of Element-Based Zero-Stress State in Arterial FSI Computations with Isogeometric Wall Discretization," in *Biomedical Technology: Modeling, Experiments and Simulation*, P. Wriggers and T. Lenarz, Eds., in Lecture Notes in Applied and Computational Mechanics. , Cham: Springer International Publishing, 2018, pp. 101–122. doi: 10.1007/978-3-319-59548-1_7.

[64] S. Sathe and T. E. Tezduyar, "Modeling of fluid–structure interactions with the space–time finite elements: contact problems," *Comput Mech*, vol. 43, no. 1, pp. 51–60, Dec. 2008, doi: 10.1007/s00466-008-0299-6.

[65] M.-C. Hsu and Y. Bazilevs, "Blood vessel tissue prestress modeling for vascular fluid–structure interaction simulation," *Finite elements in analysis and design*, vol. 47, no. 6, pp. 593–599, 2011, doi: 10.1016/j.finel.2010.12.015.

[66] K. Bäumler *et al.*, "Fluid–structure interaction simulations of patient-specific aortic dissection," *Biomechanics and Modeling in Mechanobiology*, vol. 19, no. 5, pp. 1607–1628, 2020, doi: 10.1007/s10237-020-01294-8.

[67] H. F. Bunn, "Pathogenesis and Treatment of Sickle Cell Disease," *New England Journal of Medicine*, vol. 337, no. 11, pp. 762–769, Sep. 1997, doi: 10.1056/NEJM199709113371107.

[68] F. B. Piel, M. H. Steinberg, and D. C. Rees, "Sickle Cell Disease," *New England Journal of Medicine*, vol. 376, no. 16, pp. 1561–1573, Apr. 2017, doi: 10.1056/NEJMra1510865.

[69] M. H. Steinberg, "Management of Sickle Cell Disease," *New England Journal of Medicine*, vol. 340, no. 13, pp. 1021–1030, Apr. 1999, doi: 10.1056/NEJM199904013401307.

[70] X. Li, M. Dao, G. Lykotrafitis, and G. E. Karniadakis, "Biomechanics and biorheology of red blood cells in sickle cell anemia," *Journal of Biomechanics*, vol. 50, pp. 34–41, 2017, doi: 10.1016/j.jbiomech.2016.11.022.

[71] G. B. Nash, C. S. Johnson, and H. J. Meiselman, "Influence of oxygen tension on the viscoelastic behavior of red blood cells in sickle cell disease," *Blood*, vol. 67, no. 1, pp. 110–118, 1986, doi: 10.1182/blood.v67.1.110.bloodjournal671110.

[72] D. P. Papageorgiou *et al.*, "Simultaneous polymerization and adhesion under hypoxia in sickle cell disease," *Proceedings of the National Academy of Sciences of the United States of America*, vol. 115, no. 38, pp. 9473–9478, 2018, doi: 10.1073/pnas.1807405115.

[73] D. Zhang, C. Xu, D. Manwani, P. S. Frenette, and D. S. Gottesman, “Neutrophils, platelets, and inflammatory pathways at the nexus of sickle cell disease pathophysiology,” *Blood*, vol. 127, no. 7, pp. 801–809, 2016, doi: 10.1182/blood.

[74] G. J. Kato, M. H. Steinberg, and M. T. Gladwin, “Intravascular hemolysis and the pathophysiology of sickle cell disease,” *Journal of Clinical Investigation*, vol. 127, no. 3. American Society for Clinical Investigation, pp. 750–760, Mar. 01, 2017. doi: 10.1172/JCI89741.

[75] E. Du, M. Diez-Silva, G. J. Kato, M. Dao, and S. Suresh, “Kinetics of sickle cell biorheology and implications for painful vasoocclusive crisis,” *Proceedings of the National Academy of Sciences of the United States of America*, vol. 112, no. 5, pp. 1422–1427, 2015, doi: 10.1073/pnas.1424111112.

[76] S. Usami, S. Chien, P. M. Scholtz, and J. F. Bertles, “Effect of deoxygenation on blood rheology in sickle cell disease,” *Microvascular Research*, 1975, doi: 10.1016/0026-2862(75)90069-2.

[77] X. Lu, D. K. Wood, and J. M. Higgins, “Deoxygenation Reduces Sickle Cell Blood Flow at Arterial Oxygen Tension,” *Biophysical Journal*, vol. 110, no. 12, pp. 2751–2758, 2016, doi: 10.1016/j.bpj.2016.04.050.

[78] M. Tsai, D. A. Fletcher, and W. A. Lam, “In vitro modeling of the microvascular occlusion and thrombosis that occur in hematologic diseases using microfluidic technology,” *J Clin Invest*, vol. 122, no. 1, 2012, doi: 10.1172/JCI58753.

[79] M. T. Gladwin and V. Sachdev, “Cardiovascular abnormalities in sickle cell disease,” *Journal of the American College of Cardiology*, vol. 59, no. 13. pp. 1123–1133, 2012. doi: 10.1016/j.jacc.2011.10.900.

[80] A. Aprelev, Z. Liu, and F. A. Ferrone, “The Growth of Sickle Hemoglobin Polymers,” *Biophysical Journal*, vol. 101, pp. 885–891, 2011, doi: 10.1016/j.bpj.2011.05.064.

[81] G. Di Caprio, E. Schonbrun, B. P. Gonçalves, J. M. Valdez, D. K. Wood, and J. M. Higgins, “High-throughput assessment of hemoglobin polymer in single red blood cells from sickle cell patients under controlled oxygen tension,” *Proceedings of the National Academy of Sciences of the United States of America*, vol. 116, no. 50, pp. 25236–25242, 2019, doi: 10.1073/pnas.1914056116.

[82] J. M. Higgins, D. T. Eddington, S. N. Bhatia, and L. Mahadevan, “Sickle cell vasoocclusion and rescue in a microfluidic device,” *Proceedings of the National Academy of Sciences of the United States of America*, vol. 104, no. 51, pp. 20496–20500, 2007, doi: 10.1073/pnas.0707122105.

[83] A. Simeonov, “A biophysical indicator of vaso-occlusive risk in sickle cell disease,” *Assay and Drug Development Technologies*, vol. 10, no. 3. pp. 232–234, 2012. doi: 10.1089/adt.2012.1003.lr.

[84] Z. Yao, J. Li, M. He, and C. You, “Intracranial Aneurysm in Patients with Sickle Cell Disease: A Systematic Review,” *World Neurosurgery*. 2017. doi: 10.1016/j.wneu.2017.05.139.

[85] J. M. Valdez, Y. H. Datta, J. M. Higgins, and D. K. Wood, “A microfluidic platform for simultaneous quantification of oxygen-dependent viscosity and shear thinning in sickle cell blood,” *APL Bioengineering*, vol. 3, no. 4, p. 046102, 2019, doi: 10.1063/1.5118212.

[86] H. Lei and G. E. Karniadakis, “Probing vasoocclusion phenomena in sickle cell anemia via mesoscopic simulations,” *Proceedings of the National Academy of Sciences of the United States of America*, 2013, doi: 10.1073/pnas.1221297110.

[87] S. T. Chou and R. M. Fasano, “Management of Patients with Sickle Cell Disease Using Transfusion Therapy: Guidelines and Complications,” *Hematology/Oncology Clinics of North America*, vol. 30, no. 3. pp. 591–608, 2016. doi: 10.1016/j.hoc.2016.01.011.

[88] B. P. Yawn *et al.*, “Management of sickle cell disease: Summary of the 2014 evidence-based report by expert panel members,” *JAMA - Journal of the American Medical Association*, vol. 312, no. 10. American Medical Association, pp. 1033–1048, 2014. doi: 10.1001/jama.2014.10517.

[89] J. A. Detterich, “Simple chronic transfusion therapy, a crucial therapeutic option for sickle cell disease, improves but does not normalize blood rheology: What should be our goals for transfusion therapy?,” *Clinical hemorheology and microcirculation*, vol. 68, no. 2–3, pp. 173–186, 2018, doi: 10.3233/CH-189006.

[90] L. A. Verduzco and D. G. Nathan, “Sickle cell disease and stroke,” *Blood*, vol. 114, no. 25. pp. 5117–5125, 2009. doi: 10.1182/blood-2009-05-220921.

[91] M. C. Preul, F. Cendes, N. Just, and G. Mohr, “Intracranial aneurysms and sickle cell anemia: Multiplicity and propensity for the vertebrobasilar territory,” *Neurosurgery*, vol. 42, no. 5, pp. 971–978, 1998, doi: 10.1097/00006123-199805000-00007.

[92] A. Nouh, J. Remke, and S. Ruland, “Ischemic posterior circulation stroke: a review of anatomy, clinical presentations, diagnosis, and current management,” *Frontiers In Neurology*, vol. 5, p. 30, 2014, doi: 10.3389/fneur.2014.00030.

[93] N. Wilson, K. Wang, R. W. Dutton, and C. Taylor, “A software framework for creating patient specific geometric models from medical imaging data for simulation based medical planning ofvascular surgery,” in *Lecture Notes in Computer Science (including subseries Lecture Notes in Artificial Intelligence and Lecture Notes in Bioinformatics)*, Springer Verlag, 2001, pp. 449–456. doi: 10.1007/3-540-45468-3_54.

[94] M. D. Bockman, A. P. Kansagra, S. C. Shadden, E. C. Wong, and A. L. Marsden, “Fluid Mechanics of Mixing in the Vertebrobasilar System: Comparison of Simulation and MRI,” *Cardiovascular Engineering and Technology*, vol. 3, no. 4, pp. 450–461, 2012, doi: 10.1007/s13239-012-0112-8.

[95] K. Buch *et al.*, “Quantitative Analysis of Extracranial Arterial Tortuosity in Patients with Sickle Cell Disease,” *Journal of Neuroimaging*, vol. 27, no. 4, pp. 421–427, Jul. 2017, doi: 10.1111/jon.12418.

[96] M. H. Steinberg and R. P. Hebbel, “Clinical diversity of sickle cell anemia: Genetic and cellular modulation of disease severity,” *American Journal of Hematology*, vol. 14, no. 4, pp. 405–416, Jun. 1983, doi: 10.1002/ajh.2830140412.
[97] M. W. WEATHERALL, D. R. HIGGS, H. WEISS, D. J. WEATHERALL, and G. R. SERJEANT, “Phenotype/genotype relationships in sickle cell disease: a pilot twin study,” *Clinical and Laboratory Haematology*, vol. 27, no. 6, pp. 384–390, Dec. 2005, doi: 10.1111/j.1365-2257.2005.00731.x.
[98] K. M. Saqr *et al.*, “What does computational fluid dynamics tell us about intracranial aneurysms? A meta-analysis and critical review,” *Journal of Cerebral Blood Flow and Metabolism*, 2019, doi: 10.1177/0271678X19854640.
[99] L. Campo-Deano, M. S. N. Oliveira, and F. T. Pinho, “A review of computational hemodynamics in middle cerebral aneurysms and rheological models for blood flow,” *Applied Mechanics Reviews*. 2015. doi: 10.1115/1.4028946.
[100] D. K. Wood, A. Soriano, L. Mahadevan, J. M. Higgins, and S. N. Bhatia, “A biophysical indicator of vaso-occlusive risk in sickle cell disease,” *Science Translational Medicine*, 2012, doi: 10.1126/scitranslmed.3002738.
[101] T. L. Berezina *et al.*, “Influence of storage on red blood cell rheological properties,” *Journal of Surgical Research*, 2002, doi: 10.1006/jsre.2001.6306.
[102] S. Henkelman, M. J. Dijkstra-Tiekstra, J. de Wildt-Eggen, R. Graaff, G. Rakhorst, and W. van Oeveren, “Is red blood cell rheology preserved during routine blood bank storage?,” *Transfusion*, vol. 50, no. 4, pp. 941–948, Apr. 2010, doi: 10.1111/j.1537-2995.2009.02521.x.
[103] H. Lei, D. A. Fedosov, B. Caswell, and G. E. Karniadakis, “Blood flow in small tubes: Quantifying the transition to the non-continuum regime,” *Journal of Fluid Mechanics*, 2013, doi: 10.1017/jfm.2013.91.
[104] G. R. Conway, N. R. Glass, and J. C. Wilcox, “Fitting Nonlinear Models to Biological Data by Marquardt’s Algorithm,” *Ecology*, 1970, doi: 10.2307/1935386.
[105] P. Connes, T. Alexy, J. Detterich, M. Romana, M.-D. Hardy-Dessources, and S. K. Ballas, “The role of blood rheology in sickle cell disease,” *Blood Reviews*, vol. 30, no. 2, pp. 111–118, Mar. 2016, doi: 10.1016/j.blre.2015.08.005.
[106] H. M. Szafraniec *et al.*, “Feature tracking microfluidic analysis reveals differential roles of viscosity and friction in sickle cell blood,” *Lab Chip*, vol. 22, no. 8, pp. 1565–1575, 2022, doi: 10.1039/D1LC01133B.
[107] P. Birkeland *et al.*, “Intracranial aneurysms in sickle-cell disease are associated with the hemoglobin SS genotype but not with moyamoya syndrome,” *Stroke*, vol. 47, no. 7, pp. 1710–1713, 2016, doi: 10.1161/STROKEAHA.116.012664.
[108] M. R. Debaun and F. J. Kirkham, “Errata: Central nervous system complications and management in sickle cell disease. Blood. 2016;127(7):829-838,” *Blood*, vol. 127, no. 21, p. 2647, 2016, doi: 10.1182/blood-2016-04-709626.

[109] S. Farooq and F. D. Testai, “Neurologic Complications of Sickle Cell Disease,” *Curr Neurol Neurosci Rep*, vol. 19, no. 4, p. 17, Apr. 2019, doi: 10.1007/s11910-019-0932-0.
[110] M. C. Preul, F. Cendes, N. Just, and G. Mohr, “Intracranial aneurysms and sickle cell anemia: Multiplicity and propensity for the vertebrobasilar territory,” *Neurosurgery*, vol. 42, no. 5, pp. 971–978, doi: 10.1097/00006123-199805000-00007.
[111] R. A. C. S. Brandão, G. T. C. de Carvalho, B. L. Reis, E. Bahia, and A. A. de Souza, “Intracranial aneurysms in sickle cell patients: report of 2 cases and review of the literature,” *Surgical Neurology*, vol. 72, no. 3, pp. 296–299, Sep. 2009, doi: 10.1016/j.surneu.2008.03.044.
[112] B. Berse, J. A. Hunt, R. J. Diegel, and P. Morganelli, “Hypoxia augments cytokine (transforming growth factor-beta (TGF-b) and IL-1)- induced vascular endothelial growth factor secretion by human synovial fibroblasts,” *Clinical and Experimental Immunology*, 1999.
[113] A. G. Durmowicz, D. B. Badesch, W. C. Parks, R. P. Mecham, and K. R. Stenmark, “Hypoxia-induced Inhibition of Tropoelastin Synthesis by Neonatal Calf Pulmonary Artery Smooth Muscle Cells,” *Am J Respir Cell Mol Biol*, vol. 5, no. 5, pp. 464–469, Nov. 1991, doi: 10.1165/ajrcmb/5.5.464.
[114] K. Pietila and O. Jaakkola, “Effect of hypoxia on the synthesis of glycosaminoglycans and collagen by rabbit aortic smooth muscle cells in culture,” *Atherosclerosis*, vol. 50, no. 2, pp. 183–190, Feb. 1984, doi: 10.1016/0021-9150(84)90021-2.
[115] J. Uitto and D. J. Prockop, “Synthesis and secretion of under-hydroxylated procollagen at various temperatures by cells subject to temporary anoxia,” *Biochemical and Biophysical Research Communications*, vol. 60, no. 1, pp. 414–423, Sep. 1974, doi: 10.1016/0006-291X(74)90220-4.
[116] S. E. Herrick, G. W. Ireland, D. Simon, C. N. McCollum, and M. W. J. Ferguson, “Venous Ulcer Fibroblasts Compared with Normal Fibroblasts Show Differences in Collagen but Not Fibronectin Production under Both Normal and Hypoxic Conditions,” *Journal of Investigative Dermatology*, vol. 106, no. 1, pp. 187–193, Jan. 1996, doi: 10.1111/1523-1747.ep12329920.
[117] D. S. Steinbrech *et al.*, “Fibroblast Response to Hypoxia: The Relationship between Angiogenesis and Matrix Regulation,” *Journal of Surgical Research*, vol. 84, no. 2, pp. 127–133, Jun. 1999, doi: 10.1006/jsre.1999.5627.
[118] C. I. Levene, R. Kapoor, and G. Heale, “The effect of hypoxia on the synthesis of collagen and glycosaminoglycans by cultured pig aortic endothelium,” *Atherosclerosis*, vol. 44, no. 3, pp. 327–337, Sep. 1982, doi: 10.1016/0021-9150(82)90007-7.
[119] A. Abdu, J. Gómez-Márquez, and T. K. Aldrich, “The oxygen affinity of sickle hemoglobin,” *Respiratory Physiology & Neurobiology*, vol. 161, no. 1, pp. 92–94, Mar. 2008, doi: 10.1016/j.resp.2007.12.005.
[120] P. McCurdy, L. Mahmood, and A. Sherman, “Red cell life span in sickle cell-hemoglobin C disease with a note about sickle cell-hemoglobin O ARAB,”

Blood, vol. 45, no. 2, pp. 273–279, Feb. 1975, doi: 10.1182/blood.V45.2.273.273.
[121] M. S. Bazzi, J. M. Valdez, V. H. Barocas, and D. K. Wood, “An Experimental-Computational Approach to Quantify Blood Rheology in Sickle Cell Disease,” *Biophysical journal*, vol. 119, no. 11, pp. 2307–2315, doi: 10.1016/j.bpj.2020.10.011.
[122] D. Ivanov, A. Dol, O. Pavlova, and A. Aristambekova, “Modeling of human circle of Willis with and without aneurisms,” *Acta of Bioengineering and Biomechanics; 02/2014; ISSN 1509-409X*, 2014, doi: 10.5277/ABB140214.
[123] L. Parlea, R. Fahrig, D. W. Holdsworth, and S. P. Lownie, “An Analysis of the Geometry of Saccular Intracranial Aneurysms,” 1999.
[124] R. D. Brown and J. P. Broderick, “Unruptured intracranial aneurysms: epidemiology, natural history, management options, and familial screening,” *The Lancet. Neurology*, vol. 13, no. 4, p. 393—404, Apr. 2014, doi: 10.1016/s1474-4422(14)70015-8.
[125] T. Kenner, “The measurement of blood density and its meaning,” *Basic Res Cardiol*, vol. 84, no. 2, pp. 111–124, Mar. 1989, doi: 10.1007/BF01907921.
[126] J. Feiner, “Chapter 5 - Clinical Cardiac and Pulmonary Physiology”.
[127] H. H. Billett, “Hemoglobin and hematocrit,” *Clinical Methods: The History, Physical, and Laboratory Examinations. 3rd edition*, 1990.
[128] O. O. Akinyanju, “A Profile of Sickle Cell Disease in Nigeria,” *Ann NY Acad Sci*, vol. 565, no. 1 Sickle Cell D, pp. 126–136, Jul. 1989, doi: 10.1111/j.1749-6632.1989.tb24159.x.
[129] A. S. Popel, “Theory of oxygen transport to tissue,” *Critical Reviews in Biomedical Engineering*, vol. 17, no. 3, pp. 257–321, 1989.
[130] A. V. Hill, “The possible effects of the aggregation of the molecules of hæmoglobin on its dissociation curves,” *The Journal of Physiology*, vol. 40, pp. i–vii, Jan. 1910.
[131] A. Zydney and C. K. Colton, “AUGMENTED SOLUTE TRANSPORT IN THE SHEAR FLOW OF A CONCENTRATED SUSPENSION.,” *PCH. Physicochemical hydrodynamics*, vol. 10, no. 1, pp. 77–96, 1988.
[132] J. A. Moore and C. R. Ethier, “Oxygen mass transfer calculations in large arteries,” *Journal of Biomechanical Engineering*, vol. 119, no. 4, pp. 469–475, 1997, doi: 10.1115/1.2798295.
[133] F. Chassagne *et al.*, “The effect of Dean, Reynolds and Womersley numbers on the flow in a spherical cavity on a curved round pipe. Part 1. Fluid mechanics in the cavity as a canonical flow representing intracranial aneurysms,” *Journal of Fluid Mechanics*, vol. 915, pp. 1–19, 2021, doi: 10.1017/jfm.2020.1114.
[134] K. S. Cunningham and A. I. Gotlieb, “The role of shear stress in the pathogenesis of atherosclerosis,” *Laboratory Investigation*, vol. 85, no. 1, pp. 9–23, Jan. 2005, doi: 10.1038/labinvest.3700215.
[135] B. Zhou *et al.*, “Worldwide trends in blood pressure from 1975 to 2015: a pooled analysis of 1479 population-based measurement studies with 19·1

million participants," *The Lancet*, vol. 389, no. 10064, pp. 37–55, doi: 10.1016/S0140-6736(16)31919-5.
[136] E. M. Isselbacher, "Thoracic and abdominal aortic aneurysms.," *Circulation*, vol. 111, no. 6, pp. 816–828, Feb. 2005, doi: 10.1161/01.CIR.0000154569.08857.7A.
[137] L. A. Pape *et al.*, "Aortic diameter ≥5.5 cm is not a good predictor of type A aortic dissection: Observations from the International Registry of Acute Aortic Dissection (IRAD)," *Circulation*, vol. 116, no. 10, pp. 1120–1127, 2007, doi: 10.1161/CIRCULATIONAHA.107.702720.
[138] J. A. Elefteriades, "Natural history of thoracic aortic aneurysms: Indications for surgery, and surgical versus nonsurgical risks," *Annals of Thoracic Surgery*, vol. 74, no. 5, 2002, doi: 10.1016/S0003-4975(02)04147-4.
[139] Jessica E. Wagenseil, "Bio-chemo-mechanics of thoracic aortic aneurysms," *Physiology & behavior*, vol. 176, no. 1, pp. 139–148, 2016, doi: 10.1016/j.cobme.2018.01.002.Bio-chemo-mechanics.
[140] S. Pasta *et al.*, "In Vivo Strain Analysis of Dilated Ascending Thoracic Aorta by ECG-Gated CT Angiographic Imaging," *Annals of Biomedical Engineering*, vol. 45, no. 12, pp. 2911–2920, 2017, doi: 10.1007/s10439-017-1915-4.
[141] S. Iddawela, A. Ravendren, and A. Harky, "Bio-chemo-mechanics of the thoracic aorta," *Vascular Biology*, vol. 3, no. 1, pp. R25–R33, 2021, doi: 10.1530/VB-20-0015.
[142] H. L. Cebull, V. L. Raye, and C. J. Goergen, "Recent Advances in Biomechanical Characterization of Thoracic Aortic Aneurysms," *Frontiers in cardiovascular medicine*, vol. 7, pp. 75–75, 2020, doi: 10.3389/fcvm.2020.00075.
[143] H. C. Dietz and R. E. Pyeritz, "Mutations in the human gene for fibrillin-1 (FBN1) in the Marfan syndrome and related disorders," *Human molecular genetics*, vol. 4, no. suppl_1, pp. 1799–1809, 1995, doi: 10.1093/hmg/4.suppl_1.1799.
[144] F. M. Pope *et al.*, "Patients with Ehlers-Danlos Syndrome Type IV Lack Type III Collagen," *Proceedings of the National Academy of Sciences - PNAS*, vol. 72, no. 4, pp. 1314–1316, 1975, doi: 10.1073/pnas.72.4.1314.
[145] J. Kim, J. D. Procknow, H. Yanagisawa, and J. E. Wagenseil, "Differences in genetic signaling, and not mechanical properties of the wall, are linked to ascending aortic aneurysms in fibulin-4 knockout mice," *American Journal of Physiology - Heart and Circulatory Physiology*, vol. 309, no. 1, pp. H103–H113, 2015, doi: 10.1152/ajpheart.00178.2015.
[146] R. Franken *et al.*, "Increased aortic tortuosity indicates a more severe aortic phenotype in adults with Marfan syndrome," *International Journal of Cardiology*, vol. 194, pp. 7–12, 2015, doi: 10.1016/j.ijcard.2015.05.072.
[147] D. P. J. Howard, A. Banerjee, J. F. Fairhead, A. Handa, L. E. Silver, and P. M. Rothwell, "Age-specific incidence, risk factors and outcome of acute abdominal aortic aneurysms in a defined population," *British Journal of Surgery*, vol. 102, no. 8, pp. 907–915, doi: 10.1002/bjs.9838.

[148] S. J. Mousavi and S. Avril, “Patient-specific stress analyses in the ascending thoracic aorta using a finite-element implementation of the constrained mixture theory,” *Biomechanics and Modeling in Mechanobiology*, vol. 16, no. 5, pp. 1765–1777, 2017, doi: 10.1007/s10237-017-0918-2.
[149] C. E. Korenczuk, R. Y. Dhume, K. Liao, and V. H. Barocas, “Ex Vivo Mechanical Tests and Multiscale Computational Modeling Highlight the Importance of Intramural Shear Stress in Ascending Thoracic Aortic Aneurysms,” *Journal of biomechanical engineering*, doi: 10.1115/1.4045270.
[150] J. A. Phillippi *et al.*, “Mechanism of aortic medial matrix remodeling is distinct in patients with bicuspid aortic valve,” *Journal of Thoracic and Cardiovascular Surgery*, vol. 147, no. 3, pp. 1056–1064, 2014, doi: 10.1016/j.jtcvs.2013.04.028.
[151] C. Bellini *et al.*, “Comparison of 10 murine models reveals a distinct biomechanical phenotype in thoracic aortic aneurysms,” pp. 1–8, 2017.
[152] J. Huang *et al.*, “Fibulin-4 deficiency results in ascending aortic aneurysms: A potential link between abnormal smooth muscle cell phenotype and aneurysm progression,” *Circulation Research*, vol. 106, no. 3, pp. 583–592, 2010, doi: 10.1161/CIRCRESAHA.109.207852.
[153] C. L. Papke and H. Yanagisawa, “Fibulin-4 and fibulin-5 in elastogenesis and beyond: Insights from mouse and human studies,” *Matrix Biology*, vol. 37, pp. 142–149, 2014, doi: https://doi.org/10.1016/j.matbio.2014.02.004.
[154] M. R. Bersi, C. Bellini, J. D. Humphrey, and S. Avril, “Local variations in material and structural properties characterize murine thoracic aortic aneurysm mechanics,” *Biomechanics and modeling in mechanobiology*, vol. 18, no. 1, pp. 203–218, 2018, doi: 10.1007/s10237-018-1077-9.
[155] V. P. Le, Y. Yamashiro, H. Yanagisawa, and J. E. Wagenseil, “Measuring, reversing, and modeling the mechanical changes due to the absence of Fibulin-4 in mouse arteries,” *Biomechanics and modeling in mechanobiology*, vol. 13, no. 5, pp. 1081–1095, 2014, doi: 10.1007/s10237-014-0556-x.
[156] S. A. Morris, “Arterial tortuosity in genetic arteriopathies.,” *Current opinion in cardiology*, vol. 30, no. 6, pp. 587–593, Nov. 2015, doi: 10.1097/HCO.0000000000000218.
[157] V. P. Le, R. H. Knutsen, R. P. Mecham, and J. E. Wagenseil, “Decreased aortic diameter and compliance precedes blood pressure increases in postnatal development of elastin-insufficient mice,” *American journal of physiology. Heart and circulatory physiology*, vol. 301, no. 1, p. H221, doi: 10.1152/ajpheart.00119.2011.
[158] V. P. Le *et al.*, “Mechanical factors direct mouse aortic remodelling during early maturation,” *Journal of the Royal Society interface*, vol. 12, no. 104, pp. 20141350–20141350, 2015, doi: 10.1098/rsif.2014.1350.
[159] A. Updegrove, N. M. Wilson, J. Merkow, H. Lan, A. L. Marsden, and S. C. Shadden, “SimVascular: An Open Source Pipeline for Cardiovascular Simulation,” *Annals of biomedical engineering*, vol. 45, no. 3, pp. 525–541, 2017, doi: 10.1007/s10439-016-1762-8.

[160] H. Si, “Adaptive tetrahedral mesh generation by constrained Delaunay refinement,” *International journal for numerical methods in engineering*, vol. 75, no. 7, pp. 856–880, 2008, doi: 10.1002/nme.2318.
[161] P. Moireau *et al.*, “External tissue support and fluid-structure simulation in blood flows,” *Biomechanics and Modeling in Mechanobiology*, vol. 11, no. 1–2, pp. 1–18, 2012, doi: 10.1007/s10237-011-0289-z.
[162] P. Moireau *et al.*, “Sequential identification of boundary support parameters in a fluid-structure vascular model using patient image data,” *Biomechanics and modeling in mechanobiology*, vol. 12, no. 3, pp. 475–496, 2013, doi: 10.1007/s10237-012-0418-3.
[163] P. Moireau *et al.*, “External tissue support and fluid-structure simulation in blood flows,” *Biomechanics and Modeling in Mechanobiology*, vol. 11, no. 1–2, pp. 1–18, 2012, doi: 10.1007/s10237-011-0289-z.
[164] F. Cuomo, J. Ferruzzi, J. D. Humphrey, and C. A. Figueroa, “An Experimental–Computational Study of Catheter Induced Alterations in Pulse Wave Velocity in Anesthetized Mice,” *Annals of Biomedical Engineering*, vol. 43, no. 7, pp. 1555–1570, 2015, doi: 10.1007/s10439-015-1272-0.
[165] Y. Huo, X. Guo, and G. S. Kassab, “The Flow Field along the Entire Length of Mouse Aorta and Primary Branches,” *Annals of biomedical engineering*, vol. 36, no. 5, pp. 685–699, 2008, doi: 10.1007/s10439-008-9473-4.
[166] J. Lantz and M. Karlsson, “Large eddy simulation of LDL surface concentration in a subject specific human aorta,” *Journal of biomechanics*, vol. 45, no. 3, pp. 537–542, 2011, doi: 10.1016/j.jbiomech.2011.11.039.
[167] M. S. Bazzi, J. M. Valdez, V. H. Barocas, and D. K. Wood, “An Experimental-Computational Approach to Quantify Blood Rheology in Sickle Cell Disease,” *Biophysical journal*, vol. 119, no. 11, pp. 2307–2315, doi: 10.1016/j.bpj.2020.10.011.
[168] U. Windberger, A. Bartholovitsch, R. Plasenzetti, K. J. Korak, and G. Heinze, “Whole blood viscosity, plasma viscosity and erythrocyte aggregation in nine mammalian species: Reference values and comparison of data,” *Experimental Physiology*, vol. 88, no. 3, pp. 431–440, 2003, doi: 10.1113/eph8802496.
[169] K. Bäumler *et al.*, “Fluid–structure interaction simulations of patient-specific aortic dissection,” *Biomechanics and Modeling in Mechanobiology*, vol. 19, no. 5, pp. 1607–1628, 2020, doi: 10.1007/s10237-020-01294-8.
[170] A. Zhu, C.; Vedula, V.; Parker, D.; Wilson, N.; Shadden, S.; Marsden, “A multiphysics integrated cardiac modeling,” vol. in prepara.
[171] C. Vedula, V.; Kaiser, A.; Wilson, N.; Parker, D.; Zhu, “SimVascular / svFSI GitHub.”
[172] H. Lan, A. Updegrove, N. M. Wilson, G. D. Maher, S. C. Shadden, and A. L. Marsden, “A Re-Engineered Software Interface and Workflow for the Open-Source SimVascular Cardiovascular Modeling Package,” *Journal of Biomechanical Engineering*, vol. 140, no. 2, pp. 1–11, 2018, doi: 10.1115/1.4038751.

[173] B. Y. J. Tobin, “Estimation of Relationships for Limited Dependent Variables Author (s): James Tobin Published by : The Econometric Society Stable URL : http://www.jstor.org/stable/1907382 . OF RELATIONSHIPS FOR LIMITED DEPENDENT VARIABLES ’,” *Econometrica*, vol. 26, no. 1, pp. 24–36, 1985.
[174] R. D. McKelvey and W. Zavoina, “A statistical model for the analysis of ordinal level dependent variables,” *The Journal of Mathematical Sociology*, vol. 4, no. 1, pp. 103–120, Jan. 1975, doi: 10.1080/0022250X.1975.9989847.
[175] A. Acuna *et al.*, “Computational Fluid Dynamics of Vascular Disease in Animal Models,” vol. 140, no. August, pp. 1–14, 2018, doi: 10.1115/1.4039678.
[176] M. V. Doormaal, X. Zhang, and D. A. Steinman, “Inputs for Subject-Specific Computational Fluid Dynamics Simulation of Blood Flow in the Mouse Aorta,” vol. 136, no. October, pp. 1–8, 2014, doi: 10.1115/1.4028104.
[177] F. Condemi, S. Campisi, M. Viallon, and P. Croisille, “Aortic Aneurysms Hemodynamics and Biomechanical Properties,” vol. 67, no. 4, pp. 949–956, 2020, doi: 10.1109/TBME.2019.2924955.
[178] B. R. A. M. T. Rachet *et al.*, “An Integrated Framework to Quantitatively Link Mouse-Specific Hemodynamics to Aneurysm Formation in Angiotensin II-infused ApoE 2 / 2 mice,” vol. 39, no. 9, pp. 2430–2444, 2011, doi: 10.1007/s10439-011-0330-5.
[179] F. Condemi *et al.*, “Fluid- and Biomechanical Analysis of Ascending Thoracic Aorta Aneurysm with Concomitant Aortic Insufficiency,” *Annals of biomedical engineering*, vol. 45, no. 12, pp. 2921–2932, 2017, doi: 10.1007/s10439-017-1913-6.
[180] S. Pasta *et al.*, “Shear Stress and Aortic Strain Associations With Biomarkers of Ascending Thoracic Aortic Aneurysm,” *The Annals of Thoracic Surgery*, vol. 110, no. 5, pp. 1595–1604, 2021, doi: 10.1016/j.athoracsur.2020.03.017.
[181] P. F. Davies, “Flow-mediated endothelial mechanotransduction,” *Physiological Reviews*, vol. 75, no. 3, pp. 519–560, 1995, doi: 10.1152/physrev.1995.75.3.519.
[182] M. J. Levesque and R. M. Nerem, “The Elongation and Orientation of Cultured Endothelial Cells in Response to Shear Stress,” *Journal of biomechanical engineering*, vol. 107, no. 4, pp. 341–347, 1985, doi: 10.1115/1.3138567.
[183] N. Sakamoto, N. Saito, X. Han, T. Ohashi, and M. Sato, “Effect of spatial gradient in fluid shear stress on morphological changes in endothelial cells in response to flow,” *Biochemical and biophysical research communications*, vol. 395, no. 2, pp. 264–269, 2010, doi: 10.1016/j.bbrc.2010.04.002.
[184] C. Wang, B. M. Baker, C. S. Chen, and M. A. Schwartz, “Endothelial Cell Sensing of Flow Direction,” *Arteriosclerosis, thrombosis, and vascular biology*, vol. 33, no. 9, pp. 2130–2136, 2013, doi: 10.1161/ATVBAHA.113.301826.
[185] G. De Nisco *et al.*, “Deciphering ascending thoracic aortic aneurysm hemodynamics in relation to biomechanical properties,” *Medical engineering & physics*, vol. 82, pp. 119–129, 2020, doi: 10.1016/j.medengphy.2020.07.003.

[186] F. Condemi, S. Campisi, M. Viallon, P. Croisille, J.-F. Fuzelier, and S. Avril, “Ascending thoracic aorta aneurysm repair induces positive hemodynamic outcomes in a patient with unchanged bicuspid aortic valve,” *Journal of biomechanics*, vol. 81, pp. 145–148, 2018, doi: 10.1016/j.jbiomech.2018.09.022.
[187] J. Bürk *et al.*, “Evaluation of 3D blood flow patterns and wall shear stress in the normal and dilated thoracic aorta using flow-sensitive 4D CMR,” *Journal of cardiovascular magnetic resonance*, vol. 14, no. 1, pp. 84–84, 2012, doi: 10.1186/1532-429X-14-84.
[188] J.-B. Michel, G. Jondeau, and D. M. Milewicz, “From genetics to response to injury: vascular smooth muscle cells in aneurysms and dissections of the ascending aorta,” *Cardiovascular research*, vol. 114, no. 4, pp. 578–589, 2018, doi: 10.1093/cvr/cvy006.
[189] R. O. J. H. Erfkens, R. O. L. D. Alman, and C. H. A. T. Aylor, “Quantification of Hemodynamics in Abdominal Aortic Aneurysms During Rest and Exercise Using Magnetic Resonance Imaging and Computational Fluid Dynamics,” vol. 38, no. 4, pp. 1288–1313, 2010, doi: 10.1007/s10439-010-9949-x.
[190] L. J. Kelsey, J. T. Powell, P. E. Norman, K. Miller, and B. J. Doyle, “A comparison of hemodynamic metrics and intraluminal thrombus burden in a common iliac artery aneurysm,” no. June, pp. 1–14, 2016, doi: 10.1002/cnm.2821.
[191] A. Arzani, G.-Y. Suh, R. L. Dalman, and S. C. Shadden, “A longitudinal comparison of hemodynamics and intraluminal thrombus deposition in abdominal aortic aneurysms.,” *American journal of physiology. Heart and circulatory physiology*, vol. 307, no. 12, pp. H1786-95, Dec. 2014, doi: 10.1152/ajpheart.00461.2014.
[192] M. J. O’Rourke, J. P. McCullough, and S. Kelly, “An investigation of the relationship between hemodynamics and thrombus deposition within patient-specific models of abdominal aortic aneurysm,” *Proceedings of the Institution of Mechanical Engineers, Part H: Journal of Engineering in Medicine*, vol. 226, no. 7, pp. 548–564, May 2012, doi: 10.1177/0954411912444080.
[193] J. Singh *et al.*, “Patient-specific flow descriptors and normalised wall index in peripheral artery disease: a preliminary study,” *Computer Methods in Biomechanics and Biomedical Engineering: Imaging & Visualization*, vol. 6, no. 2, pp. 119–127, Mar. 2018, doi: 10.1080/21681163.2016.1184589.
[194] E. Saliba and Y. Sia, “The ascending aortic aneurysm: When to intervene?,” *IJC Heart and Vasculature*, vol. 6, pp. 91–100, 2015, doi: 10.1016/j.ijcha.2015.01.009.
[195] D. Weiss *et al.*, “Mechanics-driven mechanobiological mechanisms of arterial tortuosity,” *Science Advances*, vol. 6, no. 49, 2020, doi: 10.1126/sciadv.abd3574.
[196] L. I. Id and J. D. H. Id, “Cell signaling model for arterial mechanobiology,” pp. 1–22, 2020, doi: 10.1371/journal.pcbi.1008161.

[197] B. Trachet, J. Bols, G. De Santis, S. Vandenberghe, B. Loeys, and P. Segers, “The impact of simplified boundary conditions and aortic arch inclusion on CFD simulations in the mouse aorta: A comparison with mouse-specific reference Data,” *Journal of Biomechanical Engineering*, vol. 133, no. 12, pp. 1–13, 2011, doi: 10.1115/1.4005479.

[198] M. A. Van Doormaal *et al.*, “Haemodynamics in the mouse aortic arch computed from MRI-derived velocities at the aortic root,” *Journal of the Royal Society Interface*, vol. 9, no. 76, pp. 2834–2844, 2012, doi: 10.1098/rsif.2012.0295.

[199] U. Morbiducci, R. Ponzini, D. Gallo, C. Bignardi, and G. Rizzo, “Inflow boundary conditions for image-based computational hemodynamics: Impact of idealized versus measured velocity profiles in the human aorta,” *Journal of Biomechanics*, vol. 46, no. 1, pp. 102–109, 2013, doi: 10.1016/j.jbiomech.2012.10.012.

[200] S. Madhavan and E. M. C. Kemmerling, “The effect of inlet and outlet boundary conditions in image-based CFD modeling of aortic flow,” *BioMedical Engineering Online*, vol. 17, no. 1, pp. 1–20, 2018, doi: 10.1186/s12938-018-0497-1.

[201] N. Choudhury *et al.*, “Local mechanical and structural properties of healthy and diseased human ascending aorta tissue,” *Cardiovascular Pathology*, vol. 18, no. 2, pp. 83–91, Mar. 2009, doi: 10.1016/J.CARPATH.2008.01.001.

[202] Hao Li *et al.*, “Technical Aspects of in vivo Small Animal CMR Imaging,” *Frontiers in physics*, vol. 8, 2020, doi: 10.3389/fphy.2020.00183.

[203] J. Concannon and J. P. Mcgarry, “Development of an FEA framework for analysis of subject-specific aortic compliance based on 4D flow MRI,” *Acta Biomaterialia*, no. xxxx, 2021, doi: 10.1016/j.actbio.2021.02.027.

[204] S. J. Mousavi and S. Avril, “Patient-specific stress analyses in the ascending thoracic aorta using a finite-element implementation of the constrained mixture theory,” *Biomechanics and Modeling in Mechanobiology*, vol. 16, no. 5, pp. 1765–1777, 2017, doi: 10.1007/s10237-017-0918-2.

[205] T. W. Hansen *et al.*, “Prognostic value of aortic pulse wave velocity as index of arterial stiffness in the general population,” *Circulation (New York, N.Y.)*, vol. 113, no. 5, pp. 664–670, 2006, doi: 10.1161/CIRCULATIONAHA.105.579342.

[206] L. Liang, M. Liu, C. Martin, J. A. Elefteriades, and W. Sun, “A machine learning approach to investigate the relationship between shape features and numerically predicted risk of ascending aortic aneurysm,” *Biomechanics and Modeling in Mechanobiology*, vol. 16, no. 5, pp. 1519–1533, 2017, doi: 10.1007/s10237-017-0903-9.

[207] E. Vignali, E. Gasparotti, S. Celi, and S. Avril, “Fully-Coupled FSI Computational Analyses in the Ascending Thoracic Aorta Using Patient-Specific Conditions and Anisotropic Material Properties,” *Frontiers in Physiology*, vol. 12, no. October, pp. 1–14, 2021, doi: 10.3389/fphys.2021.732561.

[208] T. W. Raaymakers, G. J. Rinkel, M. Limburg, and A. Algra, “Mortality and morbidity of surgery for unruptured intracranial aneurysms: a meta-analysis.,” *Stroke*, vol. 29, no. 8, pp. 1531–1538, Aug. 1998, doi: 10.1161/01.str.29.8.1531.

[209] S. Urbonavicius, G. Urbonaviciene, B. Honoré, E. W. Henneberg, H. Vorum, and J. S. Lindholt, “Potential Circulating Biomarkers for Abdominal Aortic Aneurysm Expansion and Rupture - a Systematic Review,” *European Journal of Vascular and Endovascular Surgery*, vol. 36, no. 3, pp. 273–280, Sep. 2008, doi: 10.1016/j.ejvs.2008.05.009.

[210] S. Pappu, A. Dardik, H. Tagare, and R. J. Gusberg, “Beyond Fusiform and Saccular: A Novel Quantitative Tortuosity Index May Help Classify Aneurysm Shape and Predict Aneurysm Rupture Potential,” *Annals of Vascular Surgery*, vol. 22, no. 1, pp. 88–97, Jan. 2008, doi: 10.1016/j.avsg.2007.09.004.

[211] F. Signorelli *et al.*, “Hemodynamic Stress, Inflammation, and Intracranial Aneurysm Development and Rupture: A Systematic Review,” *World Neurosurgery*, vol. 115, pp. 234–244, Jul. 2018, doi: 10.1016/j.wneu.2018.04.143.

[212] J. E. Wagenseil, N. L. Nerurkar, R. H. Knutsen, R. J. Okamoto, D. Y. Li, and R. P. Mecham, “Effects of elastin haploinsufficiency on the mechanical behavior of mouse arteries,” *American journal of physiology. Heart and circulatory physiology*, vol. 289, no. 3, p. H1209, doi: 10.1152/ajpheart.00046.2005.

[213] A. Updegrove, N. M. Wilson, J. Merkow, H. Lan, A. L. Marsden, and S. C. Shadden, “SimVascular: An Open Source Pipeline for Cardiovascular Simulation,” *Annals of biomedical engineering*, vol. 45, no. 3, pp. 525–541, 2017, doi: 10.1007/s10439-016-1762-8.

[214] H. P. Gavin, “The Levenburg-Marqurdt Algorithm For Nonlinear Least Squares Curve-Fitting Problems,” *Duke University*, pp. 1–19, 2019.

[215] F. Cuomo, S. Roccabianca, D. Dillon-Murphy, N. Xiao, J. D. Humphrey, and C. A. Figueroa, “Effects of age-associated regional changes in aortic stiffness on human hemodynamics revealed by computational modeling.,” *PLoS ONE*, vol. 12, no. 3, p. e0173177, doi: 10.1371/journal.pone.0173177.

[216] J. D. Humphrey, “Constrained Mixture Models of Soft Tissue Growth and Remodeling - Twenty Years After,” *J Elast*, vol. 145, no. 1–2, pp. 49–75, Aug. 2021, doi: 10.1007/s10659-020-09809-1.

[217] S. A. Maas, A. Erdemir, J. P. Halloran, and J. A. Weiss, “A general framework for application of prestrain to computational models of biological materials,” *Journal of the Mechanical Behavior of Biomedical Materials*, vol. 61, pp. 499–510, 2016, doi: https://doi.org/10.1016/j.jmbbm.2016.04.012.

[218] C. E. Korenczuk, R. Y. Dhume, K. K. Liao, and V. H. Barocas, “Ex Vivo Mechanical Tests and Multiscale Computational Modeling Highlight the Importance of Intramural Shear Stress in Ascending Thoracic Aortic Aneurysms,” *Journal of Biomechanical Engineering*, vol. 141, no. 12, p. 121010, Dec. 2019, doi: 10.1115/1.4045270.

[219] E. Hadler-Olsen, B. Fadnes, I. Sylte, L. Uhlin-Hansen, and J.-O. Winberg, “Regulation of matrix metalloproteinase activity in health and disease,” *FEBS J*, vol. 278, no. 1, pp. 28–45, Jan. 2011, doi: 10.1111/j.1742-4658.2010.07920.x.
[220] C. Bellini *et al.*, “Comparison of 10 murine models reveals a distinct biomechanical phenotype in thoracic aortic aneurysms,” pp. 1–8, 2017.
[221] S. Farzaneh, O. Trabelsi, B. Chavent, and S. Avril, “Identifying Local Arterial Stiffness to Assess the Risk of Rupture of Ascending Thoracic Aortic Aneurysms,” *Annals of Biomedical Engineering*, vol. 47, no. 4, pp. 1038–1050, 2019, doi: 10.1007/s10439-019-02204-5.
[222] W. Ji *et al.*, “Risk Score for Neurological Complications After Endovascular Treatment of Unruptured Intracranial Aneurysms.,” *Stroke*, vol. 47, no. 4, pp. 971–978, Apr. 2016, doi: 10.1161/STROKEAHA.115.012097.
[223] S. Baek, K. R. Rajagopal, and J. D. Humphrey, “Competition between radial expansion and thickening in the enlargement of an intracranial saccular aneurysm,” *Journal of Elasticity*, vol. 80, no. 1–3, pp. 13–31, 2005, doi: 10.1007/s10659-005-9004-6.
[224] M. F. Hadi, E. A. Sander, J. W. Ruberti, and V. H. Barocas, “Simulated remodeling of loaded collagen networks via strain-dependent enzymatic degradation and constant-rate fiber growth,” *Mechanics of materials : an international journal*, vol. 44, pp. 72–82, Jan. 2012, doi: 10.1016/j.mechmat.2011.07.003.
[225] V. H. B. Maryam Nikpasand, Ryan R. Mahutga, Lauren M. Bersie-Larson, Elizabeth Gacek, “A Hybrid Microstructural-Continuum Multiscale Approach for Modeling Hyperelastic Fibrous Soft Tissue,” *J Elast*, pp. 295–319, 2021, doi: 10.1007/s10659-021-09843-7.
[226] E. Gacek, R. R. Mahutga, and V. H. Barocas, “Hybrid discrete-continuum multiscale model of tissue growth and remodeling,” *Acta Biomaterialia*, vol. 163, pp. 7–24, Jun. 2023, doi: 10.1016/j.actbio.2022.09.040.
[227] R. H. Walker, “Special report: Transfusion risks,” *American Journal of Clinical Pathology*, vol. 88, no. 3, pp. 374–378, 1987, doi: 10.1093/ajcp/88.3.374.
[228] F. A. Braeu, R. C. Aydin, and C. J. Cyron, “Anisotropic stiffness and tensional homeostasis induce a natural anisotropy of volumetric growth and remodeling in soft biological tissues,” *Biomech Model Mechanobiol*, vol. 18, no. 2, pp. 327–345, Apr. 2019, doi: 10.1007/s10237-018-1084-x.
[229] P. L. Chandran, T. Stylianopoulos, and V. H. Barocas, “Microstructure-Based, Multiscale Modeling for the Mechanical Behavior of Hydrated Fiber Networks,” *Multiscale Model. Simul.*, vol. 7, no. 1, pp. 22–43, Jan. 2008, doi: 10.1137/070689504.
[230] C. E. Korenczuk, R. Y. Dhume, K. Liao, and V. H. Barocas, “Ex Vivo Mechanical Tests and Multiscale Computational Modeling Highlight the Importance of Intramural Shear Stress in Ascending Thoracic Aortic Aneurysms,” *Journal of biomechanical engineering*, doi: 10.1115/1.4045270.

[231] R. Dhume, E. Shih, and V. Barocas, “Multiscale model of fatigue of collagen gels,” *Biomechanics and Modeling in Mechanobiology*, vol. 18, no. 1, pp. 175–187, doi: 10.1007/s10237-018-1075-y.
[232] M. F. Hadi, E. A. Sander, and V. H. Barocas, “Multiscale Model Predicts Tissue-Level Failure From Collagen Fiber-Level Damage,” *Journal of Biomechanical Engineering*, vol. 134, no. 091005, Aug. 2012, doi: 10.1115/1.4007097.
[233] C. E. Korenczuk, R. Y. Dhume, K. K. Liao, and V. H. Barocas, “Ex vivo mechanical tests and multiscale computational modeling highlight the importance of intramural shear stress in ascending thoracic aortic aneurysms,” *Journal of biomechanical engineering*, vol. 141, no. 12, p. 121010, 2019.
[234] R. R. Mahutga, V. H. Barocas, and P. W. Alford, “The non-affine fiber network solver: A multiscale fiber network material model for finite-element analysis,” *Journal of the Mechanical Behavior of Biomedical Materials*, p. 105967, 2023.
[235] J. Li, A. Najmi, and R. M. Gray, “Image Classi cation by a Two Dimensional Hidden Markov Model”.
[236] C. Rother, V. Kolmogorov, and A. Blake, “‘GrabCut’ — Interactive Foreground Extraction using Iterated Graph Cuts”.
[237] Y. Boykov and V. Kolmogorov, “An experimental comparison of min-cut/max- flow algorithms for energy minimization in vision,” *IEEE Trans. Pattern Anal. Machine Intell.*, vol. 26, no. 9, pp. 1124–1137, Sep. 2004, doi: 10.1109/TPAMI.2004.60.
[238] B. R. Clower, D. M. Sullivan, and R. R. Smith, “Intracranial vessels lack vasa vasorum,” *Journal of Neurosurgery*, vol. 61, no. 1, pp. 44–48, Jul. 1984, doi: 10.3171/jns.1984.61.1.0044.
[239] H. Ikeda and H. Kakeya, “Targeting hypoxia-inducible factor 1 (HIF-1) signaling with natural products toward cancer chemotherapy,” *J Antibiot (Tokyo)*, vol. 74, no. 10, pp. 687–695, Oct. 2021, doi: 10.1038/s41429-021-00451-0.
[240] H. Miyata *et al.*, “Vasa vasorum formation is associated with rupture of intracranial aneurysms,” *Journal of Neurosurgery*, vol. 133, no. 3, pp. 789–799, Aug. 2019, doi: 10.3171/2019.5.JNS19405.
[241] M. Kushamae *et al.*, “Involvement of neutrophils in machineries underlying the rupture of intracranial aneurysms in rats,” *Sci Rep*, vol. 10, no. 1, Art. no. 1, Nov. 2020, doi: 10.1038/s41598-020-74594-9.
[242] D. Mallon, D. Doig, L. Dixon, A. Gontsarova, W. Jan, and F. Tona, “Neuroimaging in Sickle Cell Disease: A Review,” *Journal of Neuroimaging*, vol. 30, no. 6, pp. 725–735, 2020, doi: 10.1111/jon.12766.
[243] G. Frija *et al.*, “How to improve access to medical imaging in low- and middle-income countries ?,” *eClinicalMedicine*, vol. 38, Aug. 2021, doi: 10.1016/j.eclinm.2021.101034.
[244] J. Blacher, R. Asmar, S. Djane, G. M. London, and M. E. Safar, “Aortic Pulse Wave Velocity as a Marker of Cardiovascular Risk in Hypertensive Patients,”

Hypertension, vol. 33, no. 5, pp. 1111–1117, May 1999, doi: 10.1161/01.HYP.33.5.1111.
[245] N. M. Pahlevan *et al.*, “Intrinsic frequency for a systems approach to haemodynamic waveform analysis with clinical applications,” *J. R. Soc. Interface.*, vol. 11, no. 98, p. 20140617, Sep. 2014, doi: 10.1098/rsif.2014.0617.
[246] L. S. Mehta *et al.*, “Cardiovascular Considerations in Caring for Pregnant Patients: A Scientific Statement From the American Heart Association,” *Circulation*, vol. 141, no. 23, pp. e884–e903, Jun. 2020, doi: 10.1161/CIR.0000000000000772.
[247] K. P. Ramlakhan, M. R. Johnson, and J. W. Roos-Hesselink, “Pregnancy and cardiovascular disease,” *Nat Rev Cardiol*, vol. 17, no. 11, Art. no. 11, Nov. 2020, doi: 10.1038/s41569-020-0390-z.
[248] K. Ryczkowska, W. Adach, K. Janikowski, M. Banach, and A. Bielecka-Dabrowa, “Menopause and women’s cardiovascular health: is it really an obvious relationship?,” *Arch Med Sci*, vol. 19, no. 2, pp. 458–466, Dec. 2022, doi: 10.5114/aoms/157308.
[249] M. Sanghavi and J. D. Rutherford, “Cardiovascular Physiology of Pregnancy,” *Circulation*, vol. 130, no. 12, pp. 1003–1008, Sep. 2014, doi: 10.1161/CIRCULATIONAHA.114.009029.
[250] A. O. Mocumbi, K. Sliwa, and -Pillay P. Soma, “Medical disease as a cause of maternal mortality : the pre-imminence of cardiovascular pathology : review articles,” *Cardiovascular Journal of Africa*, vol. 27, no. 2, pp. 84–88, Mar. 2016, doi: 10.5830/CVJA-2016-018.
[251] “Interstitial Flow and Its Effects in Soft Tissues | Annual Review of Biomedical Engineering.” Accessed: Dec. 18, 2023. [Online]. Available: https://www.annualreviews.org/doi/abs/10.1146/annurev.bioeng.9.060906.151850
[252] J. R. Levick, “Flow through interstitium and other fibrous matrices,” *Q J Exp Physiol*, vol. 72, no. 4, pp. 409–437, Oct. 1987, doi: 10.1113/expphysiol.1987.sp003085.
[253] F. J. O’Brien, B. A. Harley, M. A. Waller, I. V. Yannas, L. J. Gibson, and P. J. Prendergast, “The effect of pore size on permeability and cell attachment in collagen scaffolds for tissue engineering,” *Technology and Health Care*, vol. 15, no. 1, pp. 3–17, Jan. 2007, doi: 10.3233/THC-2007-15102.
[254] J. M. Rutkowski, K. C. Boardman, and M. A. Swartz, “Characterization of lymphangiogenesis in a model of adult skin regeneration,” *American Journal of Physiology-Heart and Circulatory Physiology*, vol. 291, no. 3, pp. H1402–H1410, Sep. 2006, doi: 10.1152/ajpheart.00038.2006.
[255] S. Wang and J. M. Tarbell, “Effect of fluid flow on smooth muscle cells in a 3-dimensional collagen gel model,” *Arterioscler Thromb Vasc Biol*, vol. 20, no. 10, pp. 2220–2225, Oct. 2000, doi: 10.1161/01.atv.20.10.2220.

[256] Z. Ruszczak and W. Friess, “Collagen as a carrier for on-site delivery of antibacterial drugs,” *Adv Drug Deliv Rev*, vol. 55, no. 12, pp. 1679–1698, Nov. 2003, doi: 10.1016/j.addr.2003.08.007.
[257] M. Maeda, S. Tani, A. Sano, and K. Fujioka, “Microstructure and release characteristics of the minipellet, a collagen-based drug delivery system for controlled release of protein drugs,” *J Control Release*, vol. 62, no. 3, pp. 313–324, Dec. 1999, doi: 10.1016/s0168-3659(99)00156-x.
[258] “Elastic Moduli of Collagen Gels Can Be Predicted from Two-Dimensional Confocal Microscopy - ScienceDirect.” Accessed: Dec. 18, 2023. [Online]. Available: https://www-sciencedirect-com.ezp3.lib.umn.edu/science/article/pii/S0006349509012995
[259] “Rheology of reconstituted type I collagen gel in confined compression | Journal of Rheology | AIP Publishing.” Accessed: Dec. 18, 2023. [Online]. Available: https://pubs.aip.org/sor/jor/article/41/5/971/239215/Rheology-of-reconstituted-type-I-collagen-gel-in
[260] “Diffusion and Convection in Collagen Gels: Implications for Transport in the Tumor Interstitium - ScienceDirect.” Accessed: Dec. 18, 2023. [Online]. Available: https://www-sciencedirect-com.ezp3.lib.umn.edu/science/article/pii/S0006349502739337
[261] E. A. A. Neel, U. Cheema, J. C. Knowles, R. A. Brown, and S. N. Nazhat, “Use of multiple unconfined compression for control of collagen gel scaffold density and mechanical properties,” *Soft Matter*, vol. 2, no. 11, pp. 986–992, Oct. 2006, doi: 10.1039/B609784G.
[262] P. L. Chandran and V. H. Barocas, “Microstructural Mechanics of Collagen Gels in Confined Compression: Poroelasticity, Viscoelasticity, and Collapse,” *Journal of Biomechanical Engineering*, vol. 126, no. 2, pp. 152–166, May 2004, doi: 10.1115/1.1688774.
[263] V. Serpooshan, T. M. Quinn, N. Muja, and S. N. Nazhat, “Hydraulic permeability of multilayered collagen gel scaffolds under plastic compression-induced unidirectional fluid flow,” *Acta Biomater*, vol. 9, no. 1, pp. 4673–4680, Jan. 2013, doi: 10.1016/j.actbio.2012.08.031.
[264] J. A. Weiss, B. N. Maker, and S. Govindjee, “Finite element implementation of incompressible, transversely isotropic hyperelasticity,” *Computer Methods in Applied Mechanics and Engineering*, vol. 135, no. 1, pp. 107–128, Aug. 1996, doi: 10.1016/0045-7825(96)01035-3.
[265] R. K. Korhonen, M. S. Laasanen, J. Töyräs, R. Lappalainen, H. J. Helminen, and J. S. Jurvelin, “Fibril reinforced poroelastic model predicts specifically mechanical behavior of normal, proteoglycan depleted and collagen degraded articular cartilage,” *Journal of Biomechanics*, vol. 36, no. 9, pp. 1373–1379, Sep. 2003, doi: 10.1016/S0021-9290(03)00069-1.
[266] T. Eguchi, Y. Tomita, K. Yamamoto, Y. Morita, and E. Nakamachi, “Visco-Anisotropic Hyperelastic Finite Element Analysis of Knee Joint Considering Deformation Induced Anisotropy Evolution of Meniscus,” presented at the ASME 2017 International Mechanical Engineering Congress and Exposition,

American Society of Mechanical Engineers Digital Collection, Jan. 2018. doi: 10.1115/IMECE2017-71224.
[267] W. Lin, Q. Meng, J. Li, Z. Chen, and Z. Jin, “The effect of highly inhomogeneous biphasic properties on mechanical behaviour of articular cartilage,” *Comput Methods Programs Biomed*, vol. 206, p. 106122, Jul. 2021, doi: 10.1016/j.cmpb.2021.106122.
[268] C. J. Stender, E. Rust, P. T. Martin, E. E. Neumann, R. J. Brown, and T. J. Lujan, “Modeling the effect of collagen fibril alignment on ligament mechanical behavior,” *Biomech Model Mechanobiol*, vol. 17, no. 2, pp. 543–557, Apr. 2018, doi: 10.1007/s10237-017-0977-4.
[269] V. H. Barocas and R. T. Tranquillo, “A Finite Element Solution for the Anisotropic Biphasic Theory of Tissue-Equivalent Mechanics: The Effect of Contact Guidance on Isometric Cell Traction Measurement,” *Journal of Biomechanical Engineering*, vol. 119, no. 3, pp. 261–268, Aug. 1997, doi: 10.1115/1.2796090.
[270] P. A. Galie, R. L. Spilker, and J. P. Stegemann, “A Linear, Biphasic Model Incorporating a Brinkman Term to Describe the Mechanics of Cell-Seeded Collagen Hydrogels,” *Ann Biomed Eng*, vol. 39, no. 11, pp. 2767–2779, Nov. 2011, doi: 10.1007/s10439-011-0371-9.
[271] P. A. Wijeratne, J. H. Hipwell, D. J. Hawkes, T. Stylianopoulos, and V. Vavourakis, “Multiscale biphasic modelling of peritumoural collagen microstructure: The effect of tumour growth on permeability and fluid flow,” *PLOS ONE*, vol. 12, no. 9, p. e0184511, Sep. 2017, doi: 10.1371/journal.pone.0184511.
[272] S. McGuire, D. Zaharoff, and F. Yuan, “Nonlinear Dependence of Hydraulic Conductivity on Tissue Deformation During Intratumoral Infusion,” *Ann Biomed Eng*, vol. 34, no. 7, pp. 1173–1181, Jul. 2006, doi: 10.1007/s10439-006-9136-2.
[273] X.-Y. Zhang, J. Luck, M. W. Dewhirst, and F. Yuan, “Interstitial hydraulic conductivity in a fibrosarcoma,” *American Journal of Physiology-Heart and Circulatory Physiology*, vol. 279, no. 6, pp. H2726–H2734, Dec. 2000, doi: 10.1152/ajpheart.2000.279.6.H2726.
[274] M. R. Hill, X. Duan, G. A. Gibson, S. Watkins, and A. M. Robertson, “A theoretical and non-destructive experimental approach for direct inclusion of measured collagen orientation and recruitment into mechanical models of the artery wall,” *J Biomech*, vol. 45, no. 5, pp. 762–771, Mar. 2012, doi: 10.1016/j.jbiomech.2011.11.016.
[275] B. A. Lane, K. A. Harmon, R. L. Goodwin, M. J. Yost, T. Shazly, and J. F. Eberth, “Constitutive modeling of compressible type-I collagen hydrogels,” *Med Eng Phys*, vol. 53, pp. 39–48, Mar. 2018, doi: 10.1016/j.medengphy.2018.01.003.
[276] M. E. Susilo, B. A. Roeder, S. L. Voytik-Harbin, K. Kokini, and E. A. Nauman, “Development of a three-dimensional unit cell to model the micromechanical

response of a collagen-based extracellular matrix," *Acta Biomaterialia*, vol. 6, no. 4, pp. 1471–1486, Apr. 2010, doi: 10.1016/j.actbio.2009.11.014.
[277] C. M. Tierney, M. G. Haugh, J. Liedl, F. Mulcahy, B. Hayes, and F. J. O'Brien, "The effects of collagen concentration and crosslink density on the biological, structural and mechanical properties of collagen-GAG scaffolds for bone tissue engineering," *Journal of the Mechanical Behavior of Biomedical Materials*, vol. 2, no. 2, pp. 202–209, Apr. 2009, doi: 10.1016/j.jmbbm.2008.08.007.
[278] V. Perez-Puyana, A. Romero, and A. Guerrero, "Influence of collagen concentration and glutaraldehyde on collagen-based scaffold properties," *Journal of Biomedical Materials Research Part A*, vol. 104, no. 6, pp. 1462–1468, 2016, doi: 10.1002/jbm.a.35671.
[279] C. B. Raub, A. J. Putnam, B. J. Tromberg, and S. C. George, "Predicting bulk mechanical properties of cellularized collagen gels using multiphoton microscopy," *Acta Biomater*, vol. 6, no. 12, pp. 4657–4665, Dec. 2010, doi: 10.1016/j.actbio.2010.07.004.
[280] B. A. Roeder, K. Kokini, J. E. Sturgis, J. P. Robinson, and S. L. Voytik-Harbin, "Tensile mechanical properties of three-dimensional type I collagen extracellular matrices with varied microstructure," *J Biomech Eng*, vol. 124, no. 2, pp. 214–222, Apr. 2002, doi: 10.1115/1.1449904.
[281] S. Ramanujan, A. Pluen, T. D. McKee, E. B. Brown, Y. Boucher, and R. K. Jain, "Diffusion and Convection in Collagen Gels: Implications for Transport in the Tumor Interstitium," *Biophysical Journal*, vol. 83, no. 3, pp. 1650–1660, Sep. 2002, doi: 10.1016/S0006-3495(02)73933-7.
[282] M. C. Varley, S. Neelakantan, T. W. Clyne, J. Dean, R. A. Brooks, and A. E. Markaki, "Cell structure, stiffness and permeability of freeze-dried collagen scaffolds in dry and hydrated states," *Acta Biomater*, vol. 33, pp. 166–175, Mar. 2016, doi: 10.1016/j.actbio.2016.01.041.
[283] V. K. Lai, C. R. Frey, A. M. Kerandi, S. P. Lake, R. T. Tranquillo, and V. H. Barocas, "Microstructural and mechanical differences between digested collagen-fibrin co-gels and pure collagen and fibrin gels," *Acta Biomater*, vol. 8, no. 11, pp. 4031–4042, Nov. 2012, doi: 10.1016/j.actbio.2012.07.010.
[284] C. H. Nair, G. A. Shah, and D. P. Dhall, "Effect of temperature, ph and ionic strength and composition on fibrin network structure and its development," *Thrombosis Research*, vol. 42, no. 6, pp. 809–816, Jun. 1986, doi: 10.1016/0049-3848(86)90117-9.
[285] A. S. G. van Oosten *et al.*, "Uncoupling shear and uniaxial elastic moduli of semiflexible biopolymer networks: compression-softening and stretch-stiffening," *Sci Rep*, vol. 6, no. 1, Art. no. 1, Jan. 2016, doi: 10.1038/srep19270.
[286] B. N. Mason, A. Starchenko, R. M. Williams, L. J. Bonassar, and C. A. Reinhart-King, "Tuning three-dimensional collagen matrix stiffness independently of collagen concentration modulates endothelial cell behavior," *Acta Biomater*, vol. 9, no. 1, pp. 4635–4644, Jan. 2013, doi: 10.1016/j.actbio.2012.08.007.

[287] D. M. Knapp, V. H. Barocas, A. G. Moon, K. Yoo, L. R. Petzold, and R. T. Tranquillo, “Rheology of reconstituted type I collagen gel in confined compression,” *Journal of Rheology*, vol. 41, no. 5, pp. 971–993, Sep. 1997, doi: 10.1122/1.550817.

[288] Y. K. Zhu *et al.*, “Contraction of fibroblast-containing collagen gels: Initial collagen concentration regulates the degree of contraction and cell survival,” *In Vitro Cell.Dev.Biol.-Animal*, vol. 37, no. 1, pp. 10–16, Jan. 2001, doi: 10.1290/1071-2690(2001)037<0010:COFCCG>2.0.CO;2.

[289] R. Montesano and L. Orci, “Transforming growth factor beta stimulates collagen-matrix contraction by fibroblasts: implications for wound healing.,” *Proceedings of the National Academy of Sciences*, vol. 85, no. 13, pp. 4894–4897, Jul. 1988, doi: 10.1073/pnas.85.13.4894.

[290] D. Gullberg *et al.*, “β1 Integrin-mediated collagen gel contraction is stimulated by PDGF,” *Experimental Cell Research*, vol. 186, no. 2, pp. 264–272, Feb. 1990, doi: 10.1016/0014-4827(90)90305-T.

[291] U. Zagai, C. M. Sköld, A. Trulson, P. Venge, and J. Lundahl, “The effect of eosinophils on collagen gel contraction and implications for tissue remodelling,” *Clin Exp Immunol*, vol. 135, no. 3, pp. 427–433, Mar. 2004, doi: 10.1111/j.1365-2249.2004.02396.x.

[292] Z. Feng, M. Yamato, T. Akutsu, T. Nakamura, T. Okano, and M. Umezu, “Investigation on the Mechanical Properties of Contracted Collagen Gels as a Scaffold for Tissue Engineering,” *Artificial Organs*, vol. 27, no. 1, pp. 84–91, 2003, doi: 10.1046/j.1525-1594.2003.07187.x.

[293] C. A. Figueroa, I. E. Vignon-Clementel, K. E. Jansen, T. J. R. Hughes, and C. A. Taylor, “A coupled momentum method for modeling blood flow in three-dimensional deformable arteries,” *Computer Methods in Applied Mechanics and Engineering*, vol. 195, no. 41–43, pp. 5685–5706, 2006, doi: 10.1016/j.cma.2005.11.011.

[294] E. O. Kung *et al.*, “In vitro validation of finite element analysis of blood flow in deformable models,” *Ann Biomed Eng*, vol. 39, no. 7, pp. 1947–1960, Jul. 2011, doi: 10.1007/s10439-011-0284-7.

[295] M. Bonfanti, G. Franzetti, S. Homer-Vanniasinkam, V. Díaz-Zuccarini, and S. Balabani, “A Combined In Vivo, In Vitro, In Silico Approach for Patient-Specific Haemodynamic Studies of Aortic Dissection,” *Ann Biomed Eng*, vol. 48, no. 12, pp. 2950–2964, Dec. 2020, doi: 10.1007/s10439-020-02603-z.

[296] C. Y. Sargent *et al.*, “Hydrodynamic modulation of embryonic stem cell differentiation by rotary orbital suspension culture,” *Biotechnol Bioeng*, vol. 105, no. 3, pp. 611–626, Feb. 2010, doi: 10.1002/bit.22578.

[297] Y. Wang, B.-K. Chou, S. Dowey, C. He, S. Gerecht, and L. Cheng, “Scalable expansion of human induced pluripotent stem cells in the defined xeno-free E8 medium under adherent and suspension culture conditions,” *Stem Cell Res*, vol. 11, no. 3, pp. 1103–1116, Nov. 2013, doi: 10.1016/j.scr.2013.07.011.

[298] M.-Z. Ismadi *et al.*, “Flow Characterization of a Spinner Flask for Induced Pluripotent Stem Cell Culture Application,” *PLOS ONE*, vol. 9, no. 10, p. e106493, Oct. 2014, doi: 10.1371/journal.pone.0106493.
[299] P. Fattahi *et al.*, “Core–shell hydrogel microcapsules enable formation of human pluripotent stem cell spheroids and their cultivation in a stirred bioreactor,” *Sci Rep*, vol. 11, no. 1, Art. no. 1, Mar. 2021, doi: 10.1038/s41598-021-85786-2.

Appendix A: Computational and Experimental Comparison of the Effects of Flow-Induced Compression on the Permeability of Collagen Gels

The work presented is my contribution to the overall paper.

*Vidmar, Christopher **S., Marisa Bazzi,** and Victor K. Lai. "Computational and experimental comparison on the effects of flow-induced compression on the permeability of collagen gels." Journal of the Mechanical Behavior of Biomedical Materials 128 (2022): 105107.*

Summary

Collagen is a naturally occurring polymer and is popular in tissue engineering due to its high biocompatibility, ubiquity throughout the body, and its porous nature. The transport properties of collagen help dictate the delivery of nutrients to tissues, and the mechanical properties can help improve the function of engineered tissues.

The objective of this study is to investigate experimentally the change in permeability as collagen gels undergo flow-induced compression and compare these results with model predictions using a finite element model. We developed a horizontal apparatus to measure the hydraulic permeability of collagen gels

undergoing flow induced compression. The permeability of 1.98 mg/mL, 3.5 mg/mL, and 5 mg/mL collagen Type I rat tail hydrogels were determined experimentally by tracking the pressure drop across the gels as water flowed through the samples, which simultaneously compressed them under pressure. The Holmes-Mow model was used to fit the permeability as the gels underwent compression. A finite element model was created using FeBio to estimate the Young's modulus of collagen gels at the macroscopic level by fitting the experimental pressure vs. the compressive stretch ratio to the model. Our results suggest that the initial permeability of collagen gels decreased with increasing concentration, as expected. However, gels with a lower initial concentration compressed to a greater degree, resulting in smaller final permeabilities once fully compressed. Taken together, our work suggests that the treatment of a collagen gel as an isotropic, elastic material is sufficient to model its transport properties on a macroscopic level but is inadequate if more localized transport properties, which are dependent on network architecture (such as collagen alignment or inhomogeneous densification), are required.

S.1 Introduction

Cells reside in the extra-cellular matrix (ECM), which provides mechanical support, determines mechanical properties, and transfers signals across the cells [251]. The specific composition of the ECM is highly dependent upon tissue type, which determines its resistance to fluid flow. Specifically, fibrous materials in the ECM create high resistance to fluid flow [252]. Collagen is one such fibrous material that

is ubiquitous in the ECM, accounting for more than two-thirds of the protein content found in many soft tissues [251]. Fluid flow through the ECM is called interstitial fluid flow and helps the transport of nutrients and wastes between cells [253], helps lymphatic regeneration [254], and affects the production rates of vascular smooth muscle cells [255]. In-vitro, ECM components such as collagen have been used extensively for drug delivery applications[256], [257]. Understanding the roles and processes of interstitial fluid flow will aid in drug delivery and can be used in the advancement of tissue engineering, where the permeability of these tissue equivalents impacts the transport of nutrients through the tissues. Determining the permeability of collagen gels is one of the first steps necessary towards understanding the biotransport properties of interstitial flow.

Collagen gels are a biphasic material composed of an insoluble network of fibers and an interstitial fluid. Their biomechanical and transport properties are largely dictated by the properties of the collagen fibers and their surrounding interstitial fluid, as well as the interactions between these two components. For example, an increase in initial collagen density has been shown to increase gel modulus and strength under both tensile and compression[258], [259], while decreasing its permeability as a denser collagen network impedes fluid flow through the gel [260]. In addition, many studies have investigated how changes to the interstitial fluid impact the overall structural and biomechanical properties of collagen gels. For instance, a larger weight loss due to the expulsion of interstitial fluid in double compressed collagen gels corresponded to higher modulus and break strength

under unconfined compression compared to single compressed samples, but little difference in break strain[261]. Under confined compression, Chandran and Barocas observed inhomogeneous deformation of the collagen network, with higher fiber alignments and strains observed near the piston [262]. Similarly, Serpooshan et al.[263] showed that the formation of a denser collagen bottom layer for gels under confined compression and that the overall gel permeability decreased over time as more interstitial fluid was expelled under compression.

Computational modeling of collagen gel transport and mechanics have predicted similar dependence on microstructure and composition. These computational models generally consider collagen gels as a hyperelastic material, while incorporating biphasic theory or poroelasticity to capture transport properties [264], [265]. Hyperelastic constitutive models can incorporate the deformation of a material to study mechanical properties [266], [267], e.g., to predict the mechanical behavior of ligaments based on the orientation of collagen fibers [268]. Such models are often combined with the biphasic theory to account for the effects of fluid flow. For example, Barocas and Tranquillo developed a finite element model using the biphasic theory to describe the mechanical interactions between cells and the extracellular matrix [269], and Galie et al. utilized the same theory to model the mechanics of cell-seeded collagen hydrogels [270]. The biphasic theory can also be used with poroelastic models to study the interaction between a fluid and a deformable material. For instance, Wijeratne et al. developed a biphasic,

poroelastic model to study the impact of collagen fiber orientation on localized permeability and fluid flow within a tumor-host environment [271].

While many permeability studies involve fluid flow under an external compressive load, the combined effects of *flow-induced* compression are less investigated. This phenomenon is observed, for example, in intra-tissue drug infusion or gene delivery, where the infusion pressure necessary for convective transport of a therapeutic agent also causes deformation to the surrounding tissue (thus altering its permeability) [272, 273]. In studying intratumoral infusion mice tumor models, McGuire et al. found that collagen concentration had an effect on infusion rate, with model predictions suggesting a dependence of tissue hydraulic conductivity with infusion-induced deformation [272].

In this paper, the effect of flow-induced deformation on the permeability of simple soft tissue equivalents comprised solely of collagen is investigated and compared to model predictions using a finite element model. The hypothesis is that the permeability of collagen gels will decrease under flow-induced compression as the gels densify, and that the mechanical and transport properties of these gels may be modeled adequately using a neo-Hookean biphasic finite element model. Experiments to measure the permeability of collagen gels of different initial concentrations are coupled with finite element modeling using biphasic theory to predict and compare the mechanics of these networks. In addition to a better understanding of the transport of therapeutic agents via intra-tissue infusion, these results may also better inform the culture conditions of bioengineered tissue

equivalents cultured under an external flow, as well as provide *in vivo* properties of biological soft tissues under pressurized flow conditions.

S.2 Methods

S.2.1 Computational Model

A computational model to predict the transport and mechanical properties of flow-induced collagen gels was developed using FeBio, a free finite element software developed for the biomechanics community [28]. Biphasic theory was implemented to account for both the solid matrix and interstitial fluid in a collagen gel using the Holmes-Mow permeability model coupled with the collagen solid modeled as a neo-Hookean material [274–276]. The neo-Hookean material is defined by the strain energy function, *W*:

$$W = \frac{\mu}{2}(I_1 - 3) - \mu \, ln \, ln \, J \, + \frac{\lambda}{2}(ln \, ln \, J \,)^2$$

[78]

where I_1 is the first invariant of the right Cauchy-Green tensor. The Láme parameters from linear elasticity, λ_L and μ_L, are defined as:

$$\mu_L = \frac{E}{2(1+\nu)}$$

$$\lambda_L = \frac{E\nu}{(1+\nu)(1-2\nu)}$$

[79]

where E is Young's modulus and v is Poisson's ratio.

Macroscopically, the collagen gel was modeled as a cylinder, with a radius of 5 mm and height of 9 mm to match the size of the experimental sample. An 8-node hexahedral element library was used since this library has previously been used in finite element analysis models of collagen fibers. A butterfly center mesh was used with 6 slices, 11 segments, 8 stacks, and an r-bias of 1.25. A z-bias of 1.5 was applied to create a finer mesh at the bottom of the cylinder where the fluid flux was changing rapidly. A mesh analysis was performed until the solution was found to be independent of the mesh spacing.

S.2.2. Material Parameters

Using a collagen fiber density of 1.41 g cm^{-3} and assuming negligible collagen loss during gel preparation, the initial solid volume fractions were estimated to be 0.0014, 0.00248, and 0.00355 for the 1.98, 3.5, and 5 mg/mL gels, respectively [32]. The fluid density was set to have the same density as water. A Poisson's ratio of 0 was used since the circumferential sides of the collagen gel was held in place by the adapter, resulting in no lateral expansion during compression. The Holmes-Mow parameters, α and M, were taken from the experimental data fits. The Young's Modulus was adjusted to best match the pressure of the sample as it underwent compression (see section below for details on parameter fitting).

S.2.3 Boundary Conditions

The model was prescribed with the following boundary conditions and step sizes:

- The nodes of the bottom surface were constrained in the x, y, and z-directions. These fixed nodes represent the bottom of the sample in contact with the adapter support and the mesh, which does not move.
- The nodes of the top and circumferential surfaces were constrained in only the x and y-directions. The x and y-directions represent the lateral edges of the collagen held in place by the adapter. However, these surfaces could move in the z-direction to represent the compression of the collagen gel. A fluid flux of -0.178 mm/s was prescribed to the top surface based on the experimental volumetric flow rate of 0.014 mL s^{-1} and the inlet cross-sectional area of 0.785 cm^2.

- The nodes equivalent to the outlet size (circle with a 3.5 mm diameter) were prescribed at the bottom as a free-draining surface as seen by the red nodes in **Figure 56**. This setup represents the outside edges of the collagen gel in contact with the impermeable adapter support, with fluid flowing through the smaller outlet.

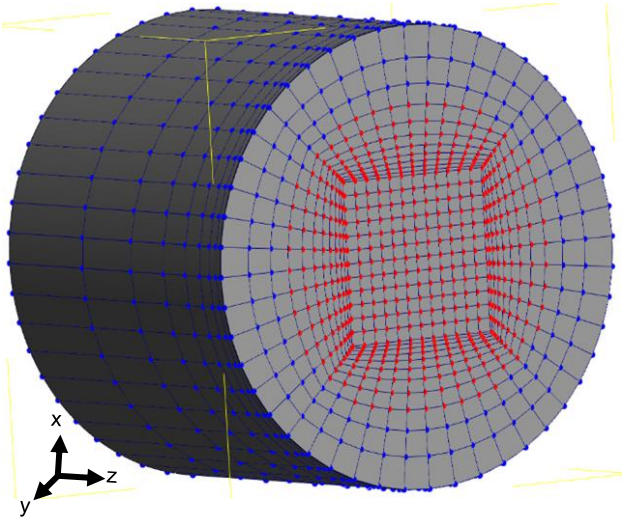

***Figure 56**: Selected nodes corresponding to the outlet of the FeBio model. Red nodes show the nodes selected for the free-draining surface and fluid flux conditions. The blue nodes indicate impermeable areas.*

- Since the volumetric flow rate was constant but the outlet had a smaller cross-sectional area than the inlet, a nodal fluid flux of 1.47 mm/s was prescribed to the same bottom surface nodes selected for the free-draining surface.

- The model ran for 200-time steps with a step size of 0.1 seconds.

- A linear pressure load was applied to the top surface and adjusted to match the maximum pressure seen experimentally. The curve editor was used such that the pressure load reached its maximum value at the very end of the run.

S.2.4 Parameter Fitting

The Young's modulus and pressure load were used as fitting parameters. The change in the elastic pressure due to the compressive stretch ratio calculated in FeBio was compared to the experimentally observed profile. The error was minimized using a damped least-squared method known as the Levenberg-Marquardt algorithm [9], [214]:

$$[J_{LM}^T W J_{LM} + diag(J_{LM}^T W J_{LM})]h = J_{LM}^T W (P - P_e)$$

[80]

where h is the update in the fitting parameters, λ is the damping factor, W is the weighting matrix, and J_{LM} is the Jacobian matrix that represents the sensitivity of the elastic pressure, P, to the change in the fitting parameters. J_{LM}^T is the transpose of J_{LM} .P_e is the pressure observed experimentally. The Jacobian was calculated numerically, and the simulation for the elastic pressure was calculated using FeBio as described above.

The fitting parameters were adjusted to minimize the chi-squared error criterion:

$$\chi^2 = \sum \left(\frac{P_i - P_{ei}}{\sigma} \right)^2$$

[81]

where P_{ei} is the experimentally measured pressure for a given compression stretch rate, and σ is the covariance.

S.3 Results

S.3.1 Model Predictions vs. Experimental Results

Figure 57 shows an example run at each collagen gel concentration of the change in pressure with compression, with **Figure 57** (a-c) providing a visual comparison of the actual experiment with model simulations, and (d - f) showing the model fits to the experimental data by varying the Young's Modulus in each case. The model pressure increased at a higher rate with increasing compression that matched well with experimental data. In addition, the final compressed length of the FeBio model was within 5% of the fully compressed length of the experimental collagen gel for each concentration, indicating that the neo-Hookean material could be used to reliably mimic the experimental data.

The fitted Young's Modulus values were found to be 120 Pa, 1020 Pa, and 2800 Pa for collagen gel concentrations of 1.98 mg/mL, 3.5 mg/mL, and 5 mg/mL, respectively, as shown in **Figure 57**g. These results are consistent with other published mechanical tests on collagen gels showing increased stiffness with increasing collagen gel concentrations [277–280].

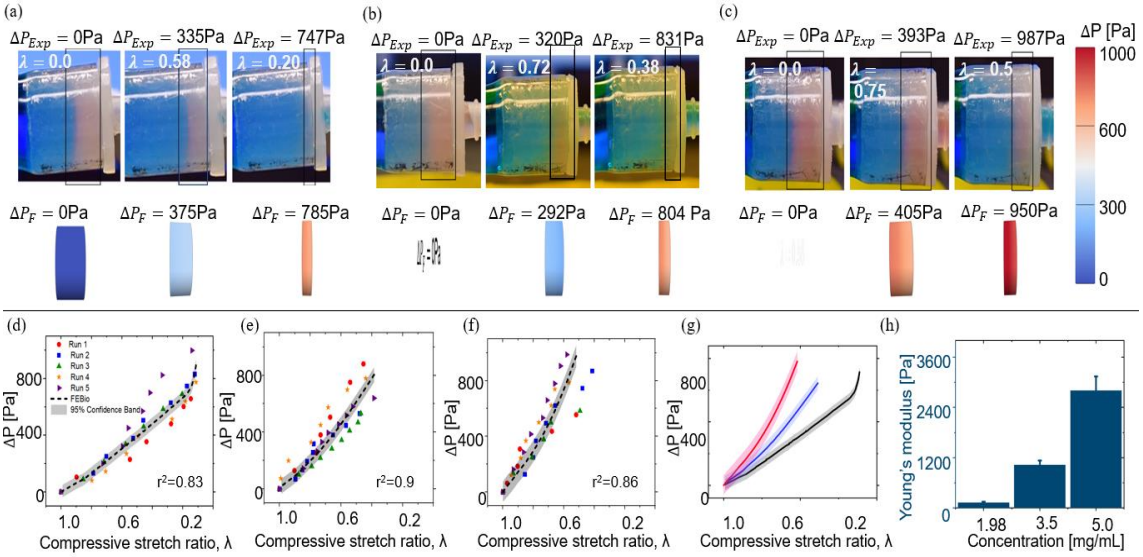

***Figure 57**: Comparison between FeBio model and experimental results. Representative example comparing the experimental results (top rows) vs. FeBio results (bottom rows) for 1.98 mg/mL collagen gels (left, a), 3.5 mg/mL collagen gels (middle, b), and 5 mg/mL collagen gels (right, c). Bottom graphs show pressure vs. compression of 5 experimental runs overlaid with the FeBio model of 1.98 mg/mL collagen gel (left, d), 3.5 mg/mL collagen gel (middle-left, e), and 5 mg/mL.*

Interestingly, at low collagen gel concentrations of 1.98mg/mL, the FeBio model showed the collagen gel compressed further in the middle compared to the edges (**Figure 58**); this phenomenon was not seen with the 3.5 or 5 mg/mL models. As seen in **Figure 58**(a), the center of the FeBio model had a final length of about 2.02 mm while the edges of the model had a final length of about 2.66 mm. This non-uniform compression is likely due to the fixed conditions assigned to the

boundaries in our model. Depending on the interaction between the gel and the

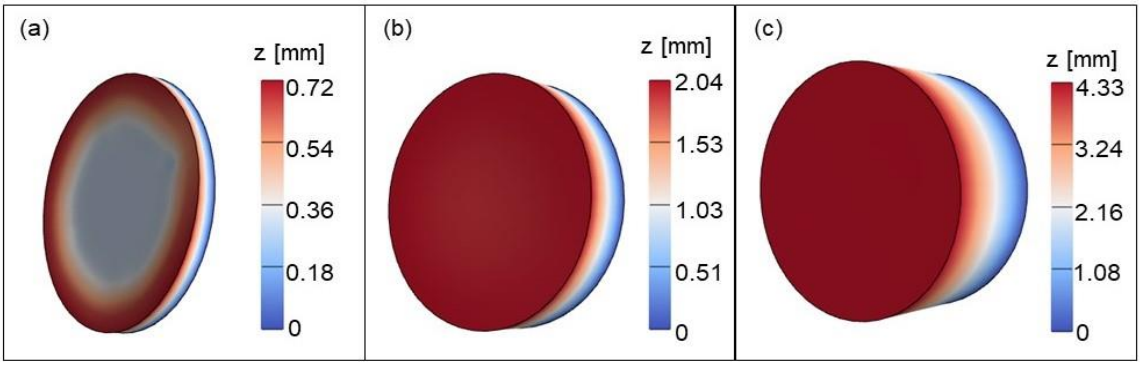

***Figure 58**. Final lengths for each collagen gel FeBio model. The 1.98 mg/mL collagen gel (left, a) compressed further in the center compared to the edge, likely due to the impermeable boundary.*

adapter wall, this same phenomenon could feasibly occur, although a different setup that can visualize the center of the sample would be required to confirm this experimentally.

The FeBio model also captured the magnitude and direction of fluid exiting the collagen gel cylinder as shown in **Figure 59**(a). Due to the impermeable adapter support along the outer edges of the collagen gel, the fluid around this region is forced towards the middle to be expelled out of the gel, resulting in a larger flux closer to the tube walls compared to the tube center. **Figure 59**(b) shows the volumetric flow rate (averaged over the entire outlet area) for the models created at each concentration. Similar trends are observed between the 3.5 mg/mL model and the 5 mg/mL model: a large initial jump in volumetric flow rate (corresponding to the initial jump in pressure at the start of the simulation) followed by a steady decrease towards the prescribed outlet fluid flux. Meanwhile, the 1.98 mg/mL model showed a similar initial jump in volumetric flow rate, followed by a steady

increase in the flow rate before a sudden drop to the prescribed volumetric flow rate. This is likely due to the increased compression of the 1.98 mg/mL collagen gel model since more interstitial fluid is expelled in the same time frame. In addition, flow rates vary inversely with collagen gel concentration, with the 5 mg/mL simulations exhibiting the lowest maximum flow rate. These results highlight the fact that interstitial fluid is expelled together with the water flowing through the sample; gels of lower concentration contain more interstitial fluid, hence a larger overall flow rate. However, it should be noted that without a flow meter at the outlet

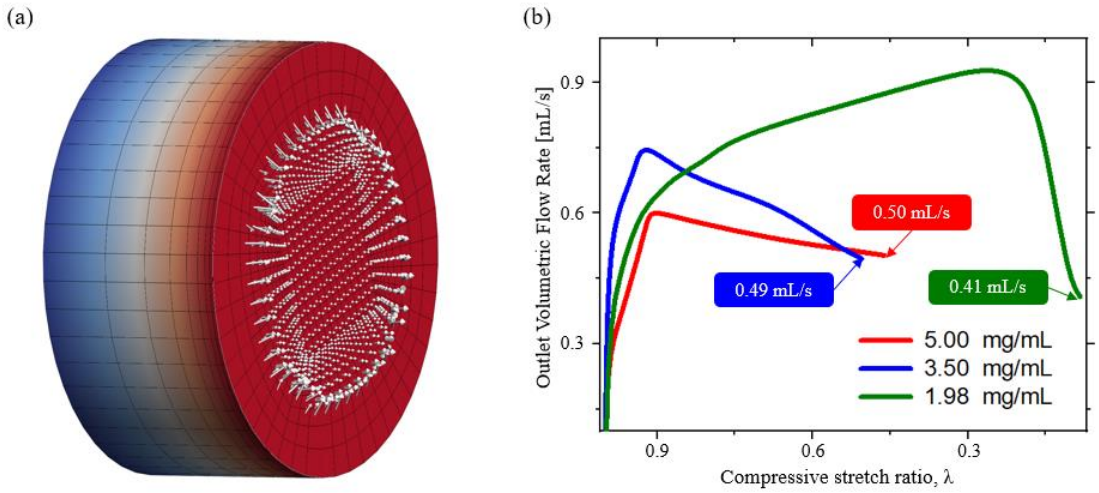

***Figure 59**: Magnitude and direction of fluid flux at the outlet (a). Fluid flux in the middle of the bottom surface is smaller than the edges of the outlet. Instantaneous volumetric flow rate vs. compressive stretch ratio (b). The outlet showed a greater initial volumetric flow rate before failing to the prescribed value. This was likely due to the expulsion of interstitial fluid as well as incoming fluid flux at the inlet.*

of the experimental setup to measure instantaneous flow rates, we were unable to confirm this phenomenon experimentally.

S4 Discussion

This paper determined the permeability of collagen hydrogels at various concentrations undergoing compression. As the collagen gel concentration increased, the corresponding initial permeability decreased, suggesting an inverse relationship between concentration and permeability. As the collagen gel concentration increases, the solid volume fraction increases, which provides greater resistance to fluid flow. The relationship shown here corroborates with the results found by Ramanujan [281],who found a permeability of about 1.00 x 10^{-15} m^2 for 10 mg/mL collagen gels and a permeability of about 1.00 x 10^{-16} m^2 for 45 mg/mL collagen gels. These collagen gels were held at a constant length (i.e., no compression) and the permeability values are 7-8 orders of magnitude smaller than the initial permeability found in this study. However, the collagen gels were initially compressed via ultracentrifugation and rehydrated at much higher concentrations than the ones produced in the present study. Conversely, another study by Varley et al. using freeze-dried collagen scaffolds found a corresponding permeability of 4.80 x 10^{-10} m^2 [282]. While the exact concentration of these scaffolds is unclear, the process of freeze-drying likely altered the composition and microstructure of the collagen network, resulting in differences in permeability values.

Our work, however, also showed an interesting result that initial gel concentration alone is not a good predictor of final gel permeability under flow-induced compression. The expected inverse relationship between gel concentration and

permeability was initially observed. However, the gel with the highest initial permeability showed the greatest amount of compression, resulting in the lowest final permeability. Microstructurally, collagen fibers are physical obstructions that hinder fluid flow, forcing the fluid to flow in tortuous paths through the network of fibers. As expected, the permeability of a collagen gel decreases as interstitial fluid is expelled, due to the densification of the collagen fibers as the network collapses onto itself. Even though the lower permeability is due to the greater degree of compression, the flip in relationship between gel concentration and final permeability after compression is counterintuitive since a higher initial density of collagen fibers should still provide higher resistance to flow after compression. This interesting phenomenon could be due to microstructural differences between the collagen networks of different concentrations whose effects become significant once the networks are densified. Previous studies have shown that microstructural differences such as fibril length distribution, connectivity and fibril diameters of an ECM network may occur due to changes in gelation conditions [279, 283, 284]. In varying the ratio of collagen and acetic acid to create gels of different concentrations, the collagen network architecture may be profoundly altered which could affect its ability to compress and its permeability, e.g., pore size, network tortuosity, or amount of entrapped fluid within the densified network. In addition, anisotropic and inhomogeneous deformations as the collagen network compresses and densifies may have profound effects on gel permeability that may not be easily modeled [262].

In comparing our fitted Young's Modulus values to published literature, previous studies have shown a wide range of the Young's Modulus of collagen gels, depending on the type of mechanical testing performed. Lai, et al. performed uniaxial tensile tests on 1.98 mg/mL collagen rings looped over T-bar grips [283] and found a tangent modulus of 7750 Pa. While this value is much larger than the Young's modulus value of 120 Pa fitted in the current study, significant differences in tensile versus compressive properties are to be expected with soft gels such as collagen gels. For example, a study by van Oosten et al. subjecting 2.5 mg/mL collagen gels to both a compressive and a tensile stress-relaxation test found the tensile Young's modulus to be 6520 Pa compared to a much lower Young's modulus in compression of 29.1 Pa [285]. These values are, however, computed at the relaxed state, which would yield much lower values compared to the compressed gels in this study which do not have time to relax. A similar mechanical test applying a 5% stepwise strain to a confined 1.5 mg/mL collagen gel yielded an equilibrium compressive modulus of 175 Pa [286]. Knapp et al. [287] conducted two different mechanical compression tests on 2 mg/mL collagen gels: a compression creep test for 5h which estimated an aggregate modulus of 6.32 Pa, and a ramp compression test to 10% strain in 120 seconds which found a short-time modulus of 318.3 Pa. This latter test is most similar to our collagen gels compressing under pressure-driven flow, and this short-time modulus is in good agreement with our 1.98 mg/mL collagen results. Taken together, the vastly different permeabilities and compressive moduli from different studies highlight the

challenges of characterizing properties of natural biomaterials such as collagen gels, which can be highly dependent on many different factors such as processing/casting techniques, biomaterial source, and testing protocols (especially so with the mechanical testing of viscoelastic materials).

This work may also be extended to the densification of collagen networks in cell-seeded tissue engineering constructs. Collagen gels contract when populated with cells, thereby changing the transport and biomechanical properties of the collagen. The degree of contraction is dependent on many factors; for instance, the current study shows the degree of compression decreases with higher initial collagen gel concentrations, consistent with other studies [288]. The cell density, incubation time, and the specific cells populated within the collagen-cell lattice can also impact the contraction of collagen gels [288, 289]. For example, Cheih, et al. found that bone marrow stromal cells contracted collagen gels to an area less than 5% of the initial area after 4 days of incubation [290]. Zagai et al. found that collagen gels in the presence of fibroblasts and eosinophils contracted to a range between 40 – 97 % of the initial collagen gel, depending on the specific composition of the cells used [291]. Feng et al. found that collagen gels in the presence of fetal bovine serum and human fibroblast contract to a final area of about 13% the original size[292]. How the transport properties of collagen gels change under this contraction was analyzed in the current study. Specifically, the permeabilities of 1.98 mg/mL, 3.5 mg/mL, and 5 mg/mL collagen gels were determined as they compressed to 14%, 40%, and 45% of the original lengths, respectively. The study by Cheih et al.

showed collagen gels contracted to a greater extent than the ones in the current study, likely due to the longer incubation times. Meanwhile, the studies by Zagai et al. and Feng et al. showed similar contraction amounts compared to the collagen gels analyzed in the current study. Therefore, the permeability values found can be used to aid in tissue engineering, specifically towards better understanding and better design of culture conditions for the delivery of nutrients to cells as the bioengineered tissue grows and remodels over time.

Appendix B: A novel perfusion bioreactor promotes the expansion of pluripotent stem cells in a 3D-bioprinted tissue chamber.

The work presented is my contribution to the overall paper.

*Komosa, Elizabeth R., Wei-Han Lin, Bhushan Mahadik, **Marisa S. Bazzi**, DeWayne Townsend, John P. Fisher, and Brenda M. Ogle. "A novel perfusion bioreactor promotes the expansion of pluripotent stem cells in a 3D-bioprinted tissue chamber." Biofabrication 16, no. 1 (2023): 014101.*

Summary

While the field of tissue engineering has progressed rapidly with the advent of 3D bioprinting and human induced pluripotent stem cells (hiPSCs), impact is limited by a lack of functional, thick tissues. One way around this limitation is to 3D bioprint tissues laden with hiPSCs. In this way, the iPSCs can proliferate to populate the thick tissue mass prior to parenchymal cell specification. Here we design a perfusion bioreactor for an hiPSC-laden, 3D-bioprinted chamber with the goal of

proliferating the hiPSCs throughout the structure prior to differentiation to generate a thick tissue model. The bioreactor, fabricated with digital light projection, was optimized to perfuse the interior of the hydrogel chamber without leaks and to provide fluid flow around the exterior as well, maximizing nutrient delivery throughout the chamber wall. After 7 days of culture, we found that intermittent perfusion (15 s every 15 min) at 3 ml min−1 provides a 1.9-fold increase in the density of stem cell colonies in the engineered tissue relative to analogous chambers cultured under static conditions. We also observed a more uniform distribution of colonies within the tissue wall of perfused structures relative to static controls, reflecting a homogeneous distribution of nutrients from the culture media. hiPSCs remained pluripotent and proliferative with application of fluid flow, which generated wall shear stresses averaging ∼1.0 dyne cm^2. Overall, these promising outcomes following perfusion of a stem cell-laden hydrogel support the production of multiple tissue types with improved thickness, and therefore increased function and utility.

S.2 Materials and methods

S.2.1. Computational simulations

To create a computational model of fluid flow in the hChaMP, pressure under flow was measured at the inlet and outlet of the bioreactor. Briefly, an acellular hChaMP was inserted in the bioreactor and attached for flow, as described above. A hemostasis valve (Qosina, cat#80395) was placed at the base of the bioreactor

inlet or outlet to allow insertion of a pressure catheter in the set-up. Pressure profiles were measured with an ADV500 PV system and a 1.4 Fr pressure catheter (Transonic) with data acquisition at a sampling rate of 5000 Hz. The interior flow was resolved using fluid–solid interaction (FSI) approach in SimVascular [213]. The wall was described using a neo-Hookean model with an elastic modulus of 1.96 kPa, per experimental results. The fluid was modeled as Newtonian with a viscosity of 1 cP. A waveform was used to describe the intermittent flow in the inlet, and a pressure matching the experimental results was imposed as boundary condition at the outlet. Simulations were run on the Minnesota Supercomputing Institute for ten cycles in order to stabilize the pressure in the system. The exterior flow was resolved using Ansys Fluent, release 20.1, assuming rigid walls. Like the interior flow simulations, the fluid was described as Newtonian fluid with a viscosity of 1 cP, and a waveform was imposed as the inlet boundary condition, with the flow rate matching the outlet results from the interior flow simulations. The outlet was set as zero-reference pressure.

S.3 Results

Upon completion of a bioreactor design that provided both interior and exterior flow, flow rates for perfusion were considered. Flow rates were optimized to minimize the shear stress experienced by cells in the hChaMP while also providing adequate nutrients throughout the entirety of the chamber. A flow rate of 3 ml min−1 was used, as rates below this did not allow fluid to reach the bottom of the chamber before exiting the chamber, creating dead zones of no flow (**Figure 60**(a)).

However, continuous flow at this rate or higher damaged the hydrogel; thus, intermittent perfusion was tested. Infrequent perfusion, 1 min every 30–60 min, caused little cell growth, presumably due to the lack of oxygen exchange within the bioreactor and hChaMP and limited waste removal. Therefore, intermittent perfusion at 15 s every 15 min was employed. This duration of flow allowed for full media changes within the interior of the hChaMP, and the frequency supported cell survival within the tissue.

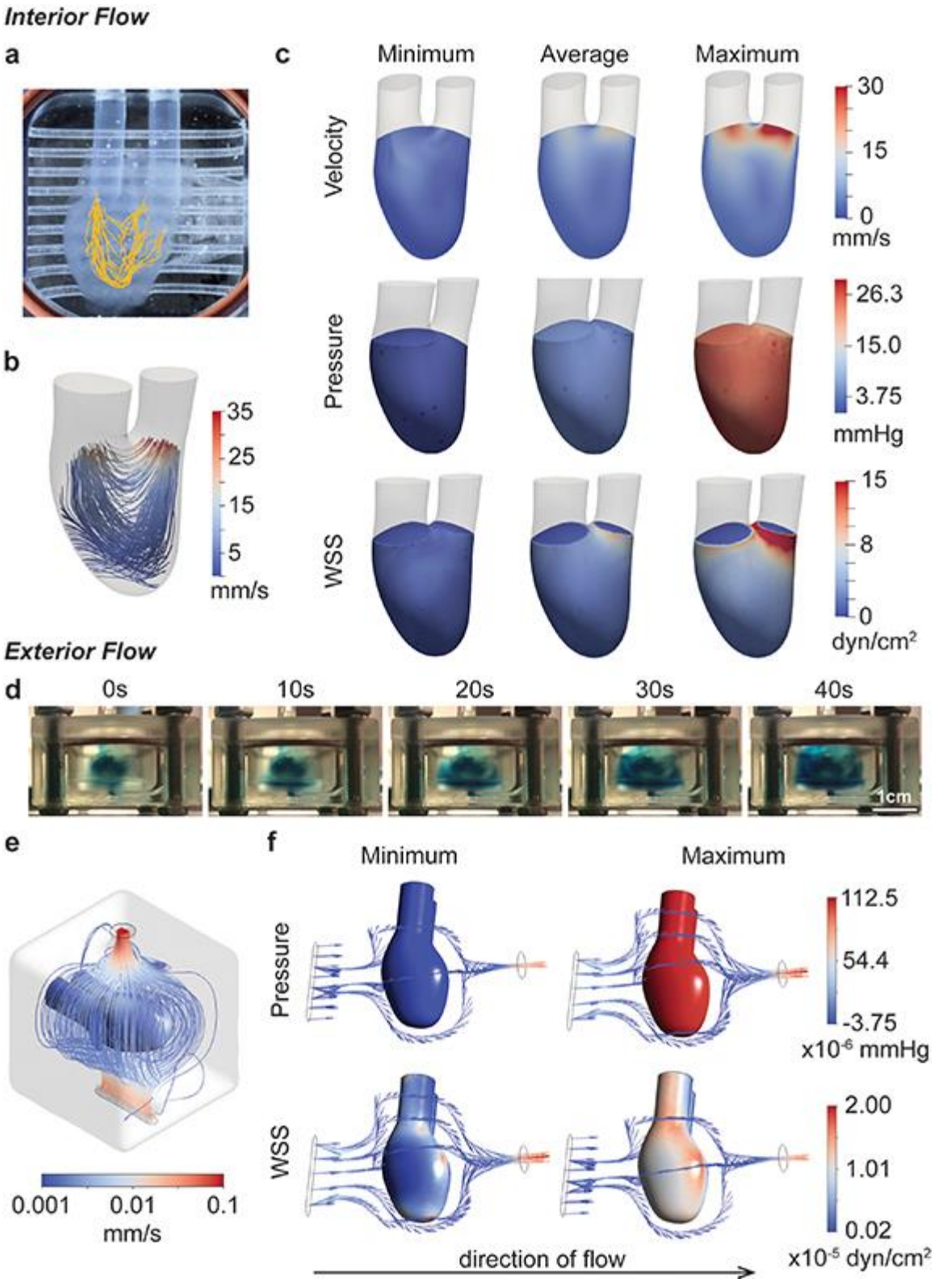
Interior Flow
a
b
35
25
15
5
mm/s
c
Minimum
Average
Maximum
Velocity
30
15
0
mm/s
Pressure
26.3
15.0
3.75
mmHg
WSS
15
8
0
dyn/cm²
Exterior Flow
d
0s
10s
20s
30s
40s
1cm
e
0.001
0.01
0.1
mm/s
f
Minimum
Maximum
Pressure
112.5
54.4
-3.75
x10⁻⁶ mmHg
WSS
2.00
1.01
0.02
x10⁻⁵ dyn/cm²
direction of flow

***Figure 60**: Fluid flow characterization. (a), (b) Flow patterns through the hChaMP chamber are summarized through particle tracking (a) and computational fluid dynamics (b). (c) Computational models provided estimates for the impact of perfusion on velocity, pressure, and wall shear stress on the interior hChaMP wall. (d) Summary of flow around the exterior of the hChaMP, demonstrated using DPBS dyed with blue food coloring. Fluid flow around the exterior is slow relative to flow through the interior of the hChaMP. (e) Computational model of flow profiles around the exterior of the hChaMP. (f) Computationally approximated values of pressure and wall shear stress caused by exterior fluid flow (with the direction of flow shown here from left to right).*

S.3.2 Approximations of fluid flow parameters

To approximate the effects of fluid flow on the hChaMP, particularly pressure and shear stress at the hChaMP walls, computational simulations were generated. Pressure profiles were measured at the hChaMP inlet and outlet using a pressure catheter inserted into a hemostasis valve at the base of Ini or Outi. Measured maximum, minimum, and average of the pressure profiles were used as the input for hChaMP flow in the computational model. SimVascular svFSI solver, an open-source software tailored for cardiovascular simulations [293], was used to solve for the internal flow profiles in the hChaMP. The software has been previously validated against in vitro models and has demonstrated its effectiveness in describing flow dynamics[294]. With this software and the 3D model of the hChaMP, fluid flow profiles matched those found from the in vitro experiment (figures 45(b)), confirming the ability of the model to replicate the system. This allowed for computation of the generated shear stress on the inner wall of the hChaMP, a critical parameter in stem cell culture.

Pressures within the hChaMP were found to be fairly uniform, where variations throughout a single pump cycle matched experimental value, with an average around 4.5–5.3 mmHg and a maximum of 25.5 mmHg (figure 45(c)). Pressure was negative at its minimum, reflecting what is seen during the pulsatile cycling of the pump. This variability in pressure did not appear to cause issues on the integrity of the hChaMP after several days of perfusion. Wall shear stress was less variable, with an average value around 1.0 dyn cm−2, and a maximum of 2.7 dyn cm−2 through most of the hChaMP chamber, although drastically increasing near Outi as fluid exited the chamber, reaching up to 15.0 dyn cm−2 (figure 45(c)).

Owing to the intricate geometries present in the external flow, Ansys Fluent was used to solve the external flow profiles. Fluent serves as a commercial alternative to the open-source SimVascular and has been extensively utilized to demonstrate fluid flow patterns in the cardiovascular system, including in vitro models [295]. Solving the external flow profiles enabled computation of wall shear stress on the exterior wall of the hChaMP. Pressures and wall shear stresses were much lower on the exterior, likely due to the large compartment size of the bioreactor and a pressure drop from Outi to Ine, leading to lower flow rates around the hChaMP (figures 45(d)–(f)).

Interestingly, pressure on the exterior depended on the location analyzed. The underside, where the fluid first contacts the hChaMP, had a higher maximum pressure than the upper side; yet the difference is fairly small, with a maximum pressure 1.13 × 10−4 mmHg for the underside and 1.05 × 10−4 mmHg for the

upper portion. Similar to the pressures found for interior flow, the minimum pressure on the exterior of the hChaMP is slightly negative, but on the magnitude of 10−6 mmHg. Wall shear stress was also much lower than on the interior, ranging from values on the order of 10−7–10−5 dyn cm−2 (figure 45(f)). Overall, interior wall shear stresses were found to be in a similar range as, and exterior shear stresses much lower than, values found in common bioreactors for stem cell expansion, which have been reported around 0.7–2.5 dyn cm−2 [296–298]. Moreover, stem cells embedded in hydrogels were found able to withstand stresses greater than 30 dyn cm−2 [299], suggesting the shear stresses approximated for our set-up are reasonable for hiPSC expansion.